Dynamical Systems in Neuroscience

Computational Neuroscience

Terrence J. Sejnowski and Tomaso A. Poggio, editors

Neural Nets in Electric Fish, Walter Heiligenberg, 1991

The Computational Brain, Patricia S. Churchland and Terrence J. Sejnowski, 1992

Dynamic Biological Networks: The Stomatogastric Nervous System, edited by Ronald M. Harris-Warrick, Eve Marder, Allen I. Selverston, and Maurice Maulins, 1992

The Neurobiology of Neural Networks, edited by Daniel Gardner, 1993

Large-Scale Neuronal Theories of the Brain, edited by Christof Koch and Joel L. Davis, 1994

The Theoretical Foundations of Dendritic Function: Selected Papers of Wilfrid Rall with Commentaries, edited by Idan Segev, John Rinzel, and Gordon M. Shepherd, 1995

Models of Information Processing in the Basal Ganglia, edited by James C. Houk, Joel L. Davis, and David G. Beiser, 1995

Spikes: Exploring the Neural Code, Fred Rieke, David Warland, Rob de Ruyter van Stevenick, and William Bialek, 1997

Neurons, Networks, and Motor Behavior, edited by Paul S. Stein, Sten Grillner, Allen I. Selverston, and Douglas G. Stuart, 1997

Methods in Neuronal Modeling: From Ions to Networks, second edition, edited by Christof Koch and Idan Segev, 1998

Fundamentals of Neural Network Modeling: Neuropsychology and Cognitive Neuroscience, edited by Randolph W. Parks, Daniel S. Levin, and Debra L. Long, 1998

Neural Codes and Distributed Representations: Foundations of Neural Computation, edited by Laurence Abbott and Terrence J. Sejnowski, 1999

Unsupervised Learning: Foundations of Neural Computation, edited by Geoffrey Hinton and Terrence J. Sejnowski, 1999

Fast Oscillations in Cortical Circuits, Roger D. Traub, John G.R. Jefferys, and Miles Al Whittington, 1999

Computational Vision: Information Processing in Perception and Visual Behavior, Hanspeter A. Mallot, 2000

Graphical Models: Foundations of Neural Computation, edited by Michael I. Jordan and Terrence J. Sejnowski, 2001

Self-Organizing Map Formation: Foundation of Neural Computation, edited by Klaus Obermayer and Terrence J. Sejnowski, 2001

Theoretical Neuroscience: Computational and Mathematical Modeling of Neural Systems, Peter Dayan and L. F. Abbott, 2001

Neural Engineering: Computation, Representation, and Dynamics in Neurobiological Systems, Chris Eliasmith and Charles H. Anderson, 2003

The Computational Neurobiology of Reaching and Pointing, edited by Reza Shadmehr and Steven P. Wise, 2005

Dynamical Systems in Neuroscience: The Geometry of Excitability and Bursting, Eugene M. Izhikevich, 2007

Dynamical Systems in Neuroscience:
The Geometry of Excitability and Bursting

Eugene M. Izhikevich

The MIT Press
Cambridge, Massachusetts
London, England

To my beautiful daughters, Liz and Kate.

Contents

Preface

Historically, much of theoretical neuroscience research concerned neuronal circuits and synaptic organization. The neurons were divided into excitatory and inhibitory types, but their electrophysiological properties were largely neglected or taken to be identical to those of Hodgkin-Huxley's squid axon. The present awareness of the importance of the electrophysiology of individual neurons is best summarized by David McCormick in the fifth edition of Gordon Shepherd's book *The Synaptic Organization of the Brain*:

> Information-processing depends not only on the *anatomical* substrates of synaptic circuits but also on the *electrophysiological* properties of neurons... Even if two neurons in different regions of the nervous system possess identical morphological features, they may respond to the same synaptic input in very different manners because of each cell's intrinsic properties.
>
> McCormick (2004)

Much of present neuroscience research concerns voltage- and second-messenger-gated currents in individual cells, with the goal of understanding the cell's intrinsic neurocomputational properties. It is widely accepted that knowing the currents suffices to determine what the cell is doing and why it is doing it. This, however, contradicts a half-century–old observation that cells having similar currents can nevertheless exhibit quite different dynamics. Indeed, studying isolated axons having presumably similar electrophysiology (all are from the crustacean *Carcinus maenas*), Hodgkin (1948) injected a DC-current of varying amplitude, and discovered that some preparations could exhibit repetitive spiking with arbitrarily low frequencies, while the others discharged in a narrow frequency band. This observation was largely ignored by the neuroscience community until the seminal paper by Rinzel and Ermentrout (1989), who showed that the difference in behavior is due to different *bifurcation* mechanisms of excitability.

Let us treat the amplitude of the injected current in Hodgkin's experiments as a bifurcation parameter: When the amplitude is small, the cell is quiescent; when the amplitude is large, the cell fires repetitive spikes. When we change the amplitude of the injected current, the cell undergoes a transition from quiescence to repetitive spiking. From the dynamical systems point of view, the transition corresponds to a bifurcation from equilibrium to a limit cycle attractor. The type of bifurcation determines the most fundamental computational properties of neurons, such as the class of excitability, the existence or nonexistence of threshold, all-or-none spikes, subthreshold oscillations, the ability to generate postinhibitory rebound spikes, bistability of resting and spiking states, whether the neuron is an integrator or a resonator, and so on.

This book is devoted to a systematic study of the relationship between electrophysiology, bifurcations, and computational properties of neurons. The reader will learn why cells having nearly identical currents may undergo distinct bifurcations, and hence they will have fundamentally different neurocomputational properties. (Conversely, cells

having quite different currents may undergo identical bifurcations, and hence they will have similar neurocomputational properties.) The major message of the book can be summarized as follows (compare with the McCormick statement above):

> Information-processing depends not only on the electrophysiological properties of neurons but also on their *dynamical properties.* Even if two neurons in the same region of the nervous system possess similar electrophysiological features, they may respond to the same synaptic input in very different manners because of each cell's bifurcation dynamics.

Nonlinear dynamical system theory is a core of computational neuroscience research, but it is not a standard part of the graduate neuroscience curriculum. Neither is it taught in most math/physics departments in a form suitable for a general biological audience. As a result, many neuroscientists fail to grasp such fundamental concepts as equilibrium, stability, limit cycle attractor, and bifurcations, even though neuroscientists constantly encounter these nonlinear phenomena.

This book introduces dynamical systems starting with simple one- and two-dimensional spiking models and continuing all the way to bursting systems. Each chapter is organized from simple to complex, so everybody can start reading the book; only the reader's background will determine where he or she stops. The book emphasizes the geometrical approach, so there are few equations but a lot of figures. Half of them are simulations of various neural models, so there are hundreds of possible exercises such as "Use MATLAB (GENESIS, NEURON, XPPAUT, etc.) and parameters in the caption of figure X to simulate the figure." Additional problems are provided at the end of each chapter; the reader is encouraged to solve at least some of them and to look at the solutions of the others at the end of the book. Problems marked [**M.S.**] or [**Ph.D.**] are suggested thesis topics.

Eugene M. Izhikevich   `www.izhikevich.com`
San Diego, California   December 19, 2005

Chapter 1

Introduction

This chapter highlights some of the most important concepts developed in the book. First, we discuss several common misconceptions regarding the spike generation mechanism of neurons. Our goal is to motivate the reader to think of a neuron not only in terms of ions and channels, as many biologists do, and not only in terms of an input/output relationship, as many theoreticians do, but also as a nonlinear dynamical system that looks at the input through the prism of its own intrinsic dynamics. We ask such questions as "What makes a neuron fire?" or "Where is the threshold?", and then outline the answers, using the geometrical theory of dynamical systems.

From a dynamical systems point of view, neurons are excitable because they are near a transition, called bifurcation, from resting to sustained spiking activity. While there is a huge number of possible ionic mechanisms of excitability and spike generation, there are only four bifurcation mechanisms that can result in such a transition. Considering the geometry of phase portraits at these bifurcations, we can understand many computational properties of neurons, such as the nature of threshold and all-or-none spiking, the coexistence of resting and spiking states, the origin of spike latencies, postinhibitory spikes, and the mechanism of integration and resonance. Moreover, we can understand how these properties are interrelated, why some are equivalent, and why some are mutually exclusive.

1.1   Neurons

If somebody were to put a gun to the head of the author of this book and ask him to name the single most important concept in brain science, he would say it is the concept of a *neuron*. There are only 10^{11} or so neurons in the human brain, much fewer than the number of non-neural cells such as glia. Yet neurons are unique in the sense that only they can transmit electrical signals over long distances. From the neuronal level we can go down to cell biophysics and to the molecular biology of gene regulation. From the neuronal level we can go up to neuronal circuits, to cortical structures, to the whole brain, and finally to the behavior of the organism. So let us see how much we understand of what is going on at the level of individual neurons.
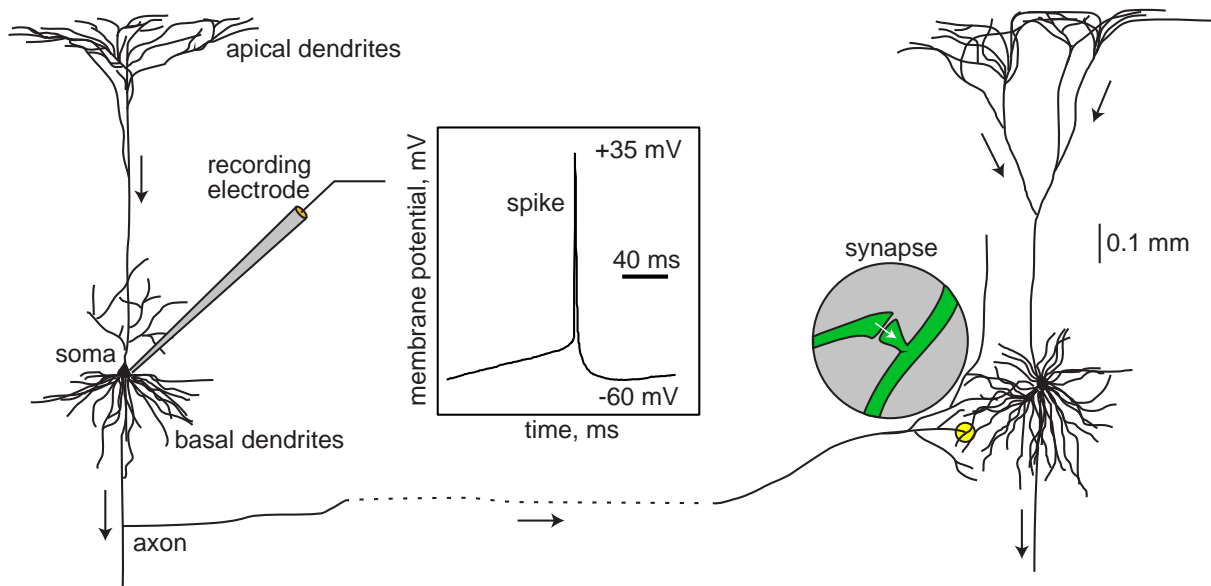
Figure 1.1: Two interconnected cortical pyramidal neurons (hand drawing) and in vitro recorded spike.

1.1.1   What Is a Spike?

A typical neuron receives inputs from more than $10,000$ other neurons through the contacts on its dendritic tree called synapses; see Fig.1.1. The inputs produce electrical transmembrane currents that change the membrane potential of the neuron. Synaptic currents produce changes, called postsynaptic potentials (PSPs). Small currents produce small PSPs; larger currents produce significant PSPs that can be amplified by the voltage-sensitive channels embedded in the neuronal membrane and lead to the generation of an *action potential* or *spike* – an abrupt and transient change of membrane voltage that propagates to other neurons via a long protrusion called an axon.

Such spikes are the main means of communication between neurons. In general, neurons do not fire on their own; they fire as a result of incoming spikes from other neurons. One of the most fundamental questions of neuroscience is *What, exactly, makes neurons fire?* What is it in the incoming pulses that elicits a response in one neuron but not in another? Why can two neurons have different responses to exactly the same input and identical responses to completely different inputs? To answer these questions, we need to understand the dynamics of spike generation mechanisms of neurons.

Most introductory neuroscience books describe neurons as integrators with a threshold: neurons sum incoming PSPs and "compare" the integrated PSP with a certain voltage value, called the firing threshold. If it is below the threshold, the neuron remains quiescent; when it is above the threshold, the neuron fires an all-or-none spike, as in Fig.1.3, and resets its membrane potential. To add theoretical plausibility to this argument, the books refer to the Hodgkin-Huxley model of spike generation in squid

Figure 1.2: What makes a neuron fire?

giant axons, which we study in chapter 2. The irony is that the Hodgkin-Huxley model does not have a well-defined threshold; it does not fire all-or-none spikes; and it is not an integrator, but a resonator (i.e., it prefers inputs having certain frequencies that resonate with the frequency of subthreshold oscillations of the neuron). We consider these and other properties in detail in this book.

1.1.2 Where Is the Threshold?

Much effort has been spent trying to experimentally determine the firing thresholds of neurons. Here, we challenge the classical view of a threshold. Let us consider two typical experiments, depicted in Fig.1.4, that are designed to measure the threshold. in Fig.1.4a, we shock a cortical neuron (i.e., we inject brief but strong pulses of current of various amplitudes to depolarize the membrane potential to various values). Is there a clear-cut voltage value, as in Fig.1.3, above which the neuron fires but below which no spikes occur? If you find one, let the author know! In Fig.1.4b we inject long but weak pulses of current of various amplitudes, which results in slow depolarization and a spike. The firing threshold, if it exists, must be somewhere in the shaded region, but where? Where does the slow depolarization end and the spike start? Is it meaningful to talk about firing thresholds at all?
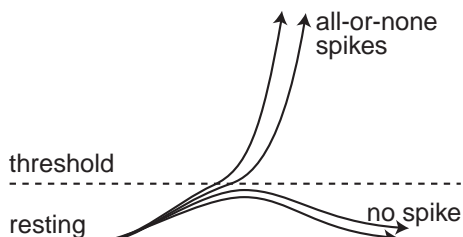
Figure 1.3: The concept of a firing threshold.
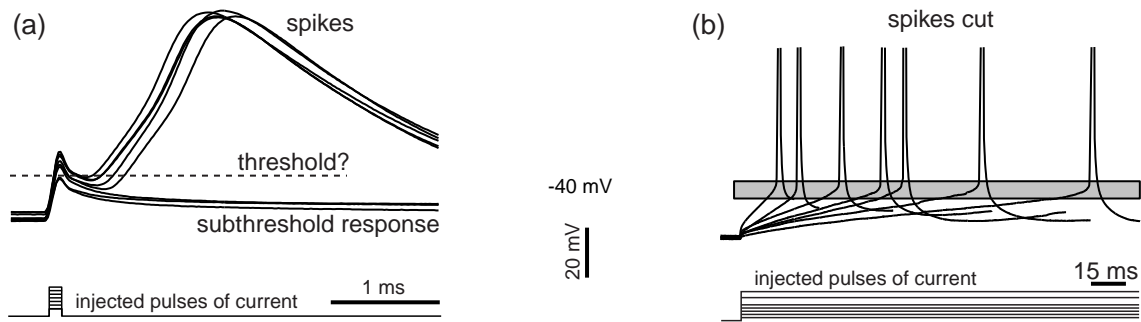
Figure 1.4: Where is the firing threshold? Shown are in vitro recordings of two layer 5 rat pyramidal neurons. Notice the differences of voltage and time scales.
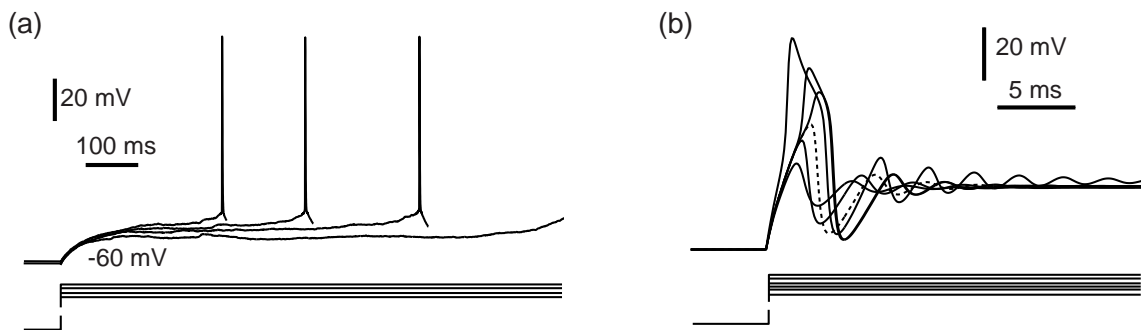
Figure 1.5: Where is the rheobase (i.e., the minimal current that fires the cell)? (a) in vitro recordings of the pyramidal neuron of layer 2/3 of a rat's visual cortex show increasing latencies as the amplitude of the injected current decreases. (b) Simulation of the $I_{\mathrm{Na,p}}+I_{\mathrm{K}}-$model (pronounced: *persistent sodium plus potassium model*) shows spikes of graded amplitude.

Perhaps, we should measure current thresholds instead of voltage thresholds. The current threshold (i.e., the minimal amplitude of injected current of infinite duration needed to fire a neuron) is called the *rheobase*. In Fig.1.5 we decrease the amplitudes of injected pulses of current to find the minimal one that still elicits a spike or the maximal one that does not. In Fig.1.5a, progressively weaker pulses result in longer latencies to the first spike. Eventually the neuron does not fire because the latency is longer than the duration of the pulse, which is 1 second in the figure. Did we really measure the neuronal rheobase? What if we waited a bit longer? How long is long enough? In Fig.1.5b the latencies do not grow, but the spike amplitudes decrease until the spikes do not look like spikes at all. To determine the current threshold, we need to draw the line and separate spike responses from "subthreshold" ones. How can we do that if the spikes are not all-or-none? Is the response denoted by the dashed line a spike?

Risking adding more confusion to the notion of a threshold, consider the following. If excitatory inputs depolarize the membrane potential (i.e., bring it closer to
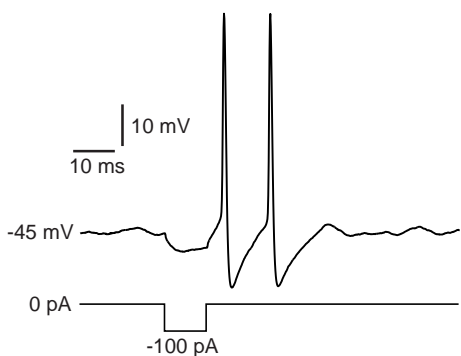
Figure 1.6: In vitro recording of rebound spikes of a rat's brainstem mesV neuron in response to a brief hyperpolarizing pulse of current.
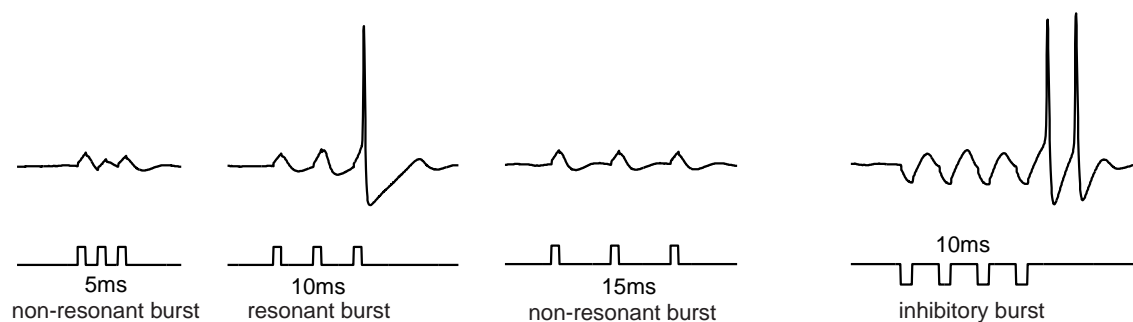
Figure 1.7: Resonant response of the mesencephalic V neuron of a rat's brainstem to pulses of injected current having a 10 ms period (in vitro).

the "firing threshold"), and inhibitory inputs hyperpolarize the potential and move it away from the threshold, then *how can the neuron in Fig.1.6 fire in response to the inhibitory input?* This phenomenon, also observed in the Hodgkin-Huxley model, is called anodal break excitation, rebound spike, or postinhibitory spike. Many biologists say that rebound responses are due to the activation and inactivation of certain slow currents, which bring the membrane potential over the threshold or, equivalently, lower the threshold upon release from the hyperpolarization – a phenomenon called a low-threshold spike in thalamocortical neurons. The problem with this explanation is that neither the Hodgkin-Huxley model nor the neuron in Fig.1.6 has these currents, and even if they did, the hyperpolarization is too short and too weak to affect the currents.

Another interesting phenomenon is depicted in Fig.1.7. The neuron is stimulated with brief pulses of current mimicking an incoming burst of three spikes. When the stimulation frequency is high (5 ms period), presumably reflecting a strong input, the neuron does not fire at all. However, stimulation with a lower frequency (10 ms period) that resonates with the frequency of subthreshold oscillation of the neuron evokes a spike response, regardless of whether the stimulation is excitatory or inhibitory. Stimulation with even lower frequency (15 ms period) cannot elicit spike response again. Thus, the neuron is sensitive only to the inputs having resonant frequency. The same pulses applied to a cortical pyramidal neuron evoke a response only in the first case (small period), but not in the other cases.

1.1.3   Why Are Neurons Different, and Why Do We Care?

Why would two neurons respond completely differently to the same input? A biologist would say that the response of a neuron depends on many factors, such as the type of voltage- and Ca^{2+}-gated channels expressed by the neuron, the morphology of its dendritic tree, the location of the input, and other factors. These factors are indeed important, but they do not determine the neuronal response per se. Rather they determine the rules that govern dynamics of the neuron. Different conductances and currents can result in the same rules, and hence in the same responses; conversely, similar currents can result in different rules and in different responses. The currents define what kind of dynamical system the neuron is.

We study ionic transmembrane currents in chapter 2. In subsequent chapters we investigate how the types of currents determine neuronal dynamics. We divide all currents into two major classes: amplifying and resonant, with the persistent Na^+ current $I_{Na,p}$ and the persistent K^+ current I_K being the typical examples of the former and the latter, respectively. Since there are tens of known currents, purely combinatorial argument implies that there are millions of different electrophysiological mechanisms of spike generation. We will show later that any such mechanism must have at least one amplifying and one resonant current. Some mechanisms, called minimal in this book, have one resonant and one amplifying current. They provide an invaluable tool in classifying and understanding the electrophysiology of spike generation.

Many illustrations in this book are based on simulations of the reduced $I_{Na,p} + I_K$-model (pronounced *persistent sodium plus potassium model*), which consists of a fast persistent Na^+ (amplifying) current and a slower persistent K^+ (resonant) current. It is equivalent to the famous and widely used Morris-Lecar $I_{Ca}+I_K$-model (Morris and Lecar 1981). We show that the model exhibits quite different dynamics, depending on the values of the parameters, e.g., the half-activation voltage of the K^+ current: in one case, it can fire in a narrow frequency range, it can exhibit coexistence of resting and spiking states, and it has damped subthreshold oscillations of membrane potential. In another case, it can fire in a wide frequency range and show no coexistence of resting and spiking and no subthreshold oscillations. Thus, seemingly inessential differences in parameter values could result in drastically distinct behaviors.

1.1.4   Building Models

To build a good model of a neuron, electrophysiologists apply different pharmacological blockers to tease out the currents that the neuron has. Then they apply different stimulation protocols to measure the kinetic parameters of the currents, such as the Boltzmann activation function, time constants, and maximal conductances. We consider all these functions in chapter 2. Next, they create a Hodgkin-Huxley-type model and simulate it using the NEURON, GENESIS, or XPP environment or MATLAB (the first two are invaluable tools for simulating realistic dendritic structures).

The problem is that the parameters are measured in different neurons and then put together into a single model. As an illustration, consider two neurons having the same
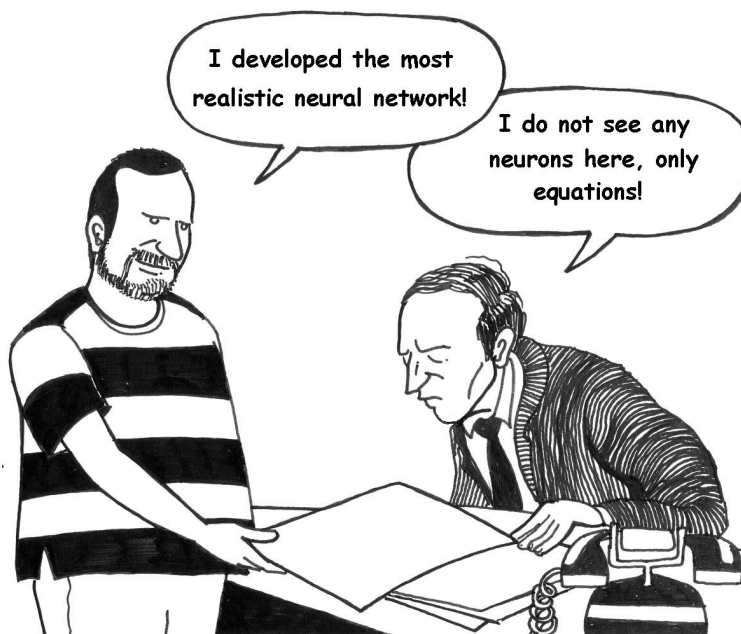
Figure 1.8: Neurons are dynamical systems.

currents, say $I_{\text{Na,p}}$ and I_{K}, and exhibiting excitable behavior; that is, both neurons are quiescent but can fire a spike in response to a stimulation. Suppose the second neuron has stronger $I_{\text{Na,p}}$, which is balanced by stronger I_{K}. If we measure Na^+ conductance using the first neuron and K^+ conductance using the second neuron, the resulting $I_{\text{Na,p}} + I_{\text{K}}$-model will have an excess of K^+ current and probably will not be able to fire spikes at all. Conversely, if we measure Na^+ and K^+ conductances using the second neuron and then the first neuron, respectively, the model would have too much Na^+ current and probably would exhibit sustained pacemaking activity. In any case, the model fails to reproduce the excitable behavior of the neurons whose parameters we measured.

Some of the parameters cannot be measured at all, so many arbitrary choices are made via a process called "fine-tuning". Navigating in the dark, possibly with the help of some biological intuition, the researcher modifies parameters, compares simulations with experiment, and repeats this trial-and-error procedure until he or she is satisfied with the results. Since seemingly similar values of parameters can result in drastically different behaviors, and quite different parameters can result in seemingly similar behaviors, how do we know that the resulting model is correct? How do we know that its behavior is equivalent to that of the neuron we want to study? And what is *equivalent* in this case? Now, you are primed to consider dynamical systems. If not, see Fig.1.8.

1.2   Dynamical Systems

In chapter 2 we introduce the Hodgkin-Huxley formalism to describe neuronal dynamics in terms of activation and inactivation of voltage-gated conductances. An important result of the Hodgkin-Huxley studies is that *neurons are dynamical systems*, so they should be studied as such. Below we mention some of the important concepts of dynamical systems theory. The reader does not have to follow all the details of this section because the concepts are explained in greater detail in subsequent chapters.

A dynamical system consists of a set of variables that describe its state and a law that describes the evolution of the state variables with time (i.e., how the state of the system in the next moment of time depends on the input and its state in the previous moment of time). The Hodgkin-Huxley model is a four-dimensional dynamical system because its state is uniquely determined by the membrane potential, V, and so-called gating variables n, m, and h for persistent K^+ and transient Na^+ currents. The evolution law is given by a four-dimensional system of ordinary differential equations.

Typically, all variables describing neuronal dynamics can be classified into four classes, according to their function and the time scale.

1. *Membrane potential.*

2. *Excitation variables*, such as activation of a Na^+ current. These variables are responsible for the upstroke of the spike.

3. *Recovery variables*, such as inactivation of a Na^+ current and activation of a fast K^+ current. These variables are responsible for the repolarization (downstroke) of the spike.

4. *Adaptation variables*, such as activation of slow voltage- or Ca^{2+}-dependent currents. These variables build up during prolonged spiking and can affect excitability in the long run.

The Hodgkin-Huxley model does not have variables of the fourth type, but many neuronal models do, especially those exhibiting bursting dynamics.

1.2.1   Phase Portraits

The power of the dynamical systems approach to neuroscience, as well as to many other sciences, is that we can tell something, or many things, about a system without knowing all the details that govern the system evolution. We do not even use equations to do that! Some may even wonder why we call it a mathematical theory.

As a start, let us consider a quiescent neuron whose membrane potential is resting. From the dynamical systems point of view, there are no changes of the state variables of such a neuron; hence it is at an equilibrium point. All the inward currents that depolarize the neuron are balanced, or equilibrated, by the outward currents that hyperpolarize it. If the neuron remains quiescent despite small disturbances and membrane noise, as in Fig.1.9a (top), then we conclude that the equilibrium is stable. Isn't
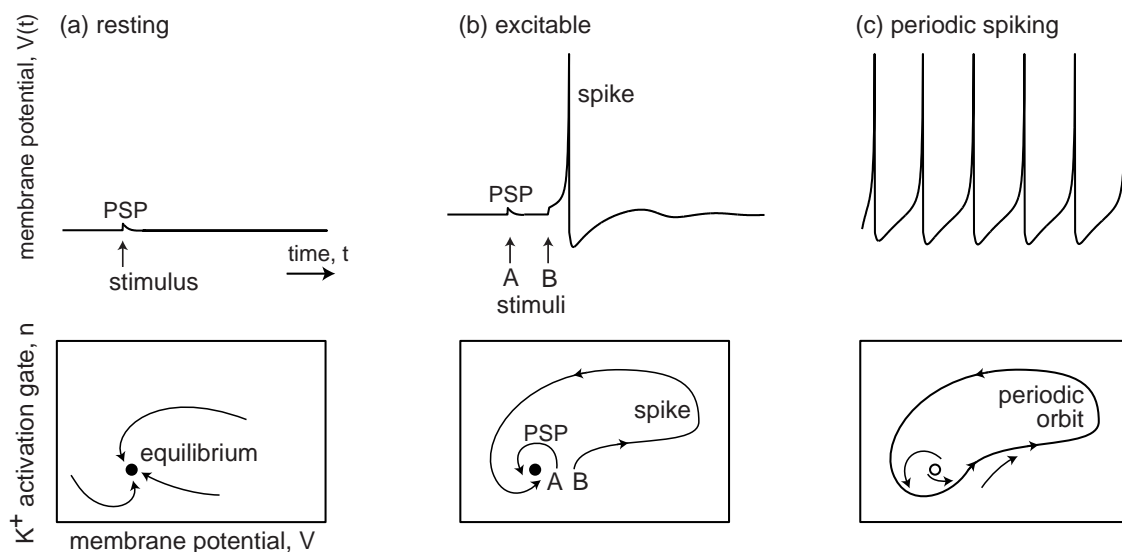
Figure 1.9: Resting, excitable, and periodic spiking activity correspond to a stable equilibrium (a and b) or limit cycle (c), respectively.

it amazing that we can reach such a conclusion without knowing the equations that describe the neuron's dynamics? We do not even know the number of variables needed to describe the neuron; it could be infinite, for all we care.

In this book we introduce the notions of equilibria, stability, threshold, and attraction domains using one- and two-dimensional dynamical systems, e.g., the $I_{\mathrm{Na,p}}+I_{\mathrm{K}}$-model with instantaneous Na^+ kinetics. The state of this model is described by the membrane potential, V, and the activation variable, n, of the persistent K^+ current, so it is a two-dimensional vector (V, n). Instantaneous activation of the Na^+ current is a function of V, so it does not result in a separate variable of the model. The evolution of the model is a trajectory $(V(t), n(t))$ on the $V \times n$ –plane. Depending on the initial point, the system can have many trajectories, such as those depicted in Fig.1.9a (bottom). Time is not explicitly present in the figure, but units of time may be thought of as plotted along each trajectory. All of the trajectories in the figure are attracted to the stable equilibrium denoted by the black dot, called an *attractor*. The overall qualitative description of dynamics can be obtained through the study of the *phase portrait* of the system, which depicts certain special trajectories (equilibria, separatrices, limit cycles) that determine the topological behavior of all the other trajectories in the phase space. Probably 50 percent of illustrations in this book are phase portraits.

A fundamental property of neurons is *excitability*, illustrated in Fig.1.9b. The neuron is resting, i.e., its phase portrait has a stable equilibrium. Small perturbations, such as A, result in small excursions from the equilibrium, denoted as PSP (postsynaptic potential). Larger perturbations, such as B, are amplified by the neuron's intrinsic dynamics and result in the spike response. To understand the dynamic mechanism of such amplification, we need to consider the geometry of the phase portrait near the resting equilibrium, i.e., in the region where the decision to fire or not to fire is made.
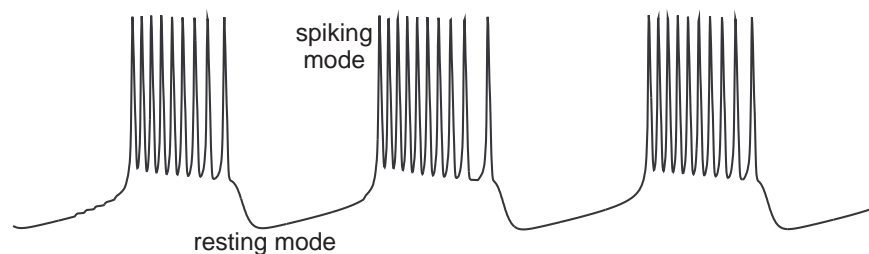
Figure 1.10: Rhythmic transitions between resting and spiking modes result in bursting behavior.
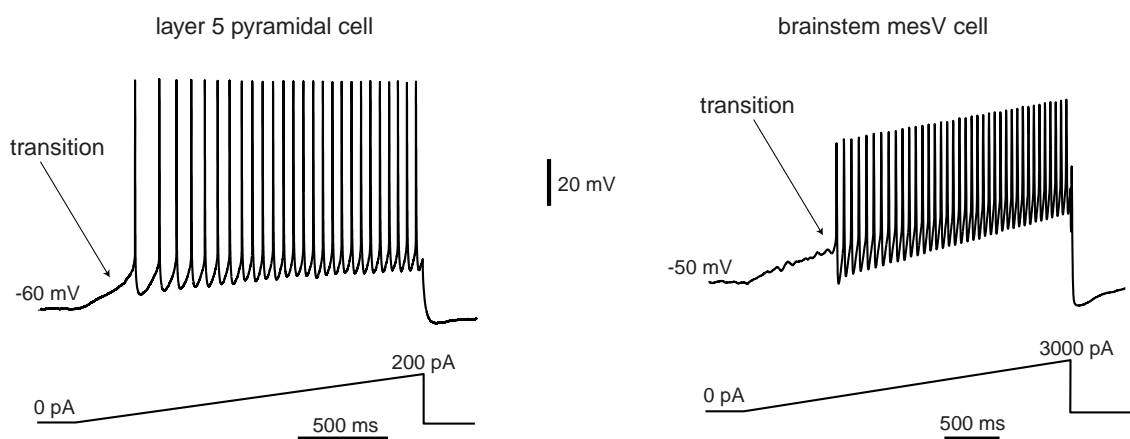
Figure 1.11: As the magnitude of the injected current slowly increases, the neurons bifurcate from resting (equilibrium) mode to tonic spiking (limit cycle) mode.

If we inject a sufficiently strong current into the neuron, we bring it to a pacemaking mode, so that it exhibits periodic spiking activity, as in Fig.1.9c. From the dynamical systems point of view, the state of such a neuron has a stable limit cycle, also known as a stable periodic orbit. The electrophysiological details of the neuron (i.e., the number and the type of currents it has, their kinetics, etc.) determine only the location, the shape, and the period of the limit cycle. As long as the limit cycle exists, the neuron can have periodic spiking activity. Of course, equilibria and limit cycles can coexist, so a neuron can be switched from one mode to another by a transient input. The famous example is the permanent extinguishing of ongoing spiking activity in the squid giant axon by a brief transient depolarizing pulse of current applied at a proper phase (Guttman et al. 1980) – a phenomenon predicted by John Rinzel (1978) purely on the basis of theoretical analysis of the Hodgkin-Huxley model. The transition between resting and spiking modes could be triggered by intrinsic slow conductances, resulting in the bursting behavior in Fig.1.10.

1.2.2 Bifurcations

Now suppose that the magnitude of the injected current is a parameter that we can control, e.g., we can ramp it up, as in Fig.1.11. Each cell in the figure is quiescent at the beginning of the ramps, so its phase portrait has a stable equilibrium and it may look like the one in Fig.1.9a or Fig.1.9b. Then it starts to fire tonic spikes, so its phase portrait has a limit cycle attractor and it may look like the one in Fig.1.9c, with a white circle denoting an unstable resting equilibrium. Apparently there is some intermediate level of injected current that corresponds to the transition from resting to sustained spiking, i.e., from the phase portrait in Fig.1.9b to Fig.1.9c. What does the transition look like?

From the dynamical systems point of view, the transition corresponds to a *bifurcation* of neuron dynamics, i.e., a qualitative change of phase portrait of the system. For example, there is no bifurcation going from the phase portrait in Fig.1.9a to that in Fig.1.9b, since both have one globally stable equilibrium; the difference in behavior is quantitative but not qualitative. In contrast, there is a bifurcation going from Fig.1.9b to Fig.1.9c, since the equilibrium is no longer stable and another attractor, limit cycle, has appeared. The neuron is not excitable in Fig.1.9a but it is in Fig.1.9b, simply because the former phase portrait is far from the bifurcation and the latter is near.

In general, neurons are excitable *because* they are near bifurcations from resting to spiking activity, so the type of the bifurcation determines the excitable properties of the neuron. Of course, the type depends on the neuron's electrophysiology. An amazing observation is that there could be millions of different electrophysiological mechanisms of excitability and spiking, but there are only four – yes, *four* – different types of bifurcations of equilibrium that a system can undergo without any additional constraints, such as symmetry. Thus, considering these four bifurcations in a general setup, we can understand excitable properties of many models, even those that have not been invented yet. What is even more amazing, we can understand excitable properties of neurons whose currents are not measured and whose models are not known, provided we can experimentally identify which of the four bifurcations the resting state of the neuron undergoes.

The four bifurcations are summarized in Fig.1.12, which plots the phase portrait before (left), at (center), and after (right) a particular bifurcation occurs. Mathematicians refer to these bifurcations as being of codimension-1 because we need to vary only one parameter, e.g., the magnitude of the injected DC current I, to observe the bifurcations reliably in simulations or experiments. There are many more codimension-2, 3, (etc.), bifurcations, but they need special conditions to be observed. We discuss these in chapter 6.

Let us consider the four bifurcations and their phase portraits in Fig.1.12. The horizontal and vertical axes are the membrane potential with instantaneous activation variable and a recovery variable, respectively. At this stage, the reader is not required to fully understand the intricacies of the phase portraits in the figure, since they will be explained systematically in later chapters.
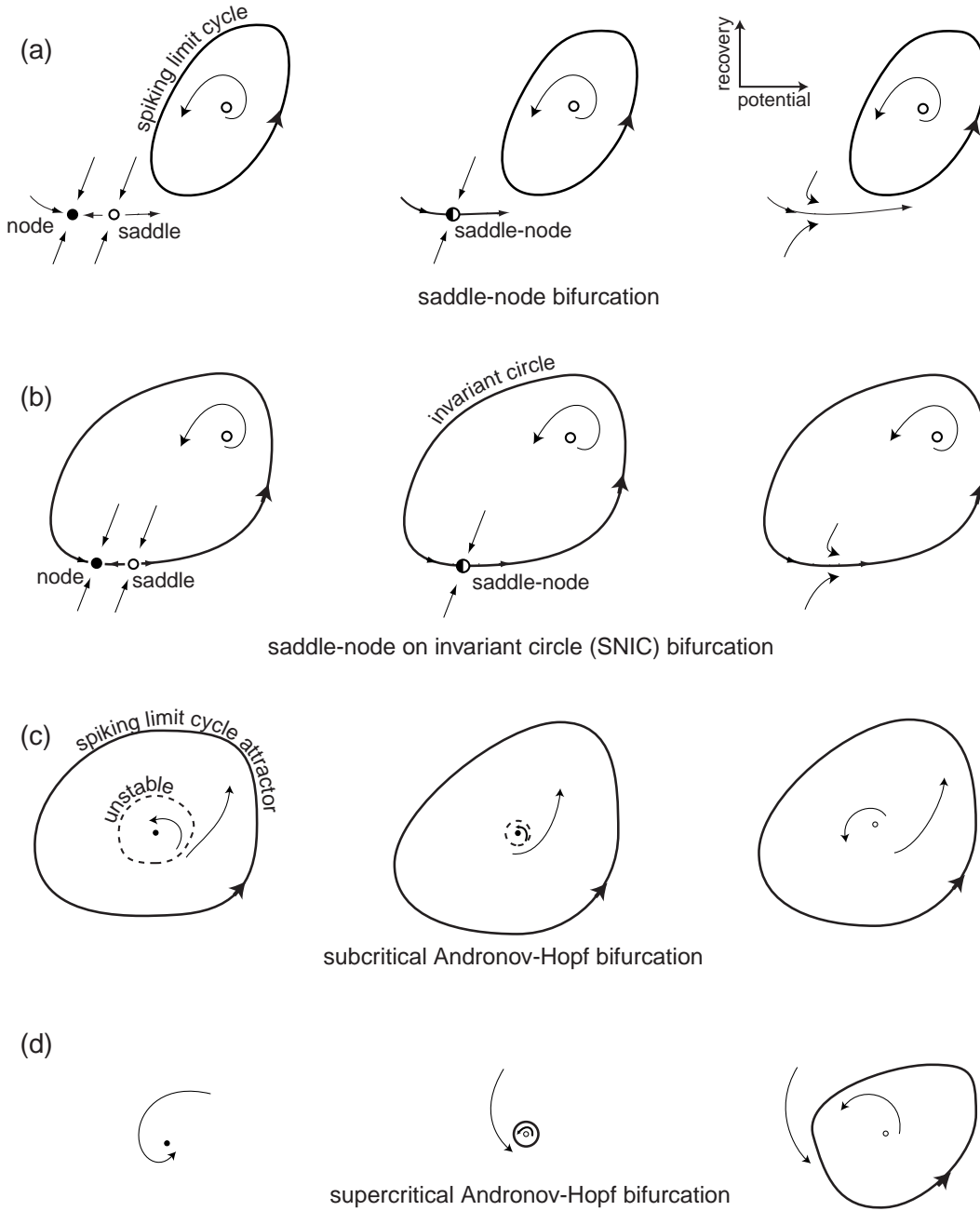
Figure 1.12: Four generic (codimension-1) bifurcations of an equilibrium state leading to the transition from resting to periodic spiking behavior in neurons.

- *Saddle-node bifurcation.* As the magnitude of the injected current or any other bifurcation parameter changes, a stable equilibrium corresponding to the resting state (black circle marked "node" in Fig.1.12a) is approached by an unstable equilibrium (white circle marked "saddle"); they coalesce and annihilate each other, as in Fig.1.12a (middle). Since the resting state no longer exists, the trajectory describing the evolution of the system jumps to the limit cycle attractor, indicating that the neuron starts to fire tonic spikes. Notice that the limit cycle, or some other attractor, must coexist with the resting state in order for the transition resting → spiking to occur.

- *Saddle-node on invariant circle bifurcation* is similar to the saddle-node bifurcation except that there is an invariant circle at the moment of bifurcation, which then becomes a limit cycle attractor, as in Fig.1.12b.

- *Subcritical Andronov-Hopf bifurcation.* A small unstable limit cycle shrinks to a stable equilibrium and makes it lose stability, as in Fig.1.12c. Because of instabilities, the trajectory diverges from the equilibrium and approaches a large-amplitude spiking limit cycle or some other attractor.

- *Supercritical Andronov-Hopf bifurcation.* The stable equilibrium loses stability and gives birth to a small-amplitude limit cycle attractor, as in Fig.1.12d. As the magnitude of the injected current increases, the amplitude of the limit cycle increases and it becomes a full-size spiking limit cycle.

Notice that there is a coexistence of resting and spiking states in the case of saddle-node and subcritical Andronov-Hopf bifurcations, but not in the other two cases. Such a coexistence reveals itself via a hysteresis behavior when the injected current slowly increases and then decreases past the bifurcation value, because the transitions "resting → spiking" and "spiking → resting" occur at different values of the current. In addition, brief stimuli applied at the appropriate times can switch the activity from spiking to resting and back. There are also spontaneous noise-induced transitions between the two modes that result in the stuttering spiking that, for instance, is exhibited by the so-called fast spiking (FS) cortical interneurons when they are kept close to the bifurcation (Tateno et al. 2004). Some bistable neurons have a slow adaptation current that activates during the spiking mode and impedes spiking, often resulting in bursting activity.

Systems undergoing Andronov-Hopf bifurcations, whether subcritical or supercritical, exhibit damped oscillations of membrane potential, whereas systems near saddle-node bifurcations, whether on or off an invariant circle, do not. The existence of small amplitude oscillations creates the possibility of resonance to the frequency of the incoming pulses, as in Fig.1.7, and other interesting features.

We refer to neurons with damped subthreshold oscillations as *resonators* and to those that do not have this property as *integrators.* We refer to the neurons that exhibit the coexistence of resting and spiking states, at least near the transition from

coexistence of resting and spiking states

Figure 1.13: Classification of neurons into monostable/bistable integrators/resonators according to the bifurcation of the resting state in Fig.1.12.
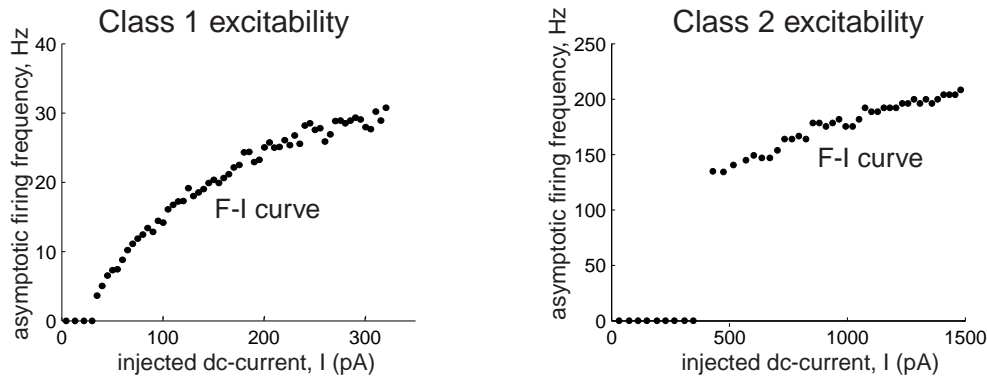
Figure 1.14: Frequency-current (F-I) curves of cortical pyramidal neuron and brainstem mesV neuron from Fig.7.3. These are the same neurons used in the ramp experiment in Fig.1.11.

resting to spiking, as *bistable*, and to those that do not, *monostable*. The four bifurcations in Fig.1.12 are uniquely defined by these two features. For example, a bistable resonator is a neuron undergoing subcritical Andronov-Hopf bifurcation, and a monostable integrator is a neuron undergoing saddle-node on invariant circle bifurcation (see Fig.1.13). Cortical fast spiking (FS) and regular spiking (RS) neurons, studied in chapter 8, are typical examples of the former and the latter, respectively.

1.2.3   Hodgkin Classification

Hodgkin (1948) was the first to study bifurcations in neuronal dynamics, years before the mathematical theory of bifurcations was developed. He stimulated squid axons with pulses of various amplitudes and identified three classes of responses:

- *Class 1 neural excitability.* Action potentials can be generated with arbitrarily low frequency, depending on the strength of the applied current.

- *Class 2 neural excitability.* Action potentials are generated in a certain frequency band that is relatively insensitive to changes in the strength of the applied current.

- *Class 3 neural excitability.* A single action potential is generated in response to a pulse of current. Repetitive (tonic) spiking can be generated only for extremely strong injected currents or not at all.

The qualitative distinction between the classes is that the frequency-current relation (the F-I curve in Fig.1.14) starts from zero and continuously increases for Class 1 neurons, is discontinuous for Class 2 neurons, and is not defined at all for Class 3 neurons.

Obviously, neurons belonging to different classes have different neurocomputational properties. Class 1 neurons, which include cortical excitatory pyramidal neurons, can smoothly encode the strength of the input into the output firing frequency, as in Fig.1.11 (left). In contrast, Class 2 neurons, such as fast-spiking (FS) cortical inhibitory interneurons, cannot do that; instead, they fire in a relatively narrow frequency band, as in Fig.1.11 (right). Class 3 neurons cannot exhibit sustained spiking activity, so Hodgkin regarded them as "sick" or "unhealthy". There are other distinctions between the classes, which we discuss later.

Different classes of excitability occur because neurons have different bifurcations of resting and spiking states – a phenomenon first explained by Rinzel and Ermentrout (1989). If ramps of current are injected to measure the F-I curves, then Class 1 excitability occurs when the neuron undergoes the saddle-node bifurcation on an invariant circle depicted in Fig.1.12b. Indeed, the period of the limit cycle attractor is infinite at the bifurcation point, and then it decreases as the bifurcation parameter – say, the magnitude of the injected current – increases. The other three bifurcations result in Class 2 excitability. Indeed, the limit cycle attractor exists and has a finite period when the resting state in Fig.1.12 undergoes a subcritical Andronov-Hopf bifurcation, so emerging spiking has a nonzero frequency. The period of the small limit cycle attractor appearing via supercritical Andronov-Hopf bifurcation is also finite, so the frequency of oscillations is nonzero, but their amplitudes are small. In contrast to the common and erroneous folklore, the saddle-node bifurcation (off-limit cycle) also results in Class 2 excitability because the limit cycle has a finite period at the bifurcation. There is a considerable latency (delay) to the first spike in this case, but the subsequent spiking has nonzero frequency. Thus, the simple scheme "Class 1 = saddle-node, Class 2 = Hopf" that permeates many publications is unfortunately incorrect.

When pulses of current are used to measure the F-I curve, as in Hodgkin's experiments, the firing frequency depends on factors besides the type of the bifurcation of the resting state. In particular, low-frequency firing can be observed in systems near Andronov-Hopf bifurcations, as we show in chapter 7. To avoid possible confusion, we define the class of excitability only on the basis of slow ramp experiments.

Hodgkin's classification has an important historical value, but it is of little use for the dynamic description of a neuron, since naming a class of excitability of a neuron does not tell much about the bifurcations of the resting state. Indeed, it says only that saddle-node on invariant circle bifurcation (Class 1) is different from the other three bifurcations (Class 2), and only when ramps are injected. Dividing neurons into

integrators and resonators with bistable or monostable activity is more informative, so we adopt the classification in Fig.1.13 in this book. In this classification, a Class 1 neuron is a monostable integrator, whereas a Class 2 neuron can be a bistable integrator or a resonator.

1.2.4   Neurocomputational properties

Using the same arrangement as in Fig.1.13, we depict typical geometry of phase portraits near the four bifurcations in Fig.1.15. Let us use the portraits to explain what happens "near the threshold", i.e., near the place where the decision to fire or not to fire is made. To simplify our geometrical analysis, we assume here that neurons receive shock inputs, i.e., brief but strong pulses of current that do not change the phase portraits, but only push or reset the state of the neuron into various regions of the phase space. We consider these and other cases in detail in chapter 7.

The horizontal axis in each plot in Fig.1.15 corresponds to the membrane potential V with instantaneous Na^+ current, and the vertical axis corresponds to a recovery variable, say activation of K^+ current. Black circles denote stable equilibria corresponding to the neuronal resting state. Spiking limit cycle attractors correspond to sustained spiking states, which exist in the two cases depicted in the left half of the figure corresponding to the bistable dynamics. The limit cycles are surrounded by shaded regions – their attraction domains. The white region is the attraction domain of the equilibrium. To initiate spiking, the external input should push the state of the system into the shaded region, and to extinguish spiking, the input should push the state back into the white region.

There are no limit cycles in the two cases depicted in the right half of the figure, so the entire phase space is the attraction domain of the stable equilibrium, and the dynamics are monostable. However, if the trajectory starts in the shaded region, it makes a large-amplitude rotation before returning to the equilibrium – a transient spike. Apparently, to elicit such a spike, the input should push the state of the system into the shaded region.

Now let us contrast the upper and lower halves of the figure, corresponding to integrators and resonators, respectively. We distinguish these two modes of operation on the basis of the existence of subthreshold oscillations near the equilibrium.

First, let us show that *inhibition impedes spiking in integrators, but can promote it in resonators.* In the integrator, the shaded region is in the depolarized voltage range, i.e., to the right of the equilibrium. Excitatory inputs push the state of the system toward the shaded region, while inhibitory inputs push it away. In resonators, both excitation and inhibition push the state toward the shaded region, because the region wraps around the equilibrium and can be reached along any direction. This explains the rebound spiking phenomenon depicted in Fig.1.6.

Integrators have all-or-none spikes; resonators may not. Indeed, any trajectory starting in the shaded region in the upper half of Fig.1.15 has to rotate around the

saddle-node bifurcation

saddle-node on invariant circle bifurcation

subcritical Andronov-Hopf bifurcation

supercritical Andronov-Hopf bifurcation
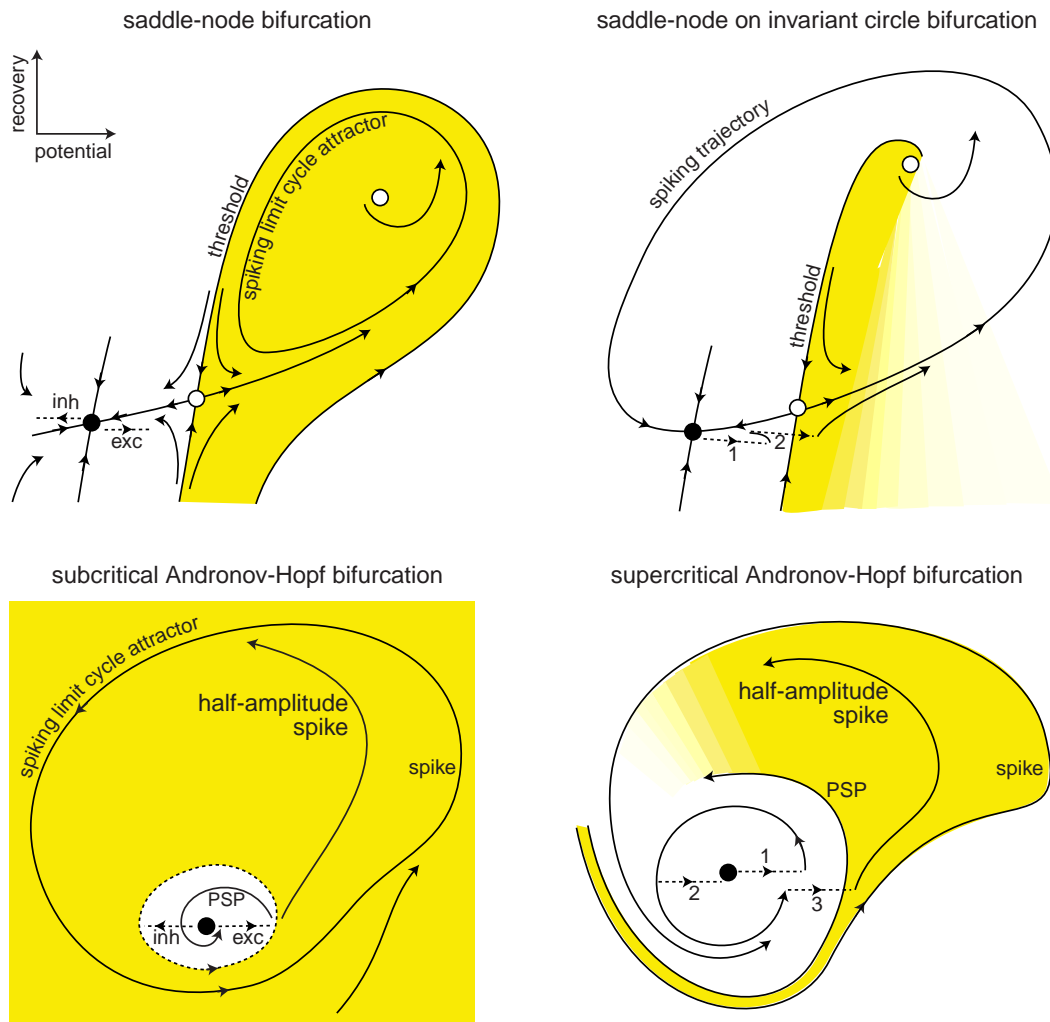
Figure 1.15: The geometry of phase portraits of excitable systems near four bifurcations can explain many neurocomputational properties (see section 1.2.4 for details).

white circle at the top that corresponds to an unstable equilibrium. Moreover, the state of the system is quickly attracted to the spiking trajectory and moves along that trajectory, thereby generating a stereotypical spike. A resonator neuron also can fire large amplitude spikes when its state is pushed to or beyond the trajectory denoted "spike". Such neurons generate subthreshold responses when the state slides along the smaller trajectory denoted PSP; they also can generate spikes of an intermediate amplitude when the state is pushed between the PSP and "spike" trajectories, which explains the partial-amplitude spiking in Fig.1.5b or in the squid axon in Fig.7.26. The set of initial conditions corresponding to such spiking is quite small, so typical spikes have large amplitudes and partial spikes are rare.

   Integrators have well-defined thresholds; resonators may not. The white circles near the resting states of integrators in Fig.1.15 are called saddles. They are stable along the

vertical direction and unstable along the horizontal direction. The two trajectories that lead to the saddle along the vertical direction are called separatrices because they separate the phase space into two regions – in this case, white and shaded. The separatrices play the role of thresholds since only those perturbations that push the state of the system beyond them result in a spike. The closer the state of the system is to the separatrices, the longer it takes to converge and then diverge from the saddle, resulting in a long *latency to the spike*. Notice that the threshold is not a point, but a tilted curve that spans a range of voltage values.

Resonators have a well-defined threshold in the case of subcritical Andronov-Hopf bifurcation: it is the small unstable limit cycle that separates the attraction domains of stable equilibrium and spiking limit cycle. Trajectories inside the small cycle spiral toward the stable equilibrium, whereas trajectories outside the cycle spiral away from it and eventually lead to sustained spiking activity. When a neuronal model is far from the subcritical Andronov-Hopf bifurcation, its phase portrait may look similar to the one corresponding to the supercritical Andronov-Hopf bifurcation. The narrow shaded band in the figure is not a threshold manifold but a fuzzy threshold set called "quasi-threshold" by FitzHugh (1955). Many resonators, including the Hodgkin-Huxley model, have quasi-thresholds instead of thresholds. The width of the quasi-threshold in the Hodgkin-Huxley model is so narrow that for all practical reasons it may be assumed to be just a curve.

Integrators integrate, resonators resonate. Now consider inputs consisting of multiple pulses, e.g., a burst of spikes. Integrators prefer high-frequency inputs; the higher the frequency, the sooner they fire. Indeed, the first spike of such an input, marked "1" in the top-right phase portrait in Fig.1.15, increases the membrane potential and shifts the state to the right, toward the threshold. Since the state of the system is still in the white area, it slowly converges back to the stable equilibrium. To cross the threshold manifold, the second pulse must arrive shortly after the first one. The reaction of a resonator to a pair of pulses is quite different. The first pulse initiates a damped subthreshold oscillation of the membrane potential, which looks like a spiral in the bottom-right phase portrait in Fig.1.15. The effect of the second pulse depends on its timing. If it arrives after the trajectory makes half a rotation, marked "2" in the figure, it cancels the effect of the first pulse. If it arrives after the trajectory makes a full rotation, marked "3" in the figure, it adds to the first pulse and either increases the amplitude of subthreshold oscillation or evokes a spike response. Thus, the response of the resonator neuron depends on the frequency content of the input, as in Fig.1.7.

Integrators and resonators constitute two major modes of activity of neurons. Most cortical pyramidal neurons, including the regular spiking (RS), intrinsically bursting (IB), and chattering (CH) types considered in Chap. 8, are integrators. So are thalamocortical neurons in the relay mode of firing, and neostriatal spiny projection neurons. Most cortical inhibitory interneurons, including the FS type, are resonators. So are brainstem mesencephalic V neurons and stellate neurons of the entorhinal cortex. Some cortical pyramidal neurons and low-threshold spiking (LTS) interneurons can be at the border of transition between integrator and resonator modes. Such a transition corre-
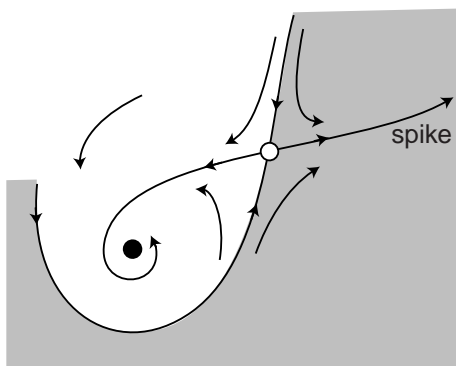
Figure 1.16: Phase portrait of a system near a Bogdanov-Takens bifurcation that corresponds to the transition from integrator to resonator mode.

sponds to another bifurcation, which has codimension-2, and hence it is less likely to be encountered experimentally. We consider this and other uncommon bifurcations in detail later. The phase portrait near the bifurcation is depicted in Fig.1.16, and it is a good exercise for the reader to explain why such a system has damped oscillations and postinhibitory responses, yet a well-defined threshold, all-or-none spikes, and possibly long latencies.

Of course, figures 1.15 and 1.16 cannot encompass all the richness of neuronal behavior, otherwise this book would be only 19pages long (this book is actually quite short; most of the space is taken by figures, exercises, and solutions). Many aspects of neuronal dynamics depend on other bifurcations, e.g., those corresponding to appearance and disappearance of spiking limit cycles. These bifurcations describe the transitions from spiking to resting, and they are especially important when we consider bursting activity. In addition, we need to take into account the relative geometry of equilibria, limit cycles, and other relevant trajectories, and how they depend on the parameters of the system, such as maximal conductances, and activation time constants. We explore all these issues systematically in subsequent chapters.

In chapter 2 we review some of the most fundamental concepts of neuron electrophysiology, culminating with the Hodgkin-Huxley model. This chapter is aimed at mathematicians learning neuroscience. In chapters 3 and 4 we use one- and two-dimensional neuronal models, respectively, to review some of the most fundamental concepts of dynamical systems, such as equilibria, limit cycles, stability, attraction domain, nullclines, phase portrait, and bifurcation. The material in these chapters, aimed at biologists learning the language of dynamical systems, is presented with the emphasis on geometrical rather than mathematical intuition. In fact, the spirit of the entire book is to explain concepts by using pictures, not equations. Chapter 5 explores phase portraits of various conductance-based models and the relations between ionic currents and dynamic behavior. In Chapter 6 we use the $I_{\mathrm{Na,p}}+I_{\mathrm{K}}$-model to systematically introduce the geometric bifurcation theory. Chapter 7, probably the most important chapter of the book, applies the theory to explain many computational properties of neurons. In fact, all the material in the previous chapters is given so that the reader can understand this chapter. In chapter 8 we use a simple phenomenological

model to simulate many cortical, hippocampal, and thalamic neurons. This chapter contains probably the most comprehensive up-to-date review of various firing patterns exhibited by mammalian neurons. In chapter 9 we introduce the electrophysiological and topological classification of bursting dynamics, as well as some useful methods to study the bursters. Finally, the last and the most mathematically advanced chapter of the book, Chap. 10, deals with coupled neurons. There we show how the details of the spike generation mechanism of neurons affect neurons' collective properties, such as synchronization.

1.2.5   Building Models (Revisited)

To have a good model of a neuron, it is not enough to put the right kind of currents together and tune the parameters so that the model can fire spikes. It is not even enough to reproduce the right input resistance, rheobase, and firing frequencies. The model has to reproduce all the neurocomputational features of the neuron, starting with the coexistence of resting and spiking states, spike latencies, subthreshold oscillations, and rebound spikes, among others.

A good way to start is to determine what kind of bifurcations the neuron under consideration undergoes and how the bifurcations depend on neuromodulators and pharmacological blockers. Instead of or in addition to measuring neuronal responses to get the kinetic parameters, we need to measure them to get the right bifurcation behavior. Only in this case we can be sure that the behavior of the model is *equivalent* to that of the neuron, even if we omitted a current or guessed some of the parameters incorrectly.

Implementation of this research program is still a pipe dream. The people who understand the mathematical aspects of neuron dynamics – those who see beyond conductances and currents – usually do not have the opportunity to do experiments. Conversely, those who study neurons in vitro or in vivo on a daily basis – those who see spiking, bursting, and oscillations; those who can manipulate the experimental setup to test practically any aspect of neuronal activity – do not usually see the value of studying phase portraits, bifurcations, and nonlinear dynamics in general. One of the goals of this book is to change this state and bring these two groups of people closer together.

<div style="background-color: yellow;">

Review of Important Concepts

- Neurons are dynamical systems.

- The resting state of neurons corresponds to a stable equilibrium; the tonic spiking state corresponds to a limit cycle attractor.

- Neurons are excitable because the equilibrium is near a bifurcation.

- There are many ionic mechanisms of spike generation, but only four generic bifurcations of equilibria.

- These bifurcations divide neurons into four categories: integrators or resonators, monostable or bistable.

- Analyses of phase portraits at bifurcations explain why some neurons have well-defined thresholds, all-or-none spikes, postinhibitory spikes, frequency preference, hysteresis, and so on, while others do not.

- These features, and not ionic currents per se, determine the neuronal responses, i.e., the kind of computations neurons do.

- A good neuronal model must reproduce not only electrophysiology but also the bifurcation dynamics of neurons.

</div>

Bibliographical Notes

Richard FitzHugh at the National Institutes of Health (NIH) pioneered the phase plane analysis of neuronal models with the view to understanding their neurocomputational properties. He was the first to analyze the Hodgkin-Huxley model (FitzHugh 1955; years before they received the Nobel Prize) and to prove that it has neither threshold nor all-or-none spikes. FitzHugh (1961) introduced the simplified model of excitability (see Fig.1.18) and showed that one can get the right kind of neuronal dynamics in models lacking conductances and currents. Nagumo et al. (1962) designed a corresponding tunnel diode circuit, so the model is called the FitzHugh-Nagumo oscillator. Chapter 8 deals with such simplified models. The history of the development of FitzHugh-Nagumo model is reviewed by Izhikevich and FitzHugh (2006).

FitzHugh's research program was further developed by John Rinzel and G. Bard Ermentrout (see Fig.1.19 and Fig.1.20). In their 1989 seminal paper, Rinzel and Ermentrout revived Hodgkin's classification of excitability and pointed out the connection between the behavior of neuronal models and the bifurcations they exhibit. (They also referred to the excitability as "type I" or "type II"). Unfortunately, many people treat

Figure 1.17: Richard FitzHugh in 1984.
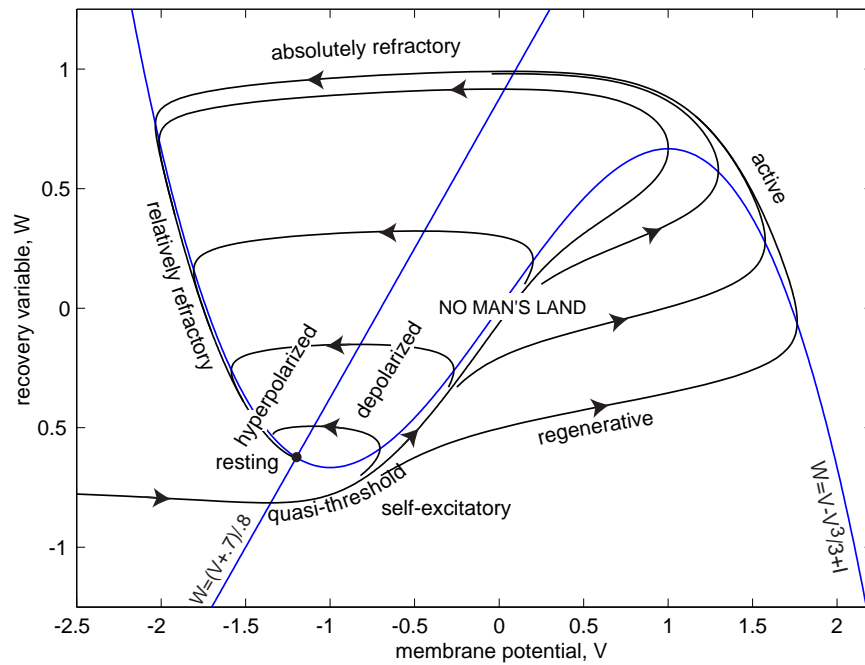
Figure 1.18: Phase portrait and physiological state diagram of FitzHugh-Nagumo model $\dot{V} = V - V^3/3 - W + I$, $\dot{W} = 0.08(V + 0.7 - 0.8W)$. The meaning of curves and trajectories is explained in chapter 4. (Reproduced from Izhikevich and FitzHugh (2006) with permission.)

Figure 1.19: John Rinzel in 2004. Depicted on his T-shirt is the cover of the first issue of *Journal of Computational Neuroscience*, in which the Pinsky-Rinzel (1994) model appeared.

Figure 1.20: G. Bard Ermentrout (G. stands for George) with his parrot, Junior, in 1983.

the connection in a simpleminded fashion and incorrectly identify "type I = saddle-node, type II = Hopf". If only life were so simple!

The geometrical analysis of neuronal models was further developed by, among others, Izhikevich (2000a), who stressed the integrator and resonator modes of operation and made connections to other neurocomputational properties.

The neuroscience and mathematics parts of this book are standard, though many connections are new. The literature sources are listed at the end of each chapter. Among many outstanding books on computational neuroscience, the author especially recommends *Spikes, Decisions, and Actions* by Wilson (1999), *Biophysics of Computation* by Koch (1999), *Theoretical Neuroscience* by Dayan and Abbott (2001), and *Foundations of Cellular Neurophysiology* by Johnston and Wu (1995). The present volume complements these excellent books in the sense that it is more ambitious, focused, and thorough in dealing with neurons as dynamical systems. Though its views may be biased by the author's philosophy and taste, the payoffs in understanding neuronal dynamics are immense, provided the reader has enough patience and perseverance to follow the author's line of thought.

The NEURON simulation environment is described by Hines (1989) and Carnevale and Hines (2006) (`http://www.neuron.yale.edu`); the GENESIS environment, by Bower and Beeman (1995) (`http://www.genesis-sim.org`); the XPP environment, by Ermentrout (2002). The author of this book uses MATLAB, which has become a standard computational tool in science and engineering. MATLAB is the registered trademark of The MathWorks, Inc. (`http://www.mathworks.com`).

Chapter 8

Simple Models

The advantage of using conductance-based models, such as the $I_{\mathrm{Na}}+I_{\mathrm{K}}$-model, is that each variable and parameter has a well-defined biophysical meaning. In particular, they can be measured experimentally. The drawback is that the measurement procedures may not be accurate: the parameters are usually measured in different neurons, averaged, and then fine-tuned (a fancy term meaning "to make arbitrary choices"). As a result, the model does not have the behavior that one sees in experiments. And even if it "looks" right, there is no guarantee that the model is accurate from the dynamical systems point of view, that is, it exhibits the same kind of bifurcations as the type of neuron under consideration.

Sometimes we do not need or cannot afford to have a biophysically detailed conductance-based model. Instead, we want a simple model that faithfully reproduces all the neurocomputational features of the neuron. In this chapter we review salient features of cortical, thalamic, hippocampal, and other neurons, and we present simple models that capture the essence of their behavior from the dynamical systems point of view.

8.1   Simplest Models

Let us start with reviewing the simplest possible models of neurons. As one can guess from their names, the integrate-and-fire and resonate-and-fire neurons capture the essence of integrators and resonators, respectively. The models are similar in many respects: both are described by linear differential equations, both have a hard firing threshold and a reset, and both have a unique stable equilibrium at rest. The only difference is that the equilibrium is a node in the integrate-and-fire case, but a focus in the resonate-and-fire case. One can model the former using only one equation, and the latter using only two equations, though multi-dimensional extensions are straightforward. Both models are useful from the analytical point of view, that is, to prove theorems.

Many scientists, including myself, refer to these neural models as "spiking models". The models have a threshold, but they lack any spike generation mechanism, that is, they cannot produce a brief regenerative depolarization of membrane potential corre-
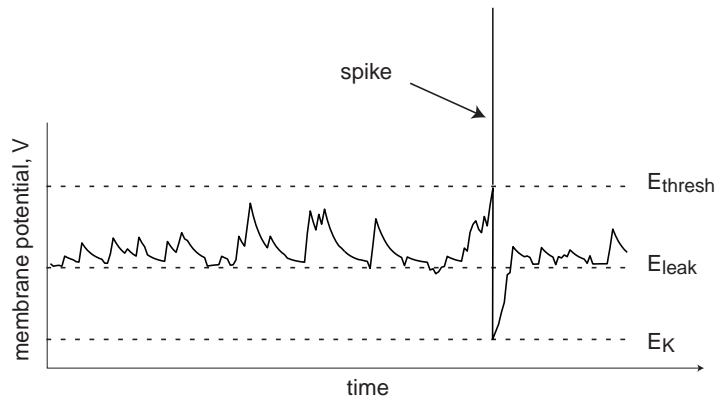
Figure 8.1: Leaky integrate-and-fire neuron with noisy input. The spike is added manually for aesthetic purposes and to fool the reader into believing that this is a spiking neuron.

sponding to the spike upstroke. Therefore, they are not *spiking models*; the spikes in figures 8.1 and 8.2, as well as in hundreds of scientific papers devoted to these models, are drawn by hand. The quadratic integrate-and-fire model is the simplest truly spiking model.

8.1.1   Integrate-and-Fire

The leaky integrate-and-fire model (Lapicque 1907; Stein 1967; Tuckwell 1988) is an idealization of a neuron having Ohmic leakage current and a number of voltage-gated currents that are completely deactivated at rest. Subthreshold behavior of such a neuron can be described by the linear differential equation

$$C\dot{V} = I - \overbrace{g_{\text{leak}}(V - E_{\text{leak}})}^{\text{Ohmic leakage}},$$

where all parameters have the same biophysical meanings as in the previous chapters. When the membrane potential V reaches the threshold value E_{thresh}, the voltage-sensitive currents instantaneously activate, the neuron is said to fire an action potential, and V is reset to E_{K}, as in Fig.8.1. After appropriate rescaling, the leaky integrate-and-fire model can be written in the form

$$\dot{v} = b - v\,, \qquad \text{if } v = 1, \text{ then } v \leftarrow 0, \tag{8.1}$$

where the resting state is $v = b$, the threshold value is $v = 1$, and the reset value is $v = 0$. Apparently the neuron is excitable when $b < 1$ and fires a periodic spike train when $b > 1$ with period $T = -\ln(1 - 1/b)$. (The reader should verify this.)

The integrate-and-fire neuron illustrates a number of important neurocomputational properties:

- *All-or-none spikes.* Since the shape of the spike is not simulated, all spikes are implicitly assumed to be identical in size and duration.

- *Well-defined threshold.* A stereotypical spike is fired as soon as $V = E_{\text{thresh}}$, leaving no room for any ambiguity (see, however, exercise 1).

- *Relative refractory period.* When $E_K < E_{leak}$, the neuron is less excitable immediately after the spike.

- *Distinction between excitation and inhibition.* Excitatory inputs ($I > 0$) bring the membrane potential closer to the threshold, and hence facilitate firing, while inhibitory inputs ($I < 0$) do the opposite.

- *Class 1 excitability.* The neuron can continuously encode the strength of an input into the frequency of spiking.

In summary, the neuron seems to be a good model for an integrator.

However, a closer look reveals that the integrate-and-fire neuron has flaws. The transition from resting to repetitive spiking occurs neither via saddle-node nor via Andronov-Hopf bifurcation, but via some other weird type of bifurcation that can be observed only in piecewise continuous systems. As a result, the F-I curve has logarithmic scaling and not the expected square-root scaling of a typical Class 1 excitable system (see, however, exercise 19 in chapter 6). The integrate-and-fire model cannot have spike latency to a transient input because superthreshold stimuli evoke immediate spikes without any delays (compare with Fig.8.8(I)). In addition, the model has some weird mathematical properties, such as non-uniqueness of solutions, as we show in exercise 1. Finally, the integrate-and-fire model is not a spiking model. Technically, it did not fire a spike in Fig.8.1, it was only "said to fire a spike", which was manually added afterward to fool the reader.

Despite all these drawbacks, the integrate-and-fire model is an acceptable sacrifice for a mathematician who wants to prove theorems and derive analytical expressions. However, using this model might be a waste of time for a computational neuroscientist who wants to simulate large-scale networks. At the end of this section we present alternative models that are as computationally efficient as the integrate-and-fire neuron, yet as biophysically plausible as Hodgkin-Huxley-type models.

8.1.2   Resonate-and-Fire

The resonate-and-fire model is a two-dimensional extension of the integrate-and-fire model that incorporates an additional low-threshold persistent K^+ current or h-current, or any other resonant current that is partially activated at rest. Let W denote the magnitude of such a current. In the linear approximation, the conductance-based equations describing neuronal dynamics can be written in the form

$$
\begin{aligned}
C\dot{V} &= I - g_{leak}(V - E_{leak}) - W \ , \\
\dot{W} &= (V - V_{1/2})/k - W \ .
\end{aligned}
$$

known as the Young (1937) model (see also equation 2-1 in FitzHugh 1969). Whenever the membrane potential reaches the threshold value, V_{thresh}, the neuron is said to fire a spike. Young did not specify what happens after the spike. The resonate-and-fire
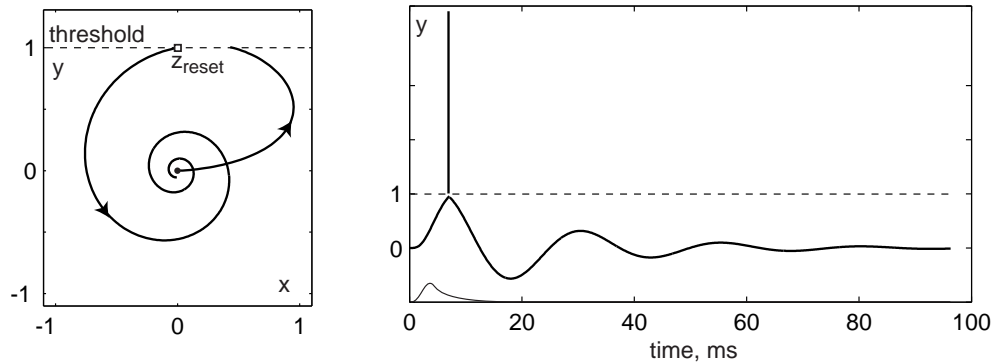
Figure 8.2: Resonate-and-fire model with $b = -0.05$, $\omega = 0.25$, and $z_{\text{reset}} = \text{i}$. The spike was added manually.

model is the Young model with the following resetting: if $V \geq V_{\text{thresh}}$, then $V \leftarrow V_{\text{reset}}$ and $W \leftarrow W_{\text{reset}}$, where V_{rest} and W_{reset} are some parameters.

When the resting state is a stable focus, the model can be recast in complex coordinates as

$$\dot{z} = (b + \text{i}\omega)z + I ,$$

where $b + \text{i}\omega \in \mathbb{C}$ is the complex eigenvalue of the resting state, and $z = x + \text{i}y \in \mathbb{C}$ is the complex-valued variable describing damped oscillations with frequency ω around the resting state. The real part, x, is a current-like variable. It describes the dynamics of the resonant current and synaptic currents. The imaginary part, y, is a voltage-like variable. The neuron is said to fire a spike when y reaches the threshold $y = 1$. Thus, the threshold is a horizontal line on the complex plane that passes through $\text{i} \in \mathbb{C}$, as in Fig.8.2, though other choices are also possible. After firing the spike, the variable z is reset to z_{reset}.

The resonate-and-fire model illustrates the most important features of resonators: damped oscillations, frequency preference, postinhibitory (rebound) spikes, and Class 2 excitability. It cannot have sustained subthreshold oscillations of membrane potential.

Integrate-and-fire and resonate-and-fire neurons do not contradict, but complement, each other. Both are linear, and hence are useful when we prove theorems and derive analytical expressions. They have the same flaws limiting their applicability, which were discussed earlier. In contrast, two simple models described below are difficult to treat analytically, but because of their universality they should be the models of choice when large-scale simulations are concerned.

8.1.3   Quadratic Integrate-and-Fire

Replacing $-v$ with $+v^2$ in (8.1) results in the *quadratic integrate-and-fire* model

$$\dot{v} = b + v^2 , \qquad \text{if } v = v_{\text{peak}}, \text{ then } v \leftarrow v_{\text{reset}}, \tag{8.2}$$

which we considered in section 3.3.8. Here v_{peak} is not a threshold, but the peak (cut off) of a spike, as we explain below. It is useful to use $v_{\text{peak}} = +\infty$ in analytical studies.
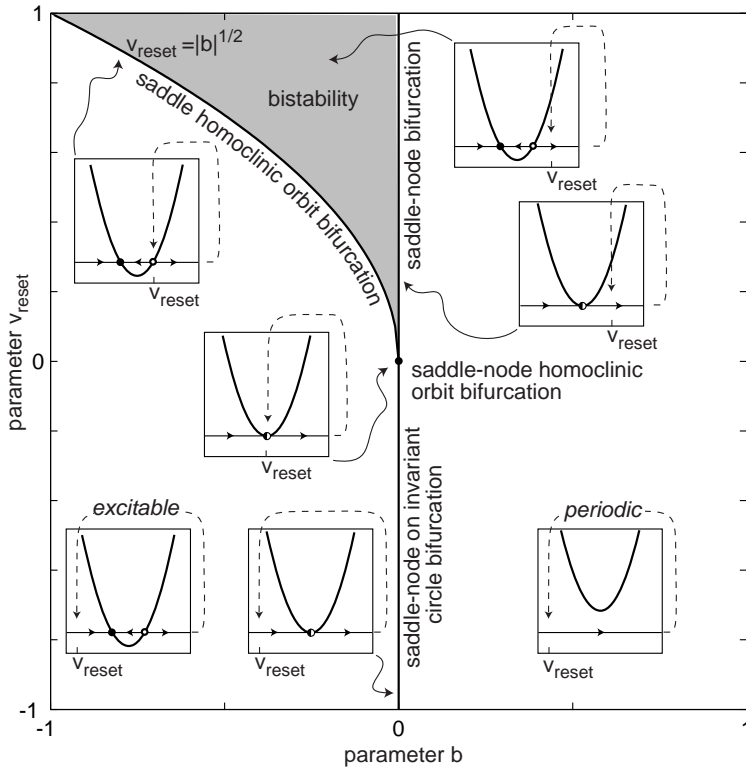
Figure 8.3: Bifurcation diagram of the quadratic integrate-and-fire neuron (8.2).

In simulations, the peak value is assumed to be large but finite, so it can be normalized to $v_{\mathrm{peak}} = 1$.

Note that $\dot{v} = b + v^2$ is a topological normal form for the saddle-node bifurcation. That is, it describes dynamics of any Hodgkin-Huxley-type system near that bifurcation, as we discuss in chapter 3 and 6. There we derived the normal form (6.3) for the $I_{\mathrm{Na,p}} + I_{\mathrm{K}}$-model and showed that the two systems agree quantitatively in a reasonably broad voltage range. By resetting v to v_{reset}, the quadratic integrate-and-fire model captures the essence of recurrence when the saddle-node bifurcation is on an invariant circle.

When $b > 0$, the right-hand side of the model is strictly positive, and the neuron fires a periodic train of action potentials. Indeed, v increases, reaches the peak, resets to v_{reset}, and then increases again, as we show in Fig.3.35 (top). In exercise 3 we prove that the period of such spiking activity is

$$T = \frac{1}{\sqrt{b}} \left(\mathrm{atan} \, \frac{v_{\mathrm{peak}}}{\sqrt{b}} - \mathrm{atan} \, \frac{v_{\mathrm{reset}}}{\sqrt{b}} \right) \quad < \frac{\pi}{\sqrt{b}} \, ,$$

so that the frequency scales as $\sqrt{b}$, as in Class 1 excitable systems.

When $b < 0$, the parabola $b + v^2$ has two zeroes, $\pm\sqrt{|b|}$. One corresponds to the stable node equilibrium (resting state), and the other corresponds to the unstable node (threshold state); see exercise 2. Subthreshold perturbations are those that keep v below the unstable node. Superthreshold perturbations are those that push v beyond the unstable node, resulting in the initiation of an action potential, reaching the peak
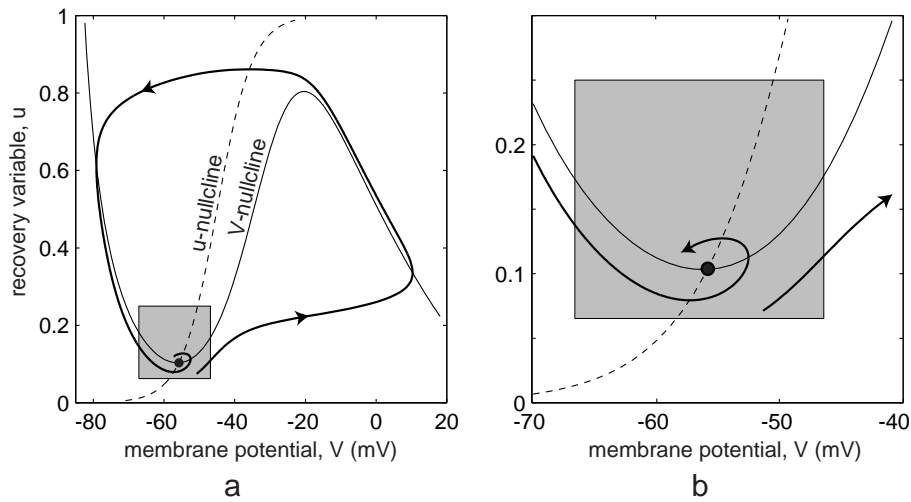
Figure 8.4: Phase portrait (a) and its magnification (b) of a typical neuronal model having voltage variable V and a recovery variable u.

value v_{peak}, and then resetting to v_{reset}. If, in addition, $v_{\text{reset}} > \sqrt{|b|}$, then there is a coexistence of resting and periodic spiking states, as in Fig.3.35 (middle). The period of the spiking state is provided in exercise 4. A two-parameter bifurcation diagram of (8.2) is depicted in Fig.8.3.

Unlike its linear predecessor, the quadratic integrate-and-fire neuron is a genuine integrator. It exhibits saddle-node bifurcation; it has a soft (dynamic) threshold; and it generates spikes with latencies, as many mammalian cells do. Besides, the model is canonical in the sense that the entire class of neuronal models near saddle-node on invariant circle bifurcation can be transformed into this model by a piecewise continuous change of variables (see section 8.1.5 and the Ermentrout-Kopell theorem in Hoppensteadt and Izhikevich 1997). In conclusion, the quadratic, and not the leaky, integrate-and-fire neuron should be used in simulations of large-scale networks of integrators. A generalization of this model is discussed next.

8.1.4   Simple Model of Choice

A striking similarity among many spiking models, discussed in chapter 5, is that they can be reduced to two-dimensional systems having a fast voltage variable and a slower "recovery" variable, which may describe activation of the K^+ current or inactivation of the Na^+ current or their combination. Typically, the fast variable has an N-shaped nullcline and the slower variable has a sigmoid-shaped nullcline. The resting state in such models is the intersection of the nullclines near the left knee, as we illustrate in Fig.8.4a. There, V and u denote the fast and the slow variable, respectively. In chapter 7 we showed that many computational properties of biological neurons can be explained by considering dynamics at the left knee.

In section 5.2.4 we derive a simple model that captures the subthreshold behavior
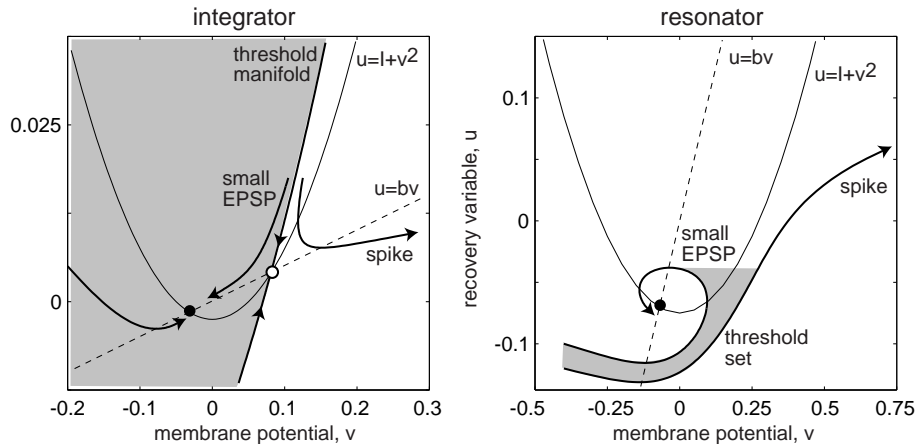
Figure 8.5: The simple model (8.3, 8.4) can be an integrator or a resonator. Compare with Fig.7.27.

in a small neighborhood of the left knee confined to the shaded square in Fig.8.4 and the initial segment of the upstroke of an action potential. In many cases, especially involving large-scale simulations of spiking models, the shape of the action potential is less important than the subthreshold dynamics leading to this action potential. Thus, retaining detailed information about the left knee and its neighborhood and simplifying the vector field outside the neighborhood is justified.

The simple model

$$\dot{v} = I + v^2 - u \qquad \text{if } v \geq 1, \text{ then} \qquad (8.3)$$
$$\dot{u} = a(bv - u) \qquad v \leftarrow c, \, u \leftarrow u + d \qquad (8.4)$$

has only four dimensionless parameters. Depending on the values of a and b, it can be an integrator or a resonator, as we illustrate in Fig.8.5. The parameters c and d do not affect steady-state subthreshold behavior. Instead, they take into account the action of high-threshold voltage-gated currents activated during the spike, and affect only the after-spike transient behavior. If there are many currents with diverse time scales, then u, a, b, and d are vectors, and (8.3) contains $\sum u$ instead of u.

The simple model may be treated as a quadratic integrate-and-fire neuron with adaptation in the simplest case $b = 0$. When $b < 0$, the model can be treated as a quadratic integrate-and-fire neuron with a passive dendritic compartment (see exercise 10). When $b > 0$, the connection to the quadratic integrate-and-fire neuron is lost, and the simple model represents a novel class of spiking models.

In the rest of this chapter we tune the simple model to reproduce spiking and bursting behavior of many known types of neurons. It is convenient to use it in the form

$$C\dot{v} = k(v - v_{\mathrm{r}})(v - v_{\mathrm{t}}) - u + I \qquad \text{if } v \geq v_{\mathrm{peak}}, \text{ then} \qquad (8.5)$$
$$\dot{u} = a\{b(v - v_{\mathrm{r}}) - u\} \qquad v \leftarrow c, \, u \leftarrow u + d \qquad (8.6)$$

where v is the membrane potential, u is the recovery current, C is the membrane capacitance, v_r is the resting membrane potential, and v_t is the instantaneous threshold potential. Though the model seems to have ten parameters, but it is equivalent to (8.3, 8.4) and hence has only four independent parameters. As we described in section 5.2.4, the parameters k and b can be found when one knows the neuron's rheobase and input resistance. The sum of all slow currents that modulate the spike generation mechanism is combined in the phenomenological variable u with outward currents taken with the plus sign.

The sign of b determines whether u is an amplifying ($b < 0$) or a resonant ($b > 0$) variable. In the latter case, the neuron sags in response to hyperpolarized pulses of current, peaks in response to depolarized subthreshold pulses, and produces rebound (postinhibitory) responses. The recovery time constant is a. The spike cutoff value is v_{peak}, and the voltage reset value is c. The parameter d describes the total amount of outward minus inward currents activated during the spike and affecting the after-spike behavior. All these parameters can easily be fitted to any particular neuron type, as we show in subsequent sections.

Implementation and Phase Portrait

The following MATLAB code simulates the model and produces Fig.8.6a.

```
C=100; vr=-60; vt=-40; k=0.7;        % parameters used for RS
a=0.03; b=-2; c=-50; d=100;          % neocortical pyramidal neurons
vpeak=35;                            % spike cutoff

T=1000; tau=1;                       % time span and step (ms)
n=round(T/tau);                      % number of simulation steps
v=vr*ones(1,n);   u=0*v;             % initial values
I=[zeros(1,0.1*n),70*ones(1,0.9*n)];% pulse of input DC current

for i=1:n-1                          % forward Euler method
    v(i+1)=v(i)+tau*(k*(v(i)-vr)*(v(i)-vt)-u(i)+I(i))/C;
    u(i+1)=u(i)+tau*a*(b*(v(i)-vr)-u(i));
    if v(i+1)>=vpeak                 % a spike is fired!
        v(i)=vpeak;                  % padding the spike amplitude
        v(i+1)=c;                    % membrane voltage reset
        u(i+1)=u(i+1)+d;             % recovery variable update
    end;
end;
plot(tau*(1:n), v);                  % plot the result
```

Note that the spikes were padded to v_{peak} to avoid amplitude jitter associated with the finite simulation time step `tau=1` ms. In Fig.8.6b we magnify the simulated voltage trace and compare it with a recording of a neocortical pyramidal neuron (dashed curve). There are two discrepancies, marked by arrows: In the first, the pyramidal neuron has (1) a sharper spike upstroke and (2) a smoother spike downstroke. The first discrepancy
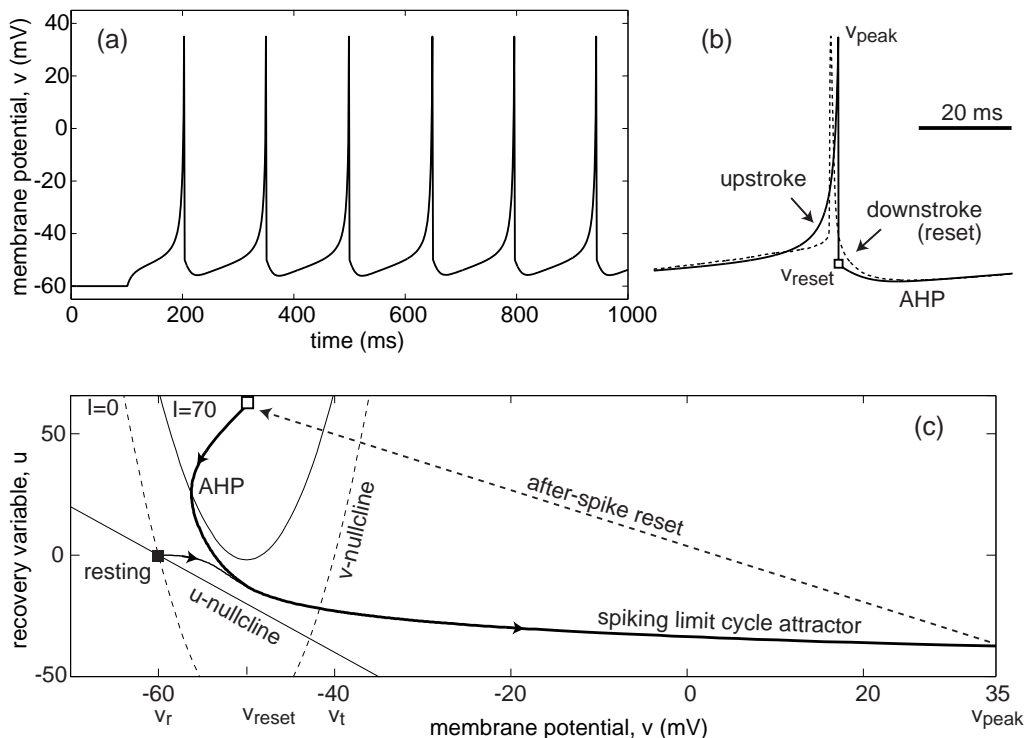
Figure 8.6: (a) Output of the MATLAB code simulating the simple model (8.5, 8.6). (b) Comparison of the simulated (solid curve) and experimental (dashed curve) voltage traces shows two major discrepancies, marked by arrows. (c) Phase portrait of the model.

can be removed by assuming that the coefficient k of the square polynomial in (8.5) is voltage-dependent (e.g., $k = 0.7$ for $v \leq v_t$ and $k = 7$ for $v > v_t$), or by using the modification of the simple model presented in exercise 13 and exercise 17. The second discrepancy results from the instantaneous after-spike resetting, and it less important because it does not affect the decision whether or when to fire. However, the slope of the downstroke may become important in studies of gap-junction-coupled spiking neurons.

The phase portrait of the simple model is depicted in Fig.8.6c. Injection of the step of DC current $I = 70$ pA shifts the v-nullcline (square parabola) upward and makes the resting state, denoted by a black square, disappear. The trajectory approaches the spiking limit cycle attractor, and when it crosses the cutoff vertical line $v_{peak} = 35$ mV, it is reset to the white square, resulting in periodic spiking behavior. Note the slow afterhyperpolarization (AHP) following the reset that is due to the dynamics of the recovery variable u. Depending on the parameters, the model can have other types of phase portraits, spiking, and bursting behavior, as we demonstrate later.

In Fig.8.7 we illustrate the difference between the integrate-and-fire neuron and the simple model. The integrate-and-fire model is said to fire spikes when the membrane potential reaches a preset threshold value. The potential is reset to a new value, and
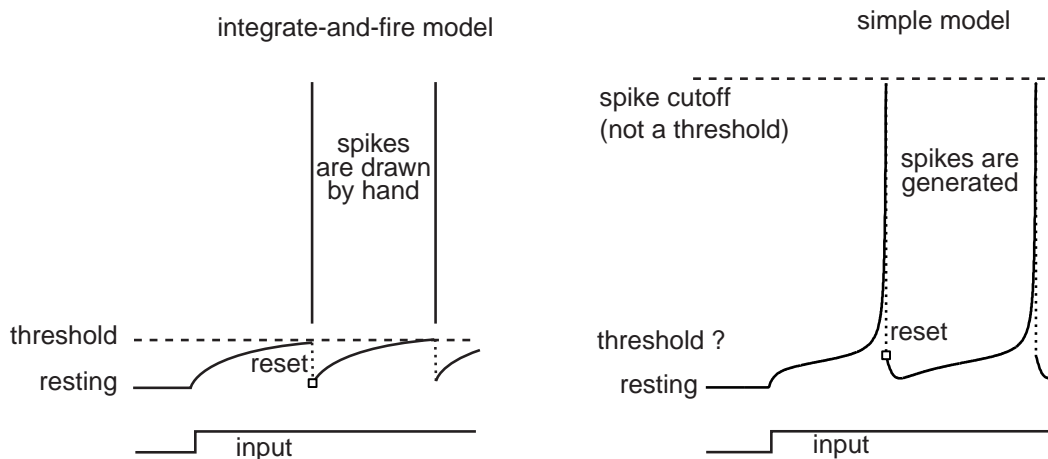
Figure 8.7: Voltage reset in the integrate-and-fire model and in the simple model.

the spikes are drawn by hand. In contrast, the simple model generates the upstroke of the spike due to the intrinsic (regenerative) properties of the voltage equation. The voltage reset occurs not at the threshold, but at the peak, of the spike. In fact, the firing threshold in the simple model *is not a parameter, but a property* of the bifurcation mechanism of excitability. Depending on the bifurcation of equilibrium, the model may not even have a well-defined threshold, a situation similar to many conductance-based models.

When numerically implementing the voltage reset, whether at the threshold or at the peak of the spike, one needs to be aware of the numerical errors, which translate into the errors of spike timing. These errors are inversely proportional to the slope of the voltage trace (i.e. $\dot{v}$) at the reset value. The slope is small in the integrate-and-fire model, so clever numerical methods are needed to catch the exact moment of threshold crossing (Hansel et al. 1998). In contrast, the slope is nearly infinite in the simple model, hence the error is infinitesimal, and no special methods are needed to identify the peak of the spike.

In Fig.8.8 we used the model to reproduce the 20 of the most fundamental neurocomputational properties of biological neurons. Let us check that the model is the simplest possible system that can exhibit the kind of behavior in the figure. Indeed, it has only one nonlinear term, v^2. Removing the term makes the model linear (between the spikes) and equivalent to the resonate-and-fire neuron. Removing the recovery variable u makes the model equivalent to the quadratic integrate-and-fire neuron with all its limitations, such as the inability to burst or to be a resonator. In summary, we found the simplest possible model capable of spiking, bursting, being an integrator or a resonator, and it should be the model of choice in simulations of large-scale networks of spiking neurons.

(A) tonic spiking
(B) phasic spiking
(C) tonic bursting
(D) phasic bursting

input dc-current
20 ms

(E) mixed mode
(F) spike frequency adaptation
(G) Class 1 excitable
(H) Class 2 excitable

(I) spike latency
(J) subthreshold oscillations
(K) resonator
(L) integrator

(M) rebound spike
(N) rebound burst
(O) threshold variability
(P) bistability

(Q) depolarizing after-potential
(R) accommodation
(S) inhibition-induced spiking
(T) inhibition-induced bursting

DAP

Figure 8.8: Summary of neurocomputational properties exhibited by the simple model; see exercise 11. The figure is reproduced, with permission, from www.izhikevich.com. (An electronic version of the figure, the MATLAB code that generates the voltage responses, and reproduction permissions are available at www.izhikevich.com.)
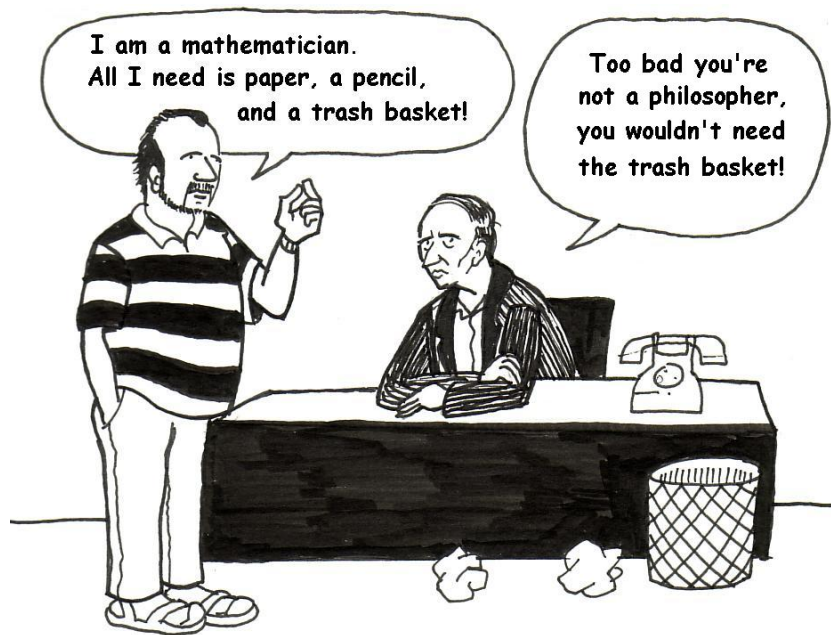
Figure 8.9: A real conversation between the author of this book and his boss.

8.1.5 Canonical Models

It is quite rare, if ever possible, to know precisely the parameters describing dynamics of a neuron (many erroneously think that the Hodgkin-Huxley model of the squid axon is an exception). Indeed, even if all ionic channels expressed by the neuron are known, the parameters describing their kinetics are usually obtained via averaging over many neurons; there are measurement errors; the parameters change slowly, and so on. Thus, we are forced to consider families of neuronal models with free parameters (e.g. the family of $I_{\mathrm{Na}}+I_{\mathrm{K}}$-models). It is more productive, from the computational neuroscience point of view, to consider families of neuronal models having a common property, e.g., the family of all integrators, the family of all resonators, or the family of "fold/homoclinic" bursters considered in the next chapter. How can we study the behavior of the entire family of neuronal models if we have no information about most of its members?

The canonical model approach addresses this issue. Briefly, a model is *canonical* for a family if there is a piecewise continuous change of variables that transforms any model from the family into this one, as we illustrate in Fig.8.10. The change of variables does not have to be invertible, so the canonical model is usually lower-dimensional, simple, and tractable. Nevertheless, it retains many important features of the family. For example, if the canonical model has multiple attractors, then each member of the family has multiple attractors. If the canonical model has a periodic solution, then each member of the family has a periodic (quasi-periodic or chaotic) solution. If the canonical model can burst, then each member of the family can burst. The advantage of this approach is that we can study universal neurocomputational properties that are shared by all members of the family because all such members can be put into the canonical form by a change of variables. Moreover, we need not actually present such
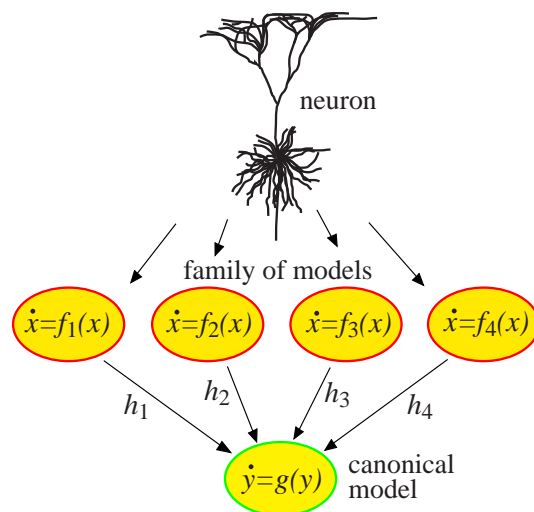
Figure 8.10: Dynamical system $\dot{y} = g(y)$ is a canonical model for the family $\{f_1, f_2, f_3, f_4\}$ of neural models $\dot{x} = f(x)$ because each such model can be transformed into the form $\dot{y} = g(y)$ by the piecewise continuous change of variables h_i.

a change of variables explicitly, so derivation of canonical models is possible even when the family is so broad that most of its members are given implicitly (e.g., the family of "all resonators").

The process of deriving canonical models is more an art than a science, since a general algorithm for doing this is not known. However, much success has been achieved in some important cases. The canonical model for a system near an equilibrium is the topological normal form at the equilibrium (Kuznetsov 1995). Such a canonical model is local, but it can be extended to describe global dynamics. For example, the quadratic integrate-and-fire model with a fixed $v_{\text{reset}} < 0$ is a global canonical model for all Class 1 excitable systems, that is, systems near saddle-node on invariant circle bifurcation. The same model with variable v_{reset} is a global canonical model for all systems near saddle-node homoclinic orbit bifurcation (considered in section 6.3.6). The phase model $\dot{\vartheta} = 1$ derived in chapter 10 is a global canonical model for the family of nonlinear oscillators having exponentially stable limit cycle attractors. Other examples of canonical models for spiking and bursting can be found in subsequent chapters of this book.

The vector-field of excitable conductance-based models in the subthreshold region and in the region corresponding to the upstroke of the spike can be converted into the simple form (8.3, 8.4), possibly with u being a vector. Therefore, the simple model (8.3, 8.4) is a *local* canonical model for the spike generation mechanism and the spike upstroke of Hodgkin-Huxley-type neuronal models. It is not a global canonical model because it ignores the spike downstroke. Nevertheless, it describes remarkably well the spiking and bursting dynamics of many biological neurons, as we demonstrate next.

excitatory

regular spiking (RS)

chattering (CH)

300 pA

100 pA

35 pA

600 pA

300 pA

200 pA

intrinsically bursting (IB)

50 mV

100 ms

600 pA

500 pA

400 pA

inhibitory

fast spiking (FS)

low threshold spiking (LTS)

late spiking (LS)

500 pA

400 pA

300 pA

200 pA

175 pA

100 pA

150 pA

delay
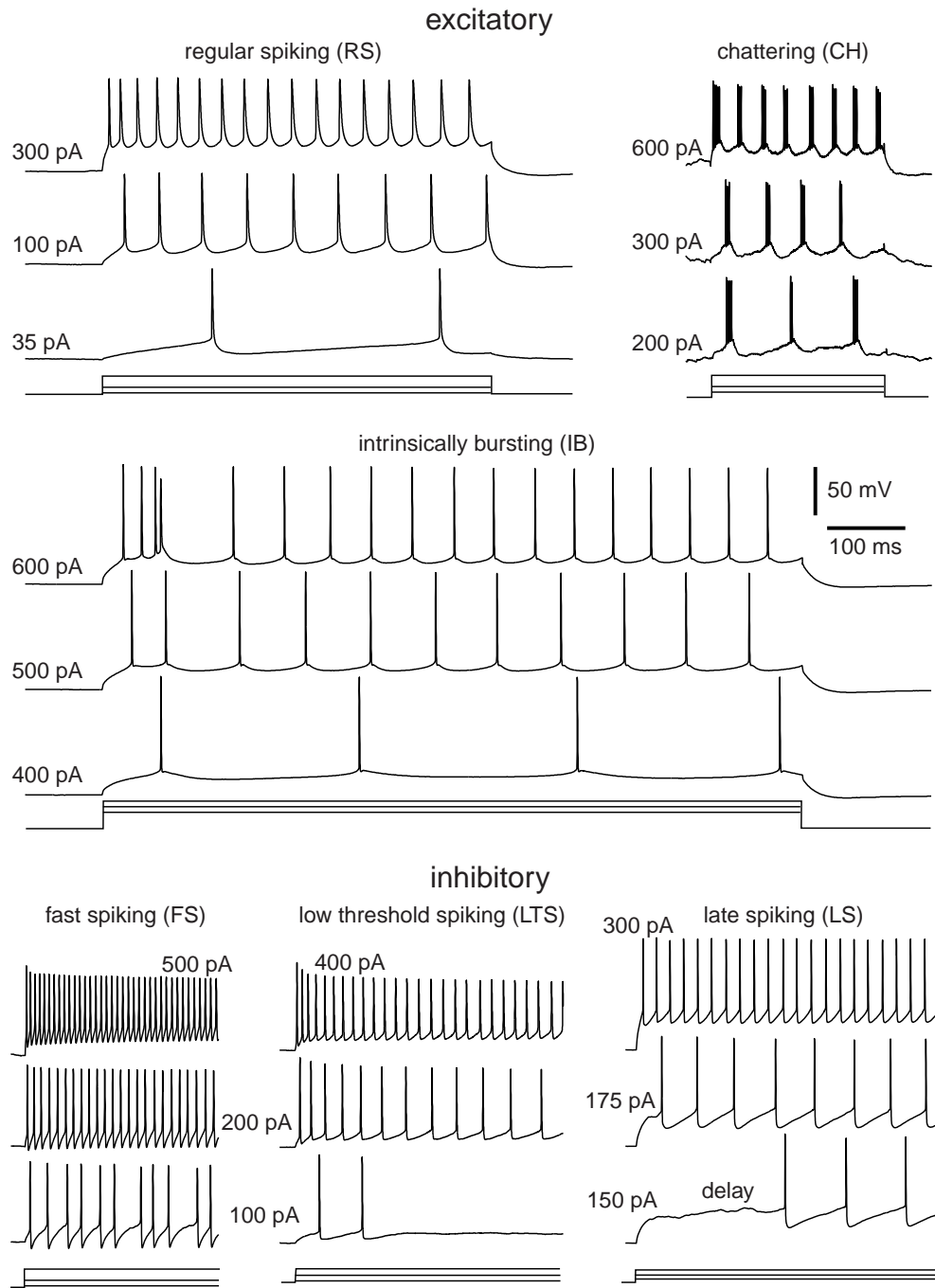
Figure 8.11: The six most fundamental classes of firing patterns of neocortical neurons in response to pulses of depolarizing DC current. RS and IB are in vitro recordings of pyramidal neurons of layer 5 of primary visual cortex of a rat; CH was recorded in vivo in cat visual cortex (area 17; data provided by D. McCormick). FS was recorded in vitro in rat primary visual cortex, LTS was recorded in vitro in layer 4 or 6 of rat barrel cortex (data provided by B. Connors). LS was recorded in layer 1 of rat's visual cortex (data provided by S. Hestrin). All recordings are plotted on the same voltage and time scale, and the data are available at www.izhikevich.com.

8.2 Cortex

In this section we consider the six most fundamental classes of firing patterns observed in the mammalian neocortex and depicted in Fig.8.11 (Connors and Gutnick 1990; Gray and McCormick 1996; Gibson et al. 1999). Though most biologists agree with the classification in the figure, many would point out that it is greatly oversimplified (Markram et al. 2004), that the distinction between the classes is not sharp, that there are subclasses within each class (Nowak et al. 2003; Toledo-Rodriguez et al. 2004), and that neurons can change their firing class depending on the state of the brain (Steriade 2004).

- (RS) Regular spiking neurons fire tonic spikes with adapting (decreasing) frequency in response to injected pulses of DC current. Most of them have Class 1 excitability in the sense that the interspike frequency vanishes when the amplitude of the injected current decreases. Morphologically, these neurons are spiny stellate cells in layer 4 and pyramidal cells in layers 2, 3, 5, and 6.

- (IB) Intrinsically bursting neurons generate a burst of spikes at the beginning of a strong depolarizing pulse of current, then switch to tonic spiking mode. They are excitatory pyramidal neurons found in all cortical layers, but are most abundant in layer 5.

- (CH) Chattering neurons fire high-frequency bursts of spikes with relatively short interburst periods; hence another name, FRB (fast rhythmic bursting). Output of such a cell fed to the loudspeaker "sounds a lot like a helicopter – cha, cha, cha – real fast", according to Gray and McCormick (1996). CH neurons were found in visual cortex of adult cats, and morphologically they are spiny stellate or pyramidal neurons of layers 2 - 4, mainly layer 3.

- (FS) Fast spiking interneurons fire high-frequency tonic spikes with relatively constant period. They exhibit Class 2 excitability (Tateno et al. 2004). When the magnitude of the injected current decreases below a certain critical value, they fire irregular spikes, switching randomly between resting and spiking states. Morphologically, FS neurons are sparsely spiny or aspiny nonpyramidal cells (basket or chandelier; see Kawaguchi and Kubota 1997) providing local inhibition along the horizontal (intra-laminar) direction of the neocortex (Bacci et al. 2003).

- (LTS) Low-threshold spiking neurons fire tonic spikes with pronounced spike frequency adaptation and rebound (postinhibitory) spikes, often called "low-threshold spikes" by biologists (hence the name). They seem to be able to fire low-frequency spike trains, though their excitability class has not yet been determined. Morphologically, LTS neurons are nonpyramidal interneurons providing local inhibition along the vertical (inter-laminar) direction of the neocortex (Bacci et al. 2003).

- (LS) Late spiking neurons exhibit voltage ramp in response to injected DC current near the rheobase, resulting in delayed spiking with latencies as long as 1 sec. There is a pronounced subthreshold oscillation during the ramp, but the discharge frequency is far less than that of FS neurons. Morphologically, LS neurons are nonpyramidal interneurons (neurogliaform; see Kawaguchi and Kubota 1997) found in all layers of neocortex (Kawaguchi 1995), especially in layer 1 (Chu et al. 2003).

Our goal is to use the simple model (8.5, 8.6) presented in section 8.1.4 to reproduce each of the firing types. We want to capture the dynamic mechanism of spike generation of each neuron, so that the model reproduces the correct responses to many types of the inputs, and not only to the pulses of DC current. We strive to have not only qualitative but also quantitative agreement with the published data on neurons' resting potential, input resistance, rheobase, F-I behavior, the shape of the upstroke of the action potential, and so on, though this is impossible in many cases, mostly because the data are contradictory. To fine-tune the model, we use recordings of real neurons. We consider the tuning successful when the quantitative difference between simulated and recorded responses is smaller than the difference between the responses of two "sister" neurons recorded in the same slice. We do not want to claim that the simple model explains the mechanism of generation of any of the firing patterns recorded in real neurons (simply because the mechanism is usually not known). Although in many instances we must resist the temptation to use the Wolfram (2002) new-kind-of-science criterion: "If it looks the same, it must be the same".

8.2.1   Regular Spiking (RS) Neurons

Regular spiking neurons are the major class of excitatory neurons in the neocortex. Many are Class 1 excitable, as we show in Fig.7.3, using in vitro recordings of a layer 5 pyramidal cell of rat primary visual cortex (see also Tateno et al. 2004). RS neurons have a transient K^+ current I_A, whose slow inactivation delays the onset of the first spike and increases the interspike period, and a persistent K^+ current I_M, which is believed to be responsible for the spike frequency adaptation seen in Fig.7.43. Let us use the simple model (8.5, 8.6) to capture qualitative and some quantitative features of typical RS neurons.

We assume that the resting membrane potential is $v_r = -60$ mV and the instantaneous threshold potential is $v_t = -40$ mV; that is, instantaneous depolarizations above -40 mV cause the neuron to fire, as in Fig.3.15. Assuming that the rheobase is 50 pA and the input resistance is 80 MΩ, we find $k = 0.7$ and $b = -2$. We take the membrane capacitance $C = 100$ pF, which yields a membrane time constant of 8 ms.

Since $b < 0$, depolarizations of v decrease u as if the major slow current is the inactivating K^+ current I_A. The inactivation time constant of I_A is around 30 ms in the subthreshold voltage range; hence one takes $a = 0.03 \approx 1/30$. The membrane potential of a typical RS neuron reaches the peak value $v_{peak} = +35$ mV during a spike (the precise value has little effect on dynamics) and then repolarizes to $c = -50$
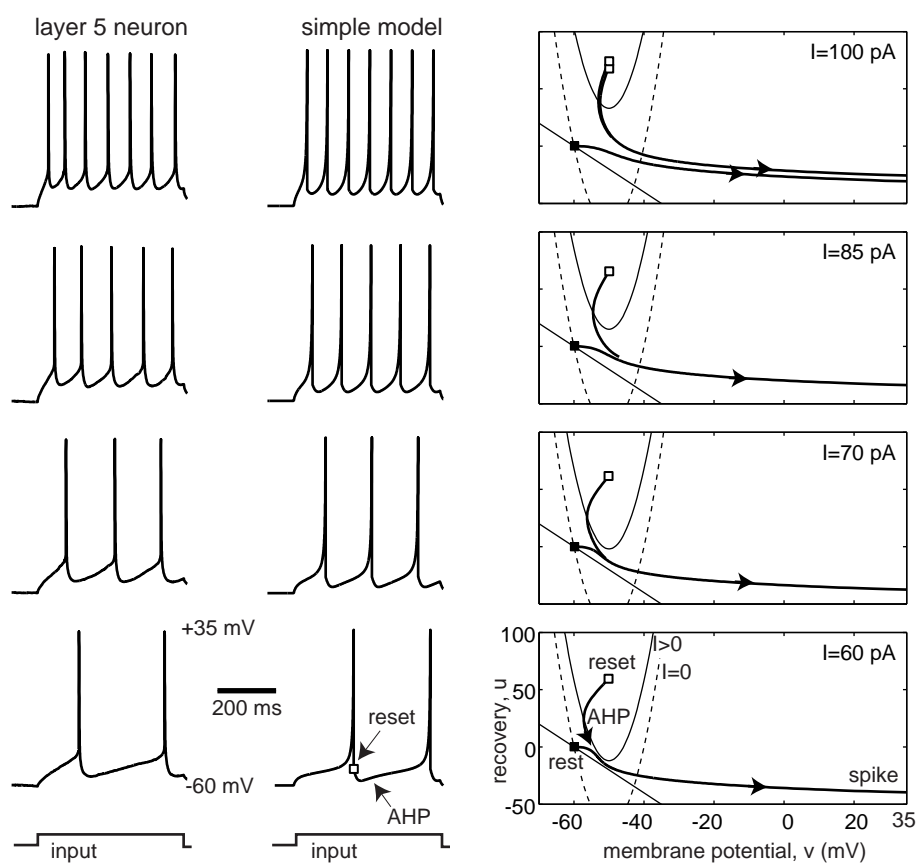
Figure 8.12: Comparison of in vitro recordings of a regular spiking (RS) pyramidal neuron with simulations of the simple model $100\dot{v} = 0.7(v + 60)(v + 40) - u + I$, $\dot{u} = 0.03\{-2(v + 60) - u\}$, if $v \geq +35$, then $v \leftarrow -50$, $u \leftarrow u + 100$.

mV or below, depending on the firing frequency. The parameter d describes the total amount of outward minus inward currents activated during the spike and affecting the after-spike behavior. Trying different values, we find that $d = 100$ gives a reasonable F-I relationship, at least in the low-frequency range.

As follows from exercise 10, one can also interpret u as the membrane potential of a passive dendritic compartment, taken with the minus sign. Thus, when $b < 0$, the variable u represents the combined action of slow inactivation of I_A and slow charging of the dendritic tree. Both processes slow the frequency of somatic spiking.

Note that we round up all the parameters, that is, we use $d = 100$ and not 93.27. Nevertheless, the simulated voltage responses in Fig.8.12 agree quantitatively with the in vitro recordings of the layer 5 pyramidal neuron used in Fig.7.3. Tweaking the parameters, considering multidimensional u, or adding multiple dendritic compartments, one can definitely improve the quantitative correspondence between the model and the in vitro data of that particular neuron, but this is not our goal here. Instead, we want to understand the qualitative dynamics of RS neurons, using the geometry of their phase portraits.
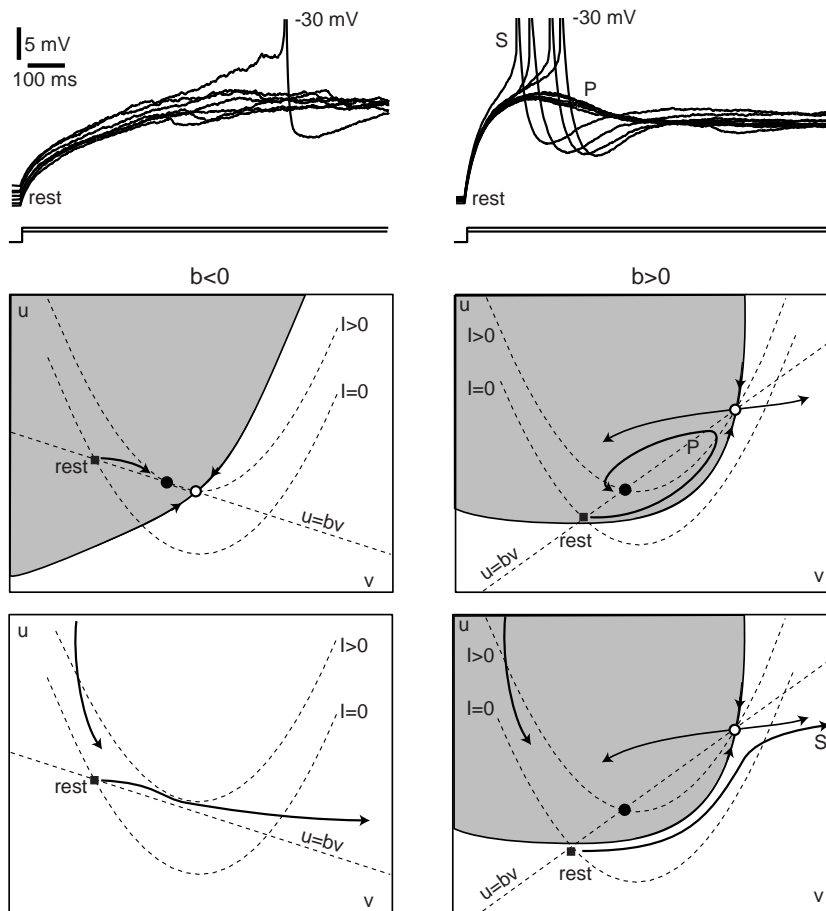
Figure 8.13: Two types of qualitative behavior of RS neurons. Some exhibit monotone responses to weak injected currents (case $b < 0$); others exhibit non-monotone overshooting responses (case $b > 0$). Shown are in vitro recordings of two RS neurons from the same slice of rat primary visual cortex while an automated procedure was trying to determine the neurons' rheobase. Phase portraits are drawn by hand and illustrate a possible dynamic mechanism of the phenomenon.

Phase Plane Analysis

Figure 8.13 shows recordings of two pyramidal RS neurons from the same slice while an automated procedure injects pulses of DC current to determine their rheobase. The neuron on the left exhibits monotonically increasing (ramping) or decreasing responses of membrane potential to weak input pulses, long latencies of the first spike, and no rebound spikes, whereas the neuron on the right exhibits non-monotone overshooting responses to positive pulses, sags and rebound spikes to negative pulses (as in Fig.7.48), relatively short latencies of the first spike, and other resonance phenomena. The even more extreme example in Fig.7.42 shows a pyramidal neuron executing a subthreshold oscillation before switching to a tonic spiking mode.

The difference between the types in Fig.8.13 can be explained by the sign of the parameter b in the simple model (8.5, 8.6), which depends on the relative contributions of amplifying and resonant slow currents and gating variables. When $b < 0$ (or $b \approx 0$; e.g., $b = 0.5$ in Fig.8.14), the neuron is a pure integrator near saddle-node on invariant circle bifurcation. Greater values of $b > 0$ put the model near the transition from an integrator to a resonator the via codimension-2 Bogdanov-Takens bifurcation studied in section 6.3.3 and 7.2.11.
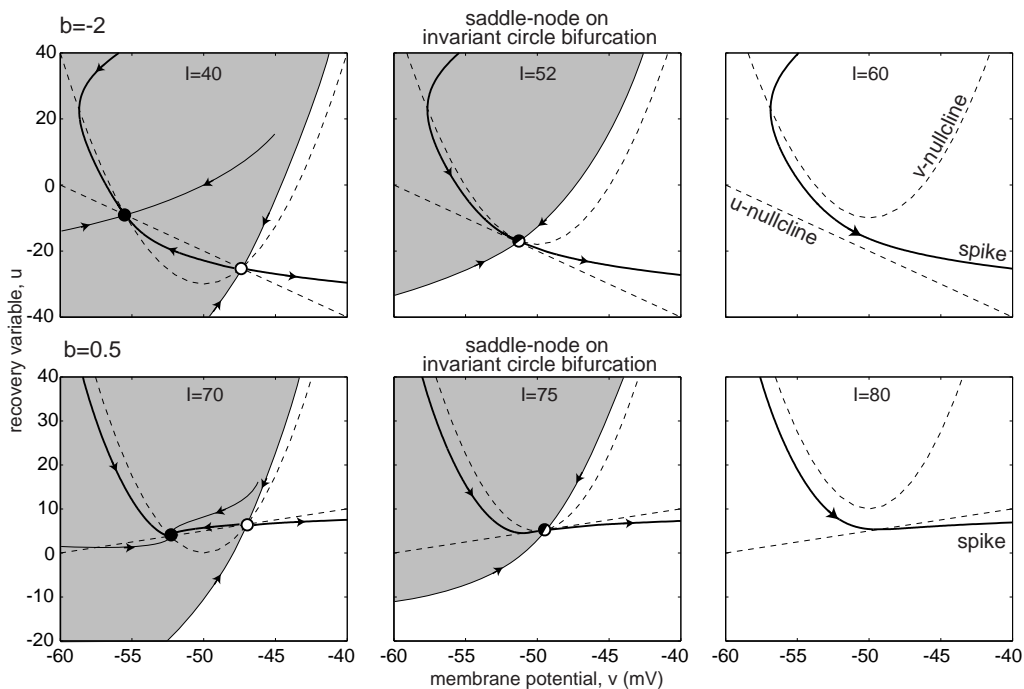
Figure 8.14: Saddle-node on invariant circle bifurcations in the RS neuron model as the magnitude of the injected current I increases.
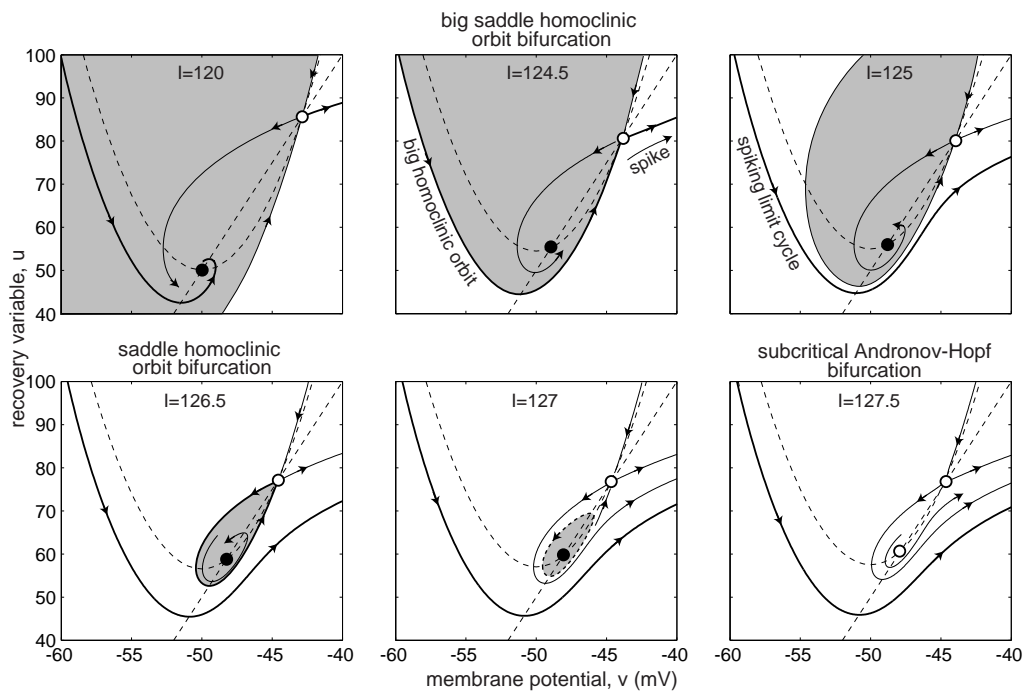
Figure 8.15: The sequence of bifurcations of the RS model neuron (8.5, 8.6) in resonator regime. Parameters are as in Fig.8.12 and $b = 5$; see also Fig.6.40.
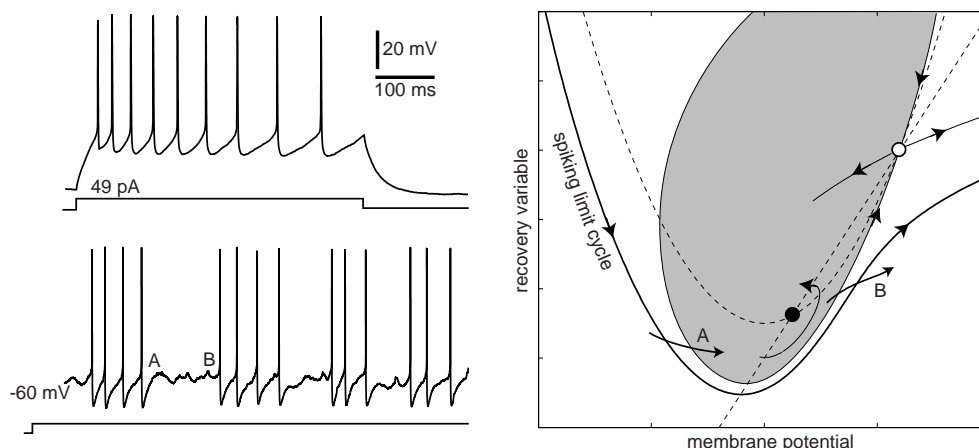
Figure 8.16: Stuttering behavior of an RS neuron. (Data provided by Dr. Klaus M. Stiefel: P28-36 adult mouse, coronal slices, 300μm, layer II/III pyramid, visual cortex.)

The sequence of bifurcations when $b > 0$ is depicted in Fig.8.15. Injection of depolarizing current below the neuron's rheobase transforms the resting state into a stable focus and results in damped oscillations of the membrane potential. The attraction domain of the focus (shaded region in the figure) is bounded by the stable manifold of the saddle. As I increases, the stable manifold makes a loop and becomes a big homoclinic orbit giving birth to a spiking limit cycle attractor. When $I = 125$, stable resting and spiking states coexist, which plays an important role in explaining the paradoxical stuttering behavior of some neocortical neurons discussed later. As I increases, the saddle quantity (i.e., the sum of eigenvalues of the saddle) becomes positive. When the stable manifold makes another, smaller loop, it gives birth to an unstable limit cycle, which then shrinks to the resting equilibrium and results in a subcritical Andronov-Hopf bifurcation.

What is the excitability class of the RS model neuron in Fig.8.15? If a slow ramp of current is injected, the resting state of the neuron becomes a stable focus and then loses stability via a subcritical Andronov-Hopf bifurcation. Hence the neuron is a resonator exhibiting Class 2 excitability. Now suppose steps of DC current of amplitude $I = 125$ pA or less are injected. The trajectory starts at the initial point $(v, u) = (-60, 0)$, which is the resting state when $I = 0$, and then approaches the spiking limit cycle. Because the limit cycle was born via a homoclinic bifurcation to the saddle, it has a large period, and hence the neuron is Class 1 excitable. Thus, depending on the nature of stimulation, that is, ramps vs. pulses, we can observe small or large spiking frequencies, at least in principle.

In practice, it is quite difficult to catch homoclinic orbits to saddles because they are sensitive to noise. Injection of a constant current just below the neuron's rheobase in Fig.8.15 would result in random transitions between the resting state and a periodic spiking state. Indeed, the two attractors coexist and are near each other, so weak membrane noise can push the trajectory in and out of the shaded region, resulting
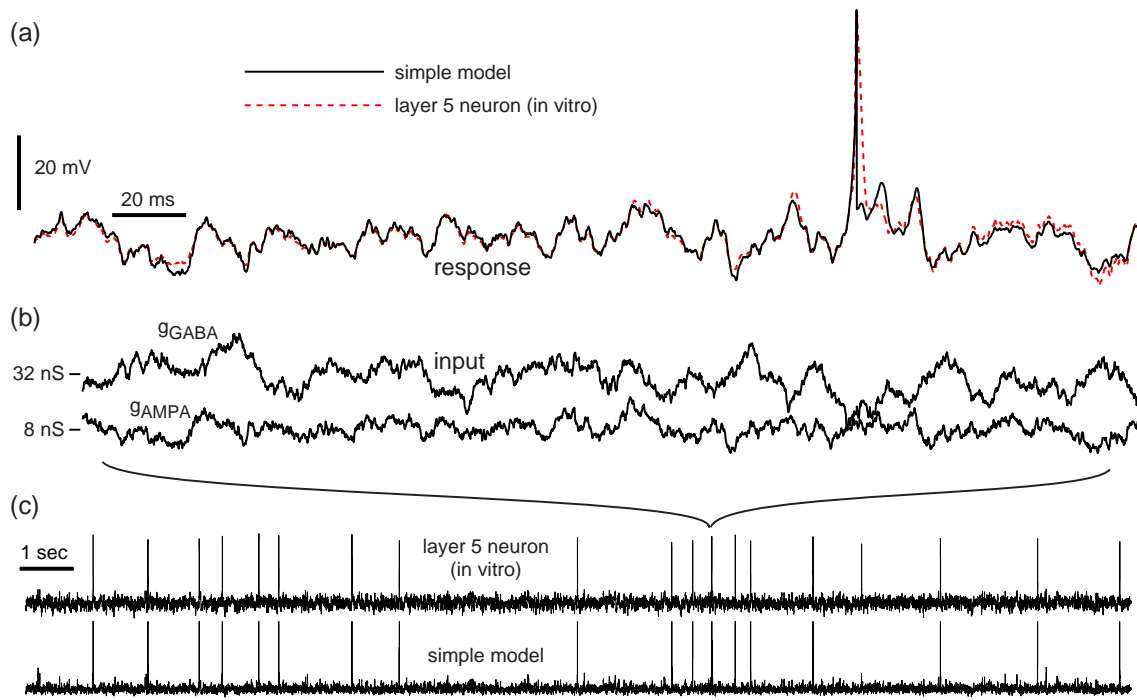
Figure 8.17: (a) Comparison of responses of a rat motor cortex layer 5 pyramidal neuron of RS type and the simple model (8.5, 8.6) to in vivo-like stochastic input (8.7) with the random conductances in (b). Part (a) is a magnification of a small region in (c). Shown are simulations of $30\dot{v} = 3(v+55)(v+42)-u+I(t)$, $\dot{u} = 0.01\{-0.25(v+55)-u\}$, if $v \geq +10$, then $v \leftarrow -40$, $u \leftarrow u + 90$. (Data provided by Niraj S. Desai and Betsy C. Walcott.)

in a stuttering spiking (illustrated in Fig.8.16) mingled with subthreshold oscillations. Such behavior is also exhibited by FS interneurons, studied later in this section.

In Vivo-like Conditions

In Fig.8.17a (dashed curve) we show the response of in vitro recorded layer 5 pyramidal neuron of rat motor cortex to fluctuating in vivo-like input. First, random excitatory and inhibitory conductances, $g_{\mathrm{AMPA}}(t)$ and $g_{\mathrm{GABA}}(t)$ (Fig.8.17b), were generated using the Ornstein-Uhlenbeck stochastic process (Uhlenbeck and Ornstein 1930), which was originally developed to describe Brownian motion, but can equally well describe in vivo-like fluctuating synaptic conductances produced by random firings (Destexhe et al. 2001). Let $E_{\mathrm{AMPA}} = 0$ mV and $E_{\mathrm{GABA}} = -65$ mV denote the reverse potentials of excitatory and inhibitory synapses, respectively. The corresponding current

$$I(t) = \overbrace{g_{\mathrm{AMPA}}(t)(E_{\mathrm{AMPA}} - V(t))}^{\text{excitatory input}} + \overbrace{g_{\mathrm{GABA}}(t)(E_{\mathrm{GABA}} - V(t))}^{\text{inhibitory input}}, \qquad (8.7)$$

was injected into the neuron, using the dynamic clamp protocol (Sharp et al. 1993), where $V(t)$ denotes the instantaneous membrane potential of the neuron. The same conductances were injected into the simple model (8.5, 8.6), whose parameters were adjusted to fit this particular neuron. The superimposed voltage traces, depicted in Fig.8.17a, show a reasonable fit. The simple model predicts more than 90 percent of spikes of the in vitro neuron, often with a submillisecond precision (see Fig.8.17c). Of course, we should not expect to get a total fit, since we do not explicitly model the sources of intrinsic and synaptic noise present in the cortical slice. In fact, presentation of the same input to the same neuron a few minutes later produces a response with spike jitter, missing spikes, and extra spikes (as in Fig.7.24) comparable with those in the simulated response.

8.2.2   Intrinsically Bursting (IB) Neurons

The class of intrinsically bursting (IB) neurons forms a continuum of cells that differ in their degree of "burstiness", and it probably should consist of subclasses. At one extreme, responses of IB neurons to injected pulses of DC current have initial stereotypical bursts (Fig.8.18a) of high-frequency spikes followed by low-frequency tonic spiking. Many IB neurons burst even when the current is barely superthreshold and not strong enough to elicit a sustained response (as in Fig.8.21, bottom traces). At the other extreme, bursts can be seen only in response to sufficiently strong current, as in Fig.8.11 or Fig.9.1b. Weaker stimulation elicits regular spiking responses. In comparison with typical RS neurons, the regular spiking response of IB neurons has lower firing frequency and higher rheobase (threshold) current, and exhibits shorter latency to the first spike and noticeable afterdepolarizations (ADPs) (Compare RS and IB cells in Fig.8.11.)

Magnifications of the responses of two IB neurons in Fig.8.18b and 8.18c show that the interspike intervals within the burst may be increasing or decreasing, possibly reflecting different ionic mechanisms of burst generation and termination. In any case, the initial high-frequency spiking is caused by the excess of the inward current or the deficit of the outward current needed to repolarize the membrane potential below the threshold. As a result, many spikes are needed to build up outward current to terminate the high-frequency burst. After the neuron recovers, it fires low-frequency tonic spikes because there is a residual outward current (or residual inactivation of inward current) that prevents the occurrence of another burst. Many IB neurons can fire two or more bursts before they switch into tonic spiking mode, as in Fig.8.18a. Below, we present two models of IB neurons, one relying on the interplay of voltage-gated currents, and the other relying on the interplay of fast somatic and slow dendritic spikes.

Let us use the available data on the IB neuron in Fig.8.11 to build a simple one-compartment model (8.5, 8.6) exhibiting IB firing patterns. The neuron has a resting state at $v_{\mathrm{r}} = -75$ mV and an instantaneous threshold at $v_{\mathrm{t}} = -45$ mV. Its rheobase is 350 pA, and the input resistance is around 30 MΩ, resulting in $k = 1.2$ and $b = 5$. The peak of the spike is at $+50$ mV, and the after-spike resetting point is around
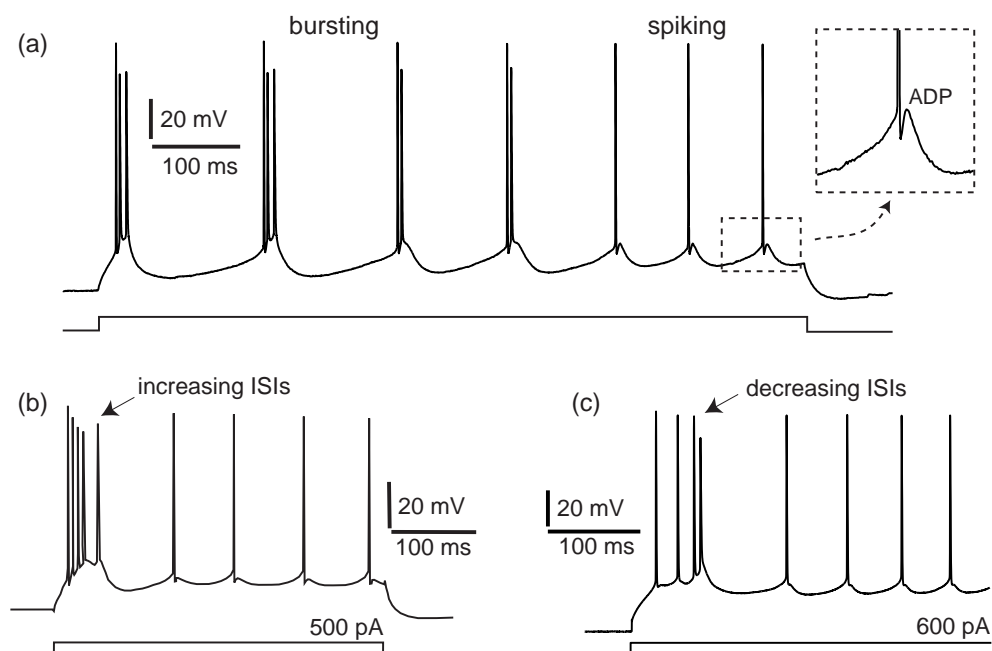
Figure 8.18: (a) bursting and spiking in an IB neuron (layer 5 of somatosensory cortex of a four week old rat at 35°C; (data provided by Greg Stuart and Maarten Kole). Note the afterdepolarization (ADP). (b) IB neuron of a cat (modified from figure 2 of Timofeev et al. 2000). (c) pyramidal neuron of rat visual cortex. Note that IB neurons may exhibit bursts with increasing or decreasing inter-spike intervals (ISIs).

$c = -56$ mV. The parameters $a = 0.01$ and $d = 130$ give a reasonable fit of the neuron's current-frequency relationship.

The phase portraits in Fig.8.19 explain the mechanism of firing of IB patterns in the simple model. When $I = 0$, the model has an equilibrium at -75 mV, which is the intersection of the v-nullcline (dashed parabola) and the u-nullcline (straight line). Injection of a depolarizing current moves the v-nullcline upward. The pulse of current of magnitude $I = 300$ pA is below the neuron's rheobase, so the trajectory moves from the old resting state (black square) to the new one (black circle). Since $b > 0$, the trajectory overshoots the new equilibrium. The pulse of magnitude $I = 370$ pA is barely above the rheobase, so the model exhibits low-frequency tonic firing with some spike frequency adaptation. Elevating the fast nullcline by injecting $I = 500$ pA transforms the first spike into a doublet. Indeed, the after-the-first-spike resetting point (white square marked "1") is below the parabola, so the second spike is fired immediately. Similarly, injection of an even stronger current of magnitude $I = 550$ pA transforms the doublet into a burst of three spikes, each raising the after-spike resetting point. Once the resetting point is inside the parabola, the neuron is in tonic spiking mode.

Figure 8.20a shows simultaneous recording of somatic and dendritic membrane potentials of a layer 5 pyramidal neuron. The somatic spike backpropagates into the
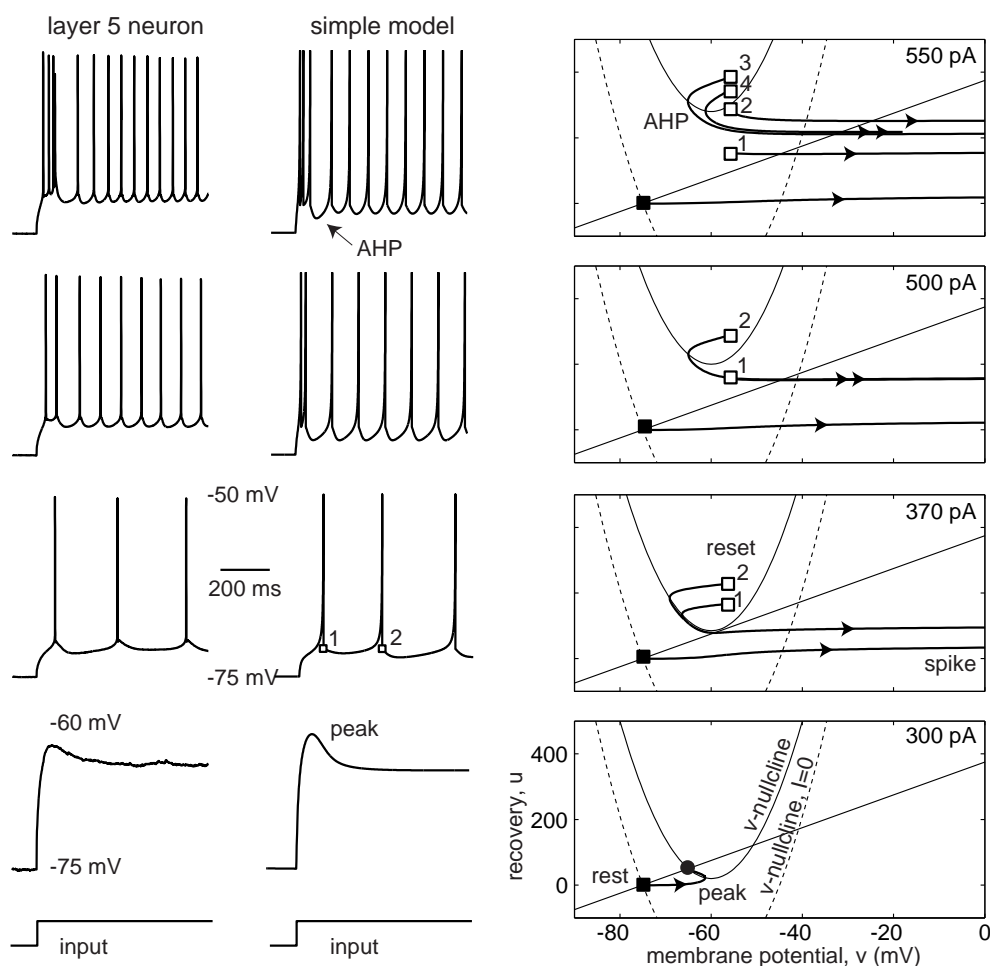
Figure 8.19: Comparison of in vitro recordings of an intrinsically bursting (IB) neuron with the simple model $150\dot{v} = 1.2(v + 75)(v + 45) - u + I$, $\dot{u} = 0.01\{5(v + 75) - u\}$, if $v \geq +50$, then $v \leftarrow -56$, $u \leftarrow u + 130$. White squares denote the reset points, numbered according to the spike number.

dendrite, activates voltage-gated dendritic Na^+ and Ca^{2+} currents (Stuart et al. 1999; Hausser et al. 2000), and results in a slower dendritic spike (clearly seen in the figure). The slow dendritic spike depolarizes the soma, resulting in an ADP, which is typical in many IB cells. Depending on the strength of the injected dc current and the state of the neuron, the ADP can be large enough to cause another somatic spike, as illustrated in Fig.7.52. The somatic spike may initiate another dendritic spike, and so on, resulting in a burst in Fig.8.20b. This mechanism is known as the dendritic-somatic Ping-Pong (Wang 1999), and it occurs in the Pinsky-Rinzel (1994) model of the hippocampal CA3 neuron, the sensory neuron of weakly electric fish (Doiron et al. 2002), and in chattering neurons considered below.

Let us build a two-compartment simple model that simulates the somatic and dendritic spike generation of IB neurons. Since we do not know the rheobase, input
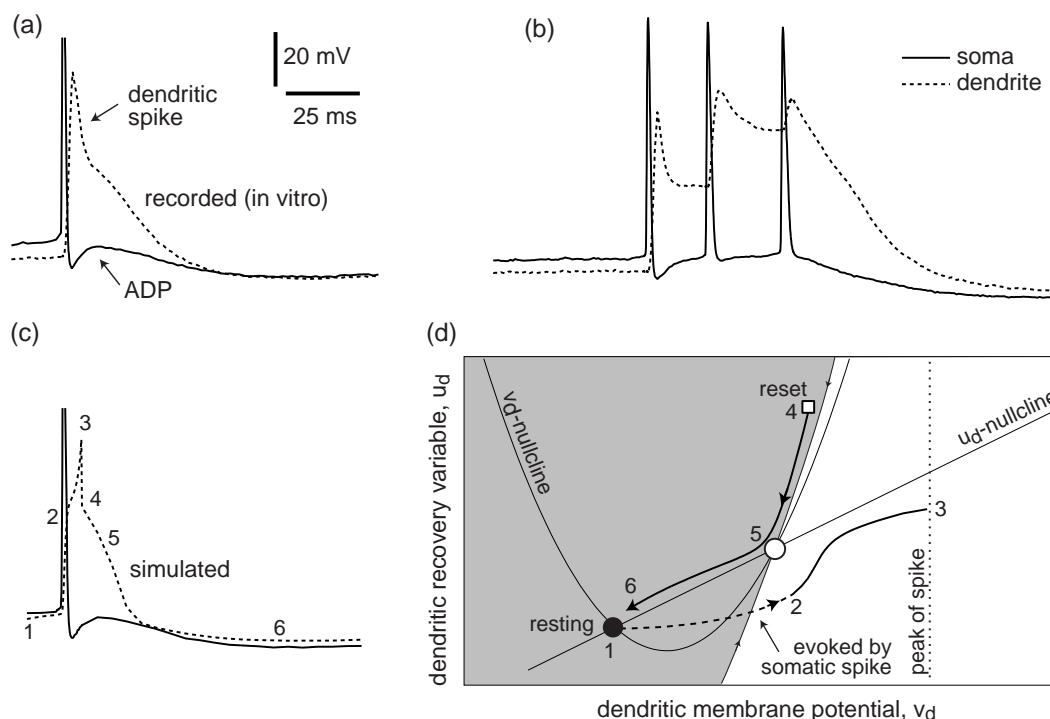
Figure 8.20: Somatic and dendritic spike (a) and burst (b) in an IB neuron. The dendritic spike in (a) is simulated in (c), using the simple model described in Fig.8.20. The phase portrait (d) describes the geometry of the dendritic spike generation mechanism. Recordings are from layer 5 of the somatosensory cortex of a four-week-old rat at 35°C; the dendritic electrode is 0.43mm from the soma. (Data provided by Greg Stuart and Maarten Kole.)

resistance, and resting and instantaneous threshold potentials of the dendritic tree of IB neurons, we cannot determine parameters of the dendritic compartment. Instead, we feed the somatic recording $V(t)$ in Fig.8.20a into the model dendritic compartment and fine-tune the parameters so that the simulated dendritic spike in Fig.8.20c "looks like" the recorded one in Fig.8.20a.

The phase portrait in Fig.8.20d explains the peculiarities of the shape of the simulated dendritic spike. The recorded somatic spike quickly depolarizes the dendritic membrane potential from point 1 to point 2, and starts the regenerative process – the upstroke of a spike. Upon reaching the peak of the spike (3), the dendritic membrane potential and the recovery variable are reset by the action of fast voltage-gated K^+ currents, which are not modeled here explicitly. The reset point (4) is near the stable manifold of the saddle, so the membrane potential slowly repolarizes (5) and returns to the resting state (6).

In Fig.8.21 we put the somatic and dendritic compartments together, adjust some of the parameters, and simulate the response of the IB neuron to pulses of current of various amplitudes. Note that the model correctly reproduces the transient burst of

layer 5 neuron   simple model
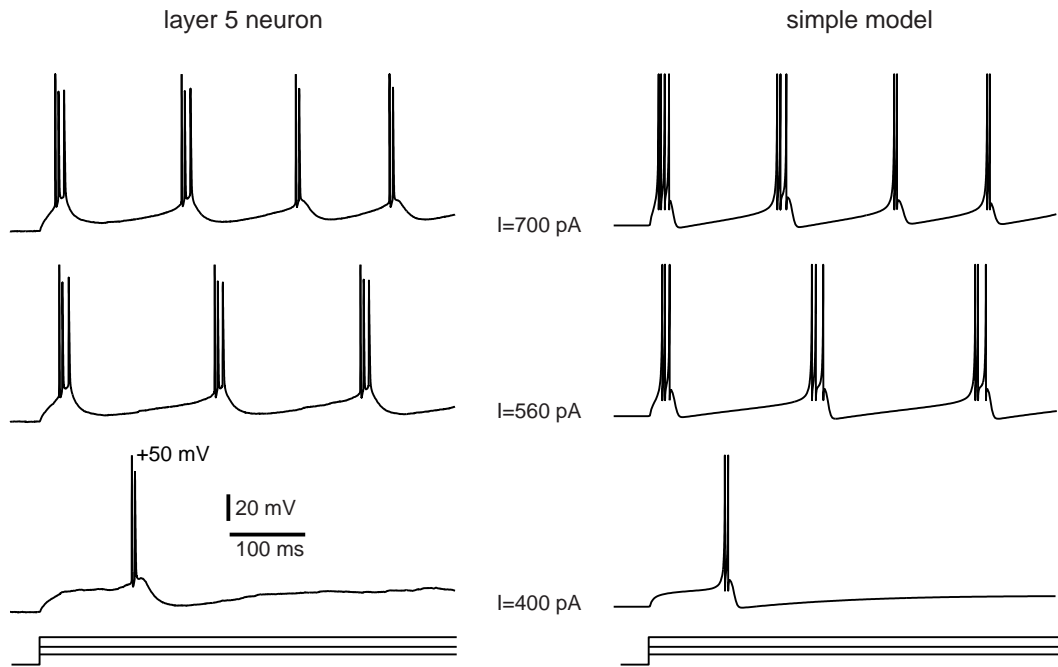
Figure 8.21: Comparison of in vitro recordings of an intrinsically bursting (IB) neuron (layer 5 of somatosensory cortex of a four-week-old rat at 35°C; data provided by Greg Stuart and Maarten Kole) with the two-compartment simple model. Soma: $150\dot{v} = 3(v + 70)(v + 45) + 50(v_d - v) - u + I$, $\dot{u} = 0.01\{5(v + 70) - u\}$, if $v \geq +50$, then $v \leftarrow -52$, $u \leftarrow u + 240$. Active dendrite: $30\dot{v}_d = (v_d + 50)^2 + 20(v - v_d) - u_d$, $\dot{u}_d = 3\{15(v_d + 50) - u_d\}$, if $v_d \geq +20$, then $v_d \leftarrow -20$, $u_d \leftarrow u_d + 500$.

two closely spaced spikes when stimulation is weak, and the rhythmic bursting with decreasing number of spikes per burst when stimulation is strong. Using this approach, one can build models of pyramidal neurons having multiple dendritic compartments, as we do next.

8.2.3   Multi-Compartment Dendritic Tree

In Fig.8.22 we simulate an IB pyramidal neuron having 47 compartments (Fig.8.22a, b), each described by a simple model with parameters provided in the caption of the figure. Our goal is to illustrate a number of interesting phenomena that occur in neuronal models having active dendrites, that is, dendrites capable of generating action potentials.

In Fig.8.22c we inject a current into compartment 4 on the apical dendrite to evoke an excitatory postsynaptic potential (EPSP) of 4 mV, which is subthreshold for the spike generation mechanism. This depolarization produces a current that passively spreads to neighboring compartments, and eventually into the somatic compartment. However, the somatic EPSP is much weaker, only 1 mV, reflecting the distance-dependent attenuation of dendritic synaptic inputs. Note also that somatic
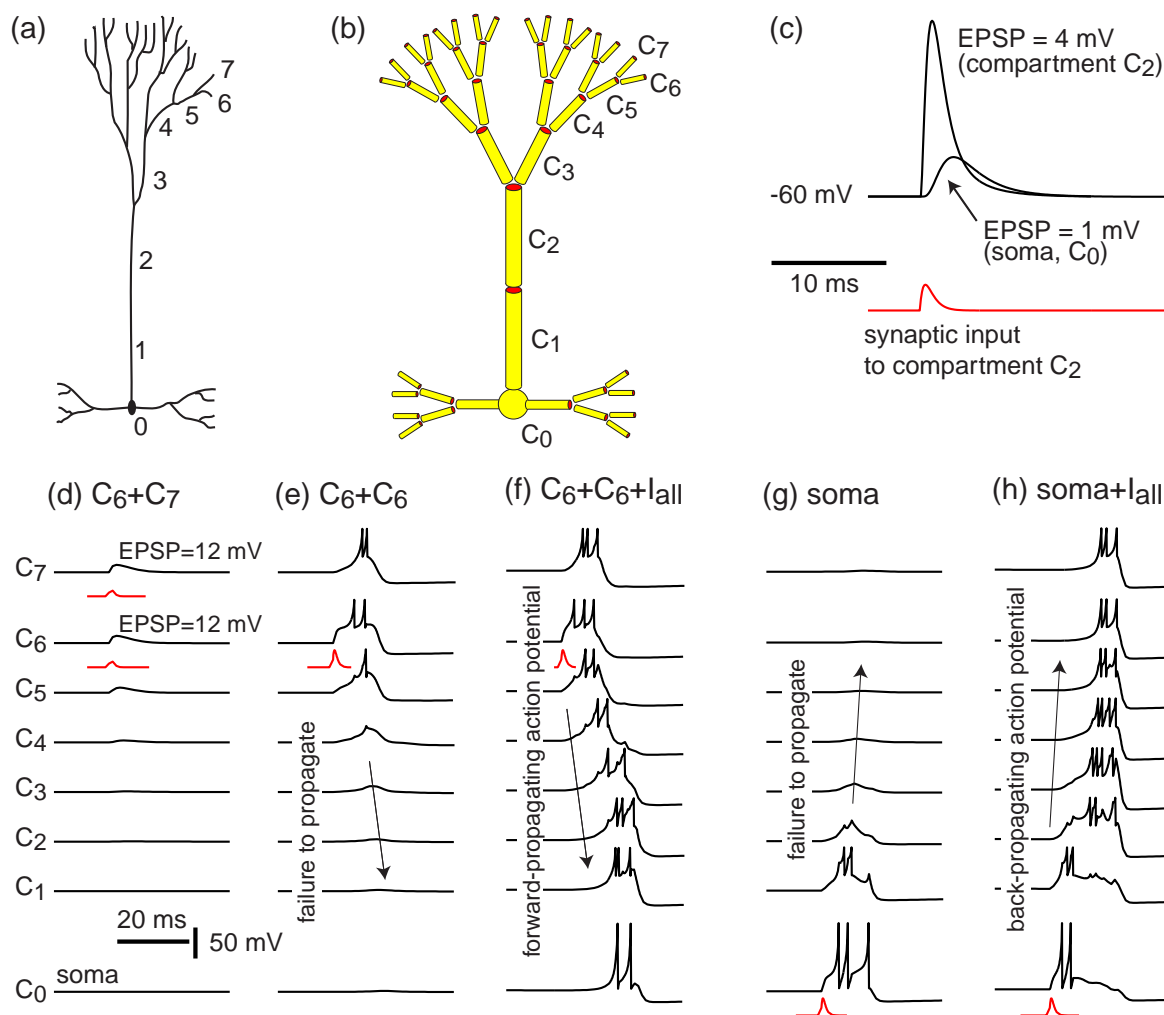
Figure 8.22: (a) Hand drawing and (b) a 47-compartment representation of a layer 5 pyramidal neuron. (c) Injection of current (simulating excitatory synaptic input) into compartment 2 evokes a large excitatory postsynaptic potential (EPSP) in that compartment, but a much smaller EPSP in the somatic compartment. (d) Synaptic inputs to compartments 6 and 7 result in large EPSPs there, but no dendritic spike. (e) The same synaptic inputs into compartment 6 result in a dendritic spike, which fails to propagate forward to the soma. (f) The same input combined with background excitation $I_{all} = 60$ pA to all compartments results in forward-propagating dendritic spikes. (g) Strong synaptic input to the soma results in a spike that fails to propagate into the dendritic tree. (h) The same input combined with injection of $I_{all} = 70$ pA to all compartments (to simulate in vivo tonic background input) promotes back-propagation of spike into the dendritic tree. Each compartment is simulated by the simple model $100\dot{v} = 3(v + 60)(v + 50) - u + I$, $\dot{u} = 0.01\{5(v + 60) - u\}$. Soma: if $v \geq +50$, then $v \leftarrow -55$, $u \leftarrow u + 500$. Dendrites: if $v \geq +10$, then $v \leftarrow -35$, $u \leftarrow u + 1000$. The conductance between any two adjacent compartments is 70 nS.

EPSP is delayed and has a wider time course, which is the result of dendritic low-pass filtering, or smoothing, of subthreshold neuronal signals. The farther the stimulation site is from the soma, the weaker, more delayed, and longer lasting the somatic EPSP is. For many years, dendrites were thought to be passive conductors whose sole purpose is to collect and low-pass filter the synaptic input.

Now, we explore the active properties of dendrites and their dependence on the location, timing, and strength of synaptic input. First, we stimulate two synapses that innervate two sister dendritic compartments, e.g., compartments 6 and 7 in Fig.8.22d that could interact via their mother compartment 5. Each synaptic input evokes a strong EPSP of 12 mV, but due to their separation, the EPSPs do not add up and no dendritic spike is fired. The resulting somatic EPSP is only 0.15 mV due to the passive attenuation. In Fig.8.22e we provide exactly the same synaptic input, but into the same compartment, i.e., compartment 6. The EPSPs add up, and result in a dendritic spike, which propagates into the mother compartment 5 and then into the sister compartment 7 (which was not stimulated), but it fails to propagate along the apical dendrite into the soma. Nevertheless, the somatic compartment exhibits an EPSP of 1.5 mV, hardly seen in the figure. Thus, the location of synaptic stimulation, all other conditions being equal, made a difference. In Fig.8.22f we combine the synaptic stimulation to compartment 6 with injection of a weak current, I_{all}, to all compartments of the neuron. This current represents a tonic background excitation to the neuron that is always present in vivo. It depolarizes the membrane potential by 2.5 mV and facilitates the propagation of the dendritic spike along the apical dendrite all the way into the soma. The same effect could be achieved by an appropriately timed excitatory synaptic input arriving at an intermediate compartment, e.g., compartment 3 or 2. Not surprisingly, an appropriately timed inhibitory input to an intermediate compartment on the apical dendrite could stop the forward-propagating dendritic spike in Fig.8.22f.

In Fig.8.22g and 8.22h we illustrate the opposite phenomenon – back-propagating spikes from soma to dendrites. A superthreshold stimulation of the somatic compartment evokes a burst of three spikes, which fails to propagate along the apical dendrites by itself, but can propagate if combined with a tonic depolarization of the dendritic tree.

We see that dendritic trees can do more than just averaging and low-pass filtering of distributed synaptic inputs. Separate parts of the tree can perform independent local signal processing and even fire dendritic spikes. Depending on the synaptic inputs to other parts of the tree, the spikes can be localized or they can forward-propagate into the soma, causing the cell to fire. Spikes at the soma can backpropagate into the dendrites, triggering spike-time-dependent processes such as synaptic plasticity.

8.2.4   Chattering (CH) Neurons

Chattering neurons, also known as fast rhythmic bursting (FRB) neurons, generate high-frequency repetitive bursts in response to injected depolarizing currents. The magnitude of the DC current determines the interburst period, which could be as long

chattering neuron (in vivo)

simple model

I=600 pA

I=400 pA

I=300 pA

+25 mV

50 ms

-40 mV

I=200 pA
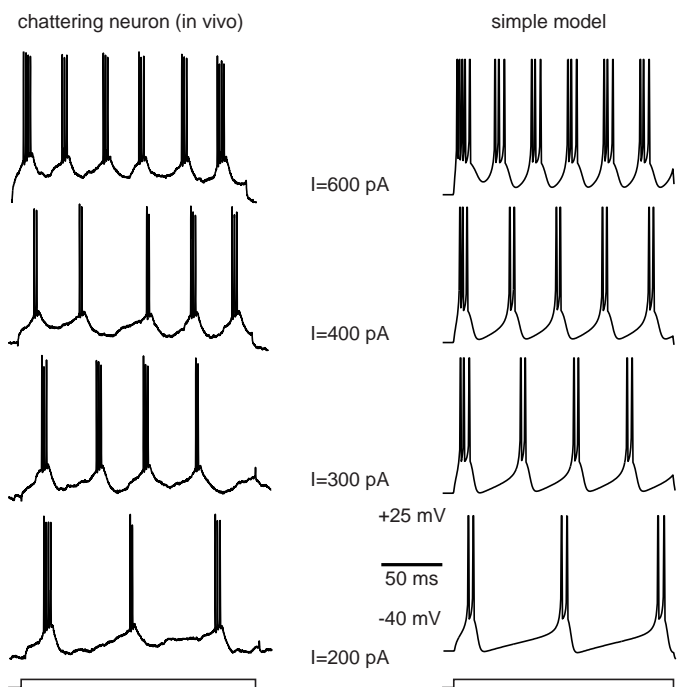
Figure 8.23: Comparison of in vivo recordings from cat primary visual cortex with simulations of the simple model $50\dot{v} = 1.5(v+60)(v+40) - u + I$, $\dot{u} = 0.03\{(v+60) - u\}$, if $v \geq +25$, then $v \leftarrow -40$, $u \leftarrow u + 150$. (Data provided by D. McCormick.)

as 100 ms or as short as 15 ms, and the number of spikes within each burst, typically two to five, as we illustrate in Fig.8.23, using in vivo recordings of a pyramidal neuron of cat visual cortex.

An RS model neuron, as shown in Fig.8.12, can easily be transformed into a CH neuron by increasing the after-spike reset voltage to $c = -40$ mV, mimicking decreased K^+ and increased Na^+ currents activated during each spike. The phase portrait in Fig.8.24 explains the mechanism of chattering of the simple model (8.5, 8.6). A step
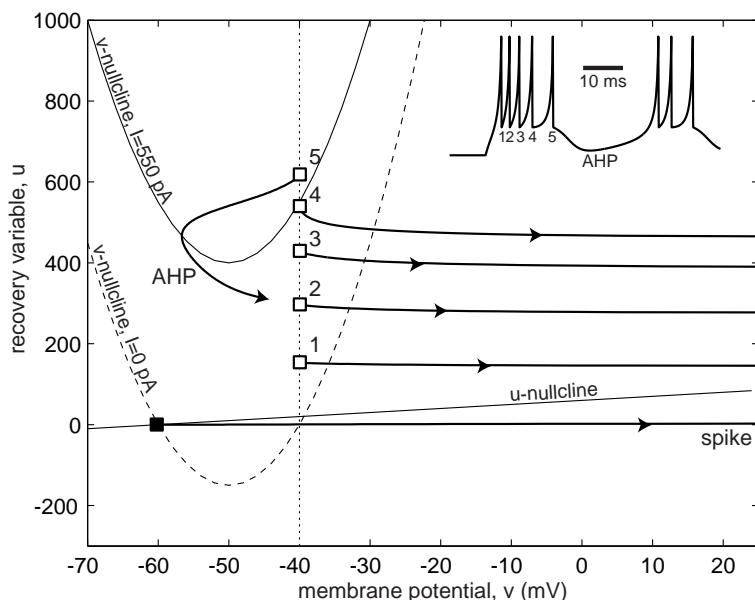
Figure 8.24: Phase portrait of the simple model in Fig.8.23 exhibiting CH firing pattern.

of depolarizing current shifts the fast quadratic nullcline upward and the trajectory quickly moves rightward to fire a spike. The after-spike reset point (white square marked "1" in the figure) is outside the parabola nullcline, so another spike is fired immediately, and so on, until the total amount of outward current is large enough to stop the burst; that is, until the variable u moves the reset point (the white square marked "5") inside the quadratic parabola. The trajectory makes a brief excursion to the left knee (afterhyperpolarization) and then moves rightward again, initiating another burst. Since the second burst starts with an elevated value of u, it has fewer spikes – a phenomenon exhibited by many CH neurons.

8.2.5   Low-Threshold Spiking (LTS) Interneurons

Low-threshold spiking interneurons behave like RS excitatory neurons ($b > 0$) in the sense that they exhibit regular spiking patterns in response to injected pulses of current (some call them regular spiking non-pyramidal (RSNP) neurons). There are some subtle differences, however. The response of an LTS cell to a weak depolarizing current consists of a phasic spike or a doublet with a relatively short latency followed by low-frequency (less than 10 Hz) subthreshold oscillation of membrane potential. Stronger pulses elicit tonic spikes with slow frequency adaptation, decreasing amplitudes, and decreasing after-hyperpolarizations, as one can see in Fig.8.11.

LTS neurons have more depolarized resting potentials, lower threshold potentials, and lower input resistances than RS neurons. To match the in vitro firing patterns of the LTS interneuron of rat barrel cortex in Fig.8.25, we take the simple model of the RS neuron and adjust the resting and instantaneous threshold potentials $v_\mathrm{r} = -56$ mV and $v_\mathrm{t} = -42$ mV, and the values $p = 1$ and $b = 8$, resulting in the rheobase current of 120 pA and the input resistance of 50 MΩ. To model the decreasing nature of the spike and AHP amplitudes, we assume that the peak of the spike and the after-spike resetting point depend on the value of the recovery variable u. This completely unnecessary cosmetic adjustment has a mild effect on the quantitative behavior of the model but gives a more "realistic" look to the simulated voltage traces in Fig.8.25.

The class of excitability of LTS neurons has not been studied systematically, though the neurons seem to be able to fire periodic spike trains with a frequency as low as that of RS neurons (Beierlein et al. 2003; Tateno and Robinson, personal communication). The conjecture that they are near saddle-node on invariant circle bifurcation, and hence are Class 1 excitable integrators, seems to be at odds with the observation that their membrane potential exhibits slow damped oscillation and that they can fire postinhibitory rebound spikes (Bacci et al. 2003a), called low-threshold spikes (hence the name – LTS neurons). They are better characterized as being at the transition from integrators to resonators, with phase portraits as in Fig.8.15.

A possible explanation for the subthreshold oscillations in LTS (and some RS) neurons is given in Fig.8.13, case $b > 0$. The resting state is a stable node when $I = 0$, but it becomes a stable focus when the magnitude of the injected current is near the neuron's rheobase. After firing a phasic spike, the trajectory spirals into the focus
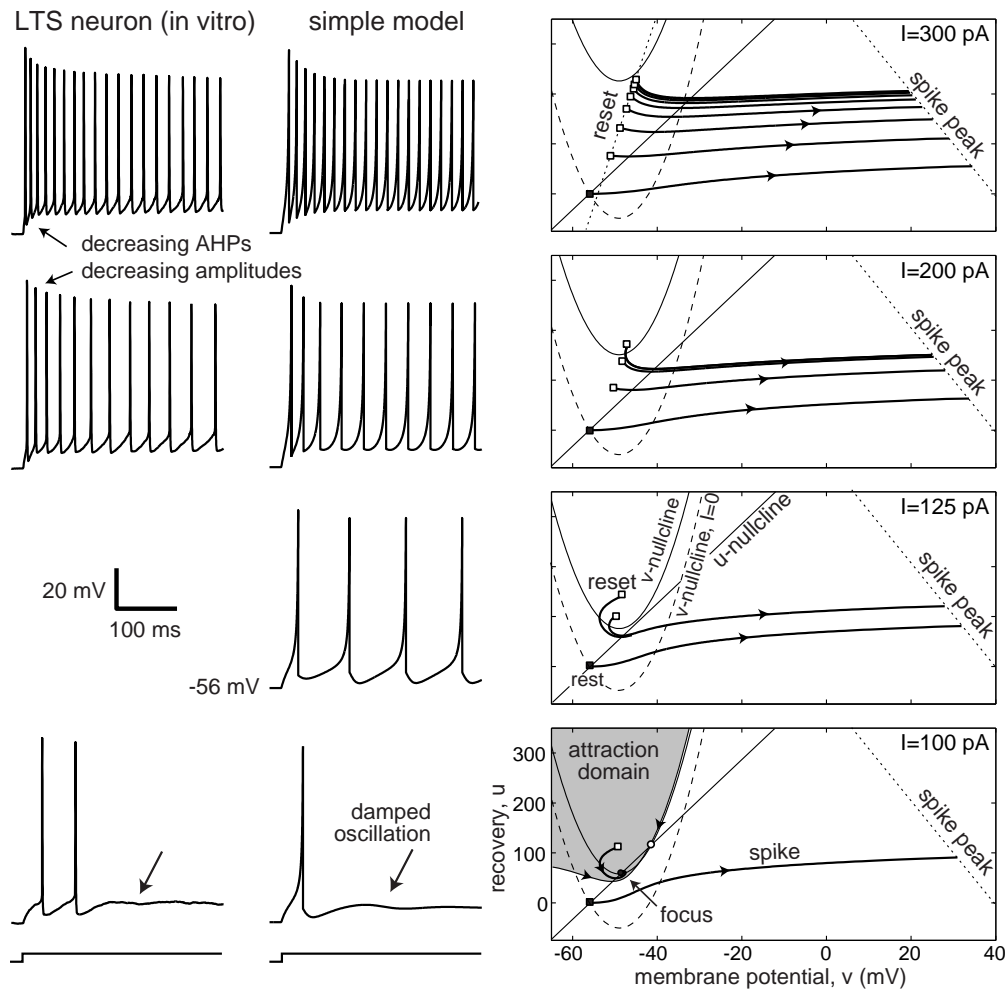
Figure 8.25: Comparison of in vitro recordings of a low threshold spiking (LTS) interneuron (rat barrel cortex; data provided by B. Connors) with simulations of the simple model $100\dot{v} = (v+56)(v+42) - u + I$, $\dot{u} = 0.03\{8(v+56) - u\}$, if $v \geq 40 - 0.1u$, then $v \leftarrow -53 + 0.04u$, $u \leftarrow \min\{u + 20, 670\}$.

exhibiting damped oscillation. Its frequency is the imaginary part of the complex-conjugate eigenvalues of the equilibrium, and it is small because the system is near Bogdanov-Takens bifurcation.

A possible explanation for the rebound spike in LTS (or some RS) neurons is given in Fig.8.26. The shaded region is the attraction domain of the resting state (black circle), which is bounded by the stable manifold of the saddle (white circle). A sufficiently strong hyperpolarizing pulse moves the trajectory to the new, hyperpolarized equilibrium (black square), which is outside the attraction domain. Upon release from the hyperpolarization, the trajectory fires a phasic spike and then returns to the resting state. Some LTS interneurons fire bursts of spikes, and for that reason are called burst-spiking non-pyramidal (BSNP) neurons.
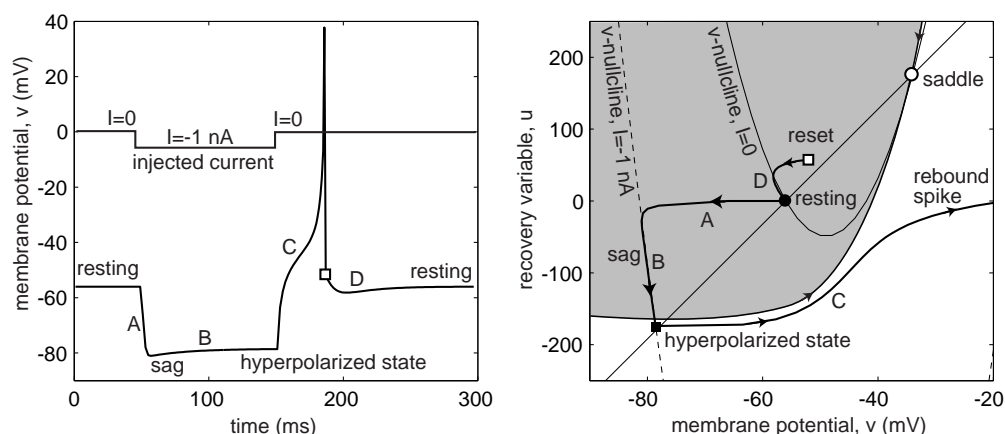
Figure 8.26: The mechanism of sag and rebound spike of the model in Fig.8.25.

8.2.6   Fast Spiking (FS) Interneurons

Fast spiking neurons fire "fast" tonic spike trains of relatively constant amplitude and frequency in response to depolarized pulses of current. In a systematic study, Tateno et al. (2004) have shown that FS neurons have Class 2 excitability in the sense that their frequency-current (F-I) relation has a discontinuity around 20 Hz. When stimulated with barely superthreshold current, such neurons exhibit irregular firing, randomly switching between spiking and fast subthreshold oscillatory mode (Kubota and Kawaguchi 1999; Tateno et al. 2004).

The absence of spike frequency adaptation in FS neurons is mostly due to the fast K^+ current that activates during the spike, produces deep AHP, completely dein-activates the Na^+ current, and thereby facilitates the generation of the next spike. Blocking the K^+ current by TEA (Erisir et al. 1999) removes AHP, leaves residual inactivation of the Na^+ current, and slows the spiking, essentially transforming the FS firing pattern into LTS.

The existence of fast subthreshold oscillations of membrane potential suggests that the resting state of the FS neurons is near the Andronov-Hopf bifurcation. Stuttering behavior at the threshold currents points to the coexistence of resting and spiking states, as in Fig.8.16, and suggests that the bifurcation is of the subcritical type. However, FS neurons do not fire postinhibitory (rebound) spikes – the feature used to distinguish them experimentally from LTS types. Thus, we cannot use the simple model (8.5, 8.6) in its present form to simulate FS neurons because the model with linear slow nullcline would fire rebound spikes according to the mechanism depicted in Fig.8.26. In addition, the simple model has a non-monotone I-V relation, whereas FS neurons have a monotone relation.

The absence of rebound responses in FS neurons means that the phenomenological recovery variable (activation of the fast K^+ current) does not decrease significantly below the resting value when the membrane potential is hyperpolarized. That is, the slow u-nullcline becomes horizontal in the hyperpolarized voltage range. Accordingly,
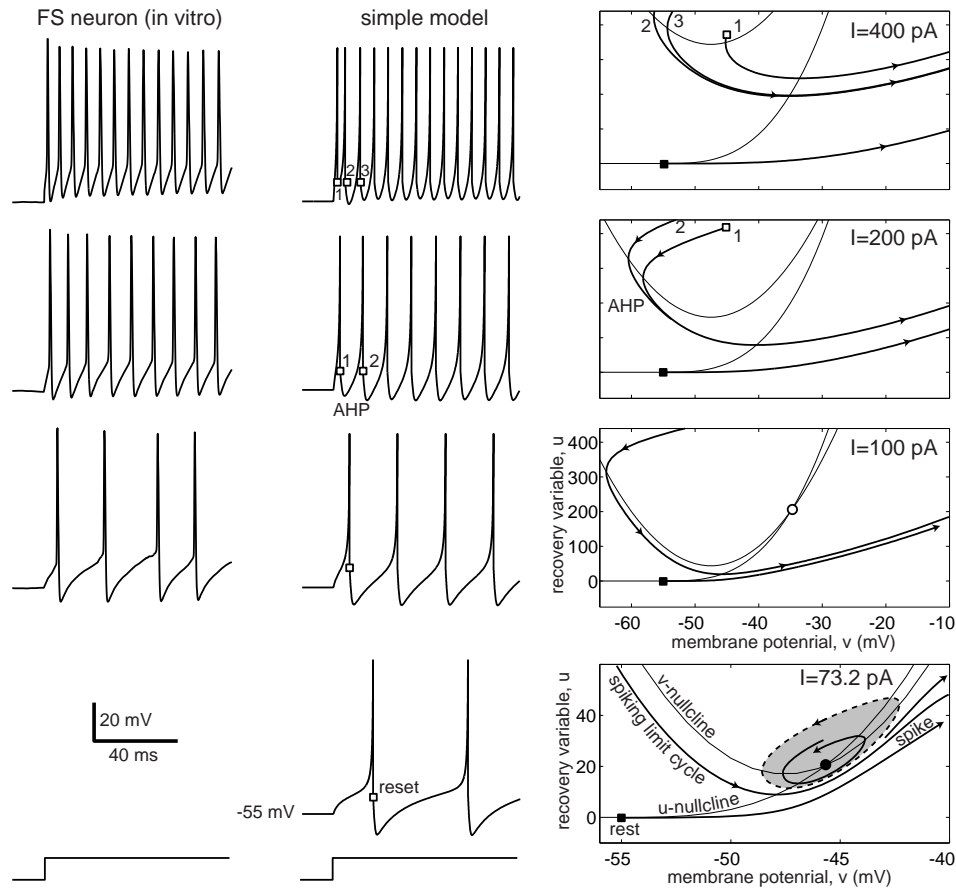
Figure 8.27: Comparison of in vitro recordings of a fast spiking (FS) interneuron of layer 5 rat visual cortex with simulations of the simple model $20\dot{v} = (v+55)(v+40) - u + I$, $\dot{u} = 0.2\{U(v) - u\}$, if $v \geq 25$, then $v \leftarrow -45$ mV. Slow nonlinear nullcline $U(v) = 0$ when $v < v_{\rm b}$ and $U(v) = 0.025(v - v_{\rm b})^3$ when $v \geq v_{\rm b}$ with $v_{\rm b} = -55$ mV. Shaded area denotes the attraction domain of the resting state.

we simulate the FS neuron in Fig.8.27, using the simple model (8.5) with nonlinear u-nullcline.

The phase portraits and bifurcation diagram of the FS neuron model are qualitatively similar to the fast subsystem of a "subHopf/fold cycle" burster: injection of DC current I creates a stable and an unstable limit cycle via fold limit cycle bifurcation. The frequency of the newborn stable cycle is around 20 Hz; hence the discontinuity of the F-I curve and Class 2 excitability. There is a bistability of resting and spiking states, as in Fig.8.27 (bottom right), so that noise can switch the state of the neuron back and forth, and result in irregular stuttering spiking with subthreshold oscillations in the $10 - 40$ Hz range between the spike trains. Further increase of I shrinks the amplitude of the unstable limit cycle, results in the subcritical Andronov-Hopf bifurcation of the resting state, removes the coexistence of attractors, and leaves only the tonic spiking mode.

LS neuron (in vitro)   simple model
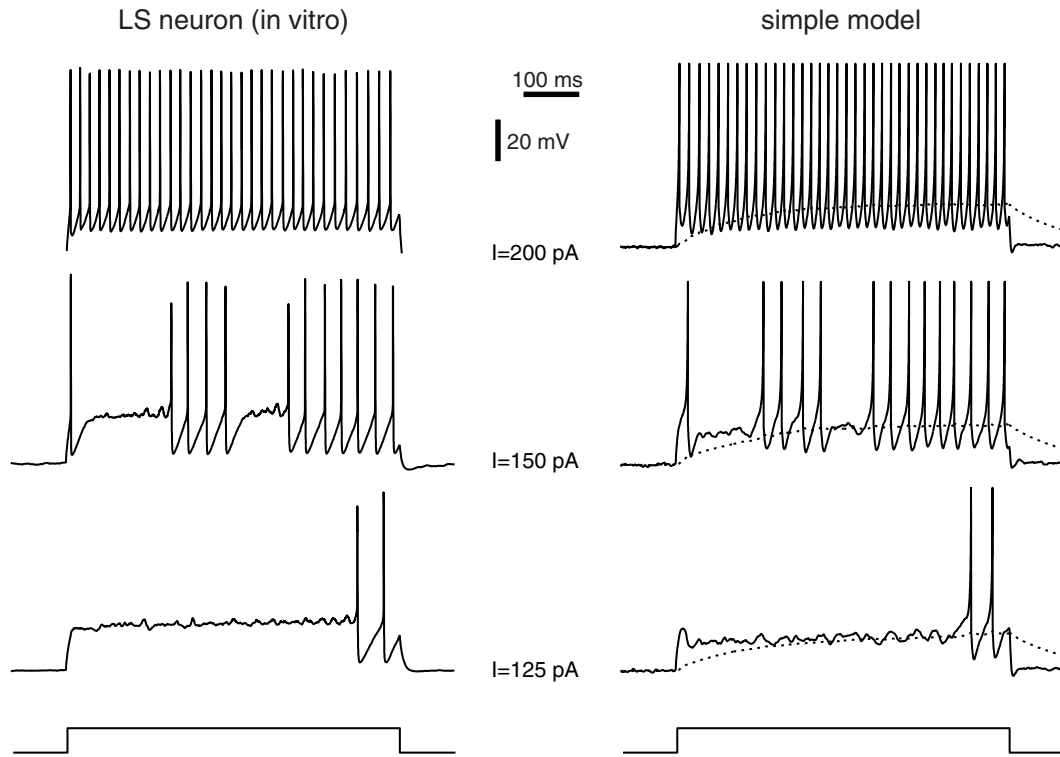
Figure 8.28: Comparison of in vitro recordings of a late spiking (LS) interneuron of layer 1 rat neocortex with simulations of the simple two-compartment model. Soma: $20\dot{v} = 0.3(v+66)(v+40) + 1.2(v_d - v) - u + I$, $\dot{u} = 0.17\{5(v+66) - u\}$, if $v \geq 30$, then $v \leftarrow -45$, $u \leftarrow u + 100$. Passive dendrite (dotted curve): $\dot{v}_d = 0.01(v - v_d)$. Weak noise was added to simulations to unmask the subthreshold oscillations. (Recordings were provided by Zhiguo Chu, Mario Galarreta, and Shaul Hestrin; traces $I = 125$ and $I = 150$ are from one cell; trace $I = 200$ is from another cell.)

8.2.7   Late Spiking (LS) Interneurons

When stimulated with long pulses of DC current, late spiking neurons exhibit a long voltage ramp, barely seen in Fig.8.28 (bottom), and then switch into a tonic firing mode. A stronger stimulation may evoke an immediate (transient) spike followed by a long ramp and a long latency to the second spike. There are pronounced fast subthreshold oscillations during the voltage ramp, indicating the existence of at least two time scales: (1) fast oscillations resulting from the interplay of amplifying and resonant currents, and (2) slow ramp resulting from the slow kinetic of an amplifying variable, such as slow inactivation of an outward current (e.g., the K^+ A-current) or slow activation of an inward current, or both. In addition, the ramp could result from the slow charging of the dendritic compartment of the neuron.

The exact mechanism responsible for the slow ramp in LS neurons is not known at present. Fortunately, we do not need to know the mechanism in order to simulate LS neurons using the simple model approach. Indeed, simple models with passive

dendrites are equivalent to simple models with linear amplifying currents. For example, the model in Fig.8.28 consists of a two-dimensional system (v, u) responsible for the spike generation mechanism at the soma and a linear equation for the passive dendritic compartment v_d.

When stimulated with the threshold current (i.e., just above the neuronal rheobase), LS neurons often exhibit the stuttering behavior seen in Fig.8.28 (middle). Subthreshold oscillations, voltage ramps, and stuttering are consistent with the following geometrical picture. Abrupt onset of stimulation evokes a transient spike followed by brief hyperpolarization and then sustained depolarization. While depolarized, the fast subsystem affects the slow subsystem, e.g., slowly charges the dendritic tree or slowly inactivates the K^+ current. In any case, there is a slow decrease of the outward current or, equivalently, a slow increase of the inward current that drives the fast subsystem through the subcritical Andronov-Hopf bifurcation. Because of the coexistence of resting and spiking states near the bifurcation, the neuron can be switched from one state to the other by the membrane noise. Once the bifurcation is passed, the neuron is in the tonic spiking mode. Overall, LS neurons can be thought of as being FS neurons with a slow subsystem that damps any abrupt changes, delays the onset of spiking, and slows the frequency of spiking.

8.2.8 Diversity of Inhibitory Interneurons

In contrast to excitatory neocortical pyramidal neurons, which have stereotypical morphological and electrophysiological classes (RS, IB, CH), inhibitory neocortical interneurons have wildly diverse classes with various firing patterns that cannot be classified as FS, LTS, or LS. Markram et al. (2004) reviewed recent results on the relationship between electrophysiology, pharmacology, immunohistochemistry, and gene expression patterns of inhibitory interneurons. An extreme interpretation of their findings is that there is a continuum of different classes of interneurons rather than a set of three classes.

Figure 8.29 summarizes five of the most ubiquitous groups in the continuum:

- (NAC) Non-accommodating interneurons fire repetitively without frequency adaptation in response to a wide range of sustained somatic current injections. Many FS and LS neurons are of this type.

- (AC) Accommodating interneurons fire repetitively with frequency adaptation and therefore do not reach the high firing rates of NAC neurons. Some FS and LS cells, but mostly LTS cells, are of this type.

- (STUT) Stuttering interneurons fire high-frequency clusters of regular spikes intermingled with unpredictable periods of quiescence. Some FS and LS cells exhibit this firing type.

- (BST) Bursting interneurons fire a cluster of three to five spikes riding on a slow depolarizing wave, followed by a strong slow AHP.
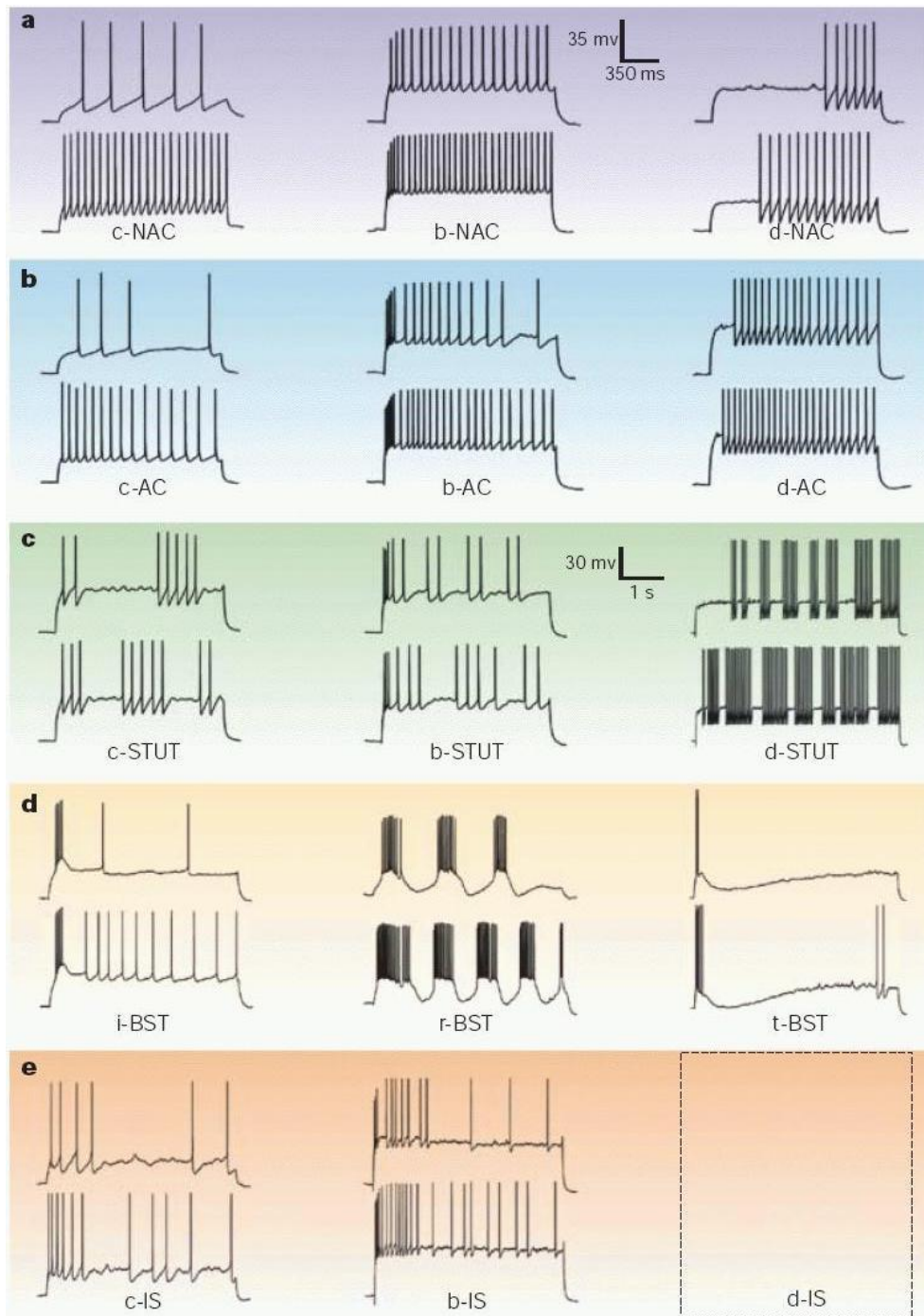
Figure 8.29: An alternative classification of neocortical inhibitory interneurons (modified from Markram et al. 2004). Five major classes: non-accommodating (NAC), accommodating (AC), stuttering (STUT), bursting (BST), and irregular spiking (IS). Most classes contain subclasses: delay (d), classic (c), and burst (b). For bursting interneurons, the three types are repetitive (r), initial (i), and transient (t). Subclass d-IS is not provided in the original picture by Markram et al.
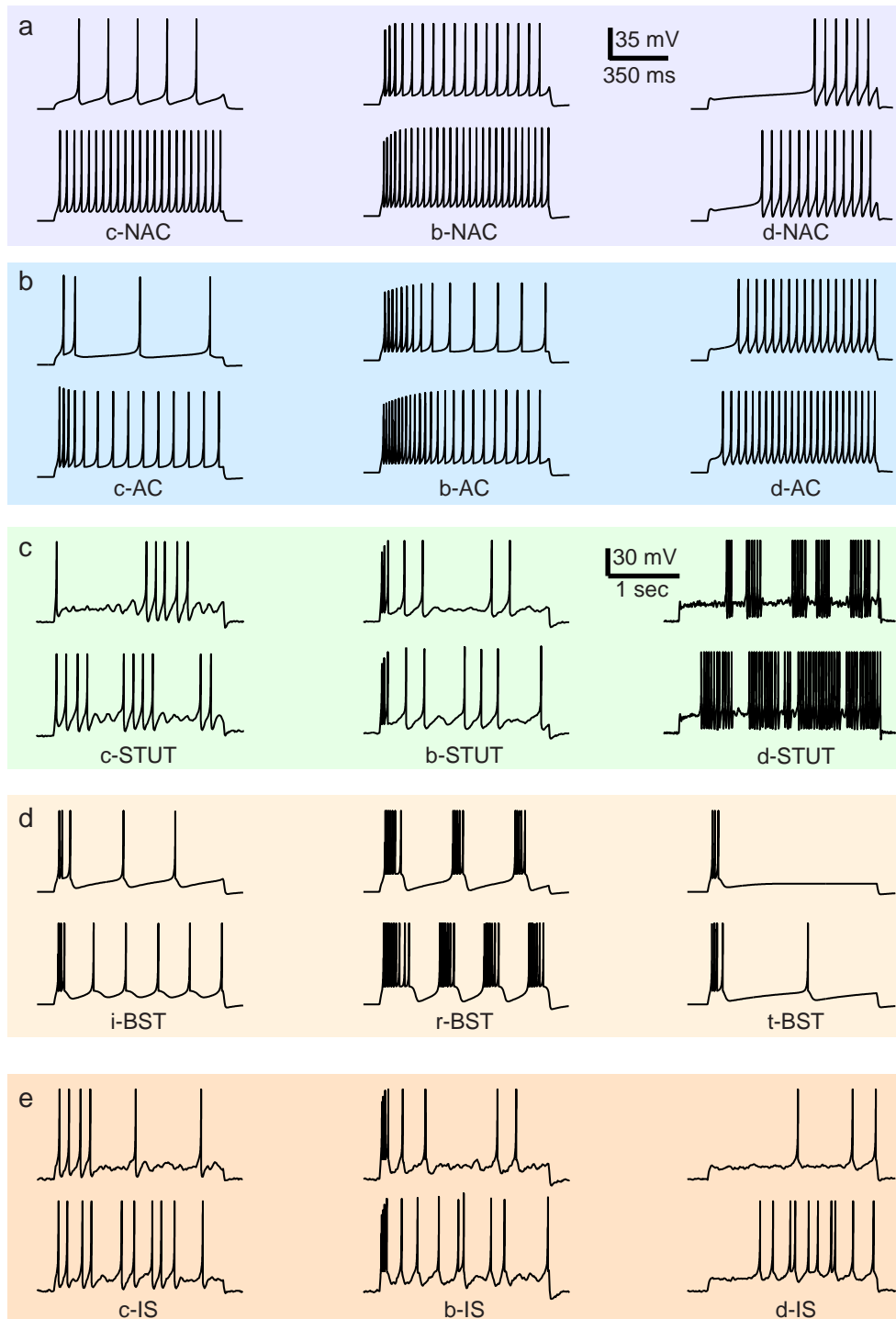
Figure 8.30: Simulations of the simple model with various parameters can reproduce all firing patterns of neocortical inhibitory interneurons in Fig.8.29.

- (IS) Irregular spiking interneurons fire single spikes randomly with pronounced frequency accommodation.

NAC and AC are the most common response types found in the neocortex. Each group can be divided into three subgroups depending on the type of the onset of the response to a step depolarization:

- (c) Classical response is when the first spike has the same shape as any other spike in the response.

- (b) Burst response is when the first three or more spikes are clustered into a burst.

- (d) Delayed response is when there is noticeable delay before the onset of spiking.

The BST type has different subdivisions: repetitive (r), initial (i), and transient (t) bursting.

In Fig.8.30 we use the simple model (8.5, 8.6) to reproduce all firing patterns of the interneurons, including the delayed irregular spiking (d-IS) pattern that was omitted from Fig.8.29. We use one-size-fits-all set of parameters: $C = 100$, $k = 1$, $v_r = -60$ mV, and $v_t = -40$ mV. We vary the parameters a, b, c, and d. We do not strive to reproduce the patterns quantitatively, but only qualitatively.

The parameters for the NAC and AC cells were similar to those for RS neurons, with an additional passive dendritic compartment for the delayed response. The parameters for the STUT and IS cells were similar to those of the LS interneuron, with some minor modifications that affect the initial burstiness and delays. Irregular stuttering in these types results from the coexistence of a stable resting equilibrium and a spiking limit cycle attractor, as in the cases of FS and LS neurons considered above. The level of intrinsic noise controls the probabilities of transitions between the attractors. The parameters for the BST cells were similar to those of IB and CH pyramidal cells. Varying the parameters a, b, c, and d, we indeed can get all the firing patterns in Fig.8.29, plus many intermediate patterns, thereby creating a continuum of types of inhibitory interneurons.

8.3   Thalamus

The thalamus is the major gateway to the neocortex in the sense that no sensory signal, such as vision, hearing, touch, or taste, etc., can reach the neocortex without passing through an appropriate thalamic nucleus. Anatomically, the thalamic system consists of three major types of neurons: thalamocortical (TC) neurons, which relay signals into the neocortex; reticular thalamic nucleus (RTN) neurons; and thalamic interneurons, which provide local reciprocal inhibition (Shepherd 2004). The three types have distinct electrophysiological properties and firing patterns.

There are undoubtedly subtypes within each type of thalamic neurons, but the classification is not as elaborate as the one in the neocortex. This, and the differences
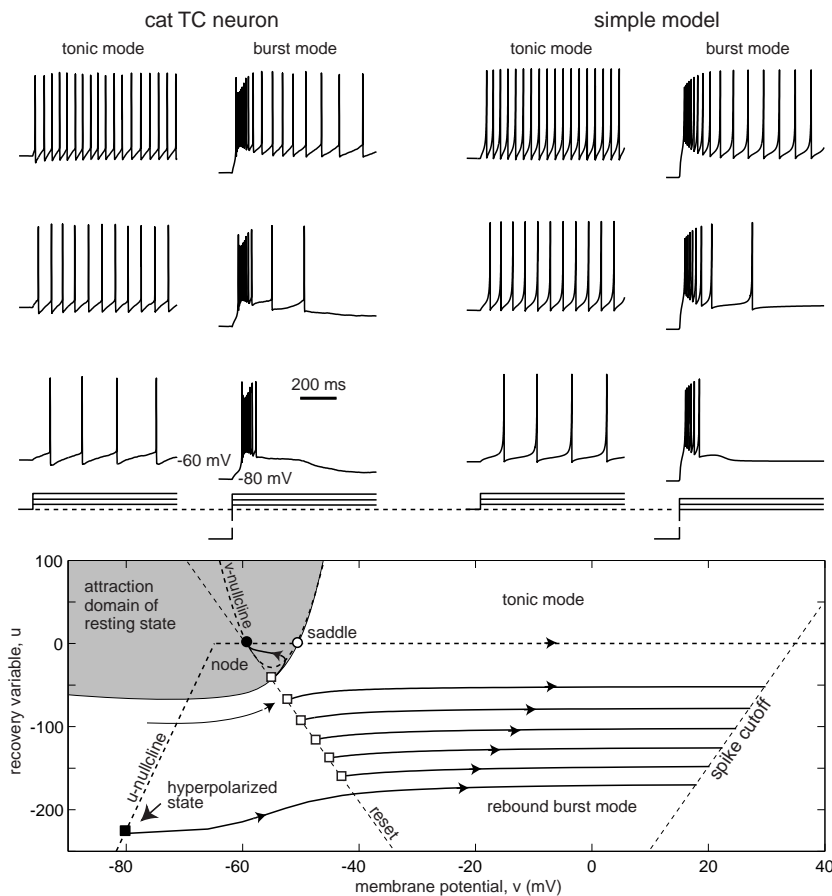
Figure 8.31: Comparison of in vitro recordings of a thalamocortical (TC) cell of cat dorsal lateral geniculate nucleus with simulations of the simple model $200\dot{v} = 1.6(v + 60)(v + 50) - u + I$, $\dot{u} = 0.01\{b(v+65)-u\}$, $b = 15$ if $v \leq -65$ and $b = 0$ otherwise. When $v \geq 35+0.1u$, then $v \leftarrow -60-0.1u$, $u \leftarrow u+10$. Injected current pulses are in 50 pA increments. In burst mode, the cell was hyperpolarized to -80 mV prior to injection of a depolarizing pulse of current. (Data provided by C. L. Cox and S. M. Sherman.)

between species, ages, and various thalamic nuclei, explain the contradictory reports of different firing patterns in presumably the same types of thalamic neurons. Below we use the simple model (8.5, 8.6) to simulate a "typical" TC, TRN, and interneuron. The reader should realize, though, that our attempt is as incomplete as the attempt to simulate a "typical" neocortical neuron ignoring the fact that there are RS, IB, CH, FS, and other cells.

8.3.1 Thalamocortical (TC) Relay Neurons

Thalamocortical (TC) relay neurons, the type of thalamic neurons that project sensory input to the cortex, have two prominent models of firing, illustrated in Fig.8.31: tonic mode and burst mode. Both modes are ubiquitous in vitro and in vivo, including awake and behaving animals, and both represent different patterns of relay of sensory information into the cortex (Sherman 2001). The transition between the firing modes depends on the degree of inactivation of a low-threshold Ca^{2+} T-current (Jahnsen and Llinas 1984; McCormick and Huguenard 1992), which in turn depends on the holding membrane potential of the TC neuron.

In tonic mode, the resting membrane potential of a TC neuron is around -60 mV, which is above the inactivation threshold of the T-current. The slow Ca^{2+} current is inactivated and is not available to contribute to spiking behavior. The neuron fires Na^+-K^+ tonic spikes with a relatively constant frequency that depends on the amplitude of the injected current and could be as low as a few Hertz (Zhan et al. 1999). Such a cell, illustrated in Fig.8.31, is a typical Class 1 excitable system near a saddle-node on invariant circle bifurcation. It exhibits regular spiking behavior similar to that of RS neocortical neurons. It relays transient inputs into outputs, and for this reason, many refer to the tonic mode as the relay mode of firing.

To switch a TC neuron into the burst mode, an injected DC current or inhibitory synaptic input must hyperpolarize the membrane potential to around -80 mV for at least $50 - 100$ ms. While it is hyperpolarized, the Ca^{2+} T-current deinactivates and becomes available. As soon as the membrane potential is returned to the resting or depolarized state, there is an excess of the inward current that drives the neuron over the threshold and results in a rebound burst of high-frequency spikes (as in Fig.8.31), called a low-threshold (LT) spike or a Ca^{2+} spike.

In Fig.8.31 (right) we simulate the TC neuron, using the simple model (8.5, 8.6), and treating u as the low-threshold Ca^{2+} current. Since the current is inactivated in the tonic mode, that is, $u \approx 0$, we take $b = 0$. The resting and threshold voltages of the neuron in the figure are $v_r = -60$ mV and $v_t = -50$ mV. The value $p = 1.6$ results in a 40 pA rheobase current and a 60 MΩ input resistance, and the membrane capacitance $C = 200$ pF gives the correct current-frequency (F-I) relationship. Thus, in the tonic mode, our model is essentially the quadratic integrate-and-fire neuron $200\dot{v} = 1.6(v + 60)(v + 50) + I$ with the after-spike reset from $+35$ mV to -60 mV.

To model slow Ca^{2+} dynamics in the burst mode, assume that hyperpolarizations below the Ca^{2+} inactivation threshold of -65 mV decrease u, thereby creating inward current. In the linear case, take $\dot{u} = 0.01\{b(v+65) - u\}$ with $b = 0$ when $v \geq -65$, and $b = 15$ when $v < -65$, resulting in the piecewise linear u-nullcline depicted in Fig.8.31 (bottom). Prolonged hyperpolarization below -65 mV decreases u and moves the trajectory outside the attraction domain of the resting state (shaded region in the figure). Upon release from the hyperpolarization, the model fires a rebound burst of spikes; the variable $u \to 0$ (inactivation of Ca^{2+}), and the trajectory reenters the attraction domain of the resting state. Steps of depolarized current produce rebound bursts followed by tonic spiking with adapting frequency. A better quantitative agreement with TC recordings can be achieved when two slow variables, u_1 and u_2, are used.

8.3.2   Reticular Thalamic Nucleus (RTN) Neurons

Reticular thalamic nucleus (RTN) neurons provide reciprocal inhibition to TC relay neurons. RTN and TC cells are similar in the sense that they have two firing modes, illustrated in Fig.8.32: They fire trains of single spikes following stimulation from resting or depolarized potentials in the tonic mode, as well as rebound bursts upon release from hyperpolarized potentials in the burst mode.
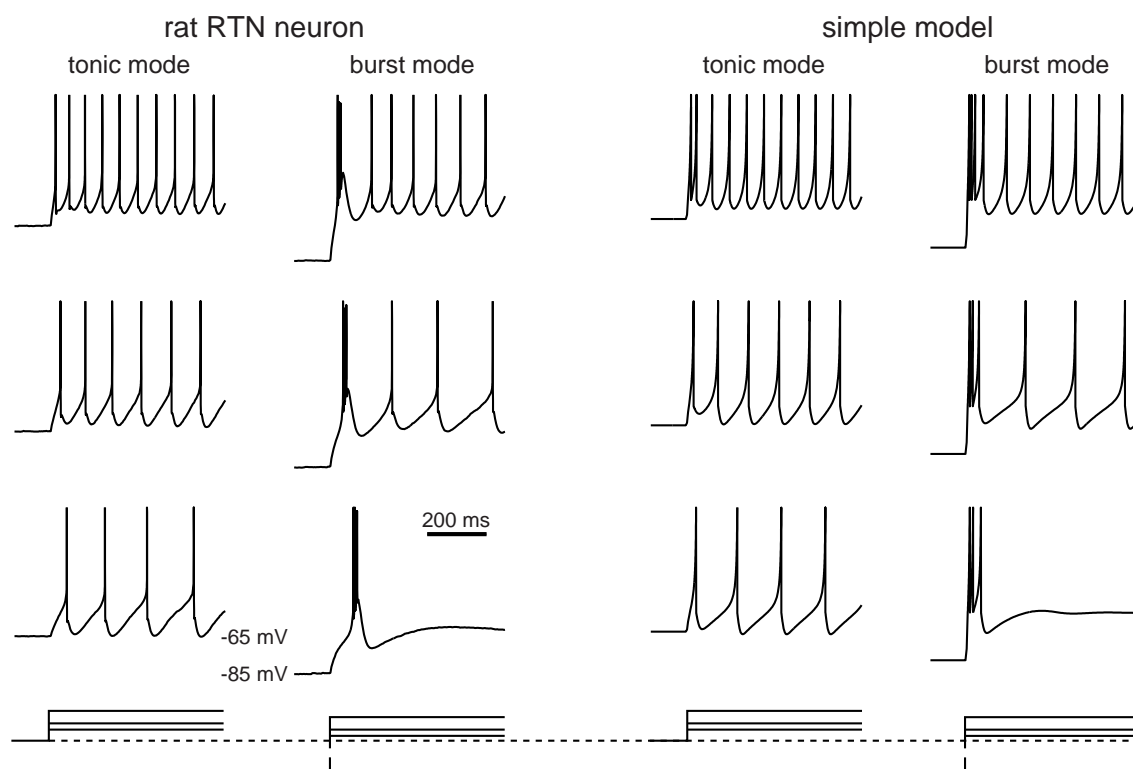
Figure 8.32: Comparison of in vitro recordings of a reticular thalamic nucleus (RTN) neuron of a rat with simulations of the simple model $40\dot{v} = 0.25(v+65)(v+45) - u + I$, $\dot{u} = 0.015\{b(v+65) - u\}$, $b = 10$ if $v \leq -65$ and $b = 2$ otherwise. When $v \geq 0$ (spike cutoff), then $v \leftarrow -55$, $u \leftarrow u + 50$. Injected current pulses are $50, 70$, and 110 pA. In burst mode, the cell was hyperpolarized to -80 mV prior to injection of a depolarizing pulse of current. (Data provided S. H. Lee and C. L. Cox.)

The parameters of the simple model in Fig.8.32 are adjusted to match the in vitro recording of the RTN cell in the figure, and they differ from the parameters of the TC model cell. Nevertheless, the mechanism of rebound bursting of the RTN neuron is the same as that of the TC neuron in Fig.8.31 (bottom). In contrast, the tonic mode of firing is different. Since $b > 0$, the model neuron is near the transition from an integrator to a resonator; it can fire transient spikes followed by slow subthreshold oscillations of membrane potential; it has coexistence of stable resting and spiking states, with the bifurcation diagram similar to the one in Fig.8.15, and it can stutter and produce clustered spikes when stimulated with barely threshold current. Interestingly, similar behavior of TC neurons was reported by Pirchio et al. (1997), Pedroarena and Llinas (1997), and Li et al. (2003). We will return to the issue of subthreshold oscillations and stuttering spiking when we consider stellate cells of entorhinal cortex in section 8.4.4.

cat thalamic interneuron   simple model
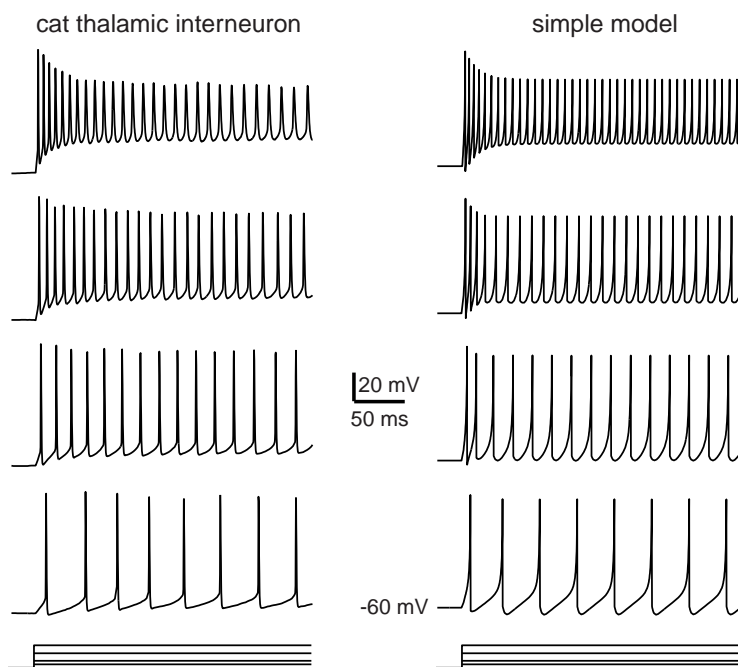
Figure 8.33: Comparison of in vitro recordings of dorsal lateral geniculate nucleus interneuron of a cat with simulations of the simple model $20\dot{v} = 0.5(v + 60)(v + 50) - u + I$, $\dot{u} = 0.05\{7(v + 60) - u\}$. When $v \geq 20 - 0.08u$ (spike cutoff), $v \leftarrow -65 + 0.08u$, $u \leftarrow \min\{u + 50, 530\}$. Injected current pulses are $50, 100, 200$, and 250 pA. (Data provided by C. L. Cox and S. M. Sherman.)

8.3.3   Thalamic Interneurons

In contrast to TC and RTN neurons, thalamic interneurons do not have a prominent burst mode, though they can fire rebound spikes upon release from hyperpolarization (Pape and McCormick 1995). They have action potentials with short duration, and they are able to generate high-frequency trains of spikes reaching 800 Hz, as do cortical FS interneurons. The simple model in Fig.8.33 reproduces all these features. Its phase portrait and bifurcation diagram are similar to those in Fig.8.15, but its dynamics has a much faster time scale.

8.4   Other Interesting Cases

The neocortical and thalamic neurons span an impressive range of dynamic behavior. Many neuronal types found in other brain regions have dynamics quite similar to some of the types discussed above, while many do not.

8.4.1   Hippocampal CA1 Pyramidal Neurons

Hippocampal pyramidal neurons and interneurons are similar to those of the neocortex, and hence could be simulated using the simple model presented in section 8.2. Let us elaborate, using the pyramidal neurons of the CA1 region of the hippocampus as an example.

Jensen et al. (1994) suggested classifying all CA1 pyramidal neurons according to their propensity to fire bursts of spikes, often called *complex spikes*. The majority (more than 80 percent) of CA1 pyramidal neurons are non-bursting cells, whereas the
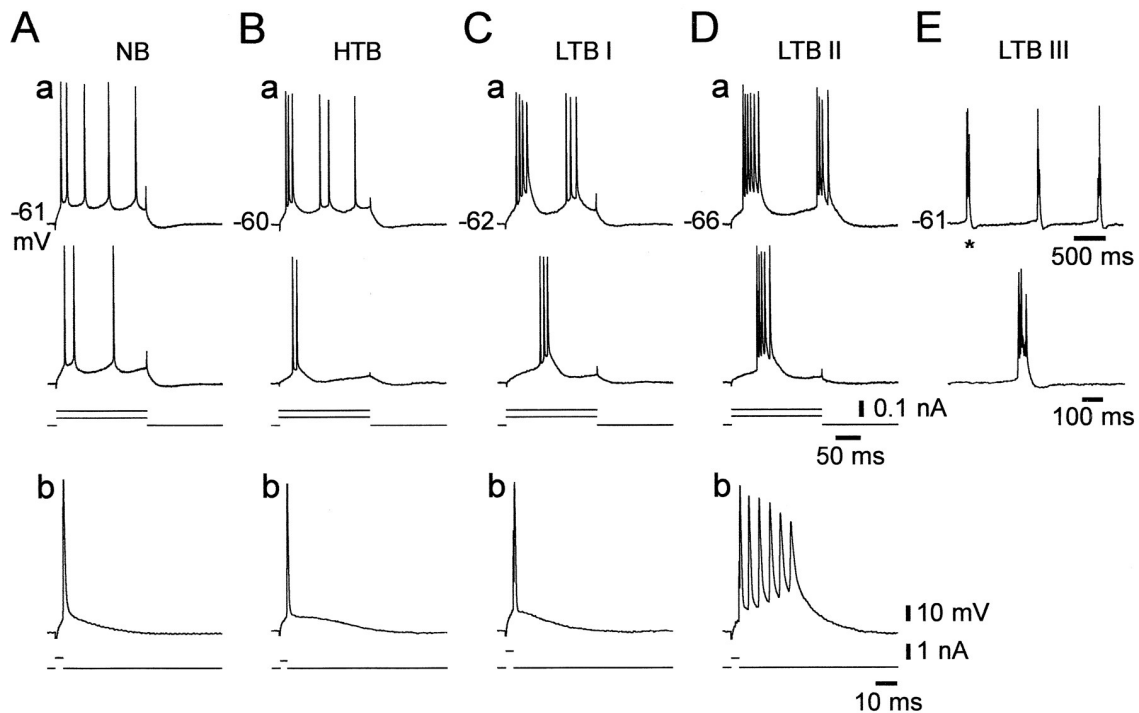
Figure 8.34: Classification of hippocampal CA1 pyramidal neurons. A–E, in vitro recordings from five different pyramidal neurons arranged according to a gradient of increasing propensity to burst. The neurons were stimulated with current pulses of 200 ms duration and amplitude 50 pA and 100 pA (a), or brief (3–5 ms) superthreshold pulses (b). The non-burster (NB) neuron fires tonic spikes in response to long pulses and a single spike in response to brief pulses. The high-threshold burster (HTB) fires bursts only in response to strong long pulses, and single spikes in response to weak or brief pulses. The grade I low-threshold burster (LTB I) generates bursts in response to long pulses of current, but single spikes in response to brief pulses. The grade II LTB (LTB II) fires bursts in response to both long (a) and brief (b) current pulses. The grade III LTB (LTB III), in addition to firing bursts in response to long and brief pulses of current (not shown), also fires spontaneous rhythmic bursts, shown in contracted and expanded time scales. (Reproduced from Su et al. 2001 with permission.)

remaining ones exhibit some form of bursts, which are defined in this context as sets of three or more closely spaced spikes. There are five different classes:

- (NB) Non-bursting cells generate accommodating trains of tonic spikes in response to depolarizing pulses of DC current, and a single spike in response to a brief superthreshold pulse of current, as in Fig.8.34A.

- (HTB) High-threshold bursters fire bursts only in response to strong long pulses of current, but fire single spikes in response to weak or brief pulses of current, as
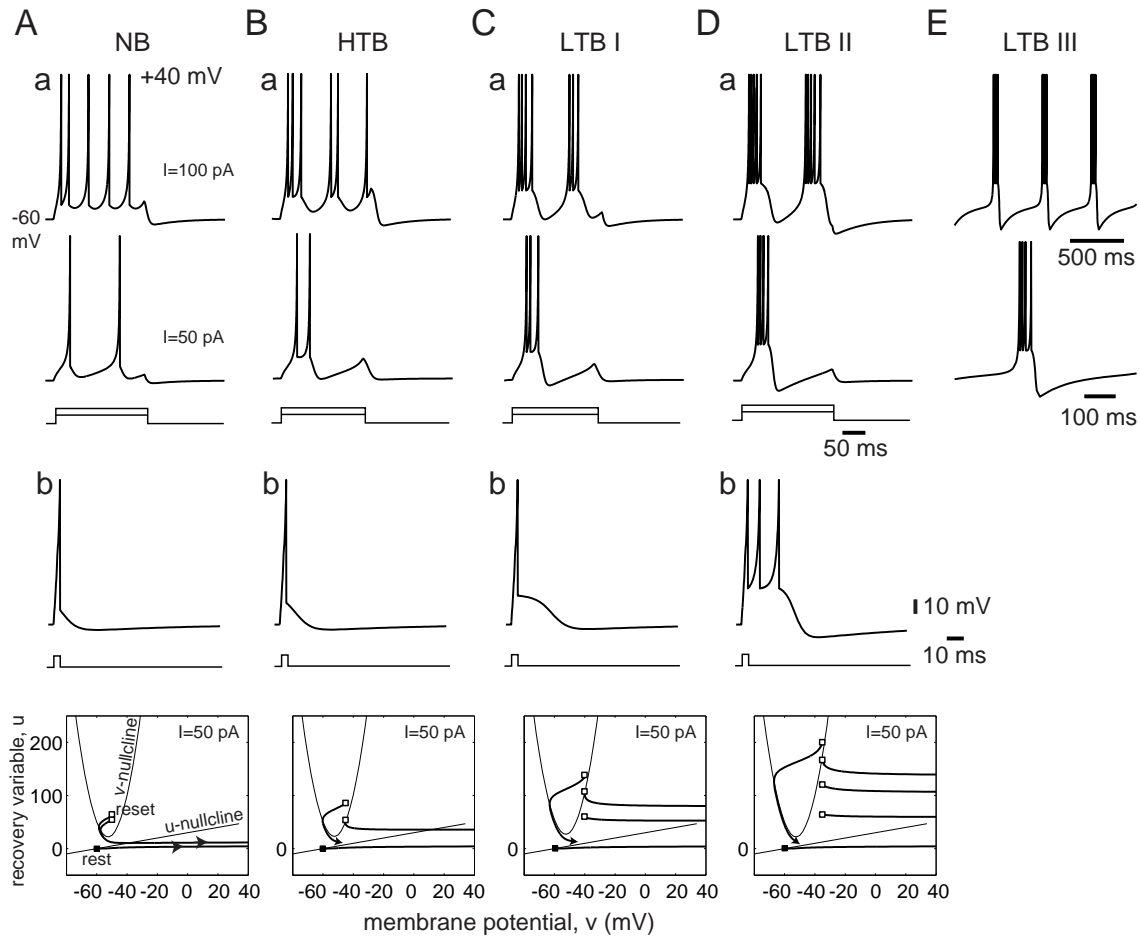
Figure 8.35: Simulations of hippocampal CA1 pyramidal neurons (compare with Fig.8.34) using simple model $50\dot{v} = 0.5(v+60)(v+45) - u + I$, $\dot{u} = 0.02\{0.5(v+60) - u\}$. When $v \geq 40$ (spike cutoff), $v \leftarrow c$ and $u \leftarrow u + d$. Here $c = -50, -45, -40, -35$ mV and $d = 50, 50, 55, 60$ for A–D, respectively. Parameters in E are the same as in D, but $I = 33$ pA.

in Fig.8.34B.

- (LTB I) Grade I low-threshold bursters fire bursts in response to long pulses, but single spikes in response to brief pulses of current, as in Fig.8.34C.

- (LTB II) Grade II low-threshold bursters fire stereotypical bursts in response to brief pulses, as in Fig.8.34D.

- (LTB III) Grade III low-threshold bursters fire rhythmic bursts spontaneously, which are depicted in Fig.8.34E, using two time scales.

NB neurons are equivalent to neocortical pyramidal neurons of the RS type, whereas HTB and LTB I neurons are equivalent to neocortical pyramidal neurons of the IB

type. The author is not aware of any systematic studies of the ability of IB neurons to fire stereotypical bursts in response to brief pulses, as in Fig.8.34Db, or to have intrinsic rhythmic activity, as in Fig.8.34E. Therefore, it is not clear whether there are any analogues of LTB grades II and III neurons in the neocortex.

The classification of hippocampal CA1 pyramidal neurons into five different classes does not imply a fundamental difference in the ionic mechanism of spike generation, but only a quantitative difference. This follows from the observation that pharmacological manipulations can gradually and reversibly transform an NB neuron into an LTB III neuron, and vice versa, by elevating the extracellular concentration of K^+ (Jensen et al. 1994), reducing extracellular Ca^{2+} (Su et al. 2001), blocking the K^+ M-current (Yue and Yaari 2004), or manipulating Ca^{2+} current dynamics in apical dendrites (Magee and Carruth 1999).

In Fig.8.35 we modify the simple model for the neocortical RS neuron to reproduce firing patterns of hippocampal pyramidal cells. To get the continuum of responses from NB to LTB II, fix all the parameters and vary only the after-spike reset parameter c by an increment of 5 mV, and the parameter d. These phenomenological parameters describe the effect of high-threshold inward and outward currents activated during each spike and affecting the after-spike behavior. Increasing c corresponds to up-regulating slow $I_{\mathrm{Na,p}}$ or down-regulating slow K^+ currents, which leads to transition from NB to LTB III in the CA1 slice (Su et al. 2001) and in the simple model in Fig.8.35. Interestingly, the same procedure results in transitions from RS to IB and possibly to CH classes in neocortical pyramidal neurons (Izhikevich 2003). This is consistent with the observation by Steriade (2004) that many neocortical neurons can change their firing classes in vivo, depending on the state of the brain.

8.4.2 Spiny Projection Neurons of Neostriatum and Basal Ganglia

Spiny projection neurons, the major class of neurons in neostriatum and basal ganglia, display a prominent bistable behavior in vivo, shown in Fig.8.36 (Wilson and Groves
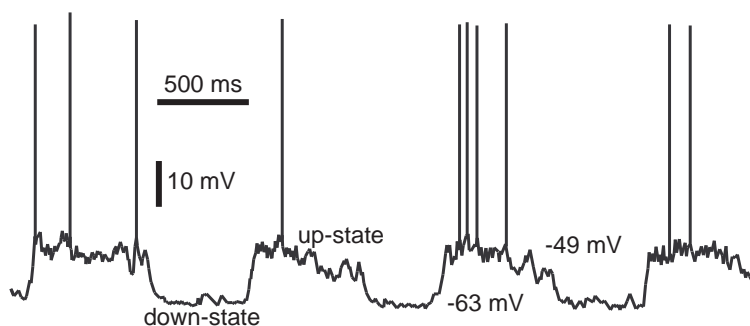
Figure 8.36: Neostriatal spiny neurons have two-state behavior in vivo. (Data provided by Charles Wilson.)
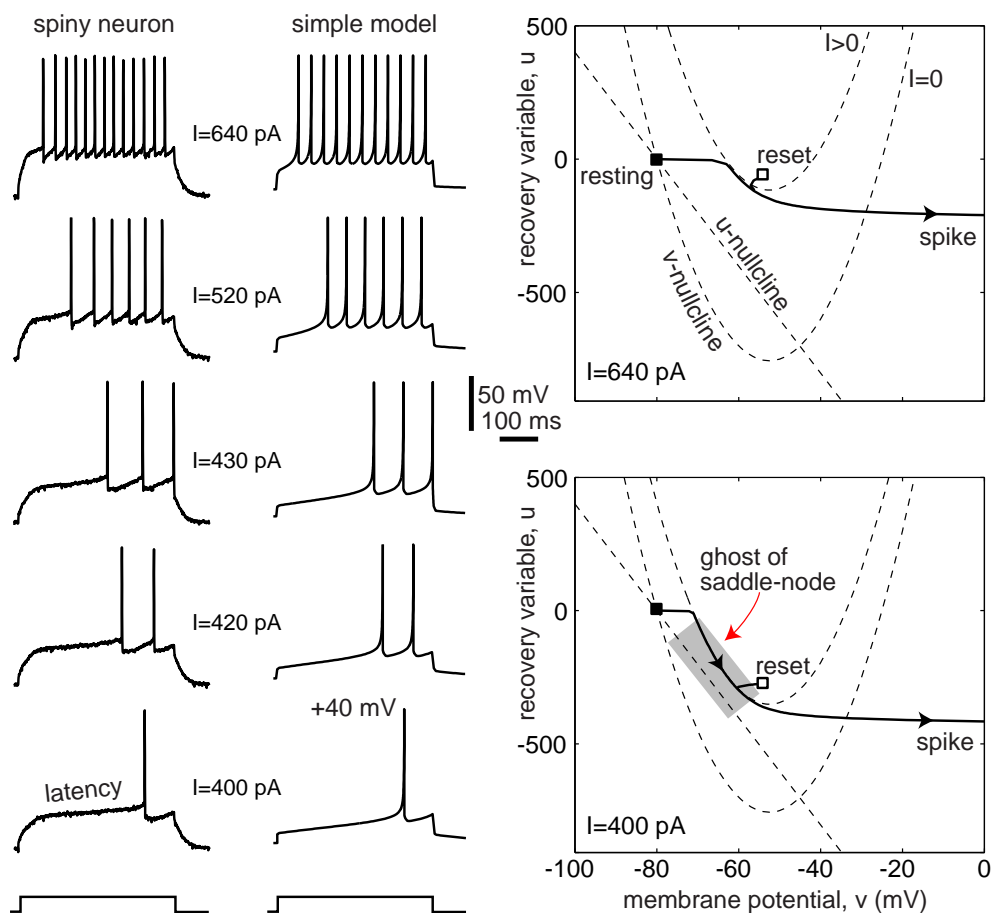
Figure 8.37: Comparison of in vitro recordings of a rat neostriatal spiny projection neuron with simulations of the simple model $50\dot{v} = (v + 80)(v + 25) - u + I$, $\dot{u} = 0.01\{-20(v+80) - u\}$, if $v \geq 40$, then $v \leftarrow -55$, $u \leftarrow u + 150$. (In vitro data provided by C. Wilson.)

1981; Wilson 1993): they shift the membrane potential from hyperpolarized to depolarized states in response to synchronous excitatory synaptic input from cortex and/or thalamus. In vitro studies of such neurons reveal a slowly inactivating K^+ A-current, which is believed to be responsible for the maintenance of the up-state and down-state, in addition to the synaptic input. Indeed, the K^+ current is completely deinactivated at the hyperpolarized potentials (down-state), and reduces the response of the neuron to any synaptic input. In contrast, prolonged depolarization (up-state) inactivates the current and makes the neuron more excitable and ready to fire spikes.

The most remarkable feature of neostriatal spiny neurons is depicted in Fig.8.37. In response to depolarizing current pulses, the neurons display a prominent slowly depolarizing (ramp) potential, and hence long latency to spike discharge (Nisenbaum et al. 1994). The ramp is mostly due to the slow inactivation of the K^+ A-current and slow charging of the dendritic tree. The delay to spike can be as long as 1 sec, but the

subsequent spike train has a shorter, relatively constant period that depends on the magnitude of the injected current – a feature consistent with the saddle-node off limit cycle bifurcation.

Let us use the simple model (8.5, 8.6) to simulate the responses of spiny neurons to current pulses. The resting membrane potential of the neuron in Fig.8.37 is around $v_r = -80$ mV, and we set $v_t = -25$ mV, $p = 1$, and $b = -20$ to get 30 MΩ input resistance and 300 pA rheobase current. We take $a = 0.01$ to reflect the slow inactivation of the K$^+$ A-current in the subthreshold voltage range. The membrane potential in the figure reaches the peak of $+40$ mV during the spike and then resets to -55 mV or lower, depending on the firing frequency. The value $d = 150$ provides a reasonable match of the interspike frequencies for all magnitudes of injected current. Note that $b < 0$, so u represents either slow inactivation of I_A or slow charging of the passive dendritic compartment, or both. In any case, it is a slow amplifying variable, which is consistent with the observation that spiny neurons do not "sag" in response to hyperpolarizing current pulses, do not "peak" in response to depolarizing pulses (Nisenbaum et al. 1994), and do not generate rebound (postinhibitory) spikes.

Injection of a depolarizing current shifts the v-nullcline of the simple model upward, and the resting state disappears via saddle-node bifurcation. The trajectory slowly moves through the ghost of the bifurcation point (shaded rectangle in the figure), resulting in the long latency to the first spike. The spike resets the trajectory to a point (white square) below the ghost, resulting in significantly smaller delays to subsequent spikes. Because the resetting point is so close to the saddle-node bifurcation point, the simple model, and probably the spiny projection neuron in the figure, are near the codimension-2 saddle-node homoclinic orbit bifurcation discussed in section 6.3.6.

8.4.3 Mesencephalic V Neurons of Brainstem

The best examples of resonators with fast subthreshold oscillations, Class 2 excitability, rebound spikes, and so on, are mesencephalic V (mesV) neurons of the brainstem (Wu et al. 2001) and primary sensory neurons of the dorsal root ganglion (Amir et al. 2002; Jian et al. 2004). MesV neurons of the brainstem have monotone I-V curves, whereas the simple model with linear equation for u does not. In Fig.8.38 we use a modification of the simple model to simulate the responses of a mesV neuron (data from Fig.7.3) to pulses of depolarizing current.

The model's phase portrait is qualitatively similar to that of the FS interneurons in Fig.8.27. The resting state is a stable focus, resulting in damped or noise-induced sustained oscillations of the membrane potential. Their amplitude and frequency depend on I and can be larger than 5 mV and 100 Hz, respectively. The focus loses stability via subcritical Andronov-Hopf bifurcation. Because of the coexistence of the resting and spiking states, the mesV neuron can burst, and so can the simple model if noise or a slow resonant variable is added.
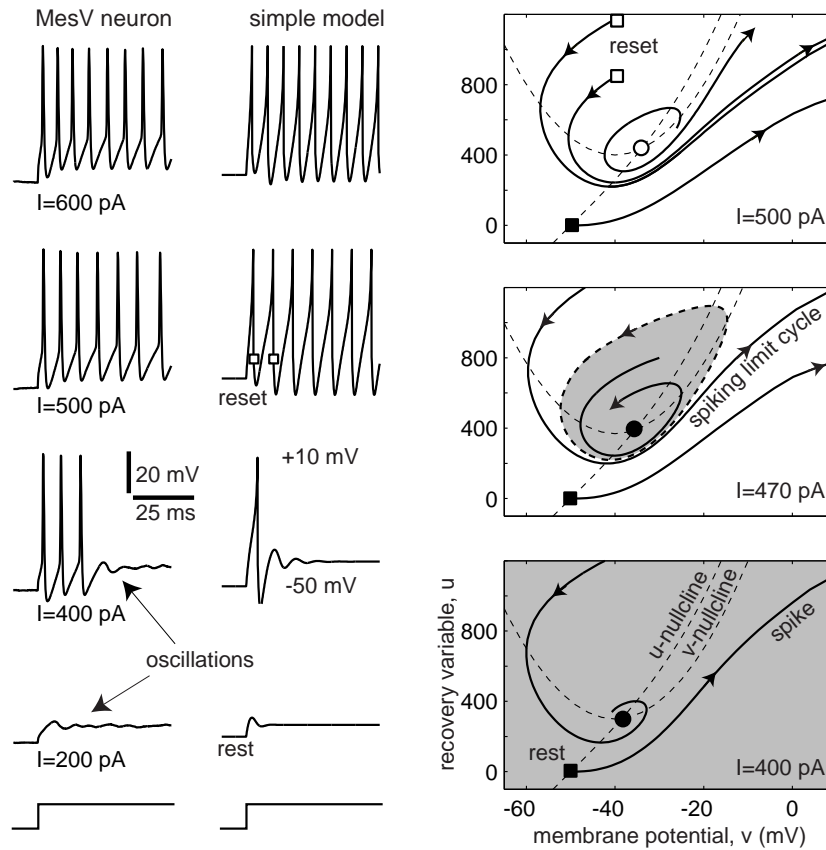
Figure 8.38: Comparison of in vitro recordings of rat brainstem mesV neuron (from Fig.7.3) with simulations of the simple model $25\dot{v} = (v + 50)(v + 30) - u + I$, $\dot{u} = 0.5\{U(v + 50) - u\}$, with cubic slow nullcline $U(x) = 25x + 0.009x^3$. If $v \geq 10$, then $v \leftarrow -40$.

8.4.4   Stellate Cells of Entorhinal Cortex

The entorhinal cortex occupies a privileged anatomical position that allows it to gate the main flow of information into and out of the hippocampus. in vitro studies show that stellate cells, a major class of neurons in the entorhinal cortex, exhibit intrinsic subthreshold oscillations with a slow dynamics of the kind shown in Fig.8.39b (Alonso and Llinas 1989; Alonso and Klink 1993; Klink and Alonso 1993; Dickson et al. 2000). The oscillations are generated by the interplay between a persistent Na$^+$ current and an h-current, and they are believed to set the theta rhythmicity in the entorhinal-hippocampal network.

The caption of Fig.8.39 provides parameters of the simple model (8.5, 8.6) that captures the slow oscillatory dynamics of an adult rat entorhinal stellate cell recorded in vitro.   The cell sags to injected hyperpolarizing current in Fig.8.39a and then fires a rebound spike upon release from hyperpolarization. From a neurophysiological point of view, the sag and the rebound response are due to the opening of the h-current; from
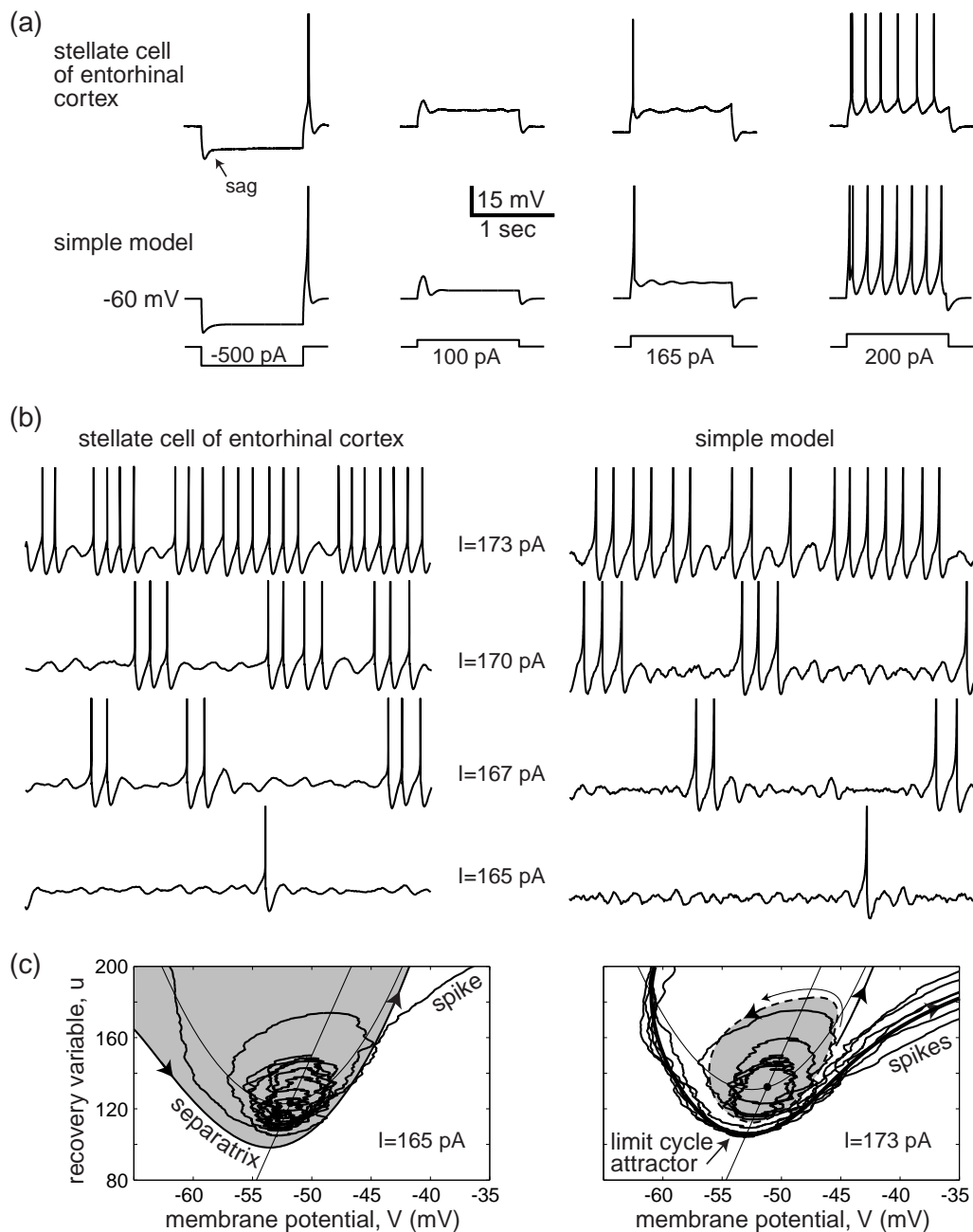
Figure 8.39: Comparison of in vitro recordings of stellate neurons of rat entorhinal cortex with simulations of the simple model $200\dot{v} = 0.75(v + 60)(v + 45) - u + I$, $\dot{u} = 0.01\{15(v + 60) - u\}$, if $v \geq 30$, then $v \leftarrow -50$. (a) Responses to steps of DC current. (b) Subthreshold oscillations and occasional spikes at various levels of injected DC current. (c) Phase portraits corresponding to two levels of injected DC current. Weak noise was added to simulations to unmask subthreshold oscillations. (Data provided by Brian Burton and John A. White. All recordings are from the same neuron, except steps of -500 pA and 200 pA were recorded from a different neuron. Spikes are cut at 0 mV.)

a theoretical point of view, they are caused by the resonant slow variable u, which could also describe deinactivation of a transient Na$^+$ current and deactivation of a low-threshold K$^+$ current. The geometrical explanation of these responses is similar to the one provided for LTS interneurons in Fig.8.26. Positive steps of current evoke a transient or a sustained spiking activity. Note that the first spike is actually a doublet in the recording and in the simulation in Fig.8.39a ($I = 200$ pA).

Stellate cells in the entorhinal cortex of adult animals can exhibit damped or sustained subthreshold oscillations in a frequency range from 5 to 15 Hz. The oscillations can be seen clearly when the cell is depolarized by injected DC current, as in Fig.8.39b. The stronger the current, the higher the amplitude and frequency of oscillations, which occasionally result in spikes or even bursts of spikes (Alonso and Klink 1993). The simple model also exhibits slow damped oscillations because its resting state is a stable focus. The focus loses stability via subcritical Andronov-Hopf bifurcation, and hence it coexists with a spiking limit cycle. To enable sustained oscillations and random spikes, we add channel noise to the v-equation (White et al. 2000).

In Fig.8.39c we explain the mechanism of random transitions between subthreshold oscillations and spikes, which is similar to the mechanism of stuttering in RS and FS neurons. When weak DC current is injected (left), the attraction domain of the resting state (shaded region) is separated from the rest of the phase space by the stable manifold to the saddle equilibrium (denoted separatrix). Noisy perturbations evoke small, sustained noisy oscillations around the resting state with an occasional spike when the separatrix is crossed. Increasing the level of injected DC current results in the series of bifurcations similar to those in Fig.8.15. As a result, there is a coexistence of a large amplitude (spiking) limit cycle attractor and a small unstable limit cycle, which encompasses the attraction domain of the resting state (right). Noisy perturbations can randomly switch the activity between these attractors, resulting in the random bursting activity in Fig.8.39b.

8.4.5   Mitral Neurons of the Olfactory Bulb

Mitral cells recorded in slices of rat main olfactory bulb exhibit intrinsic bistability of membrane potentials (Heyward et al. 2001). They spontaneously alternate between two membrane potentials separated by 10 mV: a relatively depolarized (up-state) and hyperpolarized (down-state). The membrane potential can be switched between the states by a brief depolarizing or hyperpolarizing pulse of current, as we show in Fig.7.36. In response to stimulation, the cells are more likely to fire in the up-state than in the down-state.

Current-voltage (I-V) relations of such mitral cells have three zeros in the subthreshold voltage range confirming that there are three equilibria: two stable ones corresponding to the up-state and the down-state, and one unstable, the saddle. There are no subthreshold oscillations in the down-state, hence it is a node, and the cell is an integrator. There are small-amplitude 40 Hz oscillations in the up-state; hence it is a focus, and the cell is a resonator.
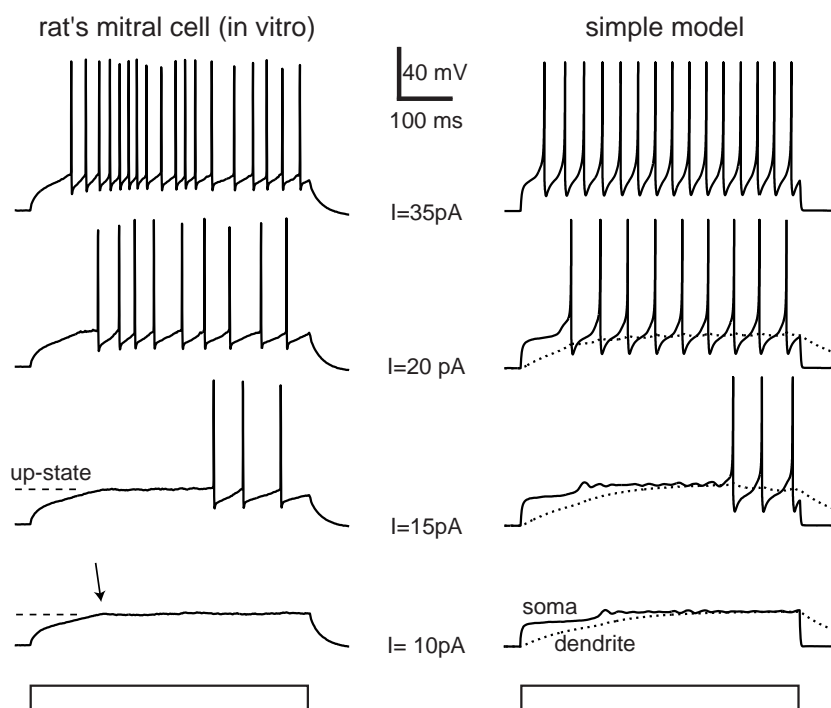
Figure 8.40: Comparison of in vitro recordings of mitral neurons of rat olfactory bulb with simulations of the simple two-compartment model. Soma: $40\dot{v} = (v+55)(v+50) + 0.5(v_d-v) - u + I$, $\dot{u} = 0.4\{(U(v)-u\}$ with $U(v) = 0$ when $v < v_b$ and $U(v) = 20(v-v_b)$ when $v \geq v_b = -48$ mV. If $v \geq 35$, then $v \leftarrow -50$. Passive dendrite (dotted curve): $\dot{v}_d = 0.0125(v - v_d)$. Weak noise was added to simulations to unmask subthreshold oscillations in the up-state. The membrane potential of the neuron is held at -75 mV by injecting a strong negative current, and then stimulated with steps of positive current. (Data provided by Philip Heyward.)

To model the bistability, we use the simple model with a piecewise linear slow nullcline that approximates nonlinear activation functions $n_\infty(v)$ near the "threshold" of the current and a passive dendritic compartment. In many respects, the model is similar to the one for late spiking (LS) cortical interneurons. In Fig.8.40 we fine-tune the model to simulate responses of a rat mitral cell to pulses of current of various amplitudes. To prevent noise-induced spontaneous transitions between the up-state and the down-state, the cell in the figure was held at -75 mV by injection of a large negative current. Its responses to weak positive pulses of current show a fast-rising phase followed by an abrupt step (arrow in the figure) to a constant value corresponding to the up-state. Increasing the magnitude of stimulation elicits trains of spikes with a considerable latency whose cause has yet to be determined experimentally. The latency could be the result of slow activation of an inward current, slow inactivation of an outward current (e.g., the K^+ A-current), or just slow charging of the dendritic compartment. All three cases correspond to an additional slow variable in the simple model, which we interpret as a membrane potential of a passive dendritic compartment.
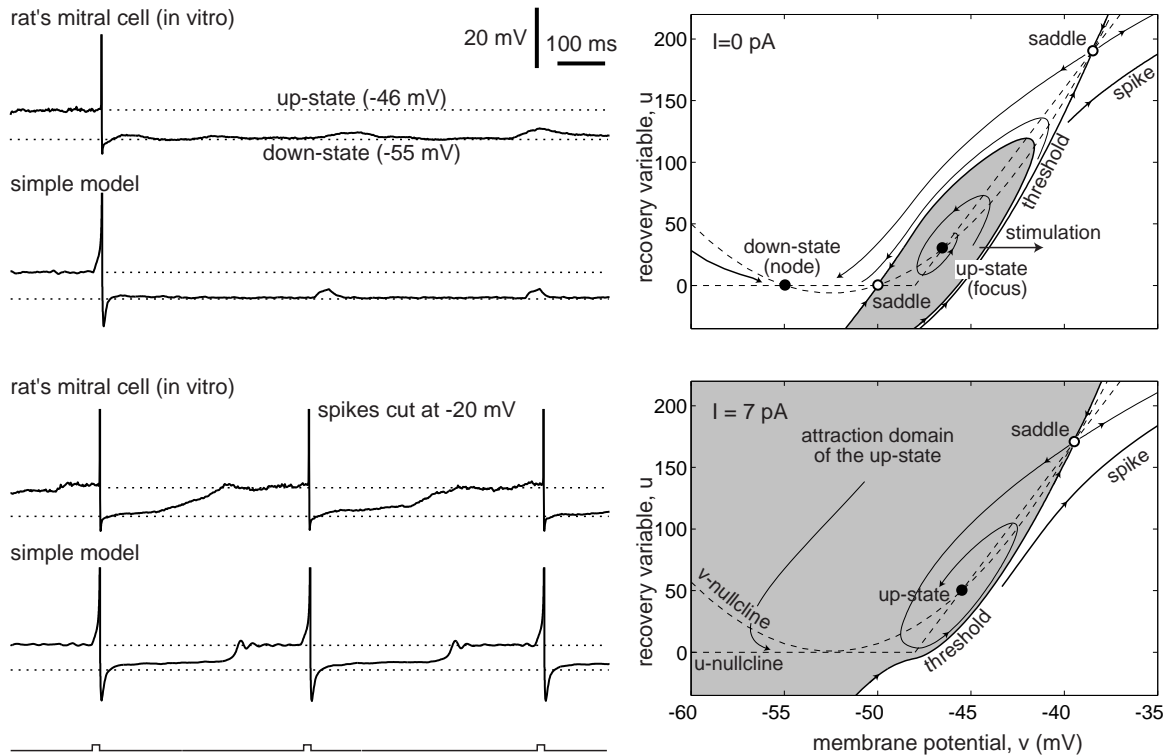
Figure 8.41: Voltage responses of a rat mitral cell and a simple model from Fig.8.40 at two different values of the holding current. *Right:* Phase portraits of somatic compartments show coexistence of stable node (down-state) and stable focus (up-state) equilibria. Spikes are emitted only from the up-state.

To understand the dynamics of the simple model, and hopefully of the mitral cell, we simulate its responses in Fig.8.41 to the activation of the olfactory nerve (ON). At the top of Fig.8.41, the cell is held at $I = 0$ pA. Its phase portrait clearly shows the coexistence of a stable node and focus equilibria separated by a saddle. The shaded region corresponds to the attraction domain of the focus equilibrium. To fire a spike from the up-state, noise or external stimulation must push the state of the system from the shaded region over the threshold to the right. The cell returns to the down-state immediately after the spike. Much stronger stimulation is needed to fire the cell from the down-state. Typically, the cell is switched to the up-state first, spends some time oscillating at 40 Hz, and then fires a spike (Heyward et al. 2001).

At the bottom of Fig.8.41, the cell is held at a slightly depolarizing current $I = 7$ pA. The node equilibrium disappears via saddle-node bifurcation, so there is no down-state, but only its ghost. Stimulation at the up-state results in a spike, after-hyperpolarization, and slow transition through the ghost of the down-state back to the up-state. Further increasing the holding current results in the stable manifold to the upper saddle (marked "threshold" in the figure) making a loop, then becoming a homoclinic trajectory to the saddle, giving birth to an unstable limit cycle which shrinks

to the focus and makes it lose stability via subcritical Andronov-Hopf bifurcation. Note that this phase portrait and the bifurcation scenario are different from the one in Fig.7.36. However, in both cases, the neuron is an integrator in the down-state and a resonator in the up-state! The same property is exhibited by cerebellar Purkinje cells (see Fig.7.37), and possibly by other neurons kept in the up-state (intrinsically or extrinsically).

Review of Important Concepts

- An integrate-and-fire neuron is a linear model having a stable *node* equilibrium, an artificial threshold, and a reset.

- A resonate-and-fire neuron is a linear model having a stable *focus* equilibrium, an artificial threshold, and a rest.

- Though technically not spiking neurons, these models are useful for analytical studies, that is, to prove theorems.

- The quadratic integrate-and-fire model captures the nonlinearity of the spike generation mechanism of real neurons having Class 1 excitability (saddle-node on invariant circle bifurcation).

- Its simple extension, model (8.5, 8.6), quantitatively reproduces subthreshold, spiking, and bursting activity of all known types of cortical and thalamic neurons in response to pulses of DC current.

- The simple model makes testable hypotheses on the dynamic mechanisms of excitability in these neurons.

- The model is especially suitable for simulations of large-scale models of the brain.

Bibliographical Notes

Many people have used the integrate-and-fire neuron, treating it as a folklore model. It was Tuckwell's *Introduction to Theoretical Neurobiology* (1988) that gave appropriate credit to its inventor, Lapicque (1907). Although better models, such as the quadratic integrate-and-fire model, are available now, many scientists continue to favor the leaky integrate-and-fire neuron mostly because of its simplicity. Such an attitude is understandable when one wants to derive analytical results. However, purely computational papers can suffer from using the model because of its weird properties, such as the logarithmic F-I curve and fixed threshold.

Figure 8.42: Louis Lapicque, the discoverer of the integrate-and-fire neuron.

The resonate-and-fire model was introduced by Izhikevich (2001a), and then by Richardson, Brunel, and Hakim (2003) and Brunel, Hakim, and Richardson (2003). These authors initially called the model "resonate-and-fire", but then changed its name to "generalized integrate-and-fire" (GIF), possibly to avoid confusion.

A better choice is the quadratic integrate-and-fire neuron in the normal form (8.2) or in the ϑ-form (8.8); see exercise 7. The ϑ-form was first suggested in the context of circle/circle (parabolic) bursting by Ermentrout and Kopell (1986a,b). Later, Ermentrout (1996) used this model to generalize numerical results of Hansel et al. (1995) on synchronization of Class 1 excitable systems, discussed in chapter 10. Hoppensteadt and Izhikevich (1997) introduced the canonical model approach, provided many examples of canonical models, and proved that the quadratic integrate-and-fire model is canonical in the sense that all Class 1 excitable systems can be transformed into this model by a piecewise continuous change of variables. They also suggested calling the model the "Ermentrout-Kopell canonical model" to honor its inventors, but most scientists follow Ermentrout and call it the "theta-neuron".

The model presented in section 8.1.4 was first suggested by Izhikevich (2000a; equations (4) and (5), with voltage reset discussed in Sect. 2.3.1) in the ϑ-form. The form presented here first appeared in Izhikevich (2003). The representation of the function $I + v^2$ in the form $(v - v_r)(v - v_t)$ was suggested by Latham et al. (2000).

We stress that the simple model is useful only when one wants to simulate large-scale networks of spiking neurons. He or she still needs to use the Hodgkin-Huxley-type conductance-based models to study the behavior of one neuron or a small network of neurons. The parameter values that match firing patterns of biological neurons presented in this chapter are only educated guesses (the same is true for conductance-based models). More experiments are needed to reveal the true spike generation mechanism of any particular neuron. An additional insight into the question, "which model is more realistic?" is in Fig.1.8.

Looking at the simple model, one gets an impression that the spike generation mechanism of RS neurons is the simplest in the neocortex. This is probably true; however, the complexity of the RS neurons, most of which are pyramidal cells, is hidden in their extensive dendritic trees having voltage- and Ca^{2+}-gated currents. Dendritic

dynamics is a subject for a 500-page book by itself, and we purposely omitted it. An interested reader is recommended to study *Dendrites* by Stuart et al. (1999), recent reviews by Hausser and Mel (2003) and Williams and Stuart (2003), and the seminal paper by Arshavsky et al. (1971; Russian language edition, 1969).

Exercises

1. (Integrate-and-fire network) The simplest implementation of a pulse-coupled integrate-and-fire neural network has the form

$$\dot{v}_i = b_i - v_i + \sum_{j \neq i} c_{ij}\delta(t - t_j) \ ,$$

   where t_j is the moment of firing of the jth neuron, that is, the moment $v_j(t_j) = 1$. Thus, whenever the jth neuron fires, the membrane potentials of the other neurons are instantaneously adjusted by $c_{ij}, \ i \neq j$. Show that the same initial conditions may result in different solutions, depending on the implementation details.

2. (Latham et al. 2000) Determine the relationship between the normal form for saddle-node bifurcation (6.2) and the equation

$$\dot{V} = a(V - V_{\text{rest}})(V - V_{\text{thresh}}) \ .$$

3. Show that the period of oscillations in the quadratic integrate-and-fire model (8.2) is

$$T = \frac{1}{\sqrt{b}} \left(\text{atan}\, \frac{v_{\text{peak}}}{\sqrt{b}} - \text{atan}\, \frac{v_{\text{reset}}}{\sqrt{b}} \right)$$

   when $b > 0$.

4. Show that the period of oscillations in the quadratic integrate-and-fire model (8.2) with $v_{\text{peak}} = 1$ is

$$T = \frac{1}{2\sqrt{|b|}} \left(\ln \frac{1 - \sqrt{|b|}}{1 + \sqrt{|b|}} - \ln \frac{v_{\text{reset}} - \sqrt{|b|}}{v_{\text{reset}} + \sqrt{|b|}} \right)$$

   when $b < 0$ and $v_{\text{reset}} > \sqrt{|b|}$.

5. Justify the bifurcation diagram in Fig.8.3.

6. Brizzi et al. (2004) have shown that shunting inhibition of cat motoneurons raises the firing threshold, and the rheobase current, and shifts the F-I curve to the right without changing the shape of the curve. Use the quadratic integrate-and-fire model to explain the effect. (Hint: Consider $\dot{v} = b - gv + v^2$ with $g \geq 0$, $v_{\text{reset}} = -\infty$, and $v_{\text{peak}} = +\infty$.)

7. (Theta neuron) Determine when the quadratic integrate-and-fire neuron (8.2) is equivalent to the theta neuron

$$\dot{\vartheta} = (1 - \cos\vartheta) + (1 + \cos\vartheta)r , \qquad (8.8)$$

where r is the bifurcation parameter and $\vartheta \in [-\pi, \pi]$ is a phase variable on the unit circle.

8. (Another theta neuron) Show that the quadratic integrate-and-fire neuron (8.2) is equivalent to

$$\dot{\vartheta} = \vartheta^2 + (1 - |\vartheta|)^2 r .$$

where $\vartheta \in [-1, 1]$ and r have the same meaning as in exercise 7. Are there any other "theta-neurons"?

9. When is the linear version of (8.3, 8.4),

$$\begin{aligned} \dot{v} &= I - v - u & \text{if } v = 1, \text{ then} \\ \dot{u} &= a(bv - u) & v \leftarrow 0, \ u \leftarrow u + d, \end{aligned}$$

equivalent to the integrate-and-fire or resonate-and-fire model?

10. Show that the simple model (8.3, 8.4) with $b < 0$ is equivalent to the quadratic integrate-and-fire neuron with a passive dendritic compartment.

11. All membrane potential responses in Fig.8.8 were obtained using model (8.3, 8.4) with appropriate values of the parameters. Use MATLAB to experiment with the model and reproduce the figure.

12. Simulate the FS spiking neuron in Fig.8.27, using the simple model (8.5, 8.6) with linear equation for u. What can you say about its possible bifurcation structure?

13. Fit the recordings of the RS neuron in Fig.8.12, using the model

$$\begin{aligned} C\dot{v} &= I - g(v - v_{\mathrm{r}}) + p(v - v_{\mathrm{t}})_+^2 - u & \text{if } v = v_{\mathrm{peak}}, \text{ then} \\ \dot{u} &= a(b(v - v_{\mathrm{r}}) - u) & v \leftarrow c, \ u \leftarrow u + d, \end{aligned}$$

where $x_+ = x$ when $x > 0$ and $x_+ = 0$ when otherwise. This model better fits the upstroke of the action potential.

14. Explore numerically the model (8.3, 8.4) with a nonlinear after-spike reset $v \leftarrow f(u), u \leftarrow g(u)$, where f and g are some functions.

15. **[M.S.]** Analyze the generalization of the system (8.3, 8.4)

$$\begin{aligned} \dot{v} &= I + v^2 + evu - u & \text{if } v = 1, \text{ then} \\ \dot{u} &= a(bv - u) & v \leftarrow c, \ u \leftarrow u + d \end{aligned}$$

where e is another parameter.

16. **[M.S.]** Analyze the generalization of the following system, related to the exponential integrate-and-fire model

$$\dot{v} = I - v + ke^v - u \qquad \text{if } v = 1, \text{ then}$$
$$\dot{u} = a(bv - u) \qquad v \leftarrow c, \, u \leftarrow u + d$$

where k is another parameter.

17. **[M.S.]** Analyze the system

$$\dot{v} = I - v + kv_+^2 - u \qquad \text{if } v = 1, \text{ then}$$
$$\dot{u} = a(bv - u) \qquad v \leftarrow c, \, u \leftarrow u + d$$

where $v_+ = v$ when $v > 0$ and $v_+ = 0$ otherwise.

18. **[M.S.]** Find an analytical solution to the system (8.3, 8.4) with time-dependent input $I = I(t)$.

19. **[M.S.]** Determine the complete bifurcation diagram of the system (8.3, 8.4).

Chapter 10

Synchronization

This chapter, found on the author's Web page (www.izhikevich.com), considers networks of tonically spiking neurons. Like any other kind of physical, chemical, or biological oscillators, such neurons could synchronize and exhibit collective behavior that is not intrinsic to any individual neuron. For example, partial synchrony in cortical networks is believed to generate various brain oscillations, such as the alpha and gamma EEG rhythms. Increased synchrony may result in pathological types of activity, such as epilepsy. Coordinated synchrony is needed for locomotion and swim pattern generation in fish. There is an ongoing debate on the role of synchrony in neural computation (see, e.g., the special issue of *Neuron* [September 1999] devoted to the binding problem).

Depending on the circumstances, synchrony can be good or bad, and it is important to know what factors contribute to synchrony and how to control it. This is the subject of the present chapter, the most advanced chapter of the book. It provides a nice application of the theory developed earlier and hopefully gives some insight into why the previous chapters may be worth mastering. Unfortunately, it is too long to be included into the book, so reviewers recommended putting it on the Web.

The goal of this chapter is to understand how the behavior of coupled neurons depends on their intrinsic dynamics. First, we introduce the method of description of an oscillation by its phase. Then, we describe various methods of reduction of coupled oscillators to phase models. The reduction method and the exact form of the phase model depend on the type of coupling (i.e., whether it is pulsed, weak, or slow) and on the type of bifurcations of the limit cycle attractor generating tonic spiking. Finally, we show how to use phase models to understand the collective dynamics of many coupled oscillators.
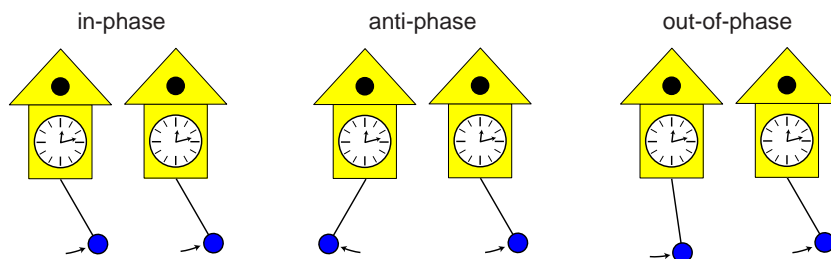
Figure 10.1: Different types of synchronization.

Review of Important Concepts

- Oscillations are described by their phase variables ϑ rotating on a circle $\mathbb{S}^1$. We define ϑ as the time since the last spike.

- The phase response curve, $\mathrm{PRC}(\vartheta)$, describes the magnitude of the phase shift of an oscillator caused by a strong pulsed input arriving at phase ϑ.

- PRC depends on the bifurcations of the spiking limit cycle, and it defines synchronization properties of an oscillator.

- Two oscillators are synchronized in-phase, anti-phase, or out-of-phase when their phase difference, $\vartheta_2 - \vartheta_1$, equals 0, half-period, or some other value, respectively; see Fig.10.1.

- Synchronized states of pulse-coupled oscillators are fixed points of the corresponding Poincare phase map.

- Weakly coupled oscillators

$$\dot{x}_i = f(x_i) + \varepsilon \sum g_{ij}(x_j)$$

can be reduced to phase models

$$\dot{\vartheta}_i = 1 + \varepsilon\, Q(\vartheta_i) \sum g_{ij}(x_j(\vartheta_j)) \ ,$$

where $Q(\vartheta)$ is the infinitesimal PRC defined by Malkin's equation.

- Weak coupling induces a slow phase deviation of the natural oscillation, $\vartheta_i(t) = t + \varphi_i$, described by the averaged model

$$\dot{\varphi}_i = \varepsilon \left(\omega_i + \sum H_{ij}(\varphi_j - \varphi_i) \right) \ ,$$

where the ω_i denote the frequency deviations, and

$$H_{ij}(\varphi_j - \varphi_i) = \frac{1}{T} \int_0^T Q(t)\, g_{ij}(x_j(t + \varphi_j - \varphi_i))\, dt$$

describe the interactions between the phases.

- Synchronization of two coupled oscillators correspond to equilibria of the one-dimensional system

$$\dot{\chi} = \varepsilon(\omega + G(\chi)) \ , \qquad \chi = \varphi_2 - \varphi_1 \ ,$$

where $G(\chi) = H_{21}(-\chi) - H_{12}(\chi)$ describes how the phase difference χ compensates for the frequency mismatch $\omega = \omega_2 - \omega_1$.

Solutions to Exercises

Solutions for chapter 2

1. $T = 20°\mathrm{C} \approx 293°\mathrm{F}$.

$$E_{\mathrm{Ion}} = \frac{RT}{zF} \ln \frac{[\mathrm{Ion}]_{\mathrm{out}}}{[\mathrm{Ion}]_{\mathrm{in}}} = \frac{8315 \cdot 293 \cdot \ln 10}{z \cdot 96480} \log_{10} \frac{[\mathrm{Ion}]_{\mathrm{out}}}{[\mathrm{Ion}]_{\mathrm{in}}} = \pm 58 \log_{10} \frac{[\mathrm{Ion}]_{\mathrm{out}}}{[\mathrm{Ion}]_{\mathrm{in}}}$$

when $z = \pm 1$. Therefore,

$$
\begin{aligned}
E_{\mathrm{K}} &= 58 \log(20/430) = -77 \text{ mV}\\
E_{\mathrm{Na}} &= 58 \log(440/50) = 55 \text{ mV}\\
E_{\mathrm{Cl}} &= -58 \log(560/65) = -54 \text{ mV}
\end{aligned}
$$

2.

$$
\begin{aligned}
I &= \bar{g}_{\mathrm{Na}}\, p\,(V - E_{\mathrm{Na}}) + \bar{g}_{\mathrm{K}}\, p\,(V - E_{\mathrm{K}}) = p\{(\bar{g}_{\mathrm{Na}} + \bar{g}_{\mathrm{K}})\, V - \bar{g}_{\mathrm{Na}}\, E_{\mathrm{Na}} - \bar{g}_{\mathrm{K}}\, E_{\mathrm{K}}\}\\
&= \underbrace{(\bar{g}_{\mathrm{Na}} + \bar{g}_{\mathrm{K}})\, p}_{\bar{g}}\; \left(V - \underbrace{\frac{\bar{g}_{\mathrm{Na}}\, E_{\mathrm{Na}} + \bar{g}_{\mathrm{K}}\, E_{\mathrm{K}}}{\bar{g}_{\mathrm{Na}} + \bar{g}_{\mathrm{K}}}}_{E}\right)
\end{aligned}
$$

3. The answer follows from the equation

$$I - g_{\mathrm{L}}(V - E_{\mathrm{L}}) = -g_{\mathrm{L}}(V - \widehat{E}_{\mathrm{L}}) , \qquad \text{where} \qquad \widehat{E}_{\mathrm{L}} = E_{\mathrm{L}} + I/g_{\mathrm{L}} .$$

4. See Fig.S.1.

Function	$V_{1/2}$	k	Function	$V_{\max}$	σ	C_{amp}	C_{base}
$n_\infty(V)$	12	15	$\tau_n(V)$	−14	50	4.7	1.1
$m_\infty(V)$	25	9	$\tau_m(V)$	27	30	0.46	0.04
$h_\infty(V)$	3	−7	$\tau_n(V)$	−2	20	7.4	1.2

Hodgkin and Huxley shifted $V_{1/2}$ and $V_{\max}$ by 65 mV so that the resting potential is at $V = 0$ mV.

5. (Willms et al. 1999)

$$
\begin{aligned}
\tilde{V}_{1/2} &= V_{1/2} - k \ln(2^{1/p} - 1) ,\\
\tilde{k} &= \frac{k}{2p(1 - 2^{-1/p})} .
\end{aligned}
$$

The first equation is obtained from the condition $m_\infty^p(\tilde{V}_{1/2}) = 1/2$. The second equation is obtained from the condition that the two functions have the same slope at $V = \tilde{V}_{1/2}$.

6. See author's Web page, www.izhikevich.com.

7. See author's Web page, www.izhikevich.com.
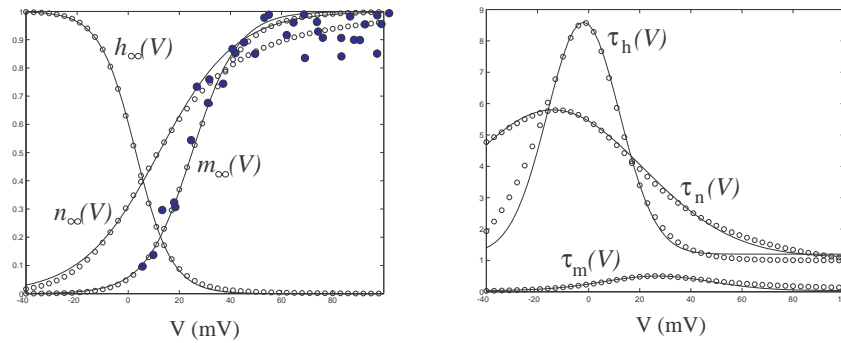
Figure S.1: *Open dots*: The steady-state (in)activation functions and voltage-sensitive time constants in the Hodgkin-Huxley model. *Filled dots*: steady-state Na^+ activation function $m_\infty(V)$ in the squid giant axon (experimental results by Hodgkin and Huxley 1952, figure 8). *Continuous curves*: Approximations by Boltzmann and Gaussian functions. See exercise 4.

Solutions for chapter 3

1. Consider the limit case: (1) activation of the Na^+ current is instantaneous, and (2) conductance kinetics of the other currents are frozen. Then, the Na^+ current will result in the nonlinear term $g_{Na}\, m_\infty(V)\,(V - E_{Na})$ with the parameter $h_\infty(V_{rest})$ incorporated into g_{Na}, and all the other currents will result in the linear leak term.

   In Fig.3.15, the activation of the Na^+ current is not instantaneous; hence the sag right after the pulses. In addition, its inactivation, and the kinetics of the other currents are not slow enough; hence the membrane potential quickly reaches the excited state and then slowly repolarizes to the resting state.

2. See Fig.S.2. The eigenvalues are negative at each equilibrium marked as a filled circle (stable), and positive at each equilibrium marked as an open circle (unstable). The eigenvalue at the bifurcation point (left equilibrium in Fig.S.2b) is zero.
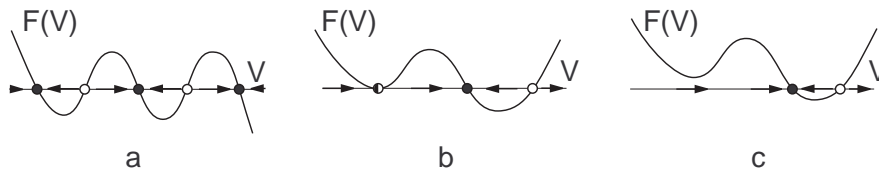
Figure S.2: Phase portraits of the system $\dot{V} = F(V)$ with given $F(V)$.

3. Phase portraits are shown in Fig.S.3.

   (a) The equation $0 = -1 + x^2$ has two solutions: $x = -1$ and $x = +1$; hence there are two equilibria in the system (a). The eigenvalues are the derivatives at each equilibrium, $\lambda = (-1 + x^2)' = 2x$, where $x = \pm 1$. Equilibrium $x = -1$ is stable because $\lambda = -2 < 0$. Equilibrium $x = +1$ is unstable because $\lambda = +2 > 0$. The same fact follows from the geometrical analysis in Fig.S.3.

(b) The equation $0 = x - x^3$ has three solutions: $x = \pm 1$ and $x = 0$; hence there are three equilibria in system (b). The eigenvalues are the derivatives at each equilibrium, $\lambda = (x - x^3)' = 1 - 3x^2$. The equilibria $x = \pm 1$ are stable because $\lambda = 1 - 3(\pm 1)^2 = -2 < 0$. The equilibrium $x = 0$ is unstable because $\lambda = 1 > 0$. The same conclusions follow from the geometrical analysis in Fig.S.3.

a   b
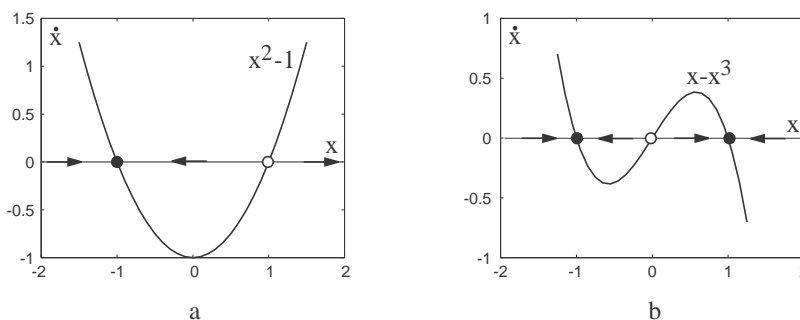
Figure S.3: Phase portraits of the systems (a) $\dot{x} = -1 + x^2$, and (b) $\dot{x} = x - x^3$.

4. The equilibrium $x = 0$ is stable in all three cases.

5. See Fig.S.4. Topologically equivalent systems are in (a), (b), and (c). In (d) there are different numbers of equilibria; no stretching or shrinking of the rubber phase line can produce new equilibria. In (e) the right equilibrium is unstable in $\dot{V} = F_1(V)$ but stable in $\dot{V} = F_2(V)$; no stretching or shrinking can change the stability of an equilibrium. In (f) the flow between the two equilibria is directed rightward in $\dot{V} = F_1(V)$ and leftward in $\dot{V} = F_2(V)$; no stretching or shrinking can change the direction of the flow.

6. (Saddle-node [fold] bifurcation in $\dot{x} = a + x^2$) The equation $0 = a + x^2$ has no real solutions when $a > 0$, and two solutions $x = \pm\sqrt{|a|}$ when $a \leq 0$. Hence there are two branches of equilibria, depicted in Fig.S.5. The eigenvalues are

$$\lambda = (a + x^2)' = 2x = \pm 2\sqrt{|a|} .$$

The lower branch $-\sqrt{|a|}$ is stable ($\lambda < 0$), and the upper branch $+\sqrt{|a|}$ is unstable ($\lambda > 0$). They meet at the saddle-node (fold) bifurcation point $a = 0$.

7.

(a) $x = -1$ at $a = 1$	(b) $x = -1/2$ at $a = 1/4$	(c) $x = 1/2$ at $a = 1/4$
(d) $x = \pm 1/\sqrt{3}$ at $a = \pm 2/(3\sqrt{3})$	(e) $x = \pm 1$ at $a = \mp 2$	(f) $x = -1$ at $a = 1$

8. (Pitchfork bifurcation in $\dot{x} = bx - x^3$) The equation $0 = bx - x^3$ has one solution $x = 0$ when $b \leq 0$, and three solutions $x = 0$, $x = \pm\sqrt{b}$ when $b > 0$. Hence there is only one branch of equilibria for $b < 0$ and three branches for $b > 0$ of the pitchfork curve depicted in Fig.S.6. The eigenvalues are
$$\lambda = (bx - x^3)' = b - 3x^2.$$

The branch $x = 0$ exists for any b, and its eigenvalue is $\lambda = b$. Thus, it is stable for $b < 0$ and unstable for $b > 0$. The two branches $x = \pm\sqrt{b}$ exist only for $b > 0$, but they are always stable because $\lambda = b - 3(\pm\sqrt{b})^2 = -2b < 0$. We see that the branch $x = 0$ loses stability when b passes the pitchfork bifurcation value $b = 0$, at which point a pair of new stable branches bifurcates (hence the name *bifurcation*). In other words, the stable branch $x = 0$ divides (bifurcates) into two stable branches when b passes 0.
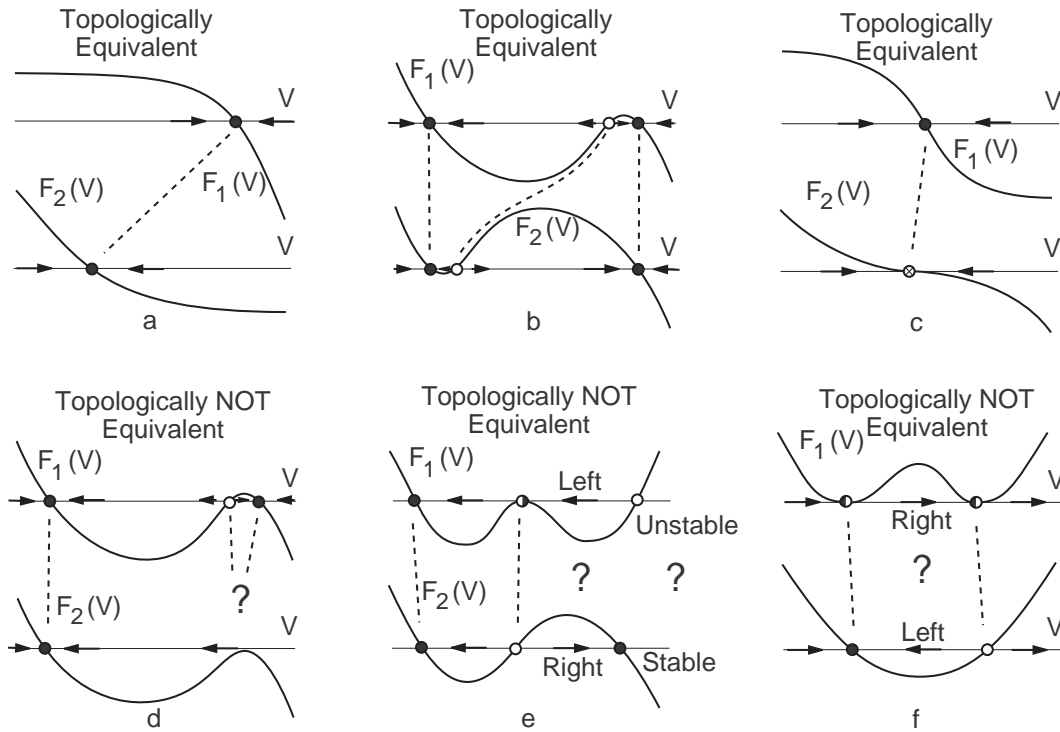
Figure S.4: Answer to chapter 3, exercise 5.

9. Recall that the current I_{Kir} is turned off by depolarization and turned on by hyperpolarization. The dynamics of the I_{Kir}-model is similar to that of the $I_{\text{Na,p}}$-model in many respects. In particular, this system can also have coexistence of two stable equilibria separated by an unstable equilibrium, which follows from the N-shaped I-V relation. Indeed, when V is hyperpolarized, the current I_{Kir} is turned on (deinactivated), and it pulls V toward E_{K}. In contrast, when V is depolarized, the current is turned off (inactivated), and does not obstruct further depolarization of V.

Use (3.11) to find the curve

$$I = g_{\text{L}}(V - E_{\text{L}}) + g_{\text{Kir}}h_{\infty}(V)(V - E_{\text{K}}) ,$$

in Fig.S.8. (The curve may not be S-shaped if a different bifurcation parameter is used, as in exercise 12a below).

The bifurcation diagram of the I_{Kir}-model (3.11) in Fig.S.8 has three branches corresponding to the three equilibria. When the parameter I is relatively small, the outward I_{Kir} current dominates and the system has only one equilibrium in the low voltage range – the down-state. When the parameter I is relatively large, the injected inward current I dominates, and the system has one equilibrium in the intermediate voltage range – the up-state. When the parameter I is in neighborhood of $I = 6$, the system exhibits bistability of the up-state and the down-state. The states appear and disappear via saddle-node bifurcations. The behavior of the I_{Kir}-model is conceptually (and qualitatively) similar to the behavior of the $I_{\text{Na,p}}$-model (3.5) even though the models have completely different ionic mechanisms for bistability.

10. The equilibrium satisfies the one-dimensional equation

$$0 = I - g_{\text{K}}n_{\infty}^4(V)(V - E_{\text{K}}) - g_{\text{Na}}m_{\infty}^3(V)h_{\infty}(V)(V - E_{\text{Na}}) - g_{\text{L}}(V - E_{\text{L}}) ,$$
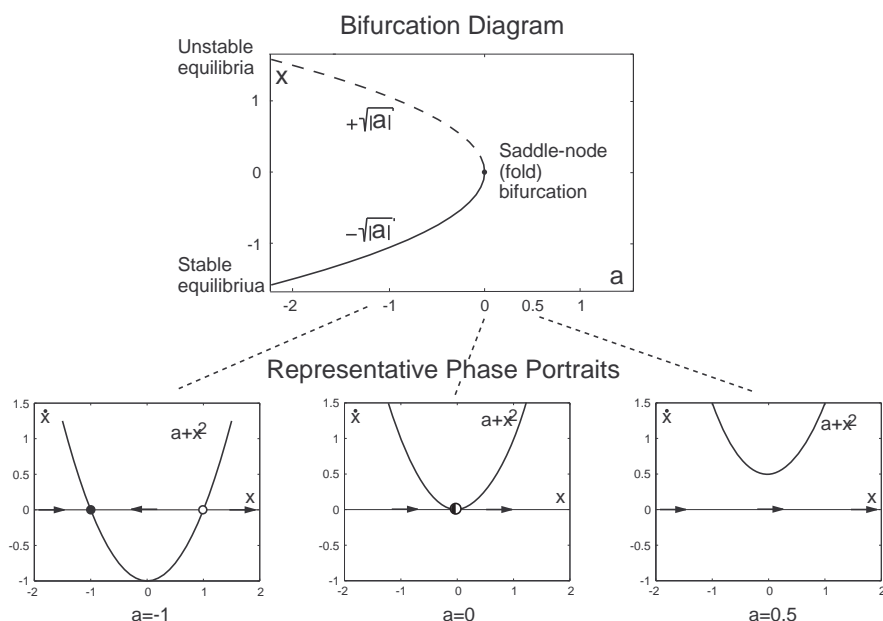
Figure S.5: Saddle-node (fold) bifurcation diagram and representative phase portraits of the system $\dot{x} = a + x^2$ (see chapter 3, exercise 6).

where all gating variables assume their asymptotic values. The solution

$$I = g_K n_\infty^4(V)(V - E_K) + g_{Na} m_\infty^3(V) h_\infty(V)(V - E_{Na}) + g_L(V - E_L)$$

is depicted in Fig.S.9. Since the curve in this figure does not have folds, there are no saddle-node bifurcations in the Hodgkin-Huxley model (with the original values of parameters).

11. The curves

$$\text{(a)} \qquad g_L(V) = -g_{Na} m_\infty(V)(V - E_{Na})/(V - E_L)$$

and

$$\text{(b)} \qquad E_L(V) = V + g_{Na} m_\infty(V)(V - E_{Na})(V - E_L)/g_L$$

are depicted in Fig.S.7.

12. The curves

$$\text{(a)} \qquad g_L(V) = \{I - g_{Kir} h_\infty(V)(V - E_K)\}/(V - E_L)$$

and

$$\text{(b)} \qquad g_{Kir}(V) = \{I - g_L(V - E_L)\}/\{h_\infty(V)(V - E_K)\}$$

are depicted in Fig.S.10. Note that the curve in Fig.S.10a does not have the S shape.

13.

$$F'(V) = -g_L - g_K m_\infty^4(V) - g_K 4 m_\infty^3(V) m_\infty'(V)(V - E_K) < 0$$

because $g_L > 0$, $m_\infty(V) > 0$, $m_\infty'(V) > 0$, and $V - E_K > 0$ for all $V > E_K$.

14.

$$F'(V) = -g_L - g_h h_\infty(V) - g_h h_\infty'(V)(V - E_h) < 0$$

because $g_L > 0$, $h_\infty(V) > 0$, but $h_\infty'(V) < 0$ and $V - E_h < 0$ for all $V < E_h$.
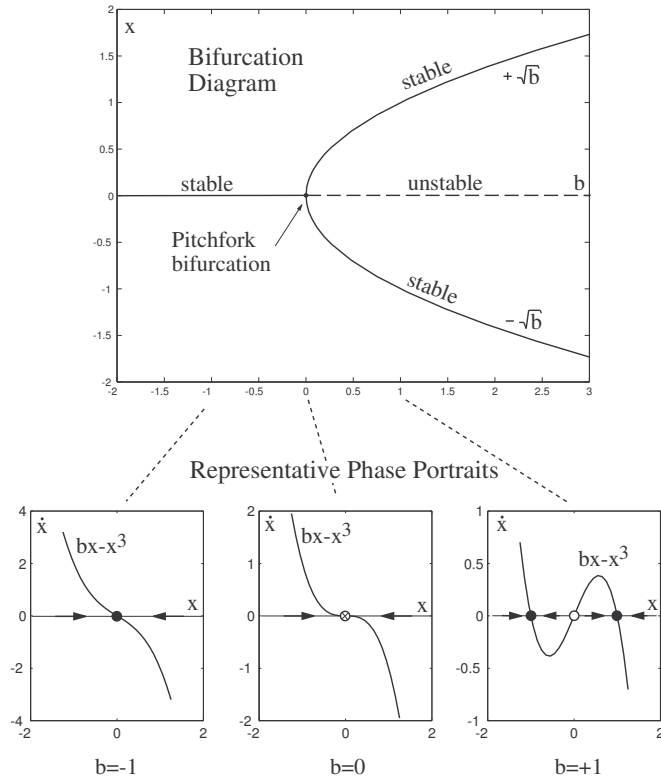
Figure S.6: Pitchfork bifurcation diagram and representative phase portraits of the system $\dot{x} = bx - x^3$ (see chapter 3, exercise 8).
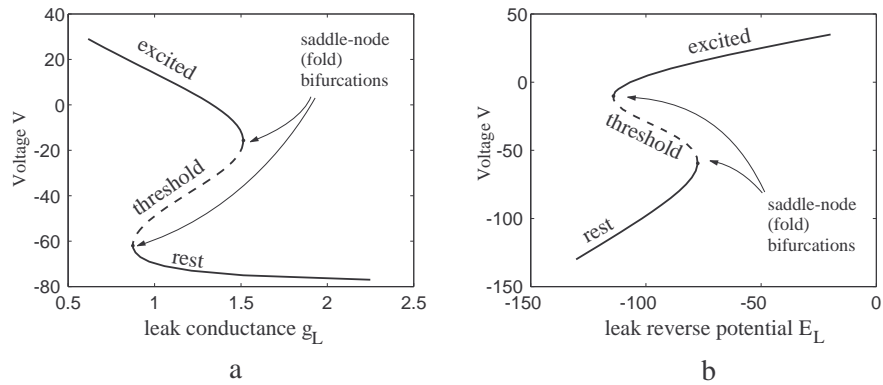
Figure S.7: Bifurcation diagrams of the $I_{\mathrm{Na,p}}$-model (3.5) with bifurcation parameters (a) g_{L} and (b) E_{L} (see chapter 3, exercise 11).
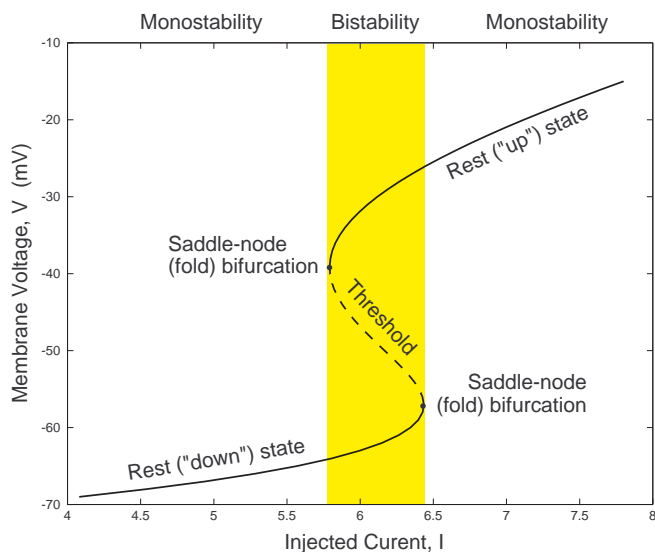
Figure S.8: Bifurcation diagram of the I_{Kir}-model (3.11).
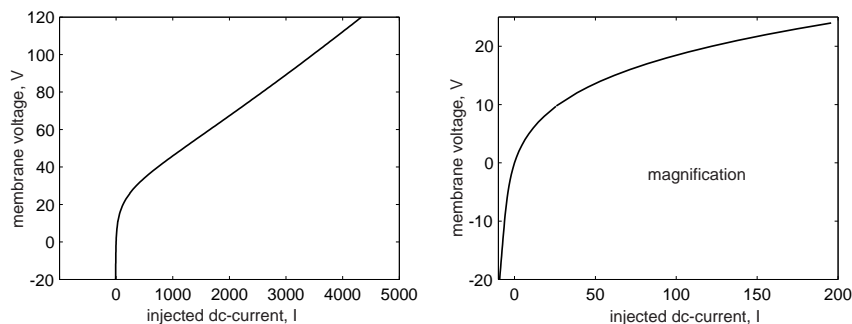
Figure S.9: Dependence of the position of equilibrium in the Hodgkin-Huxley model on the injected DC current; see exercise 10.

15. When V is sufficiently large, $\dot{V} \approx V^2$. The solution of $\dot{V} = V^2$ is $V(t) = 1/(c-t)$ (check by differentiating), where $c = 1/V(0)$. Another way to show this is to solve (3.9) for V and find the asymptote of the solution.

16. Each equilibrium of the system $\dot{x} = a + bx - x^3$ is a solution to the equation $0 = a + bx - x^3$. Treating x and b as free parameters, the set of all equilibria is given by $a = -bx + x^3$, and it looks like the cusp surface in Fig.6.34. Each point where the cusp surface folds, corresponds to a saddle-node (fold) bifurcation. The derivative with respect to x at each such point is zero; alternatively, the vector tangent to the cusp surface at each such point is parallel to the x-axis. The set of all bifurcation points is projected to the (a,b)-plane at the bottom of the figure, and it looks like a curve having two branches. To find the equation for the bifurcation curves, one needs to remember that each bifurcation point satisfies two conditions:

   - It is an equilibrium; that is, $a + bx - x^3 = 0$.

   - The derivative of $a + bx - x^3$ with respect to x is zero; that is, $b - 3x^2 = 0$.

   Solving the second equation for x and using the solution $x = \pm\sqrt{b/3}$ in the first equation yields $a = \mp 2(b/3)^{3/2}$. The point $a = b = 0$ is called a cusp bifurcation point.
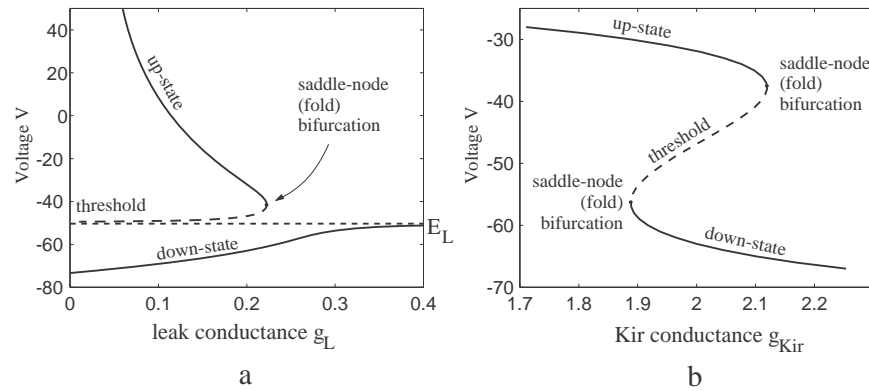
Figure S.10: Bifurcation diagrams of the I_{Kir}-model (3.11), $I = 6$, with bifurcation parameters (a) g_{L} and (b) g_{Kir} (see chapter 3, exercise 12).

17. (Gradient systems) For $\dot{V} = F(V)$ take

$$E(V) = -\int_{c}^{V} F(v)\, dv \,,$$

where c is any constant.

       a. $E(V) = 1$ b. $E(V) = -V$ c. $E(V) = V^2/2$
       d. $E(V) = V - V^3/3$ e. $E(V) = -V^2/2 + V^4/4$ f. $E(V) = -\cos V$

18. (c) implies (b) because $|x(t) - y| < \exp(-at)$ implies that $x(t) \to y$ as $t \to \infty$. (b) implies (a) according to the definition.

     (a) does not imply (b) because $x(t)$ may not approach y. For example, $y = 0$ is an equilibrium in the system $\dot{x} = 0$ (any other point is also an equilibrium). It is stable, since $|x(t) - 0| < \varepsilon$ for all $|x_0 - 0| < \varepsilon$ and all $t \geq 0$. However, it is not asymptotically stable because $\lim_{t \to \infty} x(t) = x_0 \neq 0$ regardless of how close x_0 is to 0 (unless $x_0 = 0$).

     (b) does not imply (c). For example, the equilibrium $y = 0$ in the system $\dot{x} = -x^3$ is asymptotically stable (check by differentiating that $x(t) = (2t + x_0^{-2})^{-1/2} \to 0$ is a solution with $x(0) = x_0$); however, $x(t)$ approaches 0 with a slower than exponential rate, $\exp(-at)$, for any constant $a > 0$.

Solutions for chapter 4

1. See figures S.11–S.15.

2. See Fig.S.16.

3. See figures S.17–S.21.

4. The diagram follows from the form of the eigenvalues

$$\lambda = \frac{\tau \pm \sqrt{\tau^2 - 4\Delta}}{2}\,.$$
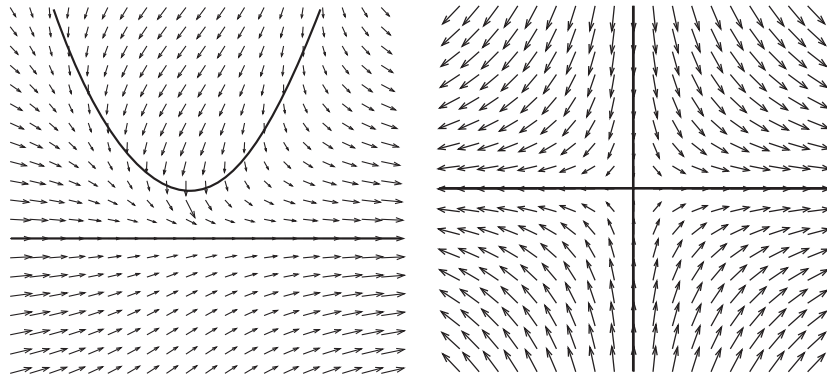
Figure S.11: Nullclines of the vector field; see also Fig.S.17.
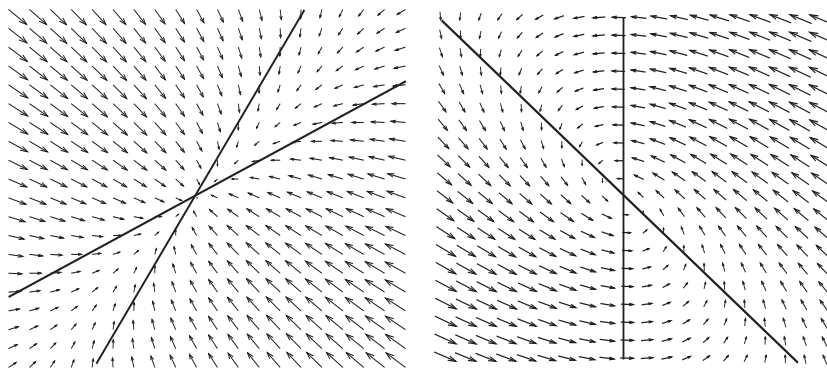
Figure S.12: Nullclines of the vector field; see also Fig.S.18.
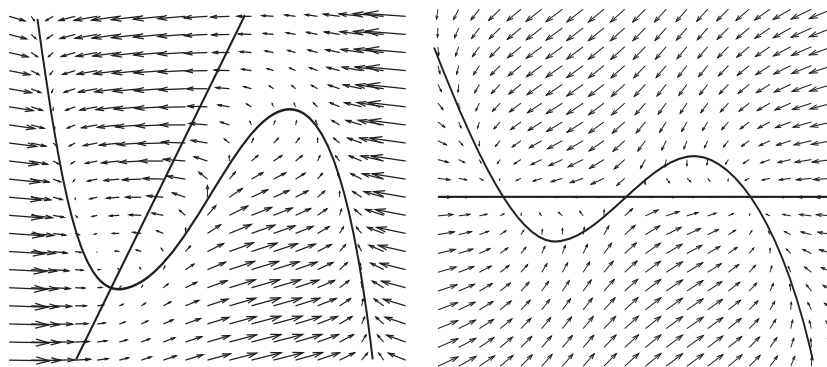
Figure S.13: Nullclines of the vector field; see also Fig.S.19.
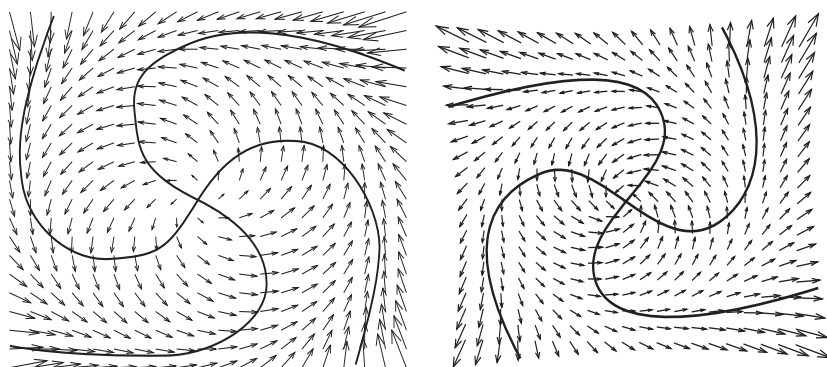
Figure S.14: Nullclines of the vector field; see also Fig.S.20.
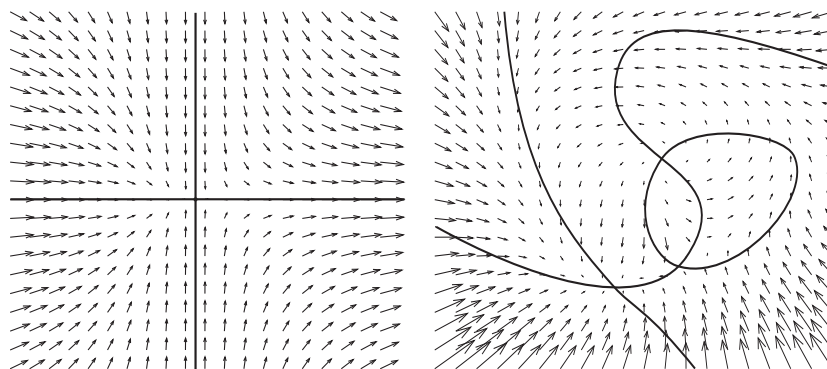
Figure S.15: Nullclines of the vector field; see also Fig.S.21.

If $\Delta < 0$ (left half-plane in Fig.4.15), then the eigenvalues have opposite signs. Indeed,

$$\sqrt{\tau^2 - 4\Delta} > \sqrt{\tau^2} = |\tau| \,,$$

whence

$$\tau + \sqrt{\tau^2 - 4\Delta} > 0 \qquad \text{and} \qquad \tau - \sqrt{\tau^2 - 4\Delta} < 0 \,.$$

The equilibrium is a saddle in this case. Now consider the case $\Delta > 0$. When $\tau^2 < 4\Delta$ (inside the parabola in Fig.4.15), the eigenvalues are complex-conjugate; hence the equilibrium is a focus. It is stable (unstable) when $\tau < 0$ ($\tau > 0$). When $\tau^2 > 4\Delta$ (outside the parabola in Fig.4.15), the eigenvalues are real. Both are negative (positive) when $\tau < 0$ ($\tau > 0$).

5. (van der Pol oscillator) The nullclines of the van der Pol oscillator,

$$y = x - x^3/3 \quad (x\text{-nullcline}) \,,$$
$$x = 0 \quad (y\text{-nullcline}) \,,$$

are depicted in Fig.S.22. There is a unique equilibrium $(0,0)$. The Jacobian matrix at the equilibrium has the form

$$L = \begin{pmatrix} 1 & -1 \\ b & 0 \end{pmatrix} \,.$$

Since $\operatorname{tr} L = 1 > 0$ and $\det L = b > 0$, the equilibrium is always an unstable focus.
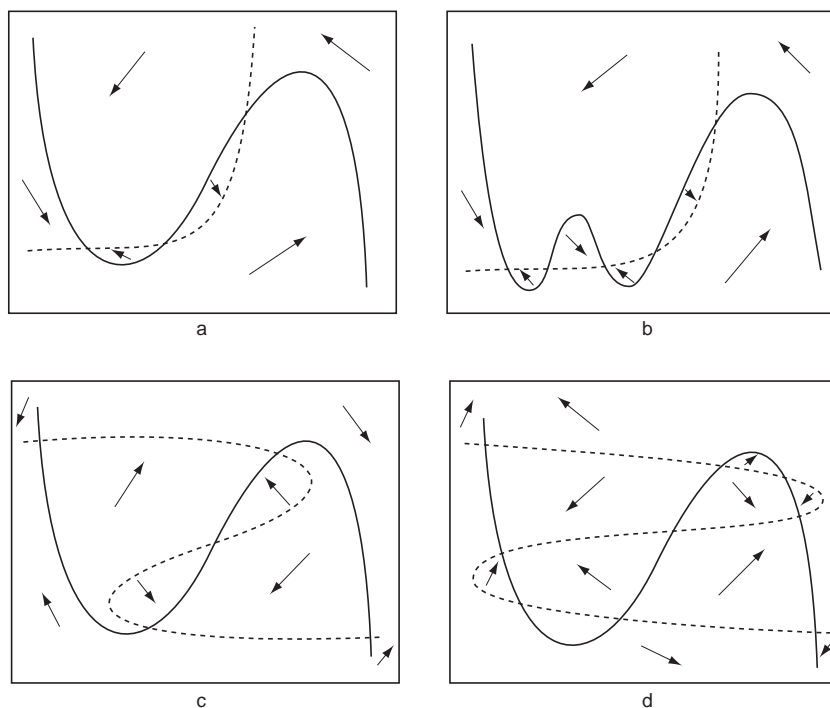
Figure S.16: Approximate directions of the vector in each region between the nullclines.

6. (Bonhoeffer–van der Pol oscillator) The nullclines of the Bonhoeffer–van der Pol oscillator with $c = 0$ have the form

$$y = x - x^3/3 \quad (x\text{-nullcline}) ,$$
$$x = a \quad (y\text{-nullcline}) ,$$

shown in Fig.S.23. They intersect at the point $x = a$, $y = a - a^3/3$. The Jacobian matrix at the equilibrium $(a, a - a^3/3)$ has the form

$$L = \left(\begin{array}{cc} 1 - a^2 & -1 \\ b & 0 \end{array} \right) .$$

Since $\operatorname{tr} L = 1 - a^2$ and $\det L = b > 0$, the equilibrium is a stable (unstable) focus when $|a| > 1$ ($|a| < 1$), as we illustrate in Fig.S.23.

7. (Hindmarsh-Rose spiking neuron) The Jacobian matrix at the equilibrium $(\bar{x}, \bar{y})$ is

$$L = \left(\begin{array}{cc} f' & -1 \\ g' & -1 \end{array} \right) ,$$

therefore

$$\operatorname{tr} L = f' - 1 \qquad \text{and} \qquad \det L = -f' + g' .$$

The equilibrium is a saddle ($\det L < 0$) when $g' < f'$, that is, in the region below the diagonal in Fig.S.24. When $g' > f'$, the equilibrium is stable ($\operatorname{tr} L < 0$) when $f' < 1$, which is the left half-plane in Fig.S.24. Using the classification in Fig.4.15, we conclude that it is a focus when $(f' - 1)^2 - 4(g' - f') < 0$, that is, when

$$g' > \frac{1}{4}(f' + 1)^2,$$
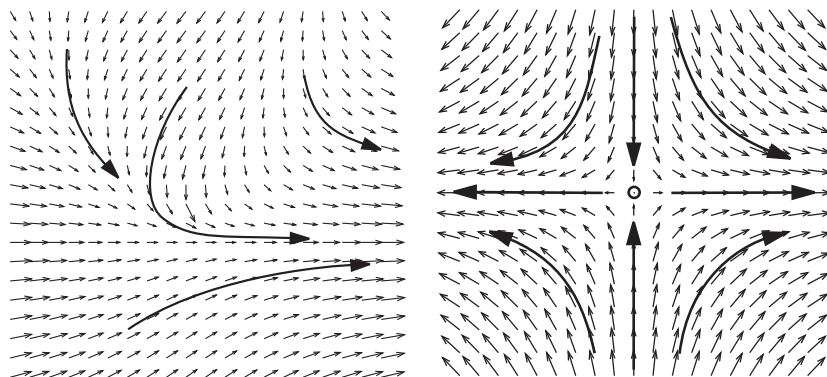
Figure S.17: *Left:* No equilibria. *Right:* Saddle equilibrium.
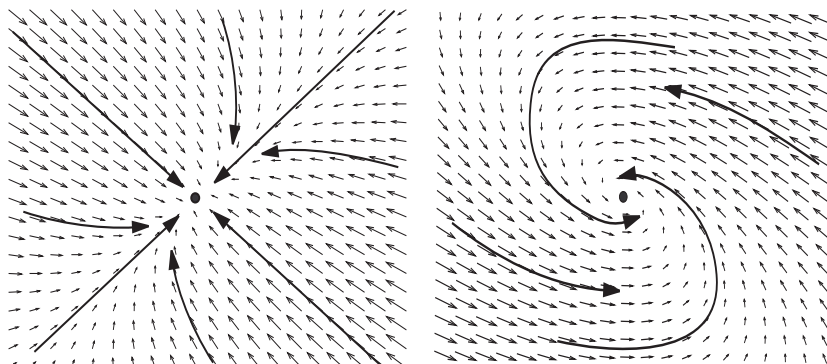
Figure S.18: *Left:* Stable node. *Right:* Stable focus.
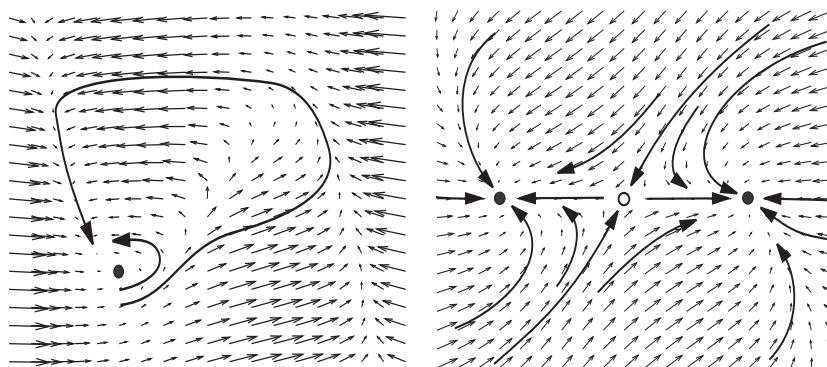
Figure S.19: *Left:* Excitable system having one stable equilibrium. *Right:* Two stable nodes separated by a saddle equilibrium.
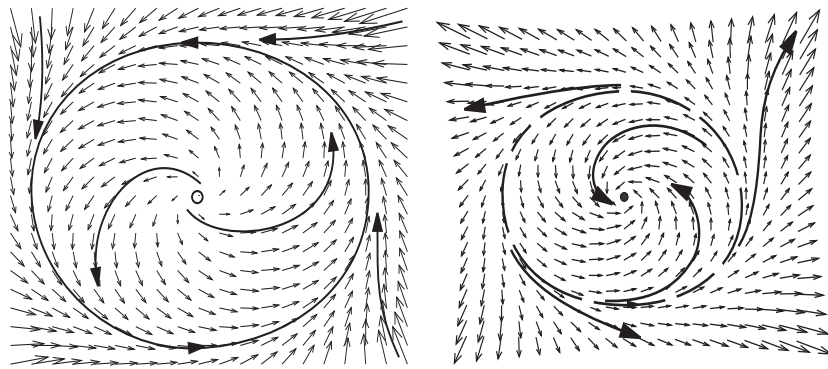
Figure S.20: *Left:* Unstable focus inside a stable limit cycle. *Right:* Stable focus inside an unstable limit cycle.
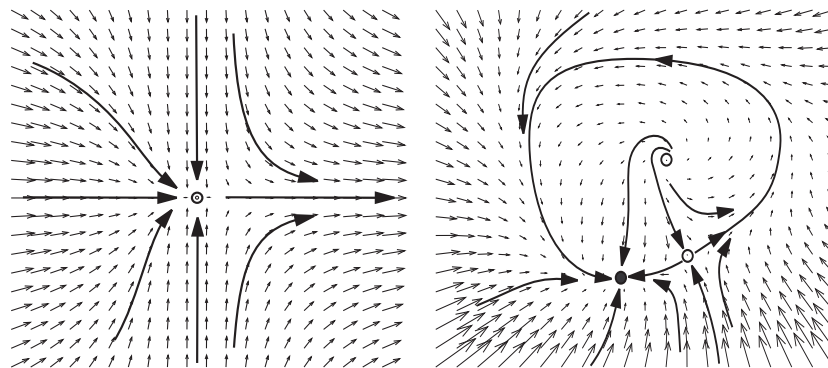
Figure S.21: *Left:* Saddle-node equilibrium. *Right:* Stable node and saddle equilibria connected by two heteroclinic trajectories, which form an invariant circle with an unstable focus inside.
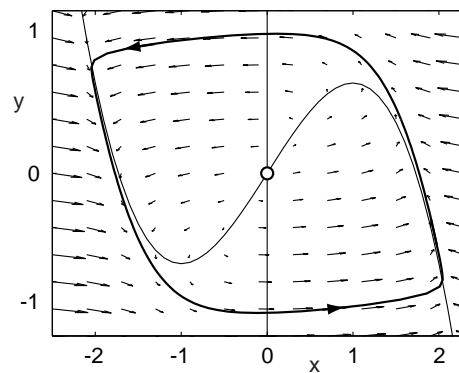
Figure S.22: Nullclines and phase portrait of the van der Pol oscillator ($b = 0.1$).
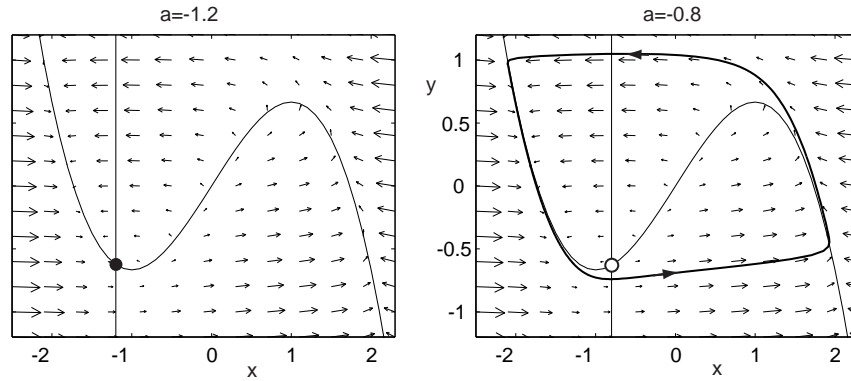
Figure S.23: Nullclines and phase portrait of the Bonhoeffer–van der Pol oscillator ($b = 0.05$ and $c = 0$).
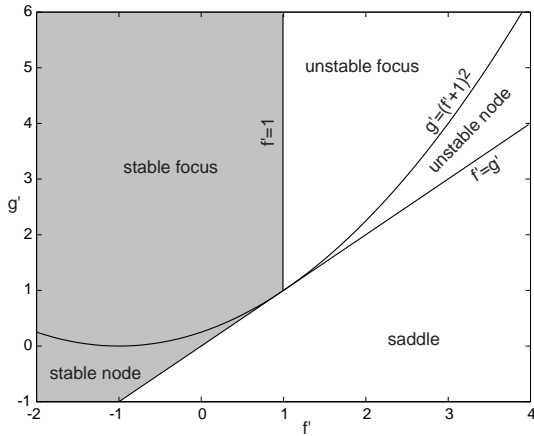
Figure S.24: Stability diagram of the Hindmarsh-Rose spiking neuron model; see exercise 7.

which is the upper part of the parabola in Fig.S.24.

8. (I_K-model) The steady-state I-V relation of the I_K-model is monotone; hence it has a unique equilibrium, which we denoted here as $(\bar{V}, \bar{m}) \in \mathbb{R}^2$, where $\bar{V} > E_K$ and $\bar{m} = m_\infty(\bar{V})$. The Jacobian at the equilibrium has the form

$$L = \begin{pmatrix} -(g_L + \bar{g}_K \bar{m}^4)/C & -4\bar{g}_K \bar{m}^3(\bar{V} - E_K)/C \\ m'_\infty(\bar{V})/\tau(\bar{V}) & -1/\tau(\bar{V}) \end{pmatrix},$$

with the signs

$$L = \begin{pmatrix} - & - \\ + & - \end{pmatrix}.$$

Obviously, $\det L > 0$ and $\operatorname{tr} L < 0$; hence the equilibrium (focus or node) is always stable.

9. (I_h-model) The steady-state I-V relation of the I_h-model is monotone; hence it has a unique equilibrium denote here as $(\bar{V}, \bar{h}) \in \mathbb{R}^2$, where $\bar{V} < E_h$ and $\bar{h} = h_\infty(\bar{V})$. The Jacobian at the equilibrium has the form

$$L = \begin{pmatrix} -(g_L + \bar{g}_h \bar{h})/C & -\bar{g}_h(\bar{V} - E_h)/C \\ h'_\infty(\bar{V})/\tau(\bar{V}) & -1/\tau(\bar{V}) \end{pmatrix},$$

with the signs

$$L = \begin{pmatrix} - & + \\ - & - \end{pmatrix}.$$
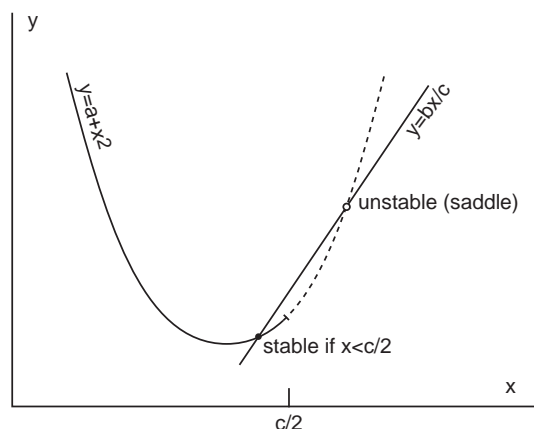
Figure S.25: The left equilibrium is stable when $x < c/2$; see exercise 11.

Obviously, $\det L > 0$ and $\operatorname{tr} L < 0$; hence the equilibrium is always stable.

10. (Bendixson's criterion) The divergence of the vector field of the I_K-model

$$
\overbrace{(-g_L - \bar{g}_K m^4)/C}^{\partial f(x,y)/\partial x} \; + \; \overbrace{-1/\tau(V)}^{\partial g(x,y)/\partial y}
$$

is always negative; hence the model cannot have a periodic orbit. Therefore, it cannot have sustained oscillations.

11. The x-nullcline is $y = a + x^2$ and the y-nullcline is $y = bx/c$, as in Fig.S.25. The equilibria (intersections of the nullclines) are

$$
\bar{x} = \frac{b/c \pm \sqrt{(b/c)^2 - 4a}}{2} \;, \qquad \bar{y} = b\bar{x}/c \;,
$$

provided that $a < \frac{1}{4}(b/c)^2$. The Jacobian matrix at $(\bar{x}, \bar{y})$ has the form

$$
L = \begin{pmatrix} 2\bar{x} & -1 \\ b & -c \end{pmatrix}
$$

with $\operatorname{tr} L = 2\bar{x} - c$ and

$$
\det L = -2\bar{x}c + b = \mp\sqrt{b^2 - 4ac^2} \;.
$$

Thus, the right equilibrium (i.e., $(b/c + \sqrt{(b/c)^2 - 4a})/2$) is always a saddle and the left equilibrium (i.e., $(b/c - \sqrt{(b/c)^2 - 4a})/2$) is always a focus or a node. It is always stable when it lies on the left branch of the parabola $y = a + x^2$ (i.e., when $\bar{x} < 0$), and also can be stable on the right branch if it is not too far from the parabola knee (i.e., if $\bar{x} < c/2$); see Fig.S.25.

Solutions for chapter 5

1. The I_A-model with instantaneous activation has the form

$$
\begin{aligned}
C\dot{V} &= I - \overbrace{g_L(V - E_L)}^{\text{leak } I_L} - \overbrace{\bar{g}_A m_\infty(V)h(V - E_K)}^{I_A} \\
\dot{h} &= (h_\infty(V) - h)/\tau(V) \;.
\end{aligned}
$$
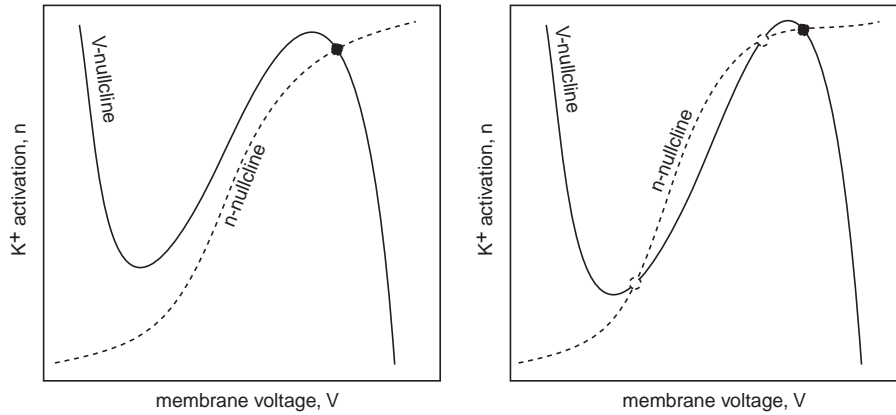
Figure S.26: Answer to exercise 2.
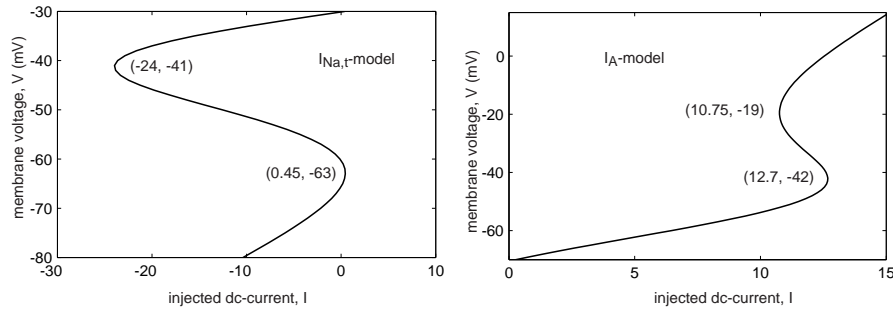
Figure S.27: The saddle-node bifurcation diagrams of the $I_{\mathrm{Na,t}}$- and I_A-minimal models.

To apply the Bendixson criterion (chapter 4, exercise 10), we first determine the divergence of this vector field

$$\frac{\partial \dot{V}}{\partial V} + \frac{\partial \dot{h}}{\partial h} = -\{g_L + \bar{g}_A m'_\infty(V)h(V - E_K) + \bar{g}_A m_\infty(V)h\}/C - 1/\tau(V) < 0 \ .$$

Since it is always negative, the I_A-model cannot have limit cycle attractors (or any other closed loop orbit).

2. See Fig.S.26.

3. The curves

$$I = g_L(V - E_L) + \bar{g}_{\mathrm{Na}}m_\infty^3(V)h_\infty(V)(V - E_{\mathrm{Na}})$$

and

$$I = g_L(V - E_L) + \bar{g}_A m_\infty(V) \, h_\infty(V)(V - E_K)$$

are depicted in Fig.S.27.

4. g is not an absolute conductance, but is taken relative to the conductance at the resting state. Negative values occur because the initial holding voltage value in the voltage-clamp experiment described in Fig.5.22a corresponds to the resting potential, at which the K^+ conductance is partially activated. Indeed, in the $I_{\mathrm{Na,p}}+I_K$-model the K^+ gating variable $n \approx 0.04$; hence the K^+ conductance is approximately 0.4 (because $\bar{g}_K = 10$). According to the procedure, this value corresponds to $g = 0$. Any small decrease in conductance would result in negative values of g. If the initial holding voltage were very negative, say below -100 mV, then the slow conductance g would have nonnegative values in the relevant voltage range (above -100 mV).

5. The curve $I_{\text{slow}}(V)$ defines slow changes of the membrane voltage. The curve $I - I_{\text{fast}}(V)$ defines fast changes. Its middle part, which has a positive slope, is unstable. If the I-V curves intersect in the middle part, the equilibrium is unstable, and the system exhibits periodic spiking: The voltage slowly slides down the left branch of the fast I-V curve toward the slow I-V curve until it reaches the left knee, and then jumps quickly to the right branch. After the jump, the voltage slowly slides up the right branch until it reaches the right knee, and then quickly jumps to the left branch along the straight line that connects the knee and the point $(E_{\text{K}}, 0)$ (see also previous exercise). Note that the direction of the jump is not horizontal, as in relaxation oscillators, but along a sloped line. On that line the slow conductance g is constant, but the slow current $I_{\text{slow}}(V) = g(V - E_{\text{K}})$ changes quickly because the driving force $V - E_{\text{K}}$ changes quickly. When the I-V curves intersect at the stable point (negative slope of $I - I_{\text{fast}}(V)$), the voltage variable may produce a single action potential, then slide slowly toward the intersection, which is a stable equilibrium.

Solutions for chapter 6

1. There are two equilibria: $x = 0$ and $x = b$. The stability is determined by the sign of the derivative

$$\lambda = (x(b - x))'_x = b - 2x$$

at the equilibrium. Since $\lambda = b$ when $x = 0$, this equilibrium is stable (unstable) when $b < 0$ ($b > 0$). Since $\lambda = -b$ when $x = b$, this equilibrium is unstable (stable) when $b < 0$ ($b > 0$).

2. (a) The system

$$\dot{x} = bx^2 , \qquad b \neq 0$$

cannot exhibit saddle-node bifurcation: It has one equilibrium for any nonzero b, or an infinite number of equilibria when $b = 0$. The equilibrium $x = 0$ is non-hyperbolic, and the non-degeneracy condition is satisfied ($a = b \neq 0$). However, the transversality condition is not satisfied at the equilibrium $x = 0$. Another example is $\dot{x} = b^2 + x^2$.

   (b) The system

$$\dot{x} = b - x^3$$

has a single stable equilibrium for any b. However, the point $x = 0$ is non-hyperbolic when $b = 0$ and the transversality condition is also satisfied. The non-degeneracy condition is violated, however.

3. It is easy to check (by differentiating) that

$$V(t) = \frac{\sqrt{c(b - b_{\text{sn}})}}{\sqrt{a}} \tan(\sqrt{ac(b - b_{\text{sn}})}t)$$

is a solution to the system. Since $\tan(-\pi/2) = -\infty$ and $\tan(+\pi/2) = +\infty$, it takes

$$T = \frac{\pi}{\sqrt{ac(b - b_{\text{sn}})}}$$

for the solution to go from $-\infty$ to $+\infty$.

4. The first system can be transformed into the second if we use complex coordinates $z = u + \mathrm{i}v$. To obtain the third system, we use polar coordinates

$$re^{\mathrm{i}\varphi} = z = u + \mathrm{i}v \in \mathbb{C} ,$$

so that

$$\overbrace{\dot{r}e^{i\varphi} + re^{i\varphi}i\dot{\varphi}}^{\dot{z}} = \overbrace{(c(b) + i\omega(b))re^{i\varphi} + (a + id)r^3 e^{i\varphi}}^{(c(b)+i\omega(b))z+(a+id)z|z|^2} .$$

Next, we divide both sides of this equation by $e^{i\varphi}$ and separate the real and imaginary parts to obtain

$$\{\dot{r} - c(b)r - ar^3\} + ir\{\dot{\varphi} - \omega(b) - dr^2\} = 0 ,$$

which we can write in the polar coordinates form.

5. (a) The equilibrium $r = 0$ of the system

$$\begin{aligned} \dot{r} &= br^3 , \\ \dot{\varphi} &= 1 , \end{aligned}$$

has a pair of complex-conjugate eigenvalues $\pm i$ for any b, and the non-degeneracy condition is satisfied for any $b \neq 0$. However, the transversality condition is violated, and the system does not exhibit Andronov-Hopf bifurcation (no limit cycle exists near the equilibrium).

(b) The equilibrium $r = 0$ for $b = 0$

$$\begin{aligned} \dot{r} &= br , \\ \dot{\varphi} &= 1 , \end{aligned}$$

has a pair of complex-conjugate eigenvalues $\pm i$ and the transversality condition is satisfied. However, the bifurcation is not of the Andronov-Hopf type because no limit cycle exists near the equilibrium for any b.

6. The Jacobian matrix at the equilibrium $(u, v) = (0, 0)$ has the form

$$L = \begin{pmatrix} b & -1 \\ 1 & b \end{pmatrix} .$$

It has eigenvalues $b \pm i$. Therefore, the loss of stability occurs at $b = 0$, and the non-hyperbolicity and transversality conditions are satisfied. Since the model can be reduced to the polar-coordinate system (see exercise 4) and $a \neq 0$, the non-degeneracy condition is also satisfied, and the system undergoes an Andronov-Hopf bifurcation.

7. Since

$$(cr + ar^3)'_r = c + 3ar^2 = c + 3a|c/a| = \begin{cases} c + 3|c| & \text{when } a > 0, \\ c - 3|c| & \text{when } a < 0, \end{cases}$$

the limit cycle is stable when $a < 0$.

8. The sequence of bifurcations is similar to that of the RS neuron in Fig.8.15. The resting state is a globally asymptotically stable equilibrium for $I < 5.64$. At this value a stable (spiking) limit cycle appears via a big saddle homoclinic orbit bifurcation. At $I = 5.8$ a small-amplitude unstable limit cycle is born via another saddle homoclinic orbit bifurcation. This cycle shrinks to the equilibrium and makes it lose stability via subcritical Andronov-Hopf bifurcation at $I = 6.5$. This unstable focus becomes an unstable node when I increases, and then it coalesces with the saddle (at $I = 7.3$) and disappears. Note that there is a saddle-node bifurcation according to the I-V relation, but it corresponds to the disappearance of an unstable equilibrium.

9. The Jacobian matrix of partial derivatives has the form

$$L = \begin{pmatrix} -I'_V(V, x) & -I'_x(V, x) \\ x'_\infty(V)/\tau(V) & -1/\tau(V) \end{pmatrix} ,$$

so that

$$\operatorname{tr} L = -\{I'_V(V, x) + 1/\tau(V)\}$$

and

$$\det L = \{I'_V(V, x) + I'_x(V, x)x'_\infty(V)\}/\tau(V) = I'_\infty(V)/\tau(V) .$$

The characteristic equation

$$\lambda^2 - \lambda \operatorname{tr} L + \det L = 0$$

has two solutions

$$\overbrace{(\operatorname{tr} L)/2}^{c} \pm \overbrace{\sqrt{\{(\operatorname{tr} L)/2\}^2 - \det L}}^{\omega}$$

which might be complex-conjugate.

10. Let $z = re^{\varphi\mathbf{i}}$; then

$$\begin{aligned} r' &= ar + r^3 - r^5 , \\ \varphi' &= \omega . \end{aligned}$$

Any limit cycle is an equilibrium of the amplitude equation, that is,

$$a + r^2 - r^4 = 0 .$$

The system undergoes fold limit cycle bifurcation when the amplitude equation undergoes a saddle-node bifurcation, that is, when

$$a + 3r^2 - 5r^4 = 0$$

(check the non-degeneracy and transversality conditions). The two equations have the non-trivial solution $(a, r) = (-1/4, 1/\sqrt{2})$.

11. The projection onto the v_1-axis is described by the equation

$$\dot{x} = \lambda_1 x , \qquad x(0) = a .$$

The trajectory leaves the square when $x(t) = ae^{\lambda_1 t} = 1$; that is, when

$$t = -\frac{1}{\lambda_1} \ln a = -\frac{1}{\lambda_1} \ln \tau(I - I_b) .$$

12. Equation (6.13) has two bifurcation parameters, b and v, and the saddle-node homoclinic bifurcation occurs when $b = b_{\mathrm{sn}}$ and $v = V_{\mathrm{sn}}$. The saddle-node bifurcation curve is the straight line $b = b_{\mathrm{sn}}$ (any v). This bifurcation is *on* an invariant circle when $v < V_{\mathrm{sn}}$ and *off* otherwise. When $b > b_{\mathrm{sn}}$, there are no equilibria and the normal form exhibits periodic spiking. When $b < b_{\mathrm{sn}}$, the normal form has two equilibria,

$$\overbrace{V_{\mathrm{sn}} - \sqrt{c|b - b_{\mathrm{sn}}|/a}}^{\text{node}} \qquad \text{and} \qquad \overbrace{V_{\mathrm{sn}} + \sqrt{c|b - b_{\mathrm{sn}}|/a}}^{\text{saddle}} .$$

The saddle homoclinic orbit bifurcation occurs when the voltage is reset to the saddle, that is, when

$$v = V_{\mathrm{sn}} + \sqrt{c|b - b_{\mathrm{sn}}|/a} .$$

13. The Jacobian matrix at an equilibrium is

$$L = \begin{pmatrix} 2v & -1 \\ ab & -a \end{pmatrix}.$$

Saddle-node condition $\det L = -2va + ab = 0$ results in $v = b/2$. Since v is an equilibrium, it satisfies $v^2 - bv + I = 0$; hence $b^2 = 4I$. The Andronov-Hopf condition $\operatorname{tr} L = 2v - a = 0$ results in $v = a/2$; hence $a^2/4 - ab/2 + I = 0$. The bifurcation occurs when $\det L > 0$, resulting in $a < b$. Combining the saddle-node and Andronov-Hopf conditions results in the Bogdanov-Takens conditions.

14. Change of variables (6.5), $v = x$ and $u = \sqrt{\mu}y$, transforms the relaxation oscillator into the form

$$\begin{aligned} \dot{x} &= f(x) - \sqrt{\mu}y \\ \dot{y} &= \sqrt{\mu}(x - b) \end{aligned} \qquad \text{with the Jacobian} \quad L = \begin{pmatrix} f'(b) & -\sqrt{\mu} \\ \sqrt{\mu} & 0 \end{pmatrix}$$

at the equilibrium $v = x = b$, $u = \sqrt{\mu}y = f(b)$. The Andronov-Hopf bifurcation occurs when $\operatorname{tr} L = f'(b) = 0$ and $\det L = \mu > 0$. Using (6.7), we find that it is supercritical when $f'''(b) < 0$ and subcritical when $f'''(b) > 0$.

15. The Jacobian matrix at the equilibrium, which satisfies $F(v) - bv = 0$, is

$$L = \begin{pmatrix} F' & -1 \\ \mu b & -\mu \end{pmatrix}.$$

The Andronov-Hopf bifurcation occurs when $\operatorname{tr} L = F' - \mu = 0$ (hence $F' = \mu$) and $\det L = \omega^2 = \mu b - \mu^2 > 0$ (hence $b > \mu$). The change of variables (6.5), $v = x$ and $u = \mu x + \omega y$, transforms the system into the form

$$\begin{aligned} \dot{x} &= -\omega y + f(x) \\ \dot{y} &= \omega x + g(x), \end{aligned}$$

where $f(x) = F(x) - \mu x$ and $g(x) = \mu[bx - F(x)]/\omega$. The result follows from (6.7).

16. The change of variables (6.5) converts the system into the form

$$\begin{aligned} \dot{x} &= F(x) + \text{linear terms} \\ \dot{y} &= \mu(G(x) - F(x))/\omega + \text{linear terms.} \end{aligned}$$

The result follows from (6.7).

17. The change of variables (6.5), $v = x$ and $u = \mu x + \omega y$, converts the system into

$$\begin{aligned} \dot{x} &= F(x) - x(\mu x + \omega y) + \text{linear terms} \\ \dot{y} &= \mu[G(x) - F(x) + x(\mu x + \omega y)]/\omega. \end{aligned}$$

The result follows from (6.7).

18. The system undergoes Andronov-Hopf bifurcation when $F_v = -\mu G_u$ and $F_u G_v < -\mu G_u^2$. We perform all the steps from (6.4) to (6.7), disregarding linear terms (they do not influence a) and the terms of the order $o(\mu)$. Let $\omega = \sqrt{-\mu F_u G_v} + \mathcal{O}(\mu)$, then $u = (\mu G_u x - \omega y)/F_u = -\omega y/F_u + \mathcal{O}(\mu)$, and

$$f(x, y) = F(x, -\omega y/F_u + \mathcal{O}(\mu)) = F(x, 0) - F_u(x, 0)\omega y/F_u + \mathcal{O}(\mu)$$

and

$$g(x, y) = (\mu/\omega)[G_u F(x, 0) - F_u G(x, 0)] + \mathcal{O}(\mu).$$

The result follows from (6.7).
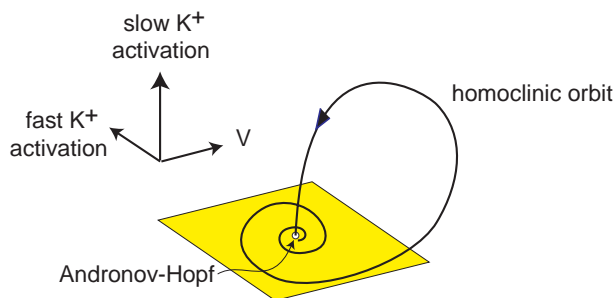
Figure S.28: Codimension-2 Shilnikov-Hopf bifurcation.

Solutions for chapter 7

1. Take $c < 0$ so that the slow w-nullcline has a negative slope.

2. The quasi-threshold contains the union of canard solutions.

3. The change of variables $z = e^{\mathbf{i}\omega t}u$ transforms the system into the form

$$\dot{u} = \varepsilon\{-u + e^{-\mathbf{i}\omega t}I(t)\}\ ,$$

   which can be averaged, yielding
   $$\dot{u} = \varepsilon\{-u + I^*(\omega)\}\ .$$

   Apparently, the stable equilibrium $u = I^*(\omega)$ corresponds to the sustained oscillation $z = e^{\mathbf{i}\omega t}I^*(\omega)$.

4. The existence of damped oscillations with frequency ω implies that the system has a focus equilibrium with eigenvalues $-\varepsilon \pm \mathbf{i}\omega$, where $\varepsilon > 0$. The local dynamics near the focus can be represented in the form (7.3). The rest of the proof is the same as the one for exercise 3.

5. Even though the slow and the fast nullclines in Fig.5.21 intersect in only one point, they continue to be close and parallel to each other in the voltage range 10 mV to 30 mV. Such a proximity creates a tunneling effect (Rush and Rinzel 1996) that prolongs the time spent near those nullclines.

6. (Shilnikov-Hopf bifurcation) The model is near a codimension-2 bifurcation having a homoclinic orbit to an equilibrium undergoing subcritical Andronov-Hopf bifurcation, as we illustrate in Fig.S.28. Many weird phenomena can happen near bifurcations of codimension-2 or higher.

Solutions for chapter 8

1. Consider two coupled neurons firing together.

2. The equation
   $$\dot{V} = c(b - b_{\mathrm{sn}}) + a(V - V_{\mathrm{sn}})^2$$

   can be written in the form
   $$\dot{V} = a(V - V_{\mathrm{rest}})(V - V_{\mathrm{thresh}})$$

   with
   $$V_{\mathrm{rest}} = V_{\mathrm{sn}} - \sqrt{c(b_{\mathrm{sn}} - b)/a} \qquad \text{and} \qquad V_{\mathrm{thresh}} = V_{\mathrm{sn}} + \sqrt{c(b_{\mathrm{sn}} - b)/a},$$
   provided that $b < b_{\mathrm{sn}}$.

3. The system $\dot{v} = b + v^2$ with $b > 0$ and the initial condition $v(0) = v_{\text{reset}}$ has the solution (check by differentiating)

$$v(t) = \sqrt{b} \tan(\sqrt{b}(t + t_0)),$$

where

$$t_0 = \frac{1}{\sqrt{b}} \text{atan} \frac{v_{\text{reset}}}{\sqrt{b}}.$$

From the condition $v(T) = v_{\text{peak}} = 1$, we find

$$T = \frac{1}{\sqrt{b}} \text{atan} \frac{1}{\sqrt{b}} - t_0 = \frac{1}{\sqrt{b}} \left(\text{atan} \frac{1}{\sqrt{b}} - \text{atan} \frac{v_{\text{reset}}}{\sqrt{b}} \right),$$

which alternatively can be written as

$$T = \frac{1}{\sqrt{b}} \text{atan} \left(\sqrt{b} \frac{v_{\text{reset}} - 1}{v_{\text{reset}} + b} \right).$$

4. The system $\dot{v} = -|b| + v^2$ with the initial condition $v(0) = v_{\text{reset}} > \sqrt{|b|}$ has the solution (check by differentiating)

$$v(t) = \sqrt{|b|} \frac{1 + e^{2\sqrt{b}(t + t_0)}}{1 - e^{2\sqrt{b}(t + t_0)}},$$

where

$$t_0 = \frac{1}{2\sqrt{|b|}} \ln \frac{v_{\text{reset}} - \sqrt{|b|}}{v_{\text{reset}} + \sqrt{|b|}}.$$

From the condition $v(T) = 1$, we find

$$T = \frac{1}{2\sqrt{|b|}} \left(\ln \frac{1 - \sqrt{|b|}}{1 + \sqrt{|b|}} - \ln \frac{v_{\text{reset}} - \sqrt{|b|}}{v_{\text{reset}} + \sqrt{|b|}} \right).$$

5. The saddle-node bifurcation occurs when $b = 0$, regardless of the value of v_{reset}, which is a straight vertical line in Fig.8.3. If $v_{\text{reset}} < 0$, then the saddle-node bifurcation is on an invariant circle. When $b < 0$, the unstable node (saddle) equilibrium is at $v = \sqrt{|b|}$. Hence, the saddle homoclinic orbit bifurcation occurs when $v_{\text{reset}} = \sqrt{|b|}$.

6. The change of variables $v = g/2 + V$, $b = g^2/4 + B$ transforms $\dot{v} = b - gv + v^2$ to $\dot{V} = B + V^2$ with $V_{\text{reset}} = -\infty$ and $V_{\text{peak}} = +\infty$. It has the threshold $V = \sqrt{B}$, the rheobase $B = 0$, and the same F-I curve as in the original model with $g = 0$. In v-coordinates, the threshold is $v = g/2 + \sqrt{b - g^2/4}$, which is greater than $\sqrt{b}$, the new rheobase is $b = g^2/4$, which is greater than $b = 0$, and the new F-I curve is the same as the old one, just shifted to the right by $g^2/4$.

7. Let $b = \varepsilon r$ with $\varepsilon \ll 1$ be a small parameter. The change of variables

$$v = \sqrt{\varepsilon} \tan \frac{\vartheta}{2}$$

uniformly transforms (8.2) into the theta-neuron form

$$\dot{\vartheta} = \sqrt{\varepsilon} \{(1 - \cos \vartheta) + (1 + \cos \vartheta)r\}.$$

on the unit circle except for the small interval $|\vartheta - \pi| < 2\sqrt[4]{\varepsilon}$ corresponding to the action potential ($v > 1$); see Hoppensteadt and Izhikevich (1997) for more details.

8. Use the change of variables

$$v = \frac{\sqrt{\varepsilon}\vartheta}{1 - |\vartheta|} \ .$$

To obtain other theta neuron models, use the change of variables

$$v = \sqrt{\varepsilon}h(\vartheta) \ ,$$

where the monotone function h maps $(-\pi, \pi)$ to $(-\infty, \infty)$ and scales like $1/(\vartheta \pm \pi)$ when $\vartheta \to \pm\pi$. The corresponding model has the form

$$\vartheta' = h^2(\vartheta)/h'(\vartheta) + r/h'(\vartheta) \ .$$

In particular, $h^2(\vartheta)/h'(\vartheta)$ exists, and is bounded and $1/h'(\vartheta) = 0$ when $\vartheta \to \pm\pi$. These imply a uniform velocity independent from the input r when ϑ passes the value $\pm\pi$ corresponding to firing a spike.

9. The equilibrium $v = I/(b+1), u = bI/(b+1)$ has the Jacobian matrix

$$L = \begin{pmatrix} -1 & -1 \\ ab & -a \end{pmatrix}$$

with $\mathrm{tr}L = -(a+1)$ and $\det L = a(b+1)$. It is a stable node (integrator) when $b < (a+1)^2/(4a) - 1$ and a stable focus (resonator) otherwise.

10. The quadratic integrate-and-fire neuron with a dendritic compartment

$$\begin{aligned} \dot{V} &= B + V^2 + g_1(V_d - V) \\ \dot{V}_d &= g_{\text{leak}}(E_{\text{leak}} - V_d) + g_2(V - V_d) \end{aligned}$$

can be written in the form (8.3, 8.4), with $v = V - g_1/2$, $u = -g_1 V_d$, $I = B - g_1^2/4 - (g_1^2 g_2 + g_{\text{leak}} E_{\text{leak}})/(g_{\text{leak}} + g_2)$, $a = g_{\text{leak}} + g_2$, and $b = -g_1 g_2/a$.

11. A MATLAB program generating the figure is provided on the author's Web page (www.izhikevich.com).

12. An example is in Fig.S.29.

13. An example is in Fig.S.30.

Solutions for chapter 9

1. (Planar burster) Izhikevich (2000a) suggested the system

$$\begin{aligned} \dot{x} &= x - x^3/3 - u + 4S(x)\cos 40u, \\ \dot{u} &= \mu x \ , \end{aligned}$$

with $S(x) = 1/(1 + e^{5(1-x)})$ and $\mu = 0.01$. It has a hedgehog limit cycle depicted in Fig.S.31.

2. (Noise-induced bursting) Noise can induce bursting in a two-dimensional system with coexistence of resting and spiking states. Indeed, noisy perturbations can randomly push the state of the system into the attraction domain of the resting state or into the attraction domain of the limit cycle attractor, as in Fig.S.32. The solution meanders between the states, exhibiting a random bursting pattern as in Fig.9.55 (right). Neocortical neurons of the RS and FS types, as well as stellate neurons of the entorhinal cortex, exhibit such bursting; see chapter 8.
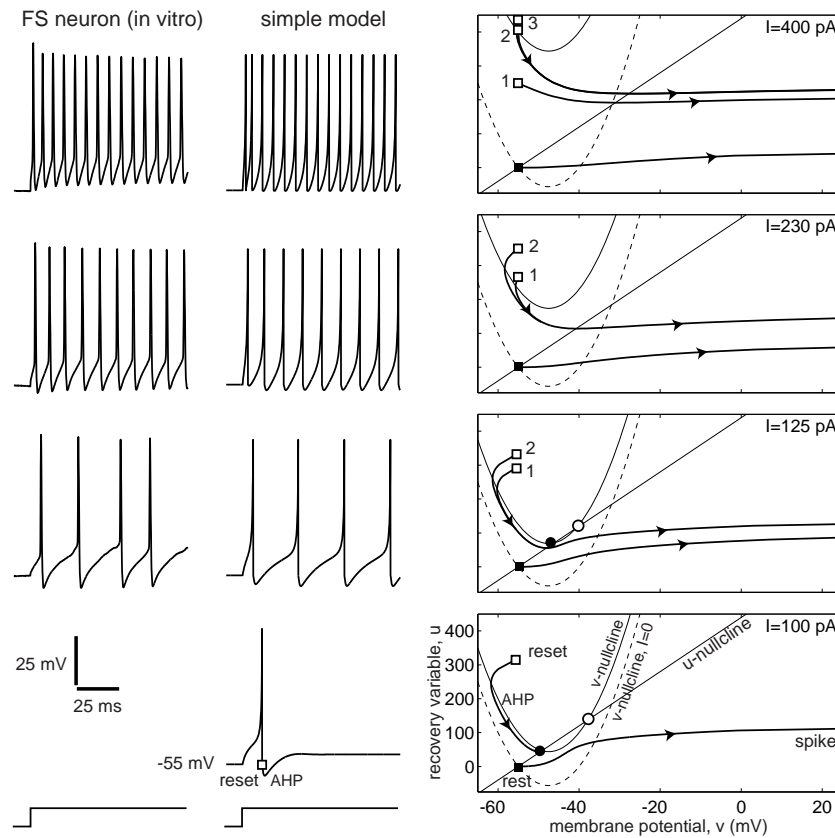
Figure S.29: Comparison of *in vitro* recordings of a fast spiking (FS) interneuron of layer 5 rat visual cortex with simulations of the simple model with linear slow nullcline $20\dot{v} = (v + 55)(v + 40) - u + I$, $\dot{u} = 0.15\{8(v + 55) - u\}$, if $v \geq 25$, then $v \leftarrow -55$, $u \leftarrow u + 200$.

3. (Noise-induced bursting) Bursting occurs because noisy perturbations push the trajectory into and out of the attraction domain of the limit cycle attractor, which coexists with the resting equilibrium; see the phase portrait in Fig.S.33.

4. (Rebound bursting in the FitzHugh-Nagumo oscillator) The oscillator is near the fold limit cycle bifurcation. The solution makes a few rotations along the ghost of the cycle before returning to rest; see Fig.S.34.

5. Yes, they can, at the end of a burst. Think of a "fold/Hopf" or "circle/Hopf" burster. The resting equilibrium is a stable focus immediately after the termination of a burst, and then it is transformed into a stable node to be ready for the circle or fold bifurcation. Even "circle/circle" bursters can exhibit such oscillations, if the resting equilibrium turns into a focus for a short period of time somewhere in the middle of a quiescent phase. In any case, the oscillations should disappear just before the transition to the spiking state.

6. (Hopf/Hopf bursting) Even though there is no coexistence of attractors, there is a hysteresis loop due to the slow passage effect through the supercritical Andronov-Hopf bifurcation; see Fig.S.35. The delayed transition to spiking creates the hysteresis loop and enables bursting.

7. (Hopf/Hopf canonical model) First, we restrict the fast subsystem to its center manifold and transform it into the normal form for supercritical Andronov-Hopf bifurcation, which after
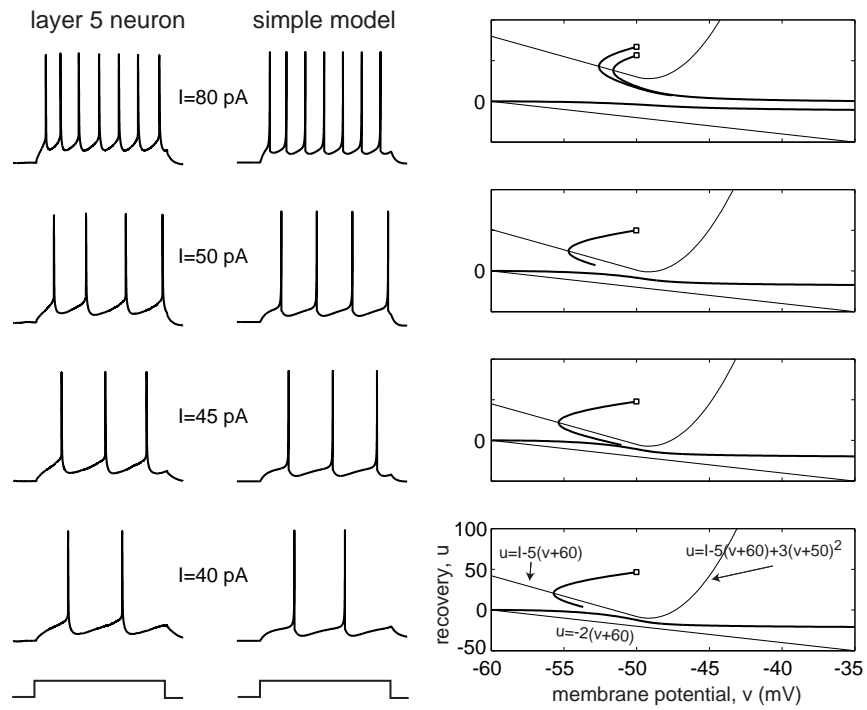
Figure S.30: Comparison of *in vitro* recordings of a regular spiking (RS) neuron with simulations of the simple model $100\dot{v} = I - 5(v+60) + 3(v+50)^2_+ - u$, $\dot{u} = 0.02\{-2(v+60) - u\}$, if $v \geq 35$, then $v \leftarrow -50$, $u \leftarrow u + 70$.
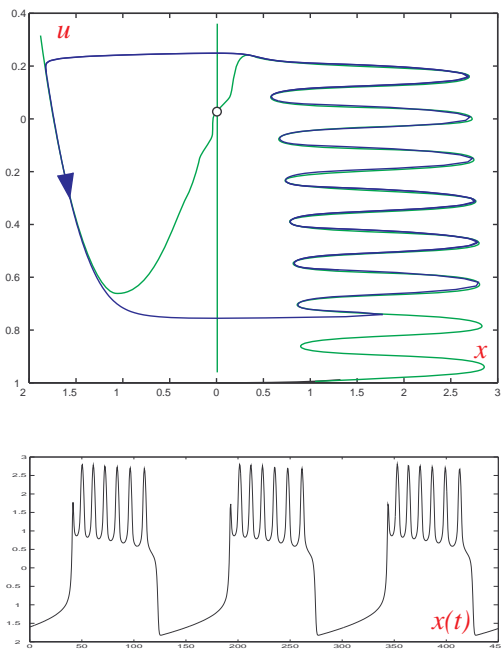
Figure S.31: Solution to exercise 1. Nullclines, a hedgehog limit cycle, and a bursting solution of a planar system. (Modified from Izhikevich 2000a.)
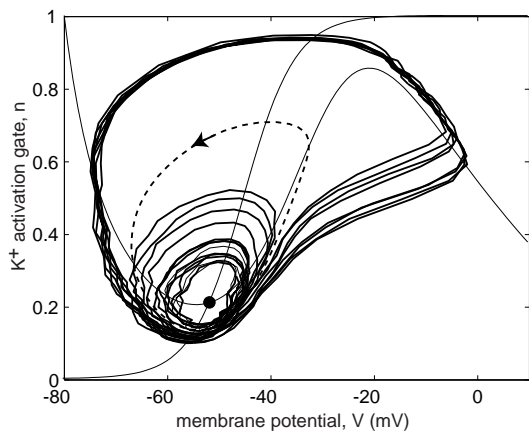
Figure S.32: Noise-induced bursting in two-dimensional system; See exercise 2.
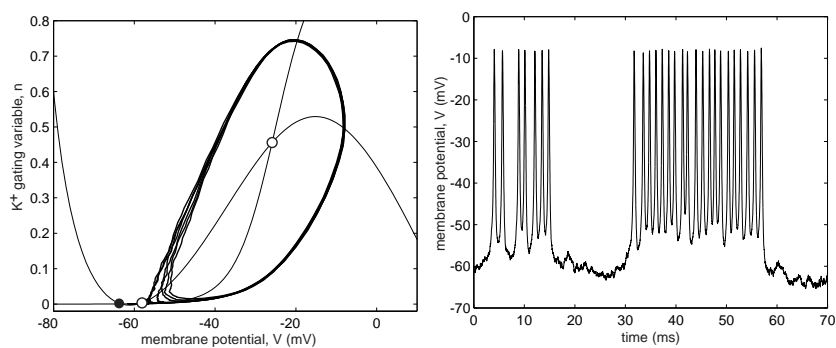
Figure S.33: Noise-induced bursting in a two-dimensional system with coexistence of an equilibrium and a limit cycle attractor; see exercise 3.
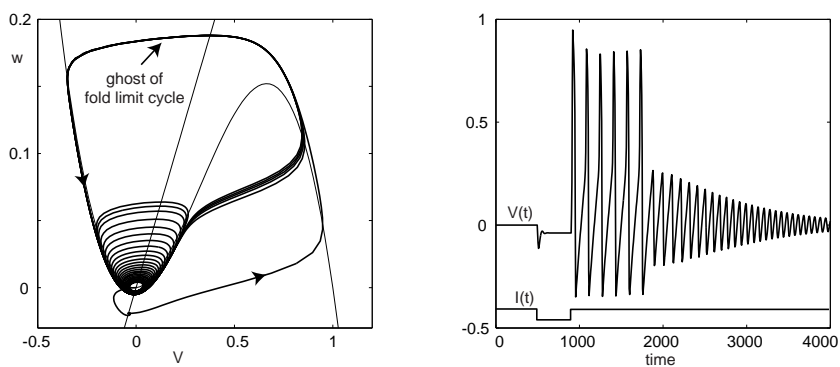
Figure S.34: Rebound bursting in the FitzHugh-Nagumo oscillator; see exercise 4.
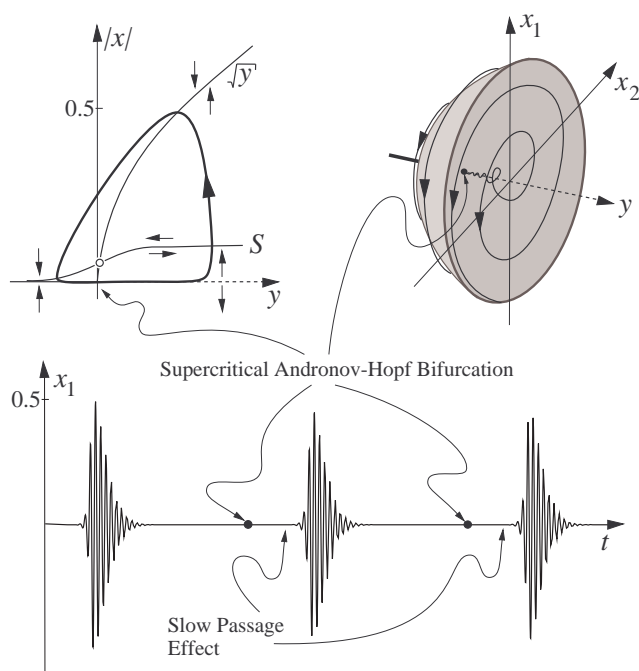
Figure S.35: Hopf/Hopf bursting without coexistence of attractors; see exercise 6. (Modified from Hoppensteadt and Izhikevich 1997.)

appropriate re-scaling, has the form

$$\dot{z} = (u + \mathrm{i}\omega)z - z|z|^2 .$$

Here, u is the deviation from the slow equilibrium u_0. The slow subsystem

$$\dot{u} = \mu g(ze^{\mathrm{i}\omega t} + \text{complex-conjugate}, u)$$

can be averaged and transformed into the canonical form.

8. (Bursting in the $I_{\mathrm{Na,t}}+I_{\mathrm{Na,slow}}$-model) First, determine the parameters of the $I_{\mathrm{Na,t}}$-model corresponding to the subcritical Andronov-Hopf bifurcation, and hence the coexistence of the resting and spiking states. Then, add a slow high-threshold persistent Na$^+$ current that activates during spiking, depolarizes the membrane potential, and stops the spiking. During resting, the current deactivates, the membrane potential hyperpolarizes, and the neuron starts to fire again.

9. Replace the slow Na$^+$ current in the exercise above with a slow dendritic compartment with dendritic resting potential far below the somatic resting potential. As the dendritic compartment hyperpolarizes the somatic compartment, the soma starts to fire (due to the inhibition-induced firing described in section 7.2.8). As the somatic compartment fires, the dendritic compartment slowly depolarizes, removes the hyperpolarization and stops firing.

10. (Bursting in the $I_{\mathrm{Na,p}}+I_{\mathrm{K}}+I_{\mathrm{Na,slow}}$-model) The time constant $\tau_{\mathrm{slow}}(V)$ is relatively small in the voltage range corresponding to the spike after-hyperpolarization (AHP). Deactivation of the Na$^+$ current during each AHP is much stronger than its activation during the spike peak. As a result, the Na$^+$ current deactivates (turns off) during the burst, and then slowly reactivates to its baseline level during the resting period, as one can see in Fig.S.36.
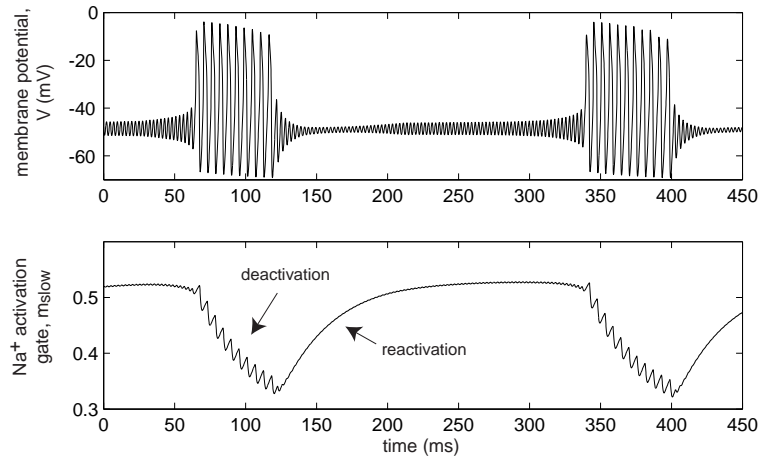
Figure S.36: Bursting in the $I_{Na,p}+I_K+I_{Na,slow}$-model. See exercise 10.
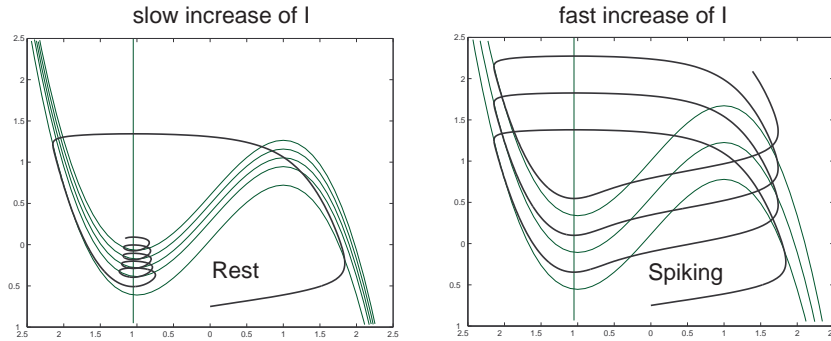
Figure S.37: The system has a unique attractor, equilibrium, yet it can exhibit repetitive spiking activity when the N-shaped nullcline is moved upward not very slowly.

11. The mechanism of spiking, illustrated in Fig.S.37, is closely related to the phenomenon of accommodation and anodal break excitation. The key feature is that this bursting is not fast-slow.

    The system has a unique attractor – a stable equilibrium – and the solution always converges to it. The slow variable I controls the vertical position of the N-shaped nullcline. If I increases, the nullcline slowly moves upward, and so does the solution, because it tracks the equilibrium. However, if the rate of change of I is not small enough, the solution cannot catch up with the equilibrium and starts to oscillate with a large amplitude. Thus, the system exhibits spiking behavior even though it does not have a limit cycle attractor for any fixed I.

12. From the first equation, we find the equivalent voltage

$$|z|^2 = |1+u|_+ = \begin{cases} 1+u & \text{if } 1+u > 0\,, \\ 0 & \text{if } 1+u \le 0\,, \end{cases}$$

    so that the reduced slow subsystem has the form

$$\begin{aligned} \dot{u} &= \mu[u - u^3 - w]\,, \\ \dot{w} &= \mu[|1+u|_+ - 1]\,, \end{aligned}$$

    and it has essentially the same dynamics as the van der Pol oscillator.
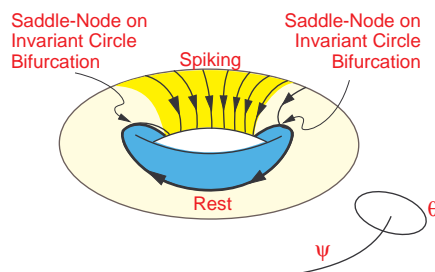
Figure S.38: Answer to exercise 13.

13. The fast equation

$$\dot{\vartheta} = 1 - \cos \vartheta + (1 + \cos \vartheta)r$$

is the Ermentrout-Kopell canonical model for Class 1 excitability, also known as the theta neuron (Ermentrout 1996). It is quiescent when $r < 0$ and fires spikes when $r > 0$. As ψ oscillates with frequency ω, the function $r = r(\psi)$ changes sign. The fast equation undergoes a saddle-node on invariant circle bifurcation; hence the system is a "circle/circle" burster of the slow-wave type; see Fig.S.38.

14. To understand the bursting dynamics of the canonical model, rewrite it in polar coordinates $z = re^{\mathrm{i}\varphi}$:

$$\begin{aligned}
\dot{r} &= ur + 2r^3 - r^5 , \\
\dot{u} &= \mu(a - r^2) , \\
\dot{\varphi} &= \omega .
\end{aligned}$$

Apparently, it is enough to consider the first two equations, which determine the oscillation profile. Nontrivial ($r \neq 0$) equilibria of this system correspond to limit cycles of the canonical model, which may look like periodic (tonic) spiking with frequency ω. Limit cycles of this system correspond to quasi-periodic solutions of the canonical model, which look like bursting; see Fig.9.37.

The first two equation above have a unique equilibrium,

$$\left(\begin{array}{c} r \\ u \end{array} \right) = \left(\begin{array}{c} \sqrt{a} \\ a^2 - 2a \end{array} \right)$$

for all μ and $a > 0$, which is stable when $a > 1$. When a decreases and passes an μ neighborhood of $a = 1$, the equilibrium loses stability via Andronov-Hopf bifurcation. When $0 < a < 1$, the system has a limit cycle attractor. Therefore, the canonical model exhibits bursting behavior. The smaller the value of a, the longer the interburst period. When $a \to 0$, the interburst period becomes infinite.

15. Take $w = I - u$. Then (9.7) becomes

$$\begin{aligned}
\dot{v} &= v^2 + w , \\
\dot{w} &= \mu(I - w) \approx \mu I .
\end{aligned}$$

16. Let us sketch the derivation. Since the fast subsystem is near saddle-node homoclinic orbit bifurcation for some $u = u_0$, a small neighborhood of the saddle-node point v_0 is invariantly foliated by stable submanifolds, as in Fig.S.39. Because the contraction along the stable submanifolds is much stronger than the dynamics along the center manifold, the fast subsystem can be mapped into the normal form $\dot{v} = q(u) + p(v - v_0)^2$ by a continuous change of variables.
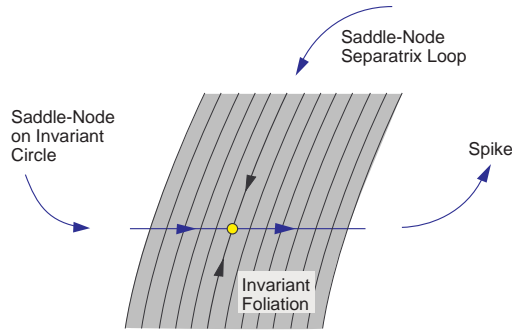
Figure S.39: A small neighborhood of the saddle-node point can be invariantly foliated by stable submanifolds.
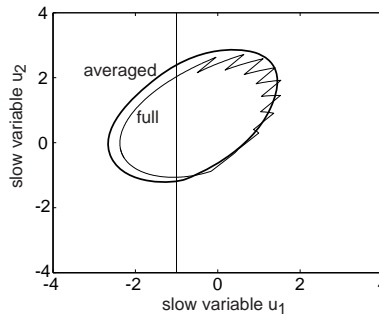
Figure S.40: exercise 18.

When v escapes the small neighborhood of v_0, the neuron is said to fire a spike, and v is reset to $v \leftarrow v_0 + c(u)$. Such a stereotypical spike also resets u by a constant d. If $g(v_0, u_0) \approx 0$, then all functions are small, and linearization and appropriate re-scaling yield the canonical model. If $g(v_0, u_0) \neq 0$, then the canonical model has the same form as in the previous exercise.

17. The derivation proceeds as in the previous exercise, yielding

$$\begin{aligned}
\dot{v} &= I + v^2 + (a, u) , \\
\dot{u} &= \mu A u .
\end{aligned}$$

where (a, u) is the scalar (dot) product of vectors $a, u \in \mathbb{R}^2$, and A is the Jacobian matrix at the equilibrium of the slow subsystem. If the equilibrium is a node, it generically has two distinct eigenvalues and two real eigenvectors. In this case, the slow subsystem uncouples into two equations, each along the corresponding eigenvector. Appropriate re-scaling gives the first canonical model. If the equilibrium is a focus, the linear part can be made triangular in order to get the second canonical model.

18. The solution of the fast subsystem

$$\dot{v} = u + v^2 , \qquad v(0) = -1 ,$$

with fixed $u > 0$ is

$$v(t) = \sqrt{u} \tan \left(\sqrt{u}\, t - \text{atan}\, \frac{1}{\sqrt{u}} \right) .$$

The interspike period, T, is defined by $v(T) = +\infty$, given by the formula

$$T(u) = \frac{1}{\sqrt{u}} \left(\frac{\pi}{2} + \text{atan}\, \frac{1}{\sqrt{u}} \right) .$$
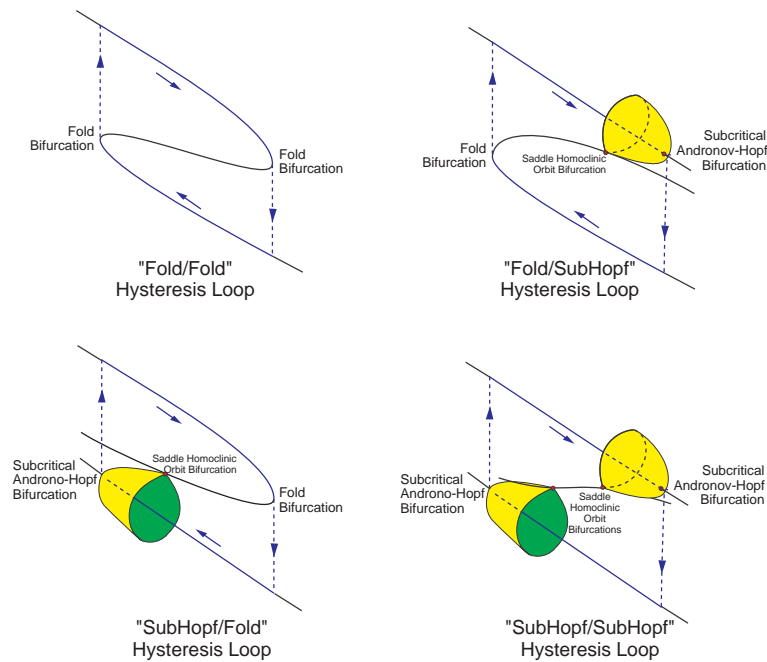
Figure S.41: Classification of point-point codimension-1 hysteresis loops.

The result follows from the integral

$$\frac{1}{T(u)} \int_0^{T(u)} d_i \, \delta(t - T(u)) \, dt = \frac{d_1}{T(u)}$$

and the relationships

$$f(u) = \frac{1}{T(u)} \qquad \text{and} \qquad \text{atan} \frac{1}{\sqrt{u}} = \text{arcot} \sqrt{u} \, .$$

Periodic solutions of the averaged system (focus case) and the full system are depicted in Fig.S.40. The deviation is due to the finite size of the parameters μ_1 and μ_2 in Fig.9.35.

19. There are only two codimension-1 bifurcations of an equilibrium that result in transitions to another equilibrium: saddle-node *off* limit cycle and subcritical Andronov-Hopf bifurcation. Hence, there are four point-point hysteresis loops, depicted in Fig.S.41. More details are provided in Izhikevich (2000a).

20. These figures are modified from Izhikevich (2000a), where one can find two models exhibiting this phenomenon. The key feature is that the slow subsystem is not too slow, and the rate of attraction to the upper equilibrium is relatively weak. The spikes are actually damped oscillations that are generated by the fast subsystem while it converges to the equilibrium. Periodic bursting is generated via the point-point hysteresis loop.

21. There are only two codimension-1 bifurcations of a small limit cycle attractor (subthreshold oscillation) on a plane that result in sharp transitions to a large-amplitude limit cycle attractor (spiking): fold limit cycle bifurcation and saddle-homoclinic orbit bifurcation; see Fig.S.42. These two bifurcations paired with any of the four bifurcations of the large-amplitude limit cycle attractor result in eight planar codimension-1 cycle-cycle bursters; see Fig.S.43. More details are provided by Izhikevich (2000a).
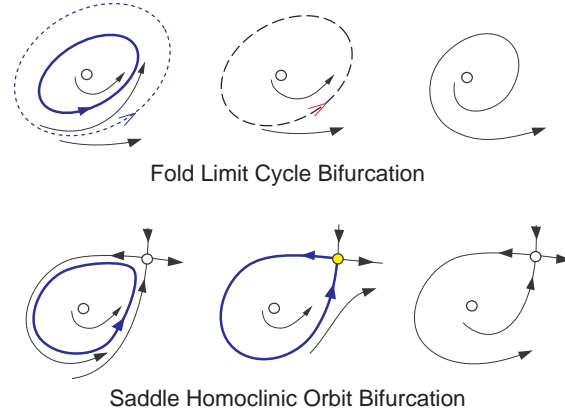
Figure S.42: Codimension-1 bifurcations of a stable limit cycle in planar systems that result in sharp loss of stability and transition to a large-amplitude (spiking) limit cycle attractor, not shown in the figure. Fold limit cycle: A stable limit cycle is approached by an unstable one, they coalesce, and then they disappear. Saddle homoclinic orbit: A limit cycle grows into a saddle. The unstable manifold of the saddle makes a loop and returns via the stable manifold (separatrix).

Bifurcations	*Saddle-Node on Invariant* **Circle**	*Saddle* **Homoclinic** *Orbit*	*Supercritical Andronov-* **Hopf**	**Fold** *Limit* **Cycle**
Fold *Limit* **Cycle**	fold cycle/ circle	fold cycle/ homoclinic	fold cycle/ Hopf	fold cycle/ fold cycle
Saddle **Homoclinic** *Orbit*	homoclinic/ circle	homoclinic/ homoclinic	homoclinic/ Hopf	homoclinic/ fold cycle

Figure S.43: Classification of codimension-1 cycle-cycle planar bursters.

References

Acebron J. A., Bonilla L. L., Vincente C. J. P., Ritort F., Spigler R. (2005) The Kuramoto model: A simple paradigm for synchronization phenomena. Review of Modern Physics, 77:137–185 .

Alonso A. and Klink R. (1993) Differential electroresponsiveness of stellate and pyramidal-like cells of medial entorhinal cortex layer II. Journal of Neurophysiology, 70:128–143.

Alonso A. and Llinas R. R. (1989) Subthreshold Na^+-dependent theta-like rhythmicity in stellate cells of entorhinal cortex layer II. Nature, 342:175–177.

Amini B., Clark J. W. Jr., and Canavier C. C. (1999) Calcium dynamics underlying pacemaker-like and burst firing oscillations in midbrain dopaminergic neurons: A computational study. Journal of Neurophysiology, 82:2249-2261.

Amir R., Michaelis M., and Devor M. (2002) Burst discharge in primary sensory neurons: Triggered by subthreshold oscillations, maintained by depolarizing afterpotentials. Journal of Neuroscience, 22:1187–1198.

Armstrong C. M. and Hille B. (1998) Voltage-gated ion channels and electrical excitability. Neuron 20:371–380.

Arnold V. I. (1965) Small denominators. I. Mappings of the circumference onto itself. Transactions of the AMS series 2, 46:213–284.

Arnold V. I., Afrajmovich V. S., Il'yashenko Yu. S., and Shil'nikov L.P. (1994) Dynamical Systems V. Bifurcation Theory and Catastrophe Theory. Berlin and New York: Springer-Verlag.

Aronson D. G., Ermentrout G. B., and Kopell N. (1990) Amplitude response of coupled oscillators. Physica D, 41:403–449.

Arshavsky Y. I., Berkinblit M. B., Kovalev S. A., Smolyaninov V. V., and Chaylakhyan L. M. (1971) An analysis of the functional properties of dendrites in relation to their structure, in: I. M. Gelfand, V.S. Gurfinkel, S.V. Fomin, M.L. Zetlin (Eds.), Models of the Structural and Functional Organization of Certain Biological Systems, pp. 25-71, Cambridge, Mass: MIT Press.

Bacci A., Rudolph U., Huguenard J. R., and Prince D.A. (2003a) Major differences in inhibitory synaptic transmission onto two neocortical interneuron subclasses. Journal of Neuroscience, 23:9664–9674.

Bacci A., Huguenard J. R., Prince D. A. (2003b) Long-lasting self-inhibition of neocortical interneurons mediated by endocannabinoids. Nature, 431:312–316.

Baer S. M., Erneux T., and Rinzel J. (1989) The slow passage through a Hopf bifurcation: Delay, memory effects, and resonances. SIAM Journal on Applied Mathematics, 49:55–71.

Baer S. M., Rinzel J., and Carrillo H. (1995) Analysis of an autonomous phase model for neuronal parabolic bursting. Journal of Mathematical Biology, 33:309–333.

Baesens C., Guckenheimer J., Kim S., and MacKay R. S. (1991) Three coupled oscillators: Mode-locking, global bifurcations and toroidal chaos. Physica D, 49:387–475.

Baker M. D. and Bostock H. (1997) Low-threshold, persistent sodium current in rat large dorsal root ganglion neurons in culture. Journal of Neurophysiology, 77:1503–1513.

Baker M. D. and Bostock H. (1998) Inactivation of macroscopic late Na^+ current and characteristics of unitary late Na^+ currents in sensory neurons. Journal of Neurophysiology, 80:2538–2549.

Bautin N. N. (1949) The behavior of dynamical systems near to the boundaries of stability. Gostekhizdat., Moscow-Leningrad, 2nd ed., Moscow: Nauka, (1984) [in Russian].

Beierlein M., Gibson J. R., and Connors B. W. (2003) Two dynamically distinct inhibitory networks in layer 4 of the neocortex. Journal of Neurophysiology, 90:2987–3000.

Bekkers J. M. (2000) Properties of voltage-gated potassium currents in nucleated patches from large layer 5 pyramidal neurons of the rat. Journal of Physiology, 525:593-609.

Benoit E. (1984) Canards de $\mathbb{R}^3$. These d'etat, Universite de Nice.

Benoit E., Callot J.-L., Diener F., and Diener M. (1981) Chasse au canards. Collectanea Mathematica, 31–32(1–3):37–119.

Bertram R., Butte M. J., Kiemel T., and Sherman A. (1995) Topological and phenomenological classification of bursting oscillations. Bulletin of Mathematical Biology 57:413–439.

Blechman I. I. (1971) Synchronization of Dynamical Systems. [in Russian: "Sinchronizatzia Dinamicheskich Sistem", Moscow:Nauka].

Bower J. M. and Beeman D. (1995) The Book of GENESIS. New York: Springer-Verlag.

Bressloff P. C. and Coombes S. (2000) Dynamics of strongly coupled spiking neurons. Neural Computation, 12:91–129.

Brizzi L., Meunier C., Zytnicki D., Donnet M., Hansel D., Lamotte d'Incamps B., and van Vreeswijk C. (2004) How shunting inhibition affects the discharge of lumbar motoneurons: a dynamic clamp study in anaesthetized cats. Journal of Physiology, 558:671–683.

Brown E., Moehlis J., and Holmes P. (2004) On the phase reduction and response dynamics of neural oscillator populations. Neural Computation, 16:673–715.

Brown T. G. (1911) The intrinsic factors in the act of progression in the mammal. Proceedings of Royal Society London B, 84:308-319.

Brunel N., Hakim V., and Richardson M. J. (2003) Firing-rate resonance in a generalized integrate-and-fire neuron with subthreshold resonance. Physical Review E, 67:051916.

Bryant H. L. and Segundo J. P. (1976) Spike initiation by transmembrane current: a white-noise analysis. Journal of Physiology, 260:279–314.

Butera R. J., Rinzel J., and Smith J. C. (1999) Models of respiratory rhythm generation in the pre-Botzinger complex. I. Bursting pacemaker neurons. Journal of Neurophysiology, 82: 382–397.

Canavier C. C., Clark J. W., and Byrne J. H. (1991) Simulation of the bursting activity of

neuron R15 in Aplysia: Role of ionic currents, calcium balance, and modulatory transmitters. Journal of Neurophysiology, 66:2107-2124.

Carnevale N. T. and Hines M. L. (2006) The NEURON Book. Cambridge: Cambridge University Press.

Cartwright M. L. and Littlewood J. E. (1945) On nonlinear differential equations of the second order: I. The equation $\ddot{y} - k(1 - y^2)\dot{y} + y = b\lambda k \cos(\lambda t + \alpha)$, k large. Journal of London Mathematical Society, 20:180–189.

del Castillo J. and Morales T. (1967) The electrical and mechanical activity of the esophageal cell of ascaris lumbricoides. The Journal of General Physiology, 50:603–629.

Chay T. R. and Cook D. L. (1988) Endogenous bursting patterns in excitable cells. Mathematical Biosciences, 90:139 –153.

Chay T. R. and Keizer J. (1983) Minimal model for membrane oscillations in the pancreatic β-cell. Biophysical Journal, 42:181-190.

Chow C. C. and Kopell N. (2000) Dynamics of spiking neurons with electrical coupling. Neural Computation, 12:1643-1678.

Chu Z., Galarreta M., and Hestrin S. (2003) Synaptic Interactions of Late-Spiking Neocortical Neurons in Layer 1, 23:96–102

Clay J. R. (1998) Excitability of the squid giant axon revisited. Journal of Neurophysiology, 80:903–913.

Cohen A. H., Holmes P. J., and Rand R. H. (1982) The nature of the coupling between segmental oscillators of the lamprey spinal generator for locomotion: A mathematical model. Journal of Mathematical Biology, 13:345–369.

Cole K. S., Guttman R., and Bezanilla F. (1970) Nerve excitation without threshold. Proceedings of the National Academy of Sciences, 65:884–891.

Collins J. J. and Stewart I. (1994) A group-theoretic approach to rings of coupled biological oscillators. Biological Cybernetics, 71:95-103.

Collins J. J. and Stewart I. (1993) Coupled nonlinear oscillators and the symmetries of animal gaits. Journal of Nonlinear Science,. 3:349–392.

Connor J. A., Walter D., and McKown R. (1977) Modifications of the Hodgkin-Huxley axon suggested by experimental results from crustacean axons. Biophysical Journal, 18:81–102.

Connors B. W. and Gutnick M. J. (1990) Intrinsic firing patterns of diverse neocortical neurons. Trends in Neuroscience, 13:99–104.

Coombes S. and Bressloff P. C. (2005) Bursting: The genesis of rhythm in the nervous system. World Scientific.

Daido H. (1996) Onset of cooperative entrainment in limit-cycle oscillators with uniform all-to-all interactions: Bifurcation of the order function. Physica D, 91:24–66.

Dayan P. and Abbott L.F. (2001) Theoretical Neuroscience. The MIT Press.

Del Negro C. A., Hsiao C.-F., Chandler S. H., and Garfinkel A. (1998) Evidence for a novel bursting mechanism in rodent trigeminal neurons. Biophysical Journal, 75:174–182.

Denjoy A. (1932) Sur les courbes definies par les equations differentielles a la surface du tore.

J. Math. Pures et Appl. 11:333-375.

Destexhe A. , Contreras D., Sejnowski T. J., and Steriade M. (1994) A model of spindle rhythmicity in the isolated thalamic reticular nucleus. Journal of Neurophysiology, 72:803–818.

Destexhe A. and Gaspard P. (1993) Bursting oscillations from a homoclinic tangency in a time delay system. Physics Letters A, 173:386–391.

Destexhe A., Rudolph M., Fellous J.M., and Sejnowski T.J. (2001) Fluctuating synaptic conductances recreate in vivo-like activity in neocortical neurons. Neuroscience, 107:13–24.

de Vries G. (1998) Multiple bifurcations in a polynomial model of bursting oscillations. Journal of Nonlinear Science, 8:281–316.

Dickson C. T., Magistretti J., Shalinsky M. H., Fransen E., Hasselmo M. E., and Alonso A. (2000) Properties and role of I_h in the pacing of subthreshold oscillations in entorhinal cortex layer II neurons. Journal of Neurophysiology, 83:2562–2579.

Doiron B., Laing C., Longtin A, and Maler L. (2002) Ghostbursting: A novel neuronal burst mechanism. Journal of Computational Neuroscience, 12:5–25.

Doiron B., Chacron M. J., Maler L., Longtin A., and Bastian J. (2003) Inhibitory feedback required for network oscillatory responses to communication but not prey stimuli. Nature, 421:539-543.

Dong C.-J. and Werblin F. S. (1995) Inwardly rectifying potassium conductance can accelerate the hyperpolarization response in retinal horizontal cells. Journal of Neurophysiology, 74:2258–2265

Eckhaus W. (1983) Relaxation oscillations including a standard chase of French ducks. Lecture Notes in Mathematics, 985:432–449.

Erisir A., Lau D., Rudy B., Leonard C. S. (1999) Function of specific K^+ channels in sustained high-frequency firing of fast-spiking neocortical interneurons. Journal of Neurophysiology, 82:2476–2489.

Ermentrout G. B. (1981) $n : m$ phase-locking of weakly coupled oscillators. Journal of Mathematical Biology, 12:327–342.

Ermentrout G. B. (1986) Losing amplitude and saving phase. In Othmer H. G., (ed.), Nonlinear Oscillations in Biology and Chemistry. Springer-Verlag.

Ermentrout G. B. (1992) Stable periodic solutions to discrete and continuum arrays of weakly coupled nonlinear oscillators. SIAM Journal on Applied Mathematics, 52:1665–1687.

Ermentrout G. B. (1994) An introduction to neural oscillators. In Neural Modeling and Neural Networks, F. Ventriglia, (ed.), Pergamon Press, Oxford, pp.79–110.

Ermentrout G. B. (1996) Type I membranes, phase resetting curves, and synchrony. Neural Computation, 8:979–1001.

Ermentrout G. B. (1998) Linearization of F-I curves by adaptation. Neural Computation, 10:1721–1729.

Ermentrout G. B. (2002) Simulating, Analyzing, and Animating Dynamical Systems: A Guide to XPPAUT for Researchers and Students (Software, Environments, Tools). SIAM.

Ermentrout G. B. (2003) Dynamical consequences of fast-rising, slow-decaying synapses in neu-

ronal networks. Neural Computation, 15:2483-2522

Ermentrout G. B. and Kopell N. (1984) Frequency plateaus in a chain of weakly coupled oscillators, I. SIAM Journal on Mathematical Analysis, 15:215–237.

Ermentrout G. B. and Kopell N. (1986a) Parabolic bursting in an excitable system coupled with a slow oscillation. SIAM Journal on Applied Mathematics 46:233–253.

Ermentrout G. B. and Kopell N. (1986b) Subcellular oscillations and bursting. Mathematical Biosciences, 78:265–291.

Ermentrout G. B. and Kopell N. (1990) Oscillator death in systems of coupled neural oscillators. SIAM Journal on Applied Mathematics, 50:125–146.

Ermentrout G. B. and Kopell N. (1991) Multiple pulse interactions and averaging in systems of coupled neural oscillators. Journal of Mathematical Biology, 29:195–217.

Ermentrout G. B. and Kopell N. (1994) Learning of phase lags in coupled neural oscillators. Neural Computation, 6:225–241.

FitzHugh R. (1955) Mathematical models of threshold phenomena in the nerve membrane. Bulletin of Mathematical Biophysics, 7:252–278.

FitzHugh R. (1960) Threshold and plateaus in the Hodgkin-Huxley nerve equations. The Journal of General Physiology. 43:867–896.

FitzHugh R. A. (1961) Impulses and physiological states in theoretical models of nerve membrane. Biophysical Journal, 1:445–466.

FitzHugh R. (1969) Mathematical models of excitation and propagation in nerve. In Schwan (ed.) Biological Engineering, New York: McGraw-Hill.

FitzHugh R. (1976) Anodal excitation in the Hodgkin-Huxley nerve model. Biophysical Journal, 16:209–226.

Fourcaud-Trocme N., Hansel D., van Vreeswijk C., and Brunel N. (2003) How spike generation mechanisms determine the neuronal response to fluctuating inputs. Journal of Neuroscience, 23:11628–11640.

Frankel P. and Kiemel T. (1993) Relative phase behavior of two slowly coupled oscillators. SIAM Journal on Applied Mathematics, 53:1436–1446.

Gabbiani F, Metzner W, Wessel R, and Koch C. (1996) From stimulus encoding to feature extraction in weakly electric fish. Nature. 384:564–567.

Geiger J. R. P. and Jonas P. (2000) Dynamic control of presynaptic Ca^{2+} inflow by fastiInactivating K^+ channels in hippocampal mossy fiber boutons. Neuron, 28:927–939.

Gerstner W. and Kistler W. M. (2002) Spiking Neuron Models: Single Neurons, Populations, Plasticity. Cambridge: Cambridge University Press.

Gibson J. R., Belerlein M., and Connors B. W. (1999) Two networks of electrically coupled inhibitory neurons in neocortex. Nature, 402:75–79.

Glass L. and MacKey M. C. (1988) From Clocks to Chaos. Princeton, N.J.: Princeton University Press.

Goel P. and Ermentrout B. (2002) Synchrony, stability, and firing patterns in pulse-coupled oscillators. Physica D, 163:191–216.

Golomb D., Yue C., and Yaari Y. (2006) Contribution of persistent Na$^+$ current and M-type K$^+$ current to somatic bursting in CA1 pyramidal cells: combined experimental and modeling study. J. Neurophys., 96:1912–1926.

Golubitsky M., Josic K. and Kaper T. J. (2001) An unfolding theory approach to bursting in fast-slow systems. In: *Global Analysis of Dynamical Systems: Festschrift Dedicated to Floris Takens on the Occasion of his 60th Birthday.* (H. W. Broer B. Krauskopf, and G. Vegter, eds.) Institute of Physics, 277–308.

Golubitsky M. and Stewart I. (2002) Patterns of oscillation in coupled cell systems. In: Geometry, Dynamics, and Mechanics: 60th Birthday Volume for J. E. Marsden. P. Newton, P. Holmes, and A. Weinstein, (eds.), Springer-Verlag, 243–286.

Gray C. M. and McCormick D. A. (1996) Chattering cells: Superficial pyramidal neurons contributing to the generation of synchronous oscillations in the visual cortex. Science. 274:109-113.

Grundfest H. (1971) Biophysics and Physiology of Excitable Membranes. W. J. Adelman (ed.), New York: Van Nostrand Reinhold.

Guckenheimer J. (1975) Isochrons and phaseless sets. Journal of Mathematical Biology, 1:259–273.

Guckenheimer J, Harris-Warrick R, Peck J, and Willms A. (1997) Bifurcation, bursting, and spike frequency adaptation. Journal of Computational Neuroscience, 4:257–277.

Guckenheimer J. and Holmes D. (1983) Nonlinear Oscillations, Dynamical Systems, and Bifurcations of Vector Fields. New York: Springer-Verlag.

Guevara M. R. and Glass L. (1982) Phase locking, periodic doubling bifurcations and chaos in a mathematical model of a periodically driven oscillator: a theory for the entrainment of biological oscillators and the generation of cardiac dysrhythmias. Journal of Mathematical Biology, 14:1–23.

Guttman R., Lewis S., and Rinzel J. (1980) Control of repetitive firing in squid axon membrane as a model for a neuroneoscillator. Journal of Physiology, 305:377–395.

Hansel D., Mato G., and Meunier C. (1995) Synchrony in excitatory neural networks. Neural Computations, 7:307–335.

Hansel D., Mato G., Meunier C., and Neltner L. (1998) On numerical simulations of integrate-and-fire neural networks. Neural Computation, 10:467–483.

Hansel D. and Mato G. (2003) Asynchronous states and the emergence of synchrony in large networks of interacting excitatory and inhibitory neurons. Neural Computation, 15:1–56.

Harris-Warrick R. M. and Flamm R. E. (1987) Multiple mechanisms of bursting in a conditional bursting neuron. Journal of Neuroscience, 7:2113–2128.

Hastings J. W. and Sweeney B. M. (1958) A persistent diurnal rhythms of luminescence in *Gonyaulax polyedra.* Biological Bulletin, 115:440–458.

Hausser M. and Mel B. (2003) Dendrites: bug or feature? Current Opinion in Neurobiology, 13:372–383.

Hausser M., Spruston N., and Stuart G. J. (2000) Diversity and dynamics of dendritic signaling. Science, 290:739–744.

Heyward P., Ennis M., Keller A., and Shipley M. T. (2001) Membrane bistability in olfactory bulb mitral cells. Journal of Neuroscience, 21:5311–5320.

Hille B. (2001) Ion Channels of Excitable Membranes. (3nd ed.) Sunderland, Mass: Sinauer.

Hindmarsh J. L. and Rose R. M. (1982) A model of the nerve impulse using two first-order differential equations. Nature 296:162–164.

Hines M. A. (1989) Program for simulation of nerve equations with branching geometries. International Journal of Biomedical Computing, 24:55–68.

Hodgkin A. L. (1948) The local electric changes associated with repetitive action in a non-medulated axon. Journal of Physiology, 107:165–181.

Hodgkin A. L. and Huxley A. F. (1952) A quantitative description of membrane current and application to conduction and excitation in nerve. Journal of Physiology, 117:500–544.

Holden L. and Erneux T. (1993a) Slow passage through a Hopf bifurcation: form oscillatory to steady state solutions. SIAM Journal on Applied Mathematics, 53:1045–1058.

Holden L. and Erneux T. (1993b) Understanding bursting oscillations as periodic slow passages through bifurcation and limit points. Journal of Mathematical Biology, 31:351–365.

Hopf E. (1942) Abzweigung einer periodischen Losung von einer stationaren Losung eines Differetialsystems. Ber. Math.-Phys. Kl. Sachs, Aca. Wiss. Leipzig, 94:1–22.

Hoppensteadt F. C. (1997) An Introduction to the Mathematics of Neurons. Modeling in the Frequency Domain. 2nd ed. Cambridge: Cambridge University Press.

Hoppensteadt F. C. (2000) Analysis and Simulations of Chaotic Systems. 2nd ed. New York: Springer-Verlag.

Hoppensteadt F. C. and Izhikevich E. M. (1996a) Synaptic organizations and dynamical properties of weakly connected neural oscillators: I. Analysis of canonical model. Biological Cybernetics, 75:117–127.

Hoppensteadt F. C. and Izhikevich E. M. (1996b) Synaptic organizations and dynamical properties of weakly connected neural oscillators. II. Learning of phase information. Biological Cybernetics, 75:129–135.

Hoppensteadt F. C. and Izhikevich E. M. (1997) Weakly Connected Neural Networks. New York: Springer-Verlag.

Hoppensteadt F. C. and Keener J. P. (1982) Phase locking of biological clocks. Journal of Mathematical Biology, 15:339–349.

Hoppensteadt F. C. and Peskin C. S.(2002) Modeling and Simulation in Medicine and the Life Sciences. 2nd ed. New York: Springer-Verlag.

Hughes S. W., Cope D. W., Toth T. L., Williams S. R., and Crunelli V. (1999) All thalamocortical neurones possess a T-type Ca^{2+} 'window' current that enables the expression of bistability-mediated activities. Journal of Physiology, 517:805–815.

Huguenard J. R. and McCormick D. A. (1992) Simulation of the currents involved in rhythmic oscillations in thalamic relay neurons. Journal of Neurophysiology, 68:1373–1383.

Hutcheon B., Miura R.M., and Puil E., (1996). Subthreshold membrane resonance in neocortical neurons. Journal of Neurophysiology, 76:683–697.

Izhikevich E. M. (1998) Phase models with explicit time delays. Physical Review E, 58:905–908.

Izhikevich E. M. (1999) Class 1 neural excitability, conventional synapses, weakly connected networks, and mathematical foundations of pulse-coupled models. IEEE Transactions On Neural Networks,10:499–507.

Izhikevich E. M. (1999) Weakly connected quasiperiodic oscillators, FM interactions, and multiplexing in the brain. SIAM Journal on Applied Mathematics, 59:2193–2223.

Izhikevich E. M. (2000a) Neural excitability, spiking, and bursting. International Journal of Bifurcation and Chaos, 10:1171–1266.

Izhikevich E. M. (2000b) Phase equations for relaxation oscillators. SIAM Journal on Applied Mathematics, 60:1789–1805.

Izhikevich E. M. (2001a) Resonate-and-fire neurons. Neural Networks, 14:883–894

Izhikevich E. M. (2001b) Synchronization of elliptic bursters. SIAM Review, 43:315–344.

Izhikevich E. M. (2002) Resonance and selective communication via bursts in neurons having subthreshold oscillations. BioSystems, 67:95–102.

Izhikevich E. M. (2003) Simple Model of Spiking Neurons. IEEE Transactions on Neural Networks, 14:1569–1572.

Izhikevich E. M. (2004) Which model to use for cortical spiking neurons? IEEE Transactions on Neural Networks, 15:1063–1070.

Izhikevich E. M. (2006) Bursting. Scholarpedia, 1(3):1300.

Izhikevich E. M., Desai N. S., Walcott E. C., and Hoppensteadt F. C. (2003) Bursts as a unit of neural information: selective communication via resonance . Trends in Neuroscience, 26:161–167.

Izhikevich E. M. and FitzHugh R. (2006) FitzHugh-Nagumo model. Scholarpedia, 1(9):1349.

Izhikevich E. M. and Hoppensteadt F. C. (2003) Slowly coupled oscillators: Phase dynamics and synchronization. SIAM Journal on Applied Mathematics, 63:1935–1953.

Izhikevich E. M. and Hoppensteadt F. C. (2004) Classification of bursting mappings. International Journal of Bifurcation and Chaos, 14:3847–3854.

Izhikevich E. M. and Kuramoto Y. (2006) Weakly coupled oscillators. Encyclopedia of Mathematical Physics, Elsevier, 5:448.

Jahnsen H. and Llinas R. (1984) Electrophysiological properties of guinea-pig thalamic neurons: An in vitro study. Journal of Physiology London, 349:205–226.

Jensen M. S., Azouz R., and Yaari Y. (1994) Variant firing patterns in rat hippocampal pyramidal cells modulated by extracellular potassium. Journal of Neurophysiology, 71:831–839.

Jian Z., Xing J.L., Yang G.S., and Hu S.J. (2004) A novel bursting mechanism of type A neurons in injured dorsal root ganglia. NeuroSignals, 13:150–156.

Johnson C. H. (1999) Forty years of PRC – what have we learned?. Chronobiology International, 16:711–743.

Johnston D. and Wu S. M. (1995) Foundations of Cellular Neurophysiology. Cambridge, Mass: MIT Press.

Katriel G. (2005) Stability of synchronized oscillations in networks of phase-oscillators. Discrete and Continuous Dynamical Systems-Series B, 5:353–364.

Kawaguchi Y. (1995) Physiological subgroups of nonpyramidal cells with specific morphological characteristics in layer II/III of rat frontal cortex. Journal of Neuroscience, 15:2638–2655.

Kawaguchi Y. and Kubota Y. (1997) GABAergic cell subtypes and their synaptic connections in rat frontal cortex. Cerebral Cortex, 7:476–486.

Kay A. R., Sugimori M., and Llinas R. (1998) Kinetic and stochastic properties of a persistent sodium current in mature guinea pig cerebellar Purkinje Cells. Journal of Neurophysiology, 80:1167–1179.

Keener J. and Sneyd J. (1998) Mathematical Physiology. New York: Springer-Verlag.

Kepler T. B., Abbott L. F., and Marder E. (1992) Reduction of conductance based neuron models. Biological Cybernetics, 66:381–387.

Kinard T. A., de Vries G., Sherman A., and Satin L. S. (1999) Modulation of the bursting properties of single mouse pancreatic beta-cells by artificial conductances. Biophysical Journal, 76:1423-35

Klink R. and Alonso A. (1993) Ionic Mechanisms for the subthreshold oscillations and differential electroresponsiveness of medial entorhinal cortex layer II neurons. Journal of Neurophysiology, 70:144–157.

Koch C. (1999) Biophysics of Computation: Information Processing in Single Neurons. New York: Oxford University Press.

Kopell N. (1986) Coupled oscillators and locomotion by fish. In Othmer H. G. (Ed.) Nonlinear Oscillations in Biology and Chemistry. Lecture Notes in Biomathematics, New York: Springer-Verlag.

Kopell N. (1995) Chains of coupled oscillators. In Arbib M. A. (Ed.) Brain Theory and Neural Networks, Cambridge, Mass: MIT press.

Kopell N. and Ermentrout G. B. (1990) Phase transitions and other phenomena in chains of coupled oscillators. SIAM Journal on Applied Mathematics 50:1014–1052.

Kopell N., Ermentrout G. B., Williams T. L. (1991) On chains of oscillators forced at one end. SIAM Journal on Applied Mathematics, 51:1397–1417.

Kopell N. and Somers D. (1995) Anti-phase solutions in relaxation oscillators coupled through excitatory interactions. Journal of Mathematical Biology, 33:261–280.

Korngreen A. and Sakmann B. (2000) Voltage-gated K^+ channels in layer 5 neocortical pyramidal neurones from young rats: Subtypes and gradients. Journal of Physiology, 525.3:621–639.

Krinskii V.I. and Kokoz Yu.M. (1973) Analysis of equations of excitable membranes - I. Reduction of the Hodgkin-Huxley equations to a second order system. Biofizika, 18:506–511.

Kuramoto Y. (1975) in H. Araki (Ed.) International Symposium on Mathematical Problems in Theoretical Physics, Lecture Notes in Physics, 39:420–422, New York: Springer-Verlag.

Kuramoto Y. (1984) Chemical Oscillations, Waves, and Turbulence. New York: Springer-Verlag.

Kuznetsov Yu. (1995) Elements of Applied Bifurcation Theory. New York: Springer-Verlag.

Lapicque L. (1907) Recherches quantitatives sur l'excitation electrique des nerfs traitee comme

une polarization. J Physiol Pathol Gen 9:620-635.

Latham P. E., Richmond B. J., Nelson P. G., and Nirenberg S. (2000) Intrinsic dynamics in neuronal networks. I. Theory. Journal of Neurophysiology, 83:808–27.

Lesica N. A and Stanley G. B. (2004) Encoding of natural scene movies by tonic and burst spikes in the lateral geniculate nucleus. Journal of Neuroscience, 24:10731–10740.

Levitan E. S., Kramer R. H., and Levitan I. B. (1987) Augmentation of bursting pacemaker activity by egg-laying hormone in Aplysia neuron R15 is mediated by a cyclic AMP-dependent increase in Ca2+ and K+ currents. Proceedings of National Academy of Sciences. 84 :6307–6311.

Levitan E. S. and Livitan I. B. (1988) A cyclic GMP analog decreases the currents underlying bursting activity in the Aplysia neuron R15. Journal of Neuroscience, 8:1162–1171.

Li J., Bickford M. E., and Guido W. (2003) Distinct firing properties of higher order thalamic relay neurons. Journal of Neurophysiology, 90: 291–299.

Lienard A. (1928) Etude des oscillations entretenues, Rev. Gen. Elec. 23:901–954.

Lisman J. (1997) Bursts as a unit of neural information: making unreliable synapses reliable. Trends in Neuroscience, 20:38–43.

Lopatin A. N., Makhina E. N., and Nichols C. G. (1994) Potassium channel block by cytoplasmic polyamines as the mechanism of intrinsic rectification. Nature, 373:366–369.

Luk W. K. and Aihara K. (2000) Synchronization and sensitivity enhancement of the Hodgkin-Huxley neurons due to inhibitory inputs. Biological Cybernetics, 82:455–467.

Magee J. C. (1998) Dendritic hyperpolarization-activated currents modify the integrative properties of hippocampal CA1 pyramidal neurons. Journal of Neuroscience, 18:7613–7624.

Magee J. C. and Carruth M. (1999) Dendritic voltage-gated ion channels regulate the action potential firing mode of hippocampal CA1 pyramidal neurons. Journal of Neurophysiology, 82:1895–1901.

Magistretti J. and Alonso A. (1999) Biophysical properties and slow voltage- dependent Inactivation of a sustained sodium current in entorhinal cortex layer-II principal neurons. Journal of General Physiology, 114:491–509.

Mainen Z. F. and Sejnowski T. J. (1995) Reliability of spike timing in neocortical neurons. Science, 268:1503–1506.

Mainen Z. F. and Sejnowski T. J. (1996) Influence of dendritic structure on firing pattern in model neocortical neurons. Nature, 382:363–366.

Malkin I. G. (1949) Methods of Poincare and Liapunov in theory of non-linear oscillations. [in Russian: "Metodi Puankare i Liapunova v teorii nelineinix kolebanii" Moscow: Gostexizdat].

Malkin I. G. (1956) Some Problems in Nonlinear Oscillation Theory. [in Russian: "Nekotorye zadachi teorii nelineinix kolebanii" Moscow: Gostexizdat].

Marder E. and Bucher D. (2001) Central pattern generators and the control of rhythmic movements. Current Biology, 11:986–996.

Markram H, Toledo-Rodriguez M, Wang Y, Gupta A, Silberberg G, and Wu C. (2004) Interneurons of the neocortical inhibitory system. Nature Review Neuroscience, 5:793–807

Medvedev G. (2005) Reduction of a model of an excitable cell to a one-dimensional map. Physica D, 202:37–59.

McCormick D. A. (2004) Membrane properties and neurotransmitter actions, in Shepherd G.M. The Synaptic Organization of the Brain. 5th ed. New York: Oxford University Press.

McCormick D. A. and Huguenard J. R. (1992) A Model of the electrophysiological properties of thalamocortical relay neurons. Journal of Neurophysiology, 68:1384–1400.

McCormick D. A. and Pape H.-C. (1990) Properties of a hyperpolarization-activated cation current and its role in rhythmic oscillation in thalamic relay neurones. Journal of Physiology, 431:291–318.

Melnikov V. K. (1963) On the stability of the center for time periodic perturbations. Transactions of Moscow Mathematical Society, 12:1–57.

Mines, G. R. (1914) On circulating excitations on heart muscles and their possible relation to tachycardia and fibrillation. Transactions of Royal Society Canada, 4:43–53.

Mirollo R. E. and Strogatz S. H. (1990) Synchronization of pulse-coupled biological oscillators. SIAM Journal on Applied Mathematics, 50:1645–1662.

Mishchenko E. F., Kolesov Yu. S., Kolesov A. Yu., and Rozov N. K. (1994) Asymptotic Methods in Singularly Perturbed Systems. New York and London: Consultants Bureau.

Morris C. and Lecar H. (1981) Voltage oscillations in the barnacle giant muscle fiber. Biophysical Journal, 35:193–213.

Murray J. D. (1993). Mathematical Biology. New York: Springer-Verlag.

Nagumo J., Arimoto S., and Yoshizawa S. (1962) An active pulse transmission line simulating nerve axon. Proc. IRE. 50:2061–2070.

Nejshtadt A. (1985) Asymptotic investigation of the loss of stability by an equilibrium as a pair of eigenvalues slowly crosses the imaginary axis. Usp. Mat. Nauk 40:190–191.

Neu J. C. (1979) Coupled chemical oscillators. SIAM Journal of Applied Mathematics, 37:307–315.

Nisenbaum E. S., Xu Z. C., and Wilson C. J. (1994) Contribution of a slowly inactivating potassium current to the transition to firing of neostriatal spiny projection neurons. Journal of Neurophysiology, 71:1174–1189.

Noble D. (1966) Applications of Hodgkin-Huxley equations to excitable tissues. Physiological Review, 46:1–50.

Nowak L. G., Azouz R., Sanchez-Vives M. V., Gray C. M., and McCormick D. A. (2003) Electrophysiological classes of cat primary visual cortical neurons in vivo as revealed by quantitative analyses. Journal of Neurophysiology, 89: 1541–1566.

Oswald A. M., Chacron M. J., Doiron B., Bastian J., and Maler L. (2004) Parallel processing of sensory input by bursts and isolated spikes. Journal of Neuroscience, 24:4351–62.

Pape H.-C., and McCormick D. A. (1995) Electrophysiological and pharmacological properties of interneurons in the cat dorsal lateral geniculate nucleus. Neuroscience, 68: 1105–1125.

Parri H. R. and Crunelli V. (1998) Sodium current in rat and cat thalamocortical neurons: Role of a non-inactivating component in tonic and burst firing, Journal of Neuroscience,

18:854–867.

Pedroarena C. and Llinas R. (1997) Dendritic calcium conductances generate high frequency oscillation in thalamocortical neurons. Proceedings of the National Academy of Sciences, 94:724–728.

Perko L. (1996) Differential Equations and Dynamical Systems, New York: Springer-Verlag.

Pernarowski M. (1994) Fast subsystem bifurcations in a slowly varied Lienard system exhibiting bursting. SIAM Journal on Applied Mathematics, 54:814–832.

Pernarowski M., Miura R. M., and Kevorkian J. (1992) Perturbation techniques for models of bursting electrical activity in pancreatic β-cells. SIAM Journal on Applied Mathematics, 52:1627–1650.

Pfeuty B., Mato G., Golomb D., Hansel D. (2003) Electrical synapses and synchrony: The role of intrinsic currents. Journal of Neuroscience, 23:6280–6294.

Pikovsky A., Rosenblum M., Kurths J. (2001) Synchronization: A Universal Concept in Nonlinear Science. Cambridge: Cambridge University Press.

Pinsky P. and Rinzel J. (1994) Intrinsic and network rhythmogenesis in a reduced Traub model of CA3 neurons. Journal of Computational Neuroscience, 1:39–60.

Pirchio M., Turner J. P., Williams S. R., Asprodini E., and Crunelli V. (1997) Postnatal development of membrane properties and delta oscillations in thalamocortical neurons of the cat dorsal lateral geniculate nucleus. Journal of Neuroscience, 17 :5428–5444.

Plant R. E. (1981) Bifurcation and resonance in a model for bursting nerve cells. Journal of Mathematical Biology, 11:15–32.

Pontryagin L. S. and Rodygin L. V. (1960) Periodic solution of a system of ordinary differential equations with a small parameter in the terms containing derivatives Sov. Math. Dokl. 1: 611–614.

Rall W. (1959) Branching dendritic trees and motoneuron membrane resistivity. Experimental Neurology, 1:491–527.

Reinagel P, Godwin D, Sherman S. M., and Koch C. (1999) Encoding of visual information by LGN bursts. Journal of Neurophysiology, 81:2558–2569.

Reuben J. P., Werman R., and Grundfest H. (1961) The ionic mechanisms of hyperpolarizing responses in lobster muscle fibers. Journal of General Physiology, 45:243–265.

Reyes A. D. and Fetz E. E. (1993) Two modes of interspike interval shortening by brief transient depolarizations in cat neocortical neurons. Journal of Neurophysiology, 69: 1661–1672.

Richardson, M. J. E., Brunel, N. and Hakim, V. (2003) From subthreshold to firing-rate resonance. Journal of Neurophysiology, 89:2538–2554.

Rinzel J. and Ermentrout G. B. (1989) Analysis of neural excitability and oscillations. In Koch C., Segev I. (eds) Methods in Neuronal Modeling, Cambridge, Mass: MIT Press.

Rinzel J. (1978) On repetitive activity in nerve. Federation Proceedings, 37:2793–2802.

Rinzel J. (1985) Bursting oscillations in an excitable membrane model. In: Sleeman B. D., Jarvis R. J., (Eds.) *Ordinary and Partial Differential Equations Proceedings of the 8th Dundee Conference*, Lecture Notes in Mathematics, 1151. Berlin: Springer, 304–316.

Rinzel J. (1987) A formal classification of bursting mechanisms in excitable systems. In: E. Teramoto, M. Yamaguti, eds. Mathematical Topics in Population Biology, Morphogenesis, and Neurosciences, vol. 71 of Lecture Notes in Biomathematics, Berlin: Springer-Verlag.

Rinzel J. and Lee Y.S. (1986) On different mechanisms for membrane potential bursting. In Othmer H.G. (Ed) Nonlinear Oscillations in Biology and Chemistry. Lecture Notes in Biomathematics, no. 66, Berlin and New York: Springer-Verlag.

Rinzel J. and Lee Y. S. (1987) Dissection of a model for neuronal parabolic bursting. Journal of Mathematical Biology, 25:653–675.

Robbins J., Trouslard J., Marsh S. J., and Brown D. A. (1992) Kinetic and pharmacological properties of the M-current in rodent neuroblastoma $\times$ glioma hybrid cells, Journal of Physiology, 451:159–185.

Rosenblum M. G. and Pikovsky A. S. (2001) Detecting direction of coupling in interacting oscillators. Physical Review E, 64, p. 045202.

Roy J. P., Clercq M., Steriade M., and Deschenes M. (1984) Electrophysiology of neurons of lateral thalamic nuclei in cat: mechanisms of long-lasting hyperpolarizations. Journal of Neurophysiology, 51:1220–1235.

Rubin J. and Terman D. (2000) Analysis of clustered firing patterns in synaptically coupled networks of oscillators. Journal of Mathematical Biology, 41:513–545.

Rubin J. and Terman D. (2002) Geometric singular perturbation analysis of neuronal dynamics. Handbook of Dynamical systems, vol. 2: Toward Applications (B. Fiedler and G. Iooss, eds.) Amsterdam: Elsevier.

Rush M. E. and Rinzel J. (1995) The potassium A-Current, low firing rates and rebound excitation in Hodgkin-Huxley models. Bulletin of Mathematical Biology, 57:899–929.

Rush M. E. and Rinzel J. (1994) Analysis of bursting in a thalamic neuron model. Biological Cybernetics, 71:281–291.

Samborskij S. N. (1985) Limit trajectories of singularly perturbed differential equations. Dokl. Akad. Nauk Ukr. SSR., A, 9:22–25.

Sanabria E. R. G., Su H., and Yaari Y. (2001) Initiation of network bursts by Ca^{2+}-dependent intrinsic bursting in the rat pilocarpine model of temporal lobe epilepsy. Journal of Physiology, 532:205–216.

Sharp A. A., O'Neil M. B., Abbott L. F., Marder E. (1993) Dynamic clamp: computer-generated conductances in real neurons. Journal of Neurophysiology, 69:992–995.

Shepherd G. M. (2004) The Synaptic Organization of the Brain. 5th ed. New York: Oxford University Press.

Sherman S. M. (2001) Tonic and burst firing: Dual modes of thalamocortical relay. Trends in Neuroscience, 24:122–126.

Shilnikov A. L., Calabrese R., and Cymbalyuk G. (2005) Mechanism of bi-stability: Tonic spiking and bursting in a neuron model. Physics Review E, 71, 056214.

Shilnikov A. L. and Cymbalyuk G. (2005) Transition between tonic spiking and bursting in a neuron model via the blue-sky catastrophe. Physical Review Letters, 94, 048101.

Shilnikov A. L. and Cymbalyuk G (2004) Homoclinic bifurcations of periodic orbits en a route

from tonic spiking to bursting in neuron models. Regular and Chaotic Dynamics, vol. 9, [2004-11-19]

Shilnikov L. P., Shilnikov A. L., Turaev D., Chua L. O. (2001) Methods of qualitative theory in nonlinear dynamics. Part II, Singapore: World Scientific.

Shilnikov L. P., Shilnikov A. L., Turaev D., Chua L.O. (1998) Methods of qualitative theory in nonlinear dynamics. Part I, Singapore: World Scientific.

Shilnikov, A. L. and Shilnikov, L. P, (1995) Dangerous and safe stability boundaries of equilibria and periodic orbits" in NDES'95, University College Dublin, Ireland, 55-63.

Shishkova M. A. (1973) Investigation of a system of differential equations with a small parameter in highest derivatives. Dokl. Adad. Nauk SSSR 209. No.3, 576–579. English transl. Sov. Math., Dokl. 14,483–487

Skinner F. K., Kopell N., Marder E. (1994) Mechanisms for oscillation and frequency control in reciprocal inhibitory model neural networks. Journal of Computational Neuroscience, 1:69–87.

Smolen P., Terman D., and Rinzel J. (1993) Properties of a bursting model with two slow inhibitory variables. SIAM Journal on Applied Mathematics, 53:861–892.

Somers D. and Kopell N. (1993) Rapid synchronization through fast threshold modulation. Biological Cybernetics, 68:393–407.

Somers D. and Kopell N. (1995) Waves and synchrony in networks of oscillators or relaxation and non-relaxation type. Physica D, 89:169–183.

Stanford I. M., Traub R. D., and Jefferys J. G. R. (1998) Limbic gamma rhythms. II. Synaptic and intrinsic mechanisms underlying spike doublets in oscillating subicular neurons. Journal of Neurophysiology, 80:162–171.

Stein R.B. (1967) Some models of neuronal variability. Biophysical Journal, 7: 37–68.

Steriade M. (2003) Neuronal Substrates of Sleep and Epilepsy. Cambridge: Cambridge University Press.

Steriade M. (2004) Neocortical cell classes are flexible entities. Nature Reviews Neuroscience, 5:121–134.

Strogatz S. H. (1994) Nonlinear Dynamics and Chaos. Readings, Mass: Addison-Wesley.

Strogatz S. H. (2000) From Kuramoto to Crawford: Exploring the onset of synchronization in populations of coupled oscillators. Physica D, 143:1–20.

Stuart G., Spruston N., Hausser M. (1999) Dendrites. New York: Oxford University Press.

Su H, Alroy G, Kirson ED, and Yaari Y. (2001) Extracellular calcium modulates persistent sodium current-dependent burst-firing in hippocampal pyramidal neurons. Journal of Neuroscience, 21:4173–4182.

Szmolyan P. and Wechselberger M. (2001) Canards in $\mathbb{R}^3$. Journal of Differential Equations, 177:419–453.

Szmolyan P. and Wechselberger M. (2004) Relaxation oscillations in $\mathbb{R}^3$. Journal of Differential Equations, 200:69–104.

Tateno T., Harsch A., and Robinson H. P. C. (2004) Threshold firing frequency-current rela-

tionships of neurons in rat somatosensor cortex: type 1 and type 2 dynamics. Journal of Neurophysiology 92:2283–2294.

Tennigkeit F., Ries C.R., Schwarz D.W.F., and Puil E. (1997) Isoflurane attenuates resonant responses of auditory thalamic neurons. Journal Neurophysiology, 78:591–596.

Terman D. (1991) Chaotic spikes arising from a model of bursting in excitable membranes. SIAM Journal on Applied Mathematics, 51:1418–1450.

Timofeev I., Grenier F., Bazhenov M., Sejnowski T. J. and Steriade M. (2000) Origin of slow cortical oscillations in deafferented cortical slabs. Cerebral Cortex, 10:1185–1199.

Toledo-Rodriguez M., Blumenfeld B., Wu C., Luo J, Attali B., Goodman P., and Markram H. (2004) Correlation maps allow neuronal electrical properties to be predicted from single-cell gene expression profiles in rat neocortex. Cerebral Cortex, 14:1310–1327.

Traub R. D., Wong R. K., Miles R., and Michelson H. (1991) A model of a CA3 hippocampal pyramidal neuron incorporating voltage-clamp data on intrinsic conductances. Journal of Neurophysiology, 66:635–650.

Tuckwell H. C. (1988) Introduction to Theoretical Neurobiology. Cambridge: Cambridge University Press.

Uhlenbeck G.E. and Ornstein L.S. (1930) On the theory of the Brownian motion. Physical Review, 36:823–841.

Van Hemmen J. L. and Wreszinski W. F. (1993) Lyapunov function for the Kuramoto model of nonlinearly coupled oscillators. Journal of Statistical Physics, 72:145–166.

van Vreeswijk C. (2000) Analysis of the asynchronous state in networks of strongly coupled oscillators. Physical Review Letters, 84:5110–5113.

van Vreeswijk C., Abbott L. F., Ermentrout G. B. (1994) When inhibition not excitation synchronizes neural firing. Journal of Computational Neuroscience, 1:313–321.

van Vreeswijk C. and Hansel D. (2001) Patterns of synchrony in neural networks with spike adaptation. Neural Computation, 13:959–992.

Wang X.-J. (1999) Fast burst firing and short-term synaptic plasticity: a model of neocortical chattering neurons. Neuroscience, 89:347–362.

Wang X.-J. and Rinzel J. (1992) Alternating and synchronous rhythms in reciprocally inhibitory model neurons. Neural Computation, 4:84–97.

Wang X.-J. and Rinzel, J. (1995) Oscillatory and bursting properties of neurons, In Brain Theory and Neural Networks. Ed. Arbib, M. A. Cambridge, Mass: MIT press.

Wechselberger M. (2005) Existence and bifurcation of Canards in $\mathbb{R}^3$ in the case of a folded node. SIAM Journal on Applied Dynamical Systems, 4:101–139.

Wessel R., Kristan W.B., and Kleinfeld D. (1999) Supralinear summation of synaptic inputs by an invertebrate neuron: Dendritic gain is mediated by an "inward rectifier" K^+ current. Journal of Neuroscience, 19:5875–5888.

White J. A., Rubinstein J. T., and Kay A. R. (2000) Channel noise in neurons. Trends in Neuroscience, 23:131–137.

Williams J. T., North R. A., and Tokimasa T. (1988) Inward rectification of resting and opiate-

activated potassium currents in rat locus coeruleus neurons. Journal of Neuroscience, 8:4299–4306.

Williams S. R. and Stuart G. J. (2003) Role of dendritic synapse location in the control of action potential. Trends in Neuroscience, 26:147–154.

Willms A. R., Baro D. J., Harris-Warrick R. M., and Guckenheimer J. (1999) An improved parameter estimation method for Hodgkin-Huxley models, Journal of Computational Neuroscience, 6:145–168.

Wilson C. J. (1993) The generation of natural firing patterns in neostriatal neurons. In Progress in Brain Research. Arbuthnott G. and Emson P. C. (eds), 277–297, Amsterdam: Elsevier.

Wilson C. J. and Groves P. M. (1981) Spontaneous firing patterns of identified spiny neurons in the rat neostriatum. Brain Research, 220:67–80.

Wilson H. R. (1999) Spikes, Decisions, and Actions: The dynamical Foundations of Neuroscience. New York: Oxford University Press.

Wilson H. R. and Cowan J. D. (1972) Excitatory and inhibitory interaction in localized populations of model neurons. Biophys J 12:1–24.

Wilson H. R. and Cowan J. D. (1973) A Mathematical theory of the functional dynamics of cortical and thalamic nervous tissue. Kybernetik, 13:55–80.

Winfree A. (1967) Biological rhythms and the behavior of populations of coupled oscillators. Journal of Theoretical Biology, 16:15–42.

Winfree A. (1974) Patterns of phase compromise in biological cycles. Journal of Mathematical Biology, 1:73–95.

Winfree A. (2001) The Geometry of Biological Time. 2nd ed. New York: Springer-Verlag.

Wolfram S. (2002) A New Kind of Science. Wolfram Media.

Wu N., Hsiao C.-F., Chandler S. (2001) Membrane resonance and subthreshold membrane oscillations in mesencephalic V neurons: participants in burst generation. Journal of Neuroscience, 21:3729–3739.

Young G. (1937) Psychometrika, 2:103.

Yuan A., Dourado M., Butler A., Walton N., Wei A., Salkoff L. (2000) SLO-2, a K^+ channel with an unusual Cl^- dependence. Nature Neuroscience, 3:771–779.

Yuan A., Santi C. M., Wei A., Wang Z. W., Pollak K., Nonet M., Kaczmarek L., Crowder C. M., and Salkoff L. (2003) The sodium-activated potassium channel is encoded by a member of the SLO gene family. Neuron. 37:765–773.

Yue C., Remy S., Su H., Beck H., and Yaari Y. (2005) Proximal persistent Na^+ channels drive spike afterdepolarizations and associated bursting in adult CA1 pyramidal cells. Journal of Neuroscience, 25:9704–9720.

Yue C. and Yaari Y. (2004) KCNQ/M channels control spike afterdepolarization and burst generation in hippocampal neurons. Journal of Neuroscience, 24:4614–4624.

Zhan X. J., Cox C. L., Rinzel J., and Sherman S. M. (1999) Current clamp and modeling studies of low-threshold calcium spikes in cells of the cat's lateral geniculate nucleus. Journal of Neurophysiology, 81:2360–2373.

Chapter 10

Synchronization (www.izhikevich.com)

This chapter is available at www.izhikevich.com. It supplements the book by Izhikevich E. M. (2007) *Dynamical Systems in Neuroscience: The Geometry of Excitability and Bursting*, Cambridge, Mass: MIT Press. The author's Web site also contains MATLAB programs and in vitro data used in the book. To cite this chapter, write (Izhikevich 2007, Chapter 10) in your papers (i.e., as if it were a printed part of the book).

In this chapter we consider networks of tonically spiking neurons. Like any other kind of physical, chemical, or biological oscillators, such neurons can synchronize and exhibit collective behavior that is not intrinsic to any individual neuron. For example, partial synchrony in cortical networks is believed to generate various brain oscillations, such as the alpha and gamma EEG rhythms. Increased synchrony may result in pathological types of activity, such as epilepsy. Coordinated synchrony is needed for locomotion and swim pattern generation in fish. There is an ongoing debate on the role of synchrony in neural computation, see e.g., the special issue of *Neuron* (September 1999) devoted to the binding problem.

Depending on the circumstances, synchrony can be good or bad, and it is important to know what factors contribute to synchrony and how to control it. This is the subject of the present chapter – the most advanced chapter of the book. It provides a nice application of the theory developed earlier and hopefully gives some insight into why the previous chapters may be worth mastering.

Our goal is to understand how the behavior of two coupled neurons depends on their intrinsic dynamics. First, we introduce the method of description of an oscillation by its phase. Then, we describe various methods of reduction of coupled oscillators to simple phase models. The reduction method and the exact form of the phase model depend on the type of coupling (i.e., whether it is pulsed, weak, or slow) and on the type of bifurcation of the limit cycle attractor generating tonic spiking. Finally, we show how to use phase models to understand the collective dynamics of many coupled
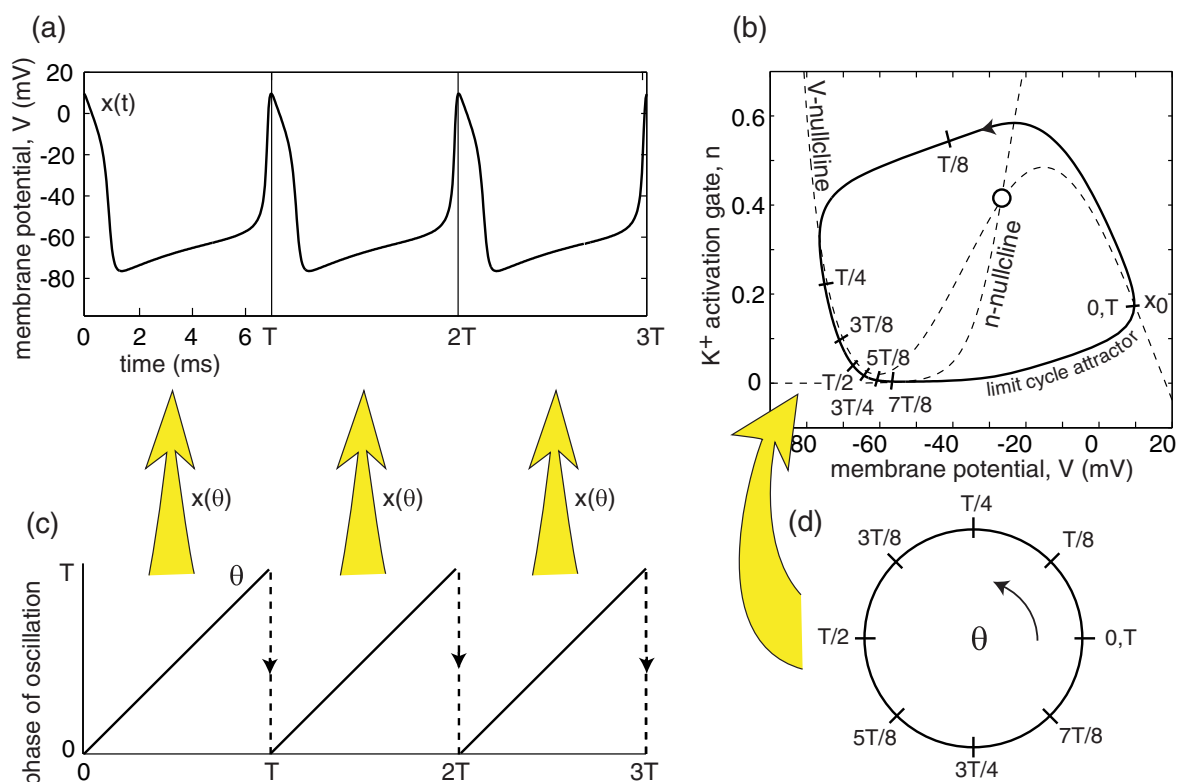
Figure 10.1: Definition of a phase of oscillation, ϑ, in the $I_{\text{Na}} + I_{\text{K}}$-model with parameters as in Fig.4.1a and $I = 10$.

oscillators.

10.1   Pulsed Coupling

In this section we consider oscillators of the form

$$\dot{x} = f(x) + A\delta(t - t_{\text{s}})\,, \qquad x \in \mathbb{R}^m, \qquad (10.1)$$

having exponentially stable limit cycles and experiencing pulsed stimulation at times t_{s} that instantaneously increases the state variable by the constant A. The Dirac delta function $\delta(t)$ is a mathematical shorthand notation for resetting x by A. The strength of pulsed stimulation, A, is not assumed to be small. Most of the results of this section can also be applied to the case in which the action of the input pulse is not instantaneous, but smeared over an interval of time, typically shorter than the period of oscillation.

10.1.1   Phase of Oscillation

Many types of physical, chemical, and biological oscillators share an astonishing feature: they can be described by a single phase variable ϑ. In the context of tonic spiking, the

phase is usually taken to be the time since the last spike, as in Fig.10.1a.

We say that a function $x(t)$ is periodic if there is a constant $T > 0$ such that $x(t + T) = x(t)$ for any t. The minimal value of the constant is the period of $x(t)$. Periodic functions appear in dynamical systems having limit cycle attractors.

The notion of the phase of oscillation is related to the notion of parametrization of a limit cycle attractor, as in Fig.10.1b. Take a point x_0 on the attractor and plot the trajectory $x(t)$ with $x(0) = x_0$. Then the phase of $x(t)$ is $\vartheta = t$. As t increases past the period T, then $2T$, an so on, the phase variable ϑ wraps around the interval $[0, T]$, jumping from T to 0; see Fig.10.1c. Gluing together the points 0 and T, as in Fig.10.1d, we can treat the interval $[0, T]$ as a circle, denoted as $\mathbb{S}^1$, with circumference T. The parametrization is the mapping of $\mathbb{S}^1$ in Fig.10.1d into the phase space $\mathbb{R}^2$ in Fig.10.1b, given by $\vartheta \mapsto x(\vartheta)$.

We could put the initial point x_0 corresponding to the zero phase anywhere else on the limit cycle, and not necessarily at the peak of the spike. The choice of the initial point introduces an ambiguity in parameterizing the phase of oscillation. Different parametrizations, however, are equivalent up to a constant phase shift (i.e., translation in time). In the rest of the chapter, ϑ always denotes the phase of oscillation, the parameter T denotes the period of oscillation, and $\vartheta = 0$ corresponds to the peak of the spike unless stated otherwise. If the system has two or more coexisting limit cycle attractors, then a separate phase variable needs to be defined for each attractor.

10.1.2   Isochrons

The phase of oscillation can also be introduced outside the limit cycle. Consider, for example, point y_0 in Fig.10.2 (top). Since the trajectory $y(t)$ is not on a limit cycle, it is not periodic. However, it approaches the cycle as $t \to +\infty$. Hence, there is some point x_0 on the limit cycle, not necessarily the closest to y_0, such that

$$y(t) \to x(t) \quad \text{as} \quad t \to +\infty . \tag{10.2}$$

Now take the phase of the nonperiodic solution $y(t)$ to be the phase of its periodic proxy $x(t)$.

Alternatively, we can consider a point on the limit cycle x_0 and find all the other points y_0 that satisfy (10.2). The set of all such points is called *the stable manifold* of x_0. Since any solution starting on the stable manifold has an asymptotic behavior indistinguishable from that of $x(t)$, its phase is the same as that of $x(t)$. For this reason, the manifold represents solutions having equal phases, and it is often referred to as being the *isochron* of x_0 (*iso*, equal; *chronos*, time, in Greek), a notion going back to Bernoulli and Leibniz.

Every point on the plane in Fig.10.2, except the unstable equilibrium, gives rise to a trajectory that approaches the limit cycle. Therefore, every point has some phase. Let $\vartheta(x)$ denote the phase of the point x. Then, isochrons are level contours of the function $\vartheta(x)$, since the function is constant on each isochron.
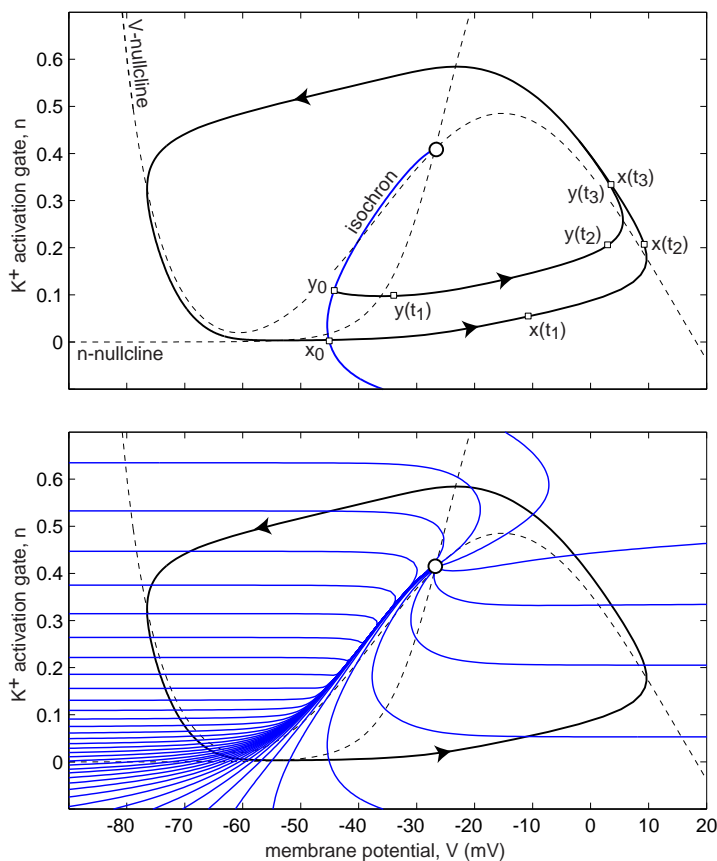
Figure 10.2: Top. An isochron, or a stable manifold, of a point x_0 on the limit cycle attractor is the set of all initial conditions y_0 such that $y(t) \rightarrow x(t)$ as $t \rightarrow +\infty$. Bottom. Isochrons of the limit cycle attractor in Fig.10.1 corresponding to 40 evenly distributed phases $nT/40$, $n = 1, \ldots, 40$.

The entire plane is foliated by isochrons. We depict only 40 representative ones in Fig.10.2. In this chapter we consider neighborhoods of exponentially stable limit cycles, where the foliation is continuous and invariant (Guckenheimer 1975):

- *Continuity.* The function $\vartheta(x)$ is continuous so that nearby points have nearby phases.

- *Invariance.* If $\vartheta(x(0)) = \vartheta(y(0))$, then $\vartheta(x(t)) = \vartheta(y(t))$ for all t. Isochrons are mapped to isochrons by the flow of the vector field.

Fig.10.3 shows the geometry of isochrons of various oscillators. The Andronov-Hopf oscillator in the figure is often called a radial isochron clock for the obvious reason. It is simple enough to be solved explicitly (see exercise 1). In general, finding isochrons is a daunting mathematical task. In exercise 3 we present a MATLAB program that finds isochrons numerically.

10.1.3   PRC

Consider a periodically spiking neuron (10.1) receiving a single brief pulse of current that increases the membrane potential by $A = 1$ mV, as in Fig.10.4 (left). Such a perturbation may not elicit an immediate spike, but it can change the timing, that is,
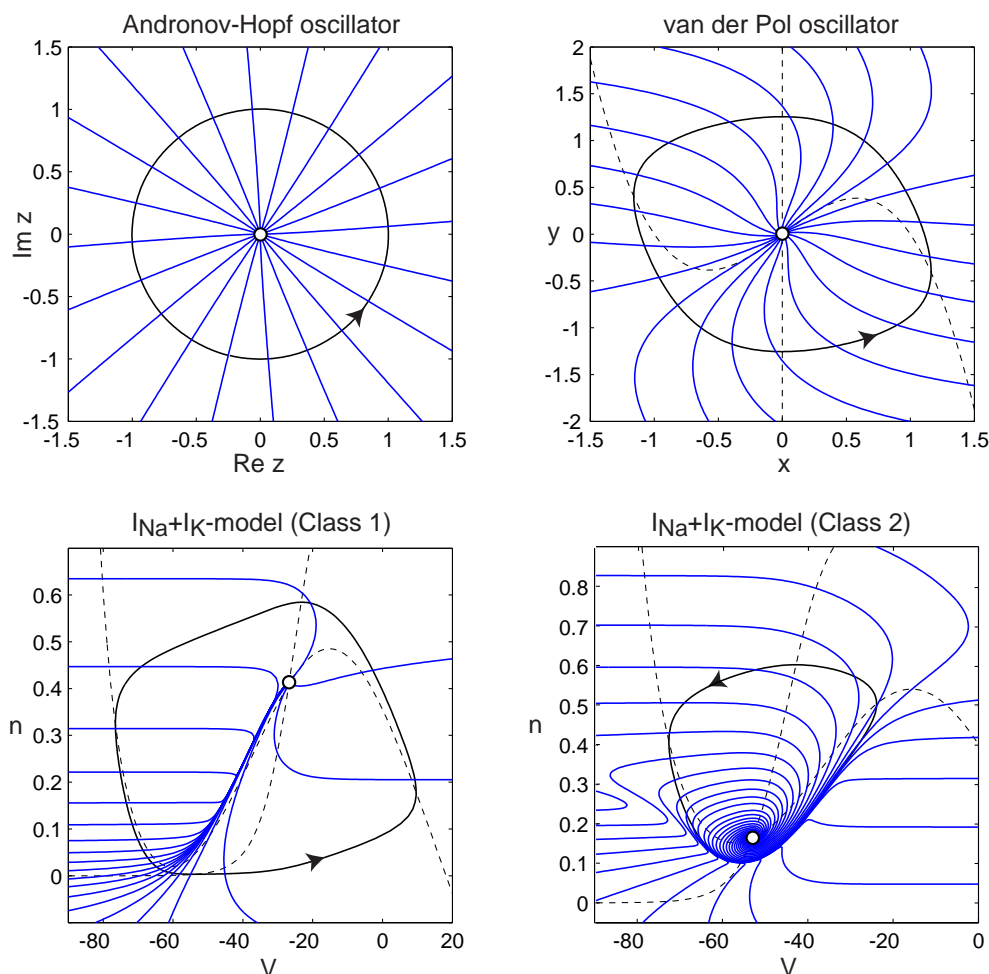
Figure 10.3: Isochrons of various oscillators. Andronov-Hopf oscillator: $\dot{z} = (1 + \mathrm{i})z - z|z|^2$, $z \in \mathbb{C}$. van der Pol oscillator: $\dot{x} = x - x^3 - y$, $\dot{y} = x$. The $I_{\mathrm{Na}} + I_{\mathrm{K}}$-model with parameters as in Fig.4.1a and $I = 10$ (Class 1) and $I = 35$ (Class 2). Only isochrons corresponding to phases $nT/20$, $n = 1, \ldots, 20$, are shown.

the phase, of the following spikes. For example, the perturbed trajectory (solid line in Fig.10.4, left) fires earlier than the free-running unperturbed trajectory (dashed line). That is, right after the perturbation, the phase, ϑ_{new}, is greater than the old phase, ϑ. The magnitude of the phase shift of the spike train depends on the exact timing of the stimulus relative to the phase of oscillation ϑ. Stimulating the neuron at different phases, we can measure the *phase response curve* (also called phase-resetting curve PRC, or spike time response curve STRC)

$$\mathrm{PRC}\,(\vartheta) = \{\vartheta_{\mathrm{new}} - \vartheta\} \qquad (\text{shift} = \text{new phase} - \text{old phase}) ,$$

depicted in Fig.10.4, right. Positive (negative) values of the function correspond to phase advances (delays) in the sense that they advance (delay) the timing of the next spike.
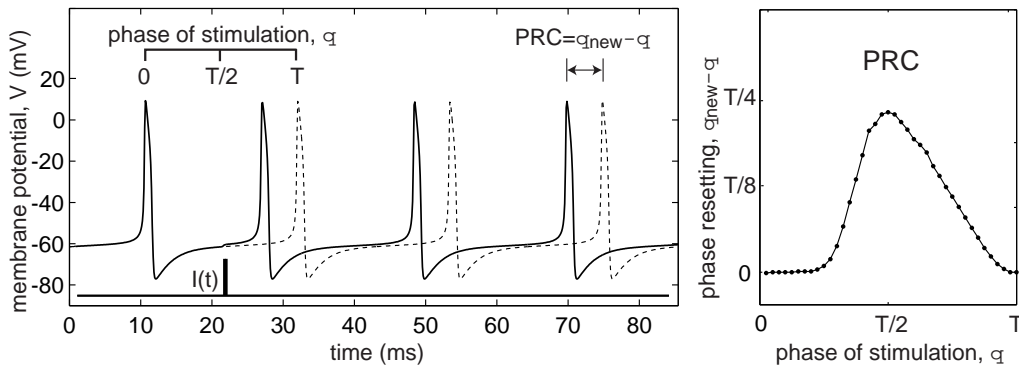
Figure 10.4: Phase response of the $I_{Na} + I_K$-model with parameters as in Fig.4.1a and $I = 4.7$. The dashed voltage trace is the free-running trajectory.

In contrast to the common folklore, the function $\text{PRC}(\vartheta)$ can be measured for an arbitrary stimulus, not necessarily weak or brief. The only caveat is that to measure the new phase of oscillation perturbed by a stimulus, we must wait long enough for transients to subside. This becomes a limiting factor when PRCs are used to study synchronization of oscillators to periodic pulses, as we do in section 10.1.5.

There is a simple geometrical relationship between the structure of isochrons of an oscillator and its PRC, illustrated in Fig.10.5 (see also exercise 6). Let us stimulate the oscillator at phase ϑ with a pulse, which moves the trajectory from point x lying on the intersection of isochron ϑ and the limit cycle attractor to a point y lying on some isochron ϑ_{new}. From the definition of PRC, it follows that $\vartheta_{new} = \vartheta + \text{PRC}(\vartheta)$.

In general, one uses simulations to determine PRCs, as we do in Fig.10.4. Using
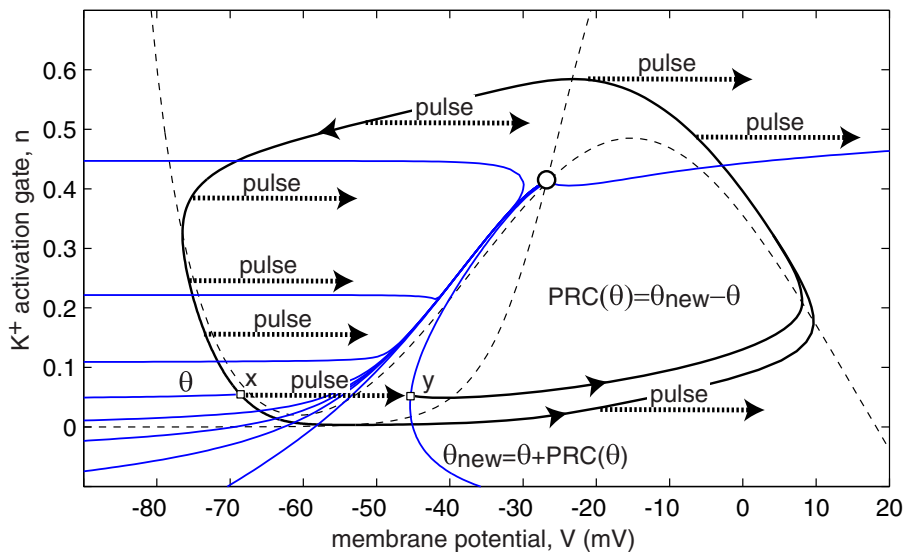
Figure 10.5: The geometrical relationship between isochrons and the phase response curve (PRC) of the $I_{Na} + I_K$-oscillator in Fig.10.1.
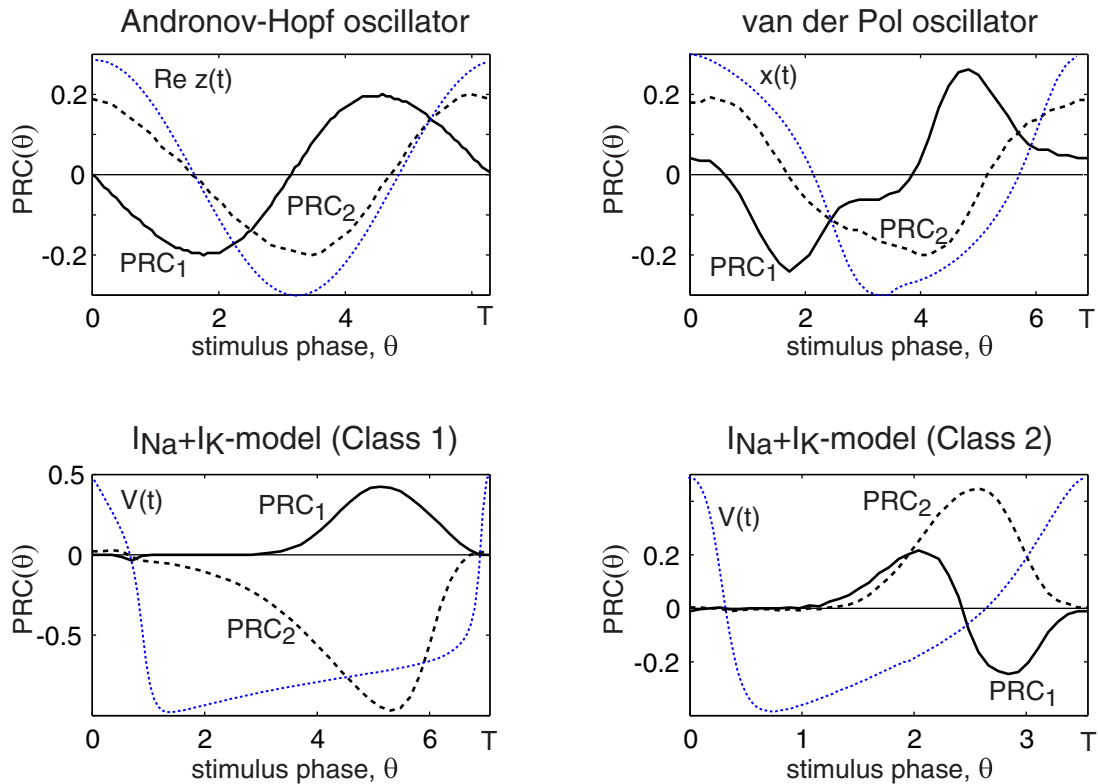
Figure 10.6: Examples of phase response curves (PRC) of the oscillators in Fig.10.3. $PRC_1(\vartheta)$: Horizontal pulses (along the first variable) with amplitudes $0.2, 0.2, 2, 0.2$ for Andnronov-Hopf, van der Pol, Class 1 and Class 2 oscillators, respectively. $PRC_2(\vartheta)$: Vertical pulses (along the second variable) with amplitudes $0.2, 0.2, 0.02, 0.002$, respectively. An example of oscillation is plotted as a dotted curve in each subplot (not to scale).

the MATLAB program presented in exercise 5, we can determine PRCs of all four oscillators in Fig.10.3 and plot them in Fig.10.6. It is a good exercise to explain the shape of each PRC in the figure, or at least its sign, using the geometry of isochrons of corresponding oscillators. In section 10.2.4 we discuss pitfalls of using the straightforward method in Fig.10.4 to measure PRCs in biological neurons, and we present a better technique.

Note that the PRC of the $I_{Na} + I_K$-model in Fig.10.6 is mainly positive in the Class 1 regime, that is, when the oscillations appear via saddle-node on invariant circle bifurcation, but changes sign in the Class 2 regime, corresponding in this case to the supercritical Andronov-Hopf bifurcation. In section 10.4 we find PRCs analytically in the case of weak coupling, and show that the PRC of a Class 1 oscillator has the shape $\sin^2 \vartheta$ (period $T = \pi$) or $1 - \cos \vartheta$ (period $T = 2\pi$), whereas that of a Class 2 oscillator has the shape $\sin \vartheta$ (period $T = 2\pi$). We show in section 10.1.7 how the synchronization properties of an oscillator depend on the shape of its PRC.

Type 1 (weak) resetting   Type 0 (strong) resetting
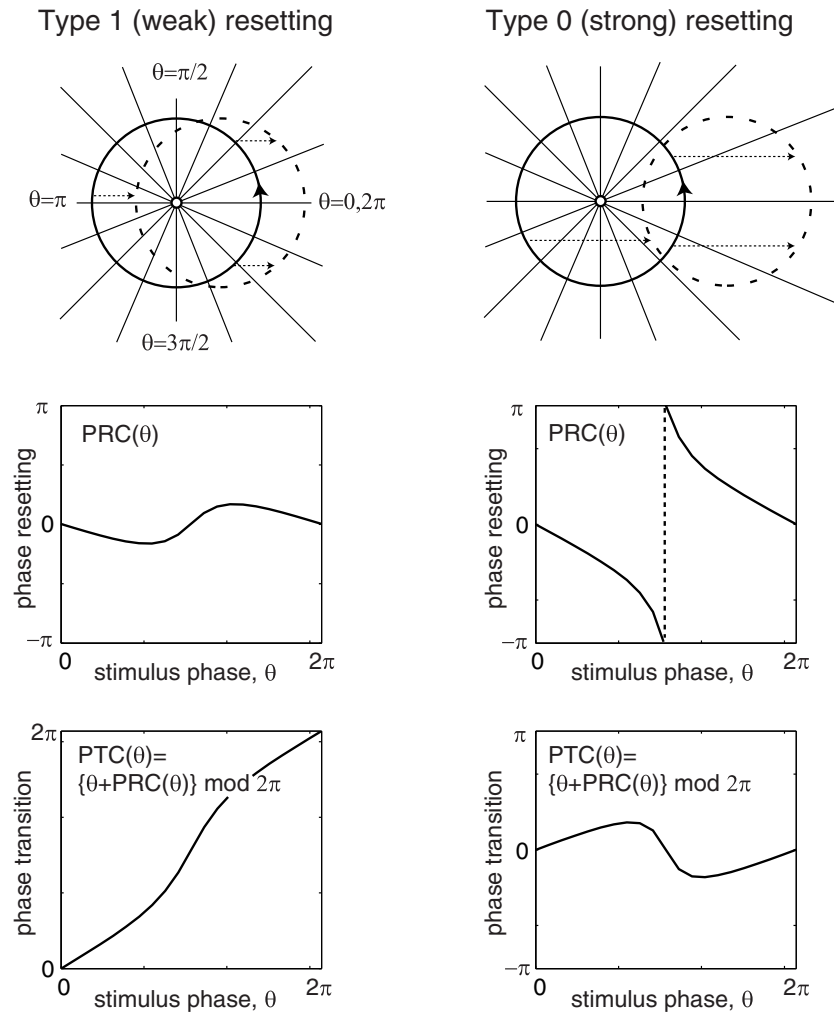
Figure 10.7: Types of phase-resetting of the Andronov-Hopf oscillator in Fig.10.3.

10.1.4   Type 0 and Type 1 Phase Response

Instead of phase-resetting curves, many researchers in the field of circadian rhythms consider *phase transition curves* (Winfree 1980)

$$\vartheta_{\text{new}} = \text{PTC}\,(\vartheta_{\text{old}}).$$

Since

$$\text{PTC}\,(\vartheta) = \{\vartheta + \text{PRC}\,(\vartheta)\}\bmod T,$$

the two approaches are equivalent. PRCs are convenient when the phase shifts are small, so that they can be magnified and seen clearly. PTCs are convenient when the phase shifts are large and comparable with the period of oscillation. We present PTCs in this section solely for the sake of review, and we use PRCs throughout the rest of the chapter.
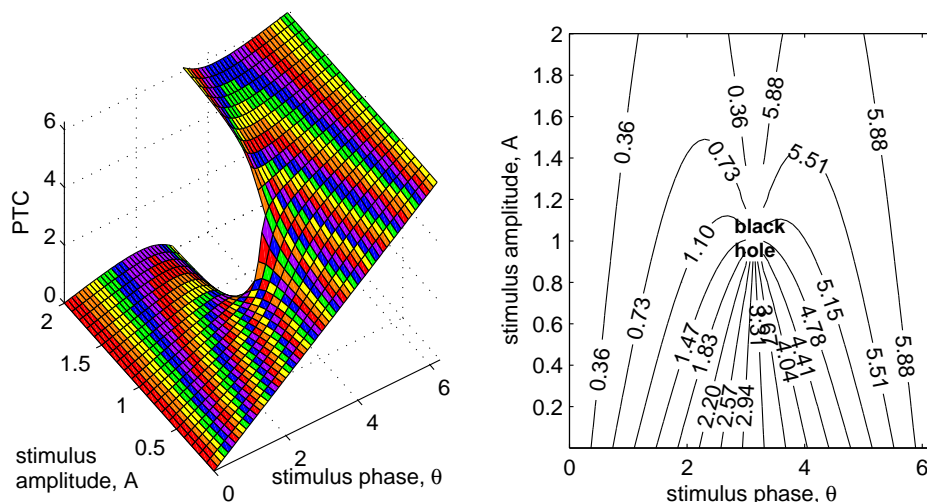
Figure 10.8: Time crystal (left) and its contour plot (right). Shown is the PTC (ϑ, A) of the Andronov-Hopf oscillator (see exercise 4).

In Fig.10.7 (top) we depict phase portraits of the Andronov-Hopf oscillator having radial isochrons and receiving pulses of magnitude $A = 0.5$ (left) and $A = 1.5$ (right). Note the drastic difference between the corresponding PRCs or PTCs. Winfree (1980) distinguishes two cases:

- *Type 1 (weak) resetting* results in continuous PRCs and PTCs with mean slope 1.

- *Type 0 (strong) resetting* results in discontinuous PRCs and PTCs with mean slope 0.

(Do not confuse these classes with Class 1, 2, or 3 excitability.) The discontinuity of the Type 0 PRC in Fig.10.7 is a topological property that cannot be removed by reallocating the initial point x_0 that corresponds to zero phase. As an exercise, prove that the discontinuity stems from the fact that the shifted image of the limit cycle (dashed circle) goes beyond the central equilibrium at which the phase is not defined.

If we vary not only the phase ϑ of the applied stimulus, but also its amplitude A, then we obtain parameterized PRC and PTC. In Fig.10.8 we plot PTC (ϑ, A) of the Andronov-Hopf oscillator (the corresponding PRC is derived in exercise 4). The surface is called *time crystal* and it can take quite amazing shapes (Winfree 1980). The contour plot of PTC (ϑ, A) in the figure contains the singularity point (black hole) that corresponds to the phaseless equilibrium of the Andronov-Hopf oscillator. Stimulation at phase $\vartheta = \pi$ with magnitude $A = 1$ pushes the trajectory into the equilibrium and stalls the oscillation.
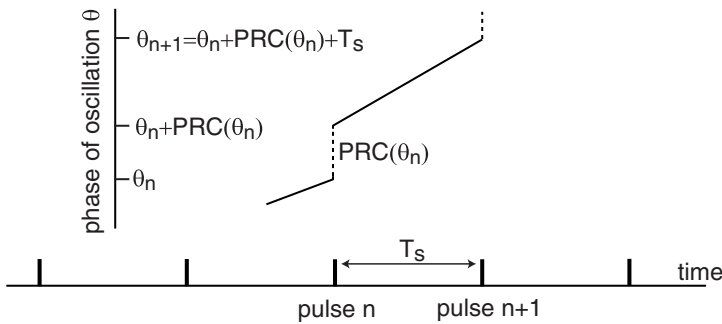
Figure 10.9: Calculation of the Poincare phase map.

10.1.5   Poincare Phase Map

The phase-resetting curve (PRC) describes the response of an oscillator to a single pulse, but it can also be used to study its response to a periodic pulse train using the following "stroboscopic" approach. Let ϑ_n denote the phase of oscillation at the time the nth input pulse arrives. Such a pulse resets the phase by $\mathrm{PRC}\,(\vartheta_n)$, so that the new phase right after the pulse is $\vartheta_n + \mathrm{PRC}\,(\vartheta_n)$ (see Fig.10.9). Let T_s denote the period of pulsed stimulation. Then the phase of oscillation before the next, $(n+1)$th, pulse is $\vartheta_n + \mathrm{PRC}\,(\vartheta_n) + T_\mathrm{s}$. Thus, we have a stroboscopic mapping of a circle to itself,

$$\vartheta_{n+1} = (\vartheta_n + \mathrm{PRC}\,(\vartheta_n) + T_\mathrm{s}) \mod T, \tag{10.3}$$

called the *Poincare phase map* (two pulse-coupled oscillators are considered in exercise 11). Knowing the initial phase of oscillation ϑ_1 at the first pulse, we can determine ϑ_2, then ϑ_3, and so on. The sequence $\{\vartheta_n\}$ with $n = 1, 2, \ldots$, is called the *orbit* of the map, and it is quite easy to find numerically.

Let us illustrate this concept using the $I_{\mathrm{Na}} + I_{\mathrm{K}}$-oscillator with PRC shown in Fig.10.4. Its free-running period is $T \approx 21.37$ ms, and the period of stimulation in Fig.10.10a is $T_\mathrm{s} = 18.37$, which results in the Poincare phase map depicted in Fig.10.10d. The cobweb in the figure is the orbit going from ϑ_1 to ϑ_2 to ϑ_3, and so on. Note that the phase ϑ_3 cannot be measured directly from the voltage trace in Fig.10.10a because pulse 2 changes the phase, so it is not the time since the last spike when pulse 3 arrives. The Poincare phase map (10.3) takes into account such multiple pulses. The orbit approaches a point (called a fixed point; see below) that corresponds to a synchronized or phase-locked state.

A word of caution is in order. Recall that PRCs are measured on the limit cycle attractor. However, each pulse displaces the trajectory away from the attractor, as in Fig.10.5. To use the PRC formalism to describe the effect of the next pulse, the oscillator must be given enough time to relax back to the limit cycle attractor. Thus, if the period of stimulation T_s is too small, or the attraction to the limit cycle is too slow, or the stimulus amplitude is too large, the Poincare phase map may be not an appropriate tool to describe the phase dynamics.
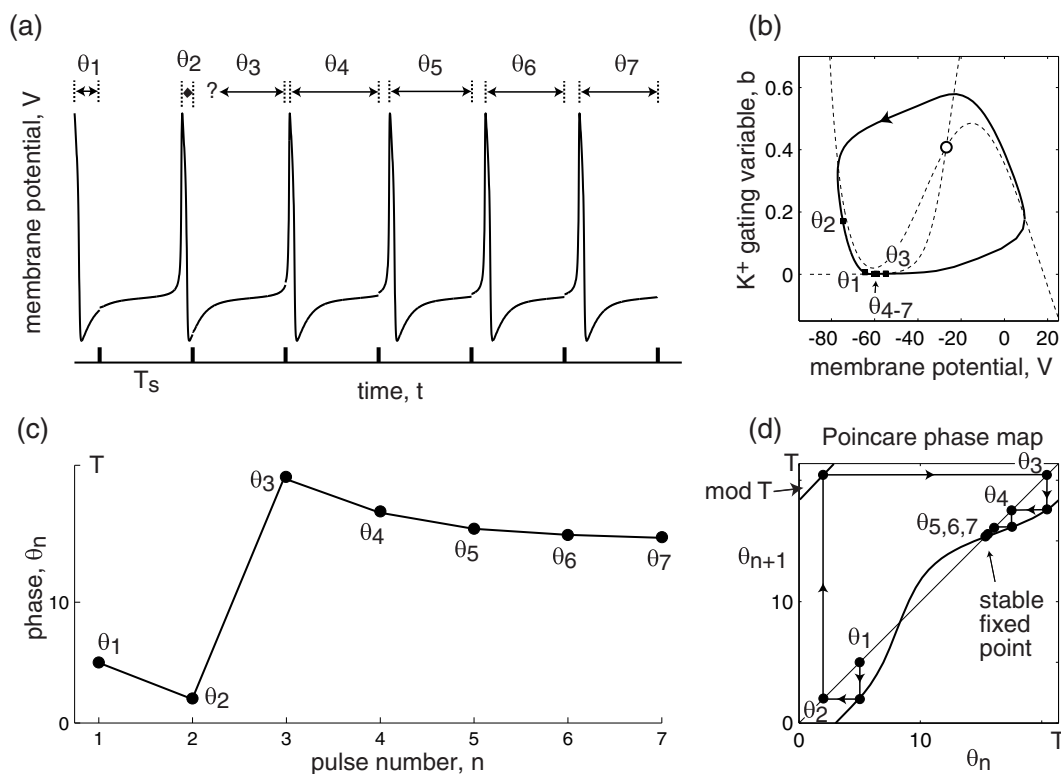
Figure 10.10: Description of synchronization of $I_{Na} + I_K$-oscillator in Fig.10.4, using Poincare phase map.

10.1.6   Fixed points

To understand the structure of orbits of the Poincare phase map (10.3), or any other map

$$\vartheta_{n+1} = f(\vartheta_n) \, , \qquad (10.4)$$

we need to find its fixed points

$$\vartheta = f(\vartheta) \qquad (\vartheta \text{ is a fixed point}),$$

which are analogues of equilibria of continuous dynamical systems. Geometrically, a fixed point is the intersection of the graph of $f(\vartheta)$ with the diagonal line $\vartheta_{n+1} = \vartheta_n$ (see Fig.10.10d or Fig.10.11). At such a point, the orbit $\vartheta_{n+1} = f(\vartheta_n) = \vartheta_n$ is fixed. A fixed point ϑ is *asymptotically stable* if it attracts all nearby orbits, i.e., if ϑ_1 is in a sufficiently small neighborhood of ϑ, then $\vartheta_n \to \vartheta$ as $n \to \infty$, as in Fig.10.11, left. The fixed point is *unstable* if any small neighborhood of the point contains an orbit diverging from it, as in Fig.10.11 (right).

The stability of the fixed point is determined by the slope

$$m = f'(\vartheta)$$

stable fixed points   unstable fixed points
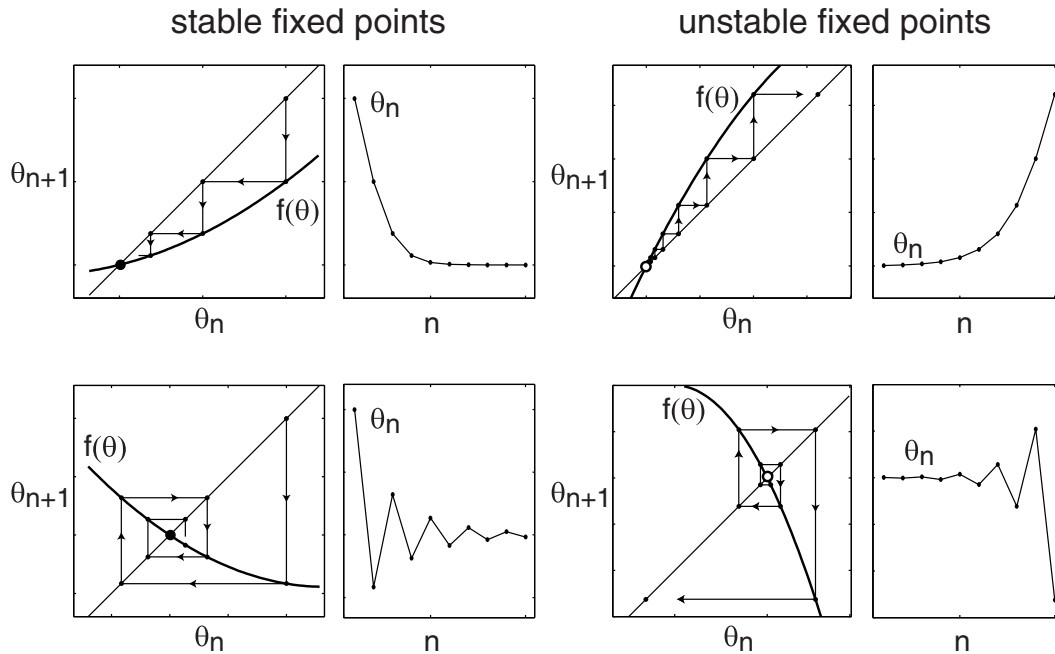
Figure 10.11: The stability of fixed points of the mapping (10.4) depends on the slope of the function f.

of the graph of f at the point, which is called the *Floquet multiplier* of the mapping. It plays the same role as the eigenvalue λ of an equilibrium of a continuous dynamical system. Mnemonically, the relationship between them is $\mu = e^{\lambda}$, to which the fixed point is stable when $|m| < 1$ ($\lambda < 0$) and unstable when $|m| > 1$ ($\lambda > 0$). Fixed points bifurcate when $|m| = 1$ (λ is zero or purely imaginary). They lose stability via flip bifurcation (a discrete analogue of Andronov-Hopf bifurcation) when $m = -1$ and disappear via fold bifurcation (a discrete analogue of saddle-node bifurcation) when $m = 1$. The former plays an important role in the period-doubling phenomenon illustrated in Fig.10.14 (bottom trace). The latter plays an important role in the cycle-slipping phenomenon illustrated in Fig.10.16.

10.1.7   Synchronization

We say that two periodic pulse trains are synchronous when the pulses occur at the same time or with a constant phase shift, as in Fig.10.12a. Each subplot in the figure contains an input pulse train (bottom) and an output spike train (top), assuming that spikes are fired at zero crossings of the phase variable, as in Fig.10.1. Such a synchronized state corresponds to a stable fixed point of the Poincare phase map (10.3). The in-phase, anti-phase, or out-of-phase synchronization corresponds to the phase shift $\vartheta = 0$, $\vartheta = T/2$, or some other value, respectively. Many scientists refer to the in-phase synchronization simply as "synchronization", and use the adjectives anti-phase and out-of-phase to denote the other types of synchronization.
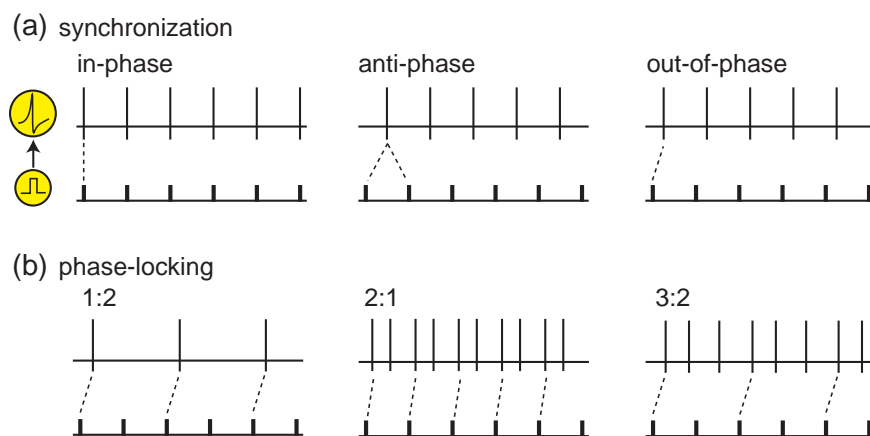
Figure 10.12: Examples of fundamental types of synchronization of spiking activity to periodic pulsed inputs (synchronization is 1:1 phase-locking).
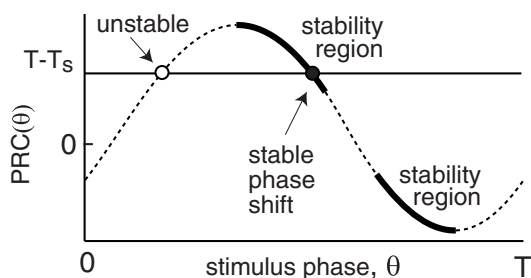
Figure 10.13: Fixed points of the Poincare phase map (10.3).

When the period of stimulation, T_s, is near the free-running period of tonic spiking, T, the fixed point of (10.3) satisfies

$$\mathrm{PRC}\,(\vartheta) = T - T_s \;,$$

that is, it is the intersection of the PRC and the horizontal line, as in Fig.10.13. Thus, synchronization occurs with a phase shift ϑ that compensates for the input period mismatch $T - T_s$. The maxima and the minima of the PRC determine the oscillator's tolerance of the mismatch. As an exercise, check that stable fixed points lie on the side of the graph with the slope

$$-2 < \mathrm{PRC}'(\vartheta) < 0 \qquad \text{(stability region)}$$

marked by the bold curves in Fig.10.13.

Now consider the Class 1 and Class 2 $I_{\mathrm{Na}} + I_{\mathrm{K}}$-oscillators shown in Fig.10.6. The PRC in the Class 1 regime is mostly positive, implying that such an oscillator can easily synchronize with faster inputs ($T - T_s > 0$) but cannot synchronize with slower inputs. Indeed, the oscillator can advance its phase to catch up with faster pulse trains, but it cannot delay the phase to wait for the slower input. Synchronization with the input having $T_s \approx T$ is only marginal. In contrast, the Class 2 $I_{\mathrm{Na}} + I_{\mathrm{K}}$-oscillator does not have this problem because its PRC has well-defined positive and negative regions.
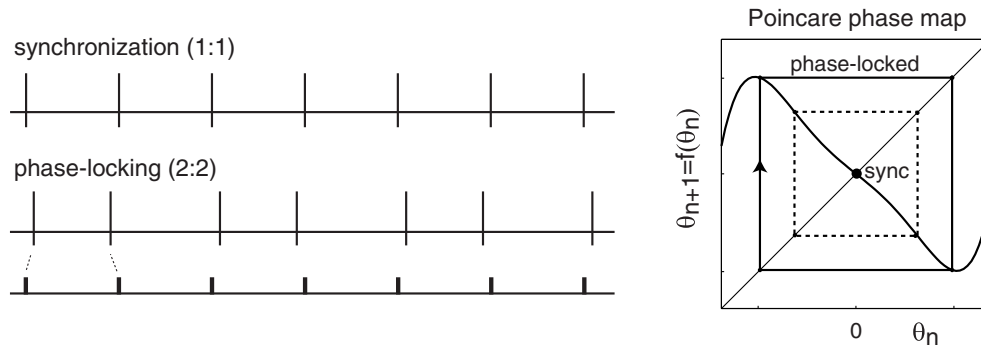
Figure 10.14: Coexistence of synchronized and phase-locked solutions corresponds to coexistence of a stable fixed point and a stable periodic orbit of the Poincare phase map.

10.1.8   Phase-Locking

The phenomenon of *p:q-phase-locking* occurs when the oscillator fires p spikes for every q input pulses, such as the 3:2-phase-locking in Fig.10.12b or the 2:2 phase-locking in Fig.10.14, which typically occurs when $pT \approx qT_s$. The integers p and q need not be relatively prime in the case of pulsed-coupled oscillators. Synchronization, that is, 1:1 phase-locking, as well as p:1 phase-locking corresponds to a fixed point of the Poincare phase map (10.3) with p fired spikes per single input pulse. Indeed, the map tells the phase of the oscillator at each pulse, but not the number of oscillations between the pulses.

Each p:q-locked solution corresponds to a stable periodic orbit of the Poincare phase map with the period q (so that $\vartheta_n = \vartheta_{n+q}$ for any n). Such orbits in maps (10.4) correspond to stable equilibria in the iterates $\vartheta_{k+1} = f^q(\vartheta_k)$, where $f^q = f \circ f \circ \cdots \circ f$ is the composition of f with itself q times. Geometrically, studying such maps is like considering every qth input pulse in Fig.10.12b and ignoring all the intermediate pulses.

Since maps can have coexistence of stable fixed points and periodic orbits, various synchronized and phase-locking states can coexist in response to the same input pulse train, as in Fig.10.14. The oscillator converges to one of the states, depending on the initial phase of oscillation, but can be switched between states by a transient input.

10.1.9   Arnold Tongues

To synchronize an oscillator, the input pulse train must have a period T_s sufficiently near the oscillator's free-running period T so that the graph of the PRC and the horizontal line in Fig.10.13 intersect. The amplitude of the function $|\mathrm{PRC}(\vartheta, A)|$ decreases as the strength of the pulse A decreases, because weaker pulses produce weaker phase shifts. Hence the region of existence of a synchronized state shrinks as $A \to 0$, and it looks like a horn or a tongue on the (T_s, A)-plane depicted in Fig.10.15, called *Arnold tongue*. Each p:q-phase-locked state has its own region of existence (p:q-tongue in the
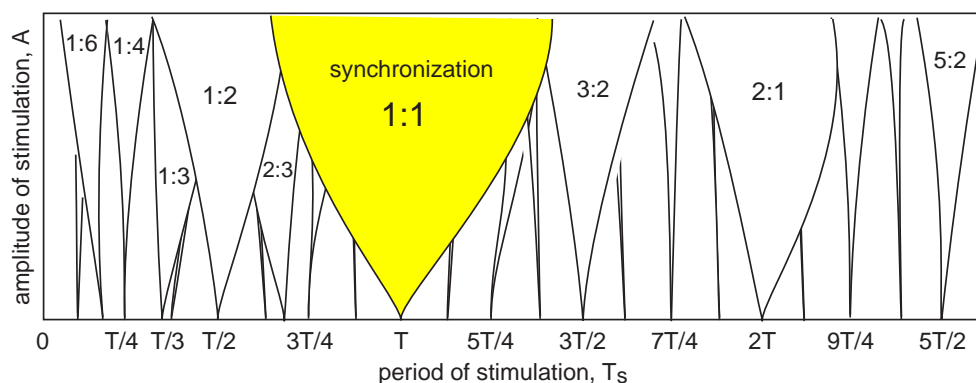
Figure 10.15: Arnold tongues are regions of existence of various phase-locked states on the "period-strength" plane.
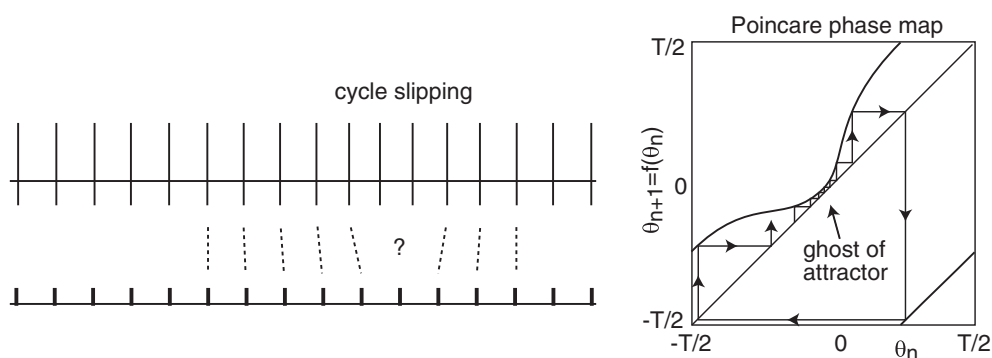
Figure 10.16: Cycle slipping phenomenon at the edge of the Arnold tongue corresponding to a synchronized state.

figure), which also shrinks to a point pT/q on the T_s-axis. The larger the order of locking, $p + q$, the narrower the tongue and the more difficult it is to observe such a phase-locked state numerically, let alone experimentally.

The tongues can overlap, leading to the coexistence of phase-locked states, as in Fig.10.14. If A is sufficiently large, the Poincare phase map (10.3) becomes noninvertible, that is, it has a region of negative slope, and there is a possibility of chaotic dynamics (Glass and Mackey 1988).

In Fig.10.16 we illustrate the *cycle slipping* phenomenon that occurs when the input period T_s drifts away from the 1:1 Arnold tongue. The fixed point of the Poincare phase map corresponding to the synchronized state undergoes a fold bifurcation and disappears. In a way similar to the case of saddle-node on invariant circle bifurcation, the fold fixed point becomes a ghost attractor that traps orbits and keeps them near the synchronized state for a long period of time. Eventually the orbit escapes, the synchronized state is briefly lost, and then the orbit returns to the ghost attractor to be trapped again. Such an intermittently synchronized orbit typically corresponds to a *p:q*-phase-locked state with a high order of locking $p + q$.
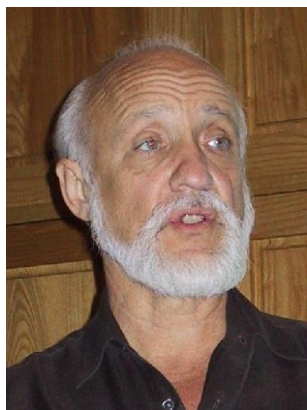
Figure 10.17: Arthur Winfree in 2001. (Photo provided by Martin Homer, University of Bristol.)

10.2   Weak Coupling

In this section we consider dynamical systems of the form

$$\dot{x} = f(x) + \varepsilon p(t) \, , \tag{10.5}$$

describing periodic oscillators, $\dot{x} = f(x)$, forced by a time-depended input $\varepsilon p(t)$, for instance, from other oscillators in a network. The positive parameter ε measures the overall strength of the input, and it is assumed to be sufficiently small, denoted as $\varepsilon \ll 1$. We do not assume $\varepsilon \to 0$ here. In fact, most of the results in this section can be cast in the form "there is an ε_0 such that for all $\varepsilon < \varepsilon_0$, the following holds. . ." (Hoppensteadt and Izhikevich 1997), with ε_0 depending on the function $f(x)$ in (10.5) and sometimes taking not so small values, such as, $\varepsilon_0 = 1$.

Note that if $\varepsilon = 0$ in (10.5), we can transform $\dot{x} = f(x)$, to $\dot{\vartheta} = 1$ using the theory presented in section 10.1. What happens when we apply the same transformation to (10.5) with $\varepsilon \neq 0$? In this section we present three different but equivalent approaches that transform (10.5) into the phase model

$$\dot{\vartheta} = 1 + \varepsilon \operatorname{PRC} (\vartheta) p(t) + o(\varepsilon) \, .$$

Here, Landau's "little oh" function $o(\varepsilon)$ denotes the error terms smaller than ε so that $o(\varepsilon)/\varepsilon \to 0$ if $\varepsilon \to 0$. For the sake of clarity of notation, we omit $o(\varepsilon)$ throughout the book, and implicitly assume that all equalities are valid up to the terms of order $o(\varepsilon)$.

Since we do not impose restrictions on the form of $p(t)$, the three methods are readily applicable to the case

$$p(t) = \sum_{s} g_s(x(t), x_s(t)) \, ,$$

where the set $\{x_s(t)\}$ denotes oscillators in the network connected to x, and $p(t)$ is the postsynaptic current.
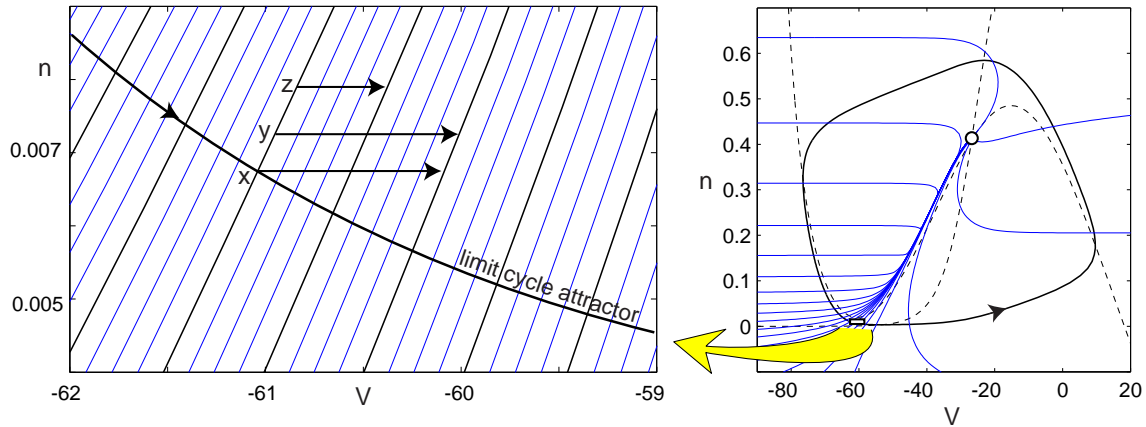
Figure 10.18: Magnification of isochrons in a small neighborhood of the limit cycle of the $I_{Na} + I_K$-model in Fig.10.3. Isochron time step: 0.025 ms on the left, 0.35 ms on the right.

10.2.1 Winfree's Approach

A sufficiently small neighborhood of the limit cycle attractor of the unperturbed ($\varepsilon = 0$) oscillator (10.5), magnified in Fig.10.18, has nearly collinear uniformly spaced isochrons. Collinearity implies that a point x on the limit cycle in Fig.10.18 has the same phase-resetting as any other point y on the isochron of x near the cycle. Uniform density of isochrons implies that the phase-resetting scales linearly with the strength of the pulse, that is, a half-pulse at point z in Fig.10.18 produces a half-resetting of the phase.

Linear scaling of PRC with respect to the strength of the pulse motivates the substitution

$$\mathrm{PRC}\,(\vartheta, A) \approx Z(\vartheta)A\,,$$

where $Z(\vartheta) = \partial\,\mathrm{PRC}(\vartheta, A)/\partial A$ at $A = 0$ is the *linear response* or *sensitivity* function (Winfree 1967) describing the slight alteration of rate, or of instantaneous frequency of oscillation, accompanying application of a small stimulus. Some call it the *infinitesimal PRC*.

Now suppose $\varepsilon \neq 0$ but is sufficiently small that the trajectory of the weakly perturbed oscillator (10.5) remains near the limit cycle attractor all the time. Let us replace the continuous input function $\varepsilon p(t)$ with the equivalent train of pulses of strength $A = \varepsilon p(t_n)h$, where h is a small interpulse interval (denoted as T_s in section 10.1), and $t_n = nh$ is the timing of the nth pulse, see Fig.10.19. We rewrite the corresponding Poincare phase map (10.3)

$$\vartheta(t_{n+1}) = \{\vartheta(t_n) + \overbrace{Z(\vartheta(t_n))\underbrace{\varepsilon p(t_n)h}_{A}}^{\mathrm{PRC}} + h\} \mod T$$
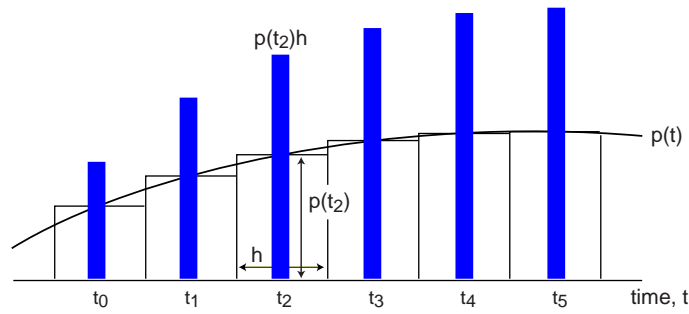
Figure 10.19: A continuous function $p(t)$ is replaced by an equivalent train of pulses of variable amplitudes.

Figure 10.20: Yoshiki Kuramoto in 1988, while he was visiting Jim Murray's institute at Oxford University. (Picture provided by Dr. Y. Kuramoto.)

in the form

$$\frac{\vartheta(t_n + h) - \vartheta(t_n)}{h} = Z(\vartheta(t_n))\varepsilon p(t_n) + 1 \; ,$$

which is a discrete version of

$$\dot{\vartheta} = 1 + \varepsilon Z(\vartheta) \cdot p(t), \tag{10.6}$$

in the limit $h \to 0$.

To be consistent with all the examples in section 10.1, we implicitly assume here that $p(t)$ perturbs only the first, voltage-like variable x_1 of the state vector $x = (x_1, \ldots, x_m) \in \mathbb{R}^m$ and that $Z(\vartheta)$ is the corresponding sensitivity function. However, the phase model (10.6) is also valid for an arbitrary input $p(t) = (p_1(t), \ldots, p_m(t))$. Indeed, let Z_i describe the linear response to perturbations of the ith state variable x_i, and $Z(\vartheta) = (Z_1(\vartheta), \ldots, Z_m(\vartheta))$ denote the corresponding linear response vector-function. Then the combined phase shift $Z_1 p_1 + \cdots + Z_m p_m$ is the dot product $Z \cdot p$ in (10.6).

10.2.2 Kuramoto's Approach

Consider the unperturbed ($\varepsilon = 0$) oscillator (10.5), and let the function $\vartheta(x)$ denote the phases of points near its limit cycle attractor. Obviously, isochrons are the level
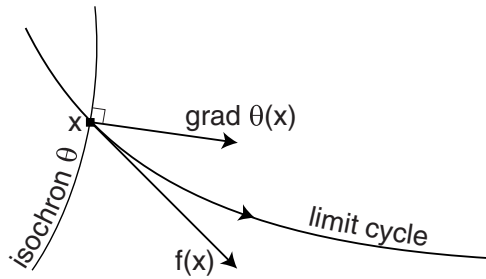
Figure 10.21: Geometrical interpretation of the vector grad ϑ.

contours of $\vartheta(x)$ since the function is constant on each isochron. Differentiating the function using the chain rule yields

$$\frac{d\vartheta(x)}{dt} = \operatorname{grad}\vartheta \cdot \frac{dx}{dt} = \operatorname{grad}\vartheta \cdot f(x) \;,$$

where $\operatorname{grad}\vartheta = (\vartheta_{x_1}(x), \ldots, \vartheta_{x_m}(x))$ is the gradient of $\vartheta(x)$ with respect to the state vector $x = (x_1, \ldots, x_m) \in \mathbb{R}^m$. However,

$$\frac{d\vartheta(x)}{dt} = 1$$

near the limit cycle because isochrons are mapped to isochrons by the flow of the vector field $f(x)$. Therefore, we obtain a useful equality,

$$\operatorname{grad}\vartheta \cdot f(x) = 1 \;. \tag{10.7}$$

Figure 10.21 shows a geometrical interpretation of $\operatorname{grad}\vartheta(x)$: it is the vector based at point x, normal to the isochron of x and with a length equal to the number density of isochrons at x. Its length can also be found from (10.7).

Kuramoto (1984) applied the chain rule to the perturbed system (10.5),

$$\frac{d\vartheta(x)}{dt} = \operatorname{grad}\vartheta \cdot \frac{dx}{dt} = \operatorname{grad}\vartheta \cdot \{f(x) + \varepsilon p(t)\} = \operatorname{grad}\vartheta \cdot f(x) + \varepsilon \operatorname{grad}\vartheta \cdot p(t) \;,$$

and, using (10.7), obtained the phase model

$$\dot{\vartheta} = 1 + \varepsilon \operatorname{grad}\vartheta \cdot p(t) \;, \tag{10.8}$$

which has the same form as (10.6). Subtracting (10.8) from (10.6) yields $(Z(\vartheta) - \operatorname{grad}\vartheta) \cdot p(t) = 0$. Since this is valid for any $p(t)$, we conclude that $Z(\vartheta) = \operatorname{grad}\vartheta$ (see also exercise 6). Thus, Kuramoto's phase model (10.8) is indeed equivalent to Winfree's model (10.8).

10.2.3 Malkin's Approach

Yet another equivalent method of reduction of weakly perturbed oscillators to their phase models follows from Malkin's theorem (1949, 1956), which we state in the simplest form below. The most abstract form and its proof are provided by Hoppensteadt and Izhikevich (1997).

Figure 10.22: Ioel Gil'evich Malkin (Иоэль Гильевич Малкин, 1907–1958).

Malkin's theorem. Suppose the unperturbed ($\varepsilon = 0$) oscillator in (10.5) has an exponentially stable limit cycle of period T. Then its phase is described by the equation

$$\dot{\vartheta} = 1 + \varepsilon Q(\vartheta) \cdot p(t) , \qquad (10.9)$$

where the T-periodic function Q is the solution to the linear "adjoint" equation

$$\dot{Q} = -\{Df(x(t))\}^{\top} Q , \qquad \text{with} \quad Q(0) \cdot f(x(0)) = 1 , \qquad (10.10)$$

where $Df(x(t))^{\top}$ is the transposed Jacobian of f (matrix of partial derivatives) at the point $x(t)$ on the limit cycle, and the normalization condition can be replaced by $Q(t) \cdot f(x(t)) = 1$ for any, and hence all, t. Here $Q \cdot f$ is the dot product of two vectors, which is the same as $Q^{\top} f$.

Though this theorem looks less intuitive than the methods of Winfree and Kuramoto, it is actually more useful because (10.10) can be solved numerically quite easily. Applying the MATLAB procedure in exercise 12 to the four oscillators in Fig.10.3, we plot their functions Q in Fig.10.23. It is not a coincidence that each component of Q looks like PRC along the first or second state variable, shown in Fig.10.6. Subtracting (10.9) from (10.8) or from (10.6), we conclude that

$$Z(\vartheta) = \operatorname{grad} \vartheta(x) = Q(\vartheta) ,$$

(see also exercise 7), so that we can determine the linear response function of the phase model using any of the three alternative methods: via PRCs, via isochrons, or solving the adjoint equation (10.10). This justifies the reason why many refer to the function simply as PRC, implicitly assuming that it is measured to the infinitesimal stimuli and then normalized by the stimulus amplitude.

10.2.4   Measuring PRCs Experimentally

In Fig.10.24 we exploit the relationship (10.9) and measure the infinitesimal PRCs of a layer 5 pyramidal neuron of mouse visual cortex. First, we stimulate the neuron with 40 pA DC current to elicit periodic spiking. Initially, the firing period starts at 50 ms, and then relaxes to the averaged value of 110 ms (Fig.10.24a). The standard method of finding PRCs consists in stimulating the neuron with brief pulses of current at different
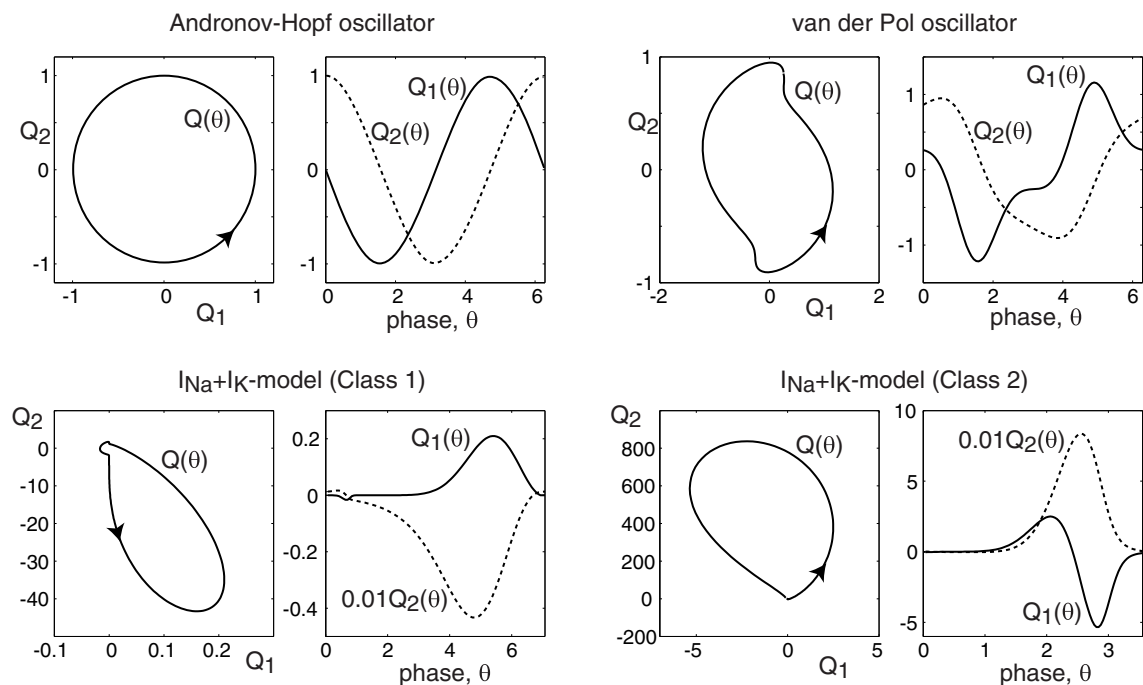
Figure 10.23: Solutions $Q = (Q_1, Q_2)$ to adjoint problem (10.10) for oscillators in Fig.10.3.

phases of the cycle and measuring the induced phase shift, which can be approximated by the difference between two successive periods of oscillation. The method works well in models (see exercise 5), but should be used with caution in real neurons because their firing is too noisy, as we demonstrate in Fig.10.24b. Thus, one needs to apply hundreds, if not thousands, of pulses and then average the resulting phase deviations (Reyes and Fetz 1993).

Starting with time 10 sec, we inject a relatively weak noisy current $\varepsilon p(t)$ that continuously perturbs the membrane potential (Fig.10.24c) and, hence, the phase of oscillation (the choice of $p(t)$ is important; its Fourier spectrum must span a range of frequencies that depends on the frequency of firing of the neuron). Knowing $\varepsilon p(t)$, the moments of firing of the neuron, which are zero crossings $\vartheta(t) = 0$, and the relationship

$$\dot{\vartheta} = 1 + \text{PRC}(\vartheta)\varepsilon p(t) ,$$

we solve the inverse problem for the infinitesimal $\text{PRC}(\vartheta)$ and plot the solution in Fig.10.24d. As one expects, the PRC is mostly positive, maximal just before the spike and almost zero during the spike. It would resemble the PRC in Fig.10.23 ($Q_1(\vartheta)$ in Class 1) if not for the dip in the middle, for which we have no explanation (probably it is due to overfitting). The advantage of this method is that it is more immune to noise, because intrinsic fluctuations are spread over the entire $p(t)$ and not concentrated at the moments of pulses – unless, of course $p(t)$, consists of random pulses, in which case this method is equivalent to the standard one. The drawback is that we need to solve
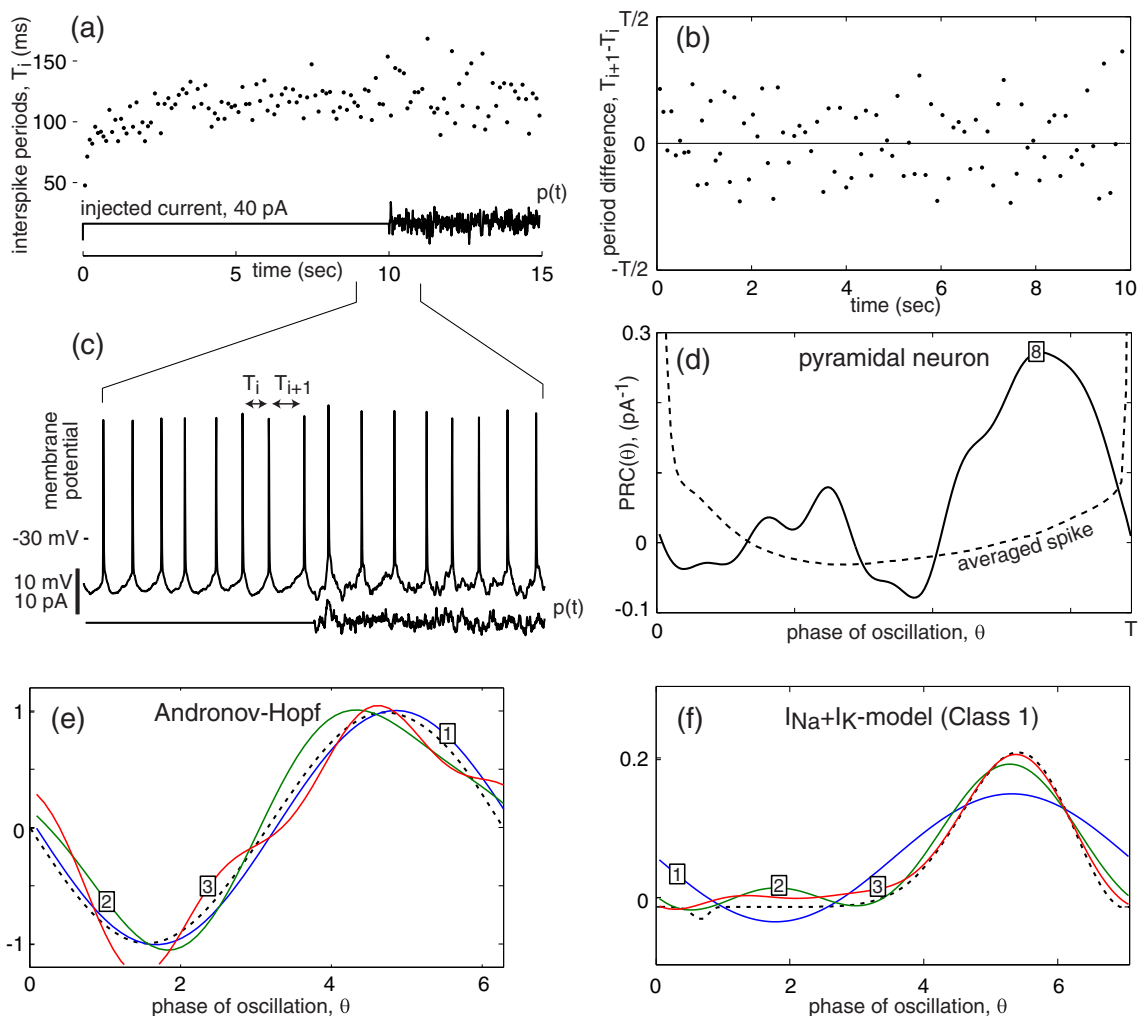
Figure 10.24: Measuring the infinitesimal PRC experimentally in a layer 5 pyramidal neuron of mouse visual cortex. (a) Interspike periods in response to the injection of DC current. (b) Differences between successive periods. (c) Spiking 1 second before and after the noisy current $p(t)$ is injected. (d) Infinitesimal PRC of the neuron (continuous curve) obtained from 40 cycles and the MATLAB program in exercise 13 (first eight Fourier terms). Averaged voltage trace during the spike (dotted curve) is plotted for reference. The same procedure is applied to (e) the Andronov-Hopf oscillator and (f) the $I_{Na,p}+I_K$-model. Numbers in boxes represent the number of Fourier terms used to fit the curve; theoretical curves (functions $Q_1(\vartheta)$ from Fig.10.23) are dashed.
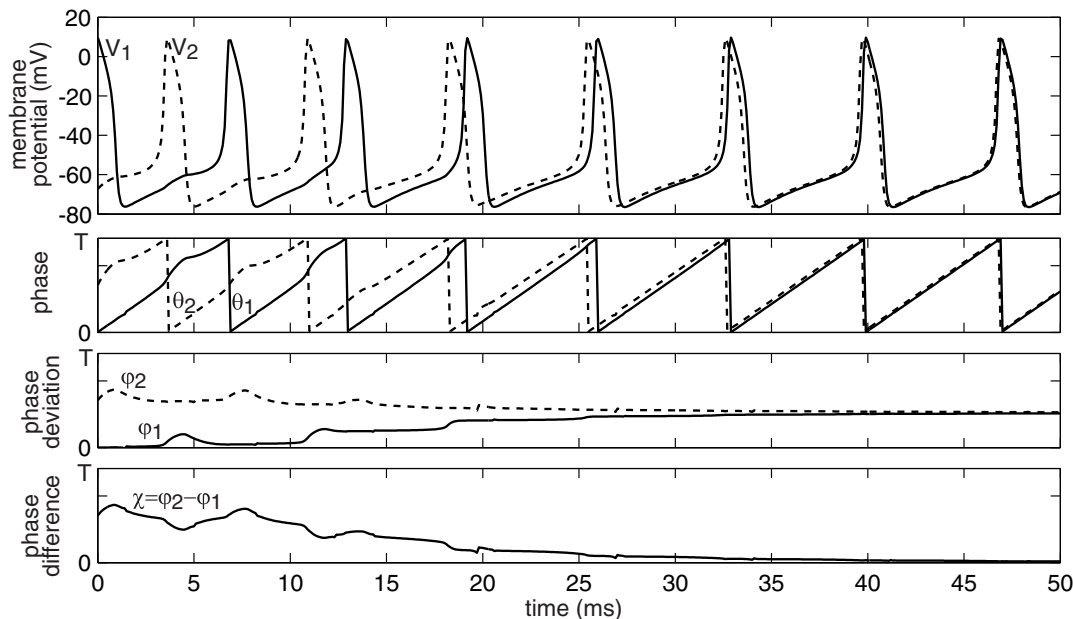
Figure 10.25: The relationship between membrane potential oscillation of two neurons, V_1 (solid) and V_2 (dashed), their phases, phase deviations, and phase difference. Shown are simulation of two $I_{\text{Na}} + I_{\text{K}}$-models with parameters as in Fig.10.3 and coupled symmetrically via gap junctions $0.1(V_j - V_i)$ (see section 2.3.4).

the equation above, which we do in exercise 13, using an optimization technique.

10.2.5   Phase Model for Coupled Oscillators

Now consider n weakly coupled oscillators of the form

$$\dot{x}_i = f_i(x_i) + \varepsilon \overbrace{\sum_{j=1}^{n} g_{ij}(x_i, x_j)}^{p_i(t)}, \quad x_i \in \mathbb{R}^m , \tag{10.11}$$

and assume that the oscillators, when uncoupled ($\varepsilon = 0$), have equal free-running periods $T_1 = \cdots = T_n = T$. Applying any of the three methods above to such a weakly perturbed system, we obtain the corresponding phase model

$$\dot{\vartheta}_i = 1 + \varepsilon\, Q_i(\vartheta_i) \cdot \overbrace{\sum_{j=1}^{n} g_{ij}(x_i(\vartheta_i), x_j(\vartheta_j))}^{p_i(t)} , \tag{10.12}$$

where each $x_i(\vartheta_i)$ is the point on the limit cycle having phase ϑ_i. Note that (10.11) is defined in $\mathbb{R}^{nm}$, whereas the phase model (10.12) is defined on the n-torus, denoted as $\mathbb{T}^n$.

To study collective properties of the network, such as synchronization, it is convenient to represent each $\vartheta_i(t)$ as

$$\vartheta_i(t) = t + \varphi_i , \qquad (10.13)$$

with the first term capturing the *fast* free-running natural oscillation $\dot{\vartheta}_i = 1$, and the second term capturing the *slow* network-induced build-up of *phase deviation* from the natural oscillation. The relationship between $x_i(t)$, $\vartheta_i(t)$ and $\varphi_i(t)$ is illustrated in Fig.10.25.

Substituting (10.13) into (10.12) results in

$$\dot{\varphi}_i = \varepsilon \, Q_i(t + \varphi_i) \cdot \sum_{j=1}^{n} g_{ij}(x_i(t + \varphi_i), x_j(t + \varphi_j)) . \qquad (10.14)$$

Note that the right-hand side is of order ε, reflecting the slow dynamics of phase deviations φ_i seen in Fig.10.25. Thus, it contains two time scales: fast oscillations (variable t) and slow phase modulation (variables φ). The classical method of averaging, reviewed by Hoppensteadt and Izhikevich (1997, Chap. 9), consists in a near-identity change of variables that transforms the system into the form

$$\dot{\varphi}_i = \varepsilon\omega_i + \varepsilon \sum_{j \neq i}^{n} H_{ij}(\varphi_j - \varphi_i) , \qquad (10.15)$$

where

$$H_{ij}(\varphi_j - \varphi_i) = \frac{1}{T} \int_0^T Q_i(t) \cdot g_{ij}(x_i(t), x_j(t + \varphi_j - \varphi_i)) \, dt , \qquad (10.16)$$

and each $\omega_i = H_{ii}(\varphi_i - \varphi_i) = H_{ii}(0)$ describes a constant frequency deviation from the free-running oscillation. Figure 10.26 depicts the functions H_{ij} corresponding to
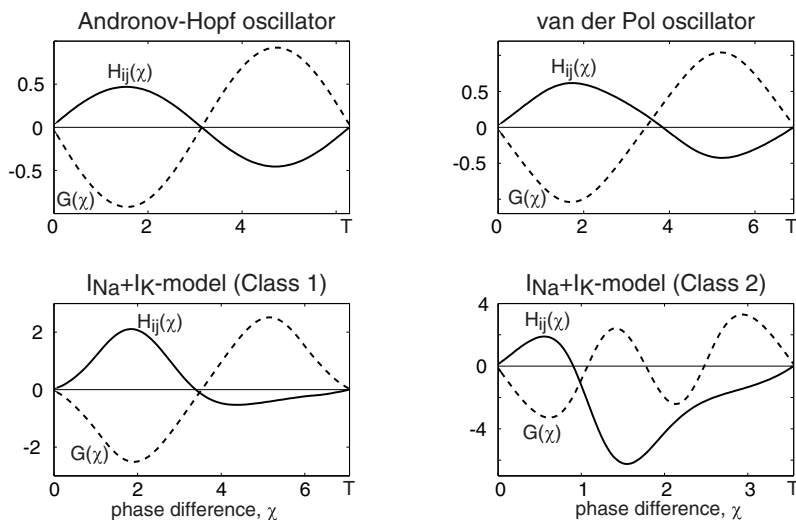
Figure 10.26: Solid curves. Functions $H_{ij}(\chi)$ defined by (10.16) with the input $g(x_i, x_j) = (x_{j1} - x_{i1}, 0)$ corresponding to electrical synapse via gap-junction. Dashed curves. Functions $G(\chi) = H_{ji}(-\chi) - H_{ij}(\chi)$. Parameters are as in Fig.10.3.

gap-junction (i.e., electrical; see section 2.3.4) coupling of oscillators in Fig.10.3. Prove that $H(\chi) = Q(\chi) \cdot A/T$ in the case of pulse-coupling (10.1), so that $H(\chi)$ is just re-scaled PRC.

A special case of (10.15) occurs when H is replaced by its first Fourier term, sin. The resulting system, written in the slow time $\tau = \varepsilon t$,

$$\varphi_i' = \omega_i + \sum_{j=1}^{n} c_{ij} \sin(\varphi_j - \varphi_i + \psi_{ij}),$$

is called the *Kuramoto phase model* (Kuramoto 1975). Here, the frequency deviations ω_i are interpreted as intrinsic frequencies of oscillators. The strengths of connections c_{ij} are often assumed to be equal to K/n for some constant K, so that the model can be studied in the limit $n \to \infty$. The phase deviations ψ_{ij} are often neglected for the sake of simplicity.

To summarize, we transformed the weakly coupled system (10.11) into the phase model (10.15) with H given by (10.16) and each Q being the solution to the adjoint problem (10.10). This constitutes the Malkin theorem for weakly coupled oscillators (Hoppensteadt and Izhikevich 1997, theorem 9.2).

10.3 Synchronization

Consider two coupled phase variables (10.12) in a general form

$$\begin{aligned} \dot{\vartheta}_1 &= h_1(\vartheta_1, \vartheta_2), \\ \dot{\vartheta}_2 &= h_2(\vartheta_1, \vartheta_2), \end{aligned}$$

with some positive functions h_1 and h_2. Since each phase variable is defined on the circle $\mathbb{S}^1$, the state space of this system is the 2-torus $\mathbb{T}^2 = \mathbb{S}^1 \times \mathbb{S}^1$ depicted in Fig.10.27, with ϑ_1 and ϑ_2 being the longitude and the latitude, respectively. The torus can be represented as a square with vertical and horizontal sides identified, so that a solution disappearing at the right side of the square appears at the left side.

The coupled oscillators above are said to be *frequency-locked* when there is a periodic trajectory on the 2-torus, which is called a *torus knot*. It is said to be of type (p, q) if ϑ_1 makes p rotations while ϑ_2 makes q rotations, and p and q are relatively prime integers, that is, they do not have a common divisor greater than 1. Torus knots of type (p, q) produce $p{:}q$ frequency-locking, e.g., the 2:3 frequency-locking in Fig.10.27. A 1:1 frequency-locking is called *entrainment*. There can be many periodic orbits on the torus, with stable orbits between unstable ones. Since the orbits on the 2-torus cannot intersect, they are all knots of the same type, resulting in the same $p{:}q$ frequency-locking.

Let us follow a trajectory on the torus and count the number of rotations of the phase variables. The limit of the ratio of rotations as $t \to \infty$ is independent of the trajectory we follow, and it is called the *rotation number* of the torus flow. It is rational
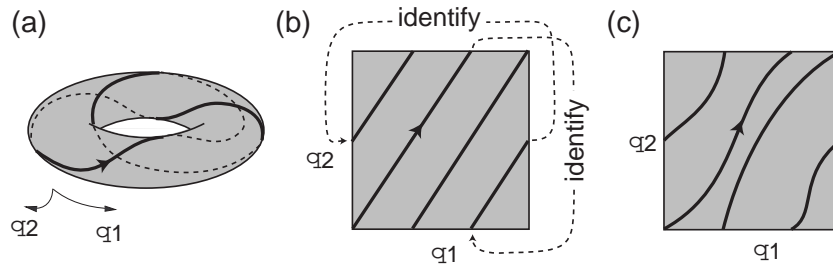
Figure 10.27: Torus knot of type $(2, 3)$ (a) and its representation on the square (b). The knot produces frequency-locking and phase-locking. (c) Torus knot that does not produce phase-locking.
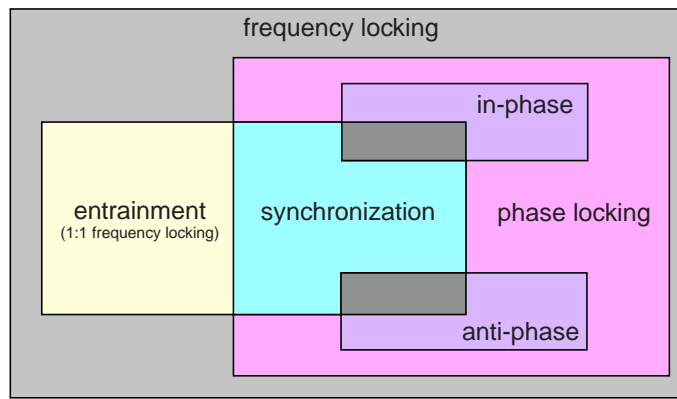
Figure 10.28: Various degrees of locking of oscillators.

if and only if there is a (p, q) periodic orbit, in which case the rotation number is p/q. An irrational rotation number implies there are no periodic orbits, and it corresponds to a *quasi-periodic* or *multifrequency* torus flow. Oscillators exhibit *phase drifting* in this case. Denjoy (1932) proved that such coupled oscillators are topologically equivalent to the uncoupled system $\dot{\vartheta}_1 = r$, $\dot{\vartheta}_2 = 1$ with irrational r.

Suppose the oscillators are frequency-locked; that is, there is a *p:q* limit cycle attractor on the torus. We say that the oscillators are *p:q phase-locked* if

$$q\vartheta_1(t) - p\vartheta_2(t) = \text{const}$$

on the cycle. The value of the constant determines whether the locking is in-phase (const$= 0$), anti-phase (const$= T/2$; half-period), or out-of-phase. Frequency-locking does not necessarily imply phase-locking: the $(2,3)$ torus knot in Fig.10.27b corresponds to phase-locking, whereas that in Fig.10.27c does not. Frequency-locking without phase-locking is called *phase trapping*. Finally, *synchronization* is a 1:1 phase-locking. The phase difference $\vartheta_2 - \vartheta_1$ is also called *phase lag* or *phase lead*. The relationships between all these definitions are shown in Fig.10.28.

Frequency-locking, phase-locking, entrainment, and synchronization of a network of $n > 2$ oscillators are the same as pairwise locking, entrainment, and synchronization
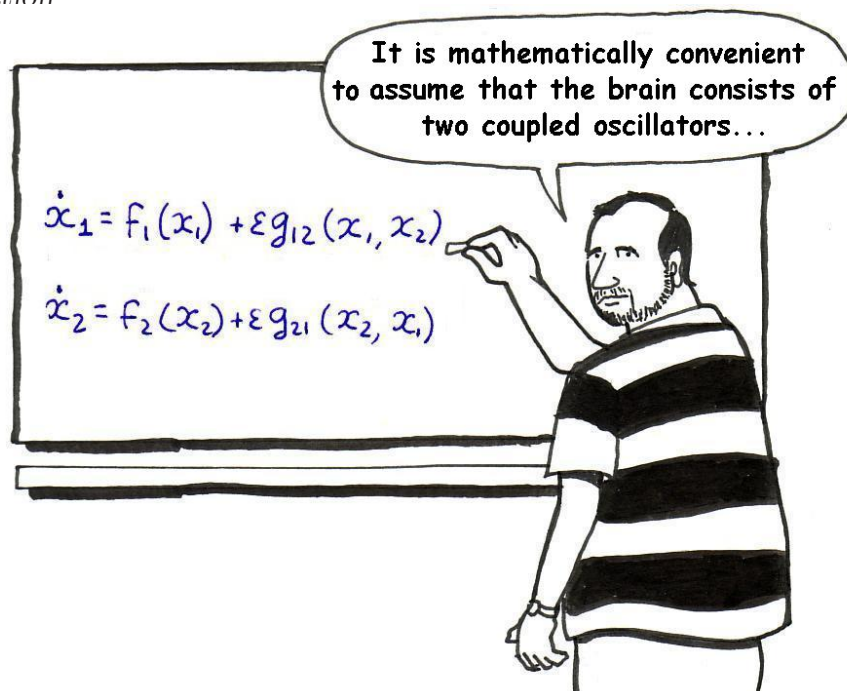
Figure 10.29: A major part of computational neuroscience concerns coupled oscillators.

of the oscillators comprising the network. In addition, a network can exhibit partial synchronization when only a subset of oscillators is synchronized.

Synchronization of oscillators with nearly identical frequencies is described by the phase model (10.15). Existence of one equilibrium of (10.15) implies the existence of the entire circular family of equilibria, since translation of all φ_i by a constant phase shift does not change the phase differences $\varphi_j - \varphi_i$, and hence the form of (10.15). This family corresponds to a limit cycle of (10.11), on which all oscillators, $x_i(t + \varphi_i)$, have equal frequencies and constant phase shifts (i.e., they are synchronized, possibly out-of-phase).

10.3.1 Two Oscillators

Consider (10.11) with $n = 2$, describing two coupled oscillators, as in Fig.10.29. Let us introduce the "slow" time $\tau = \varepsilon t$ and rewrite the corresponding phase model (10.15) in the form

$$
\begin{aligned}
\varphi_1' &= \omega_1 + H_1(\varphi_2 - \varphi_1) \,, \\
\varphi_2' &= \omega_2 + H_2(\varphi_1 - \varphi_2) \,,
\end{aligned}
$$

where $' = d/d\tau$ is the derivative with respect to slow time. Let $\chi = \varphi_2 - \varphi_1$ denote the phase difference between the oscillators. Then the two-dimensional system above becomes the one-dimensional

$$
\chi' = \omega + G(\chi) \,, \tag{10.17}
$$
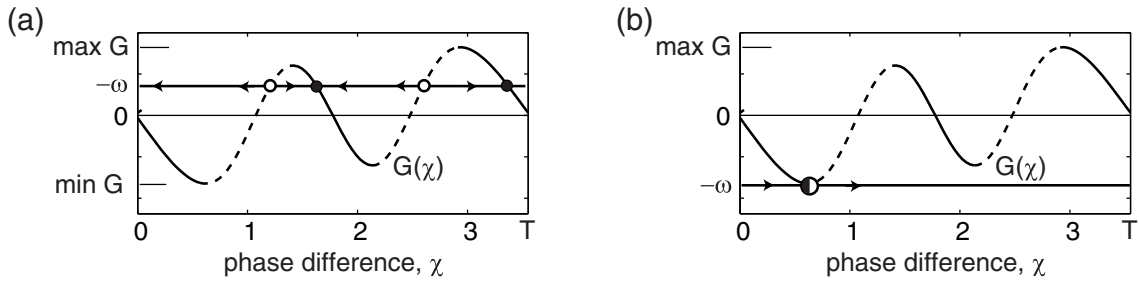
Figure 10.30: Geometrical interpretation of equilibria of the phase model (10.17) for gap-junction-coupled Class 2 $I_{Na} + I_K$-oscillators (see Fig.10.26).

where

$$\omega = \omega_2 - \omega_1 \qquad \text{and} \qquad G(\chi) = H_2(-\chi) - H_1(\chi)$$

are the frequency mismatch and the anti-symmetric part of the coupling, respectively (illustrated in Fig.10.26, dashed curves). A stable equilibrium of (10.17) corresponds to a stable limit cycle of the phase model.

All equilibria of (10.17) are solutions to $G(\chi) = -\omega$, and they are intersections of the horizontal line $-\omega$ with the graph of G, as illustrated in Fig.10.30a. They are stable if the slope of the graph is negative at the intersection. If the oscillators are identical, then $G(\chi) = H(-\chi) - H(\chi)$ is an odd function (i.e., $G(-\chi) = -G(\chi)$), and $\chi = 0$ and $\chi = T/2$ are always equilibria (possibly unstable) corresponding to the in-phase and anti-phase synchronized solutions. The stability condition of the in-phase synchronized state is

$$G'(0) = -2H'(0) < 0 \qquad \text{(stability of in-phase synchronization)}$$

The in-phase synchronization of electrically (gap-junction) coupled oscillators in Fig.10.26 is stable because the slope of G (dashed curves) is negative at $\chi = 0$. Simulation of two coupled $I_{Na} + I_K$-oscillators in Fig.10.25 confirms that. Coupled oscillators in the Class 2 regime also have a stable anti-phase solution, since $G' < 0$ at $\chi = T/2$ in Fig.10.30a.

The max and min values of the function G determine the tolerance of the network for the frequency mismatch ω, since there are no equilibria outside this range. Geometrically, as ω increases (the second oscillator speeds up), the horizontal line $-\omega$ in Fig.10.30a slides downward, and the phase difference $\chi = \varphi_2 - \varphi_1$ increases, compensating for the frequency mismatch ω. When $\omega > - \min G$, the second oscillator becomes too fast, and the synchronized state is lost via saddle-node on invariant circle bifurcation (see Fig.10.30b). This bifurcation corresponds to the annihilation of stable and unstable limit cycles of the weakly coupled network, and the resulting activity is called *drifting*, *cycle slipping*, or *phase walk-through*. The variable χ slowly passes the ghost of the saddle-node point, where $G(\chi) \approx 0$, then increases past T, appears at 0, and approaches the ghost again, thereby slipping a cycle and walking through all the phase values $[0, T]$. The frequency of such slipping scales as $\sqrt{\omega + \min G}$; see section 6.1.2.
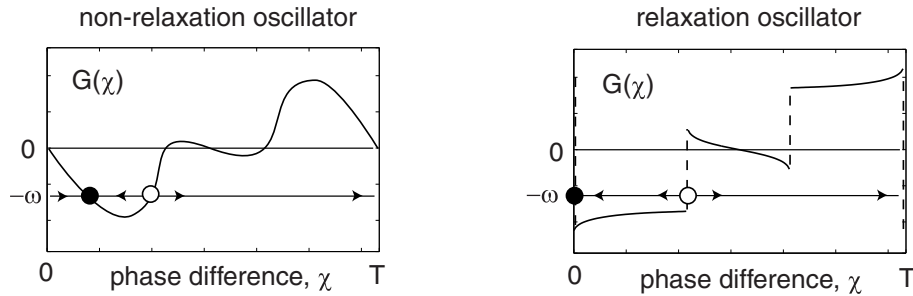
Figure 10.31: Functions $G(\chi)$ for weakly coupled oscillators of non-relaxation (smooth) and relaxation types. The frequency mismatch ω creates a phase difference in the smooth case, but not in the relaxation case.

In Fig.10.31 we contrast synchronization properties of weakly coupled oscillators of relaxation and non-relaxation type. The function $G(\chi)$ of the former has a negative discontinuity at $\chi = 0$ (section 10.4.4). An immediate consequence is that the in-phase synchronization is rapid and persistent in the presence of the frequency mismatch ω. Indeed, if G is smooth, then χ slows down while it approaches the equilibrium $\chi = 0$. As a result, complete synchronization is an asymptotic process that requires an infinite period of time to attain. In contrast, when G is discontinuous at 0, the variable χ does not slow down, and it takes a finite period of time to lock. Changing the frequency mismatch ω shifts the root of $-\omega = G(\chi)$ in the continuous case, but not in the discontinuous case. Hence, the in-phase synchronized state $\chi = 0$ of coupled relaxation oscillators exists and is stable in a wide range of ω.

10.3.2 Chains

Understanding the synchronization properties of two coupled oscillators helps one in studying the dynamics of chains of $n > 2$ oscillators

$$\varphi_i' = \omega_i + H^+(\varphi_{i+1} - \varphi_i) + H^-(\varphi_{i-1} - \varphi_i) \,, \tag{10.18}$$

where the functions H^+ and H^- describe the coupling in the ascending and descending directions of the chain, as in Fig.10.32. Any phase-locked solution of (10.18) has the form $\varphi_i(\tau) = \omega_0\tau + \phi_i$, where ω_0 is the common frequency of oscillation and ϕ_i are constants. These satisfy n conditions

$$
\begin{aligned}
\omega_0 &= \omega_1 + H^+(\phi_2 - \phi_1) \,, \\
\omega_0 &= \omega_i + H^+(\phi_{i+1} - \phi_i) + H^-(\phi_{i-1} - \phi_i) \,, \qquad i = 2, \ldots, n-1 \,, \\
\omega_0 &= \omega_n + H^-(\phi_{n-1} - \phi_n) \,.
\end{aligned}
$$

A solution with $\phi_1 < \phi_2 < \cdots < \phi_n$ or with $\phi_1 > \phi_2 > \cdots > \phi_n$ (as in Fig.10.32) is called a *traveling wave*. Indeed, the oscillators oscillate with a common frequency ω_0 but with different phases that increase or decrease monotonically along the chain.
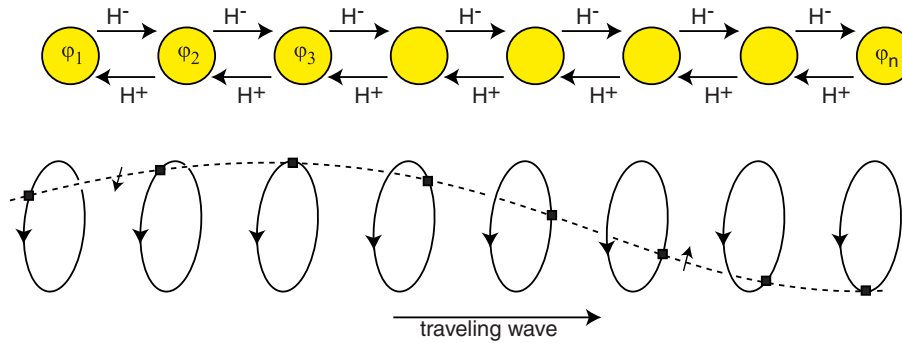
Figure 10.32: Traveling wave solutions in chains of oscillators (10.18) describe undulatory locomotion and central pattern generation.

Such a behavior is believed to correspond to central pattern generation (CPG) in crayfish, undulatory locomotion in lampreys and dogfish, and peristalsis in vascular and intestinal smooth muscles. Below we consider two fundamentally different mechanisms of generation of traveling waves.

Frequency Differences

Suppose the connections in (10.18) look qualitatively similar to those in Fig.10.26, in particular, $H^+(0) = H^-(0) = 0$. If the frequencies are all equal, then the in-phase synchronized solution $\varphi_1 = \cdots = \varphi_n$ exists and is stable. A traveling wave exists when the frequencies are not all equal.

Let us seek the conditions for the existence of a traveling wave with a constant phase shift, say $\chi = \phi_{i+1} - \phi_i$, along the chain. Subtracting each equation from the second one, we find that

$$0 = \omega_2 - \omega_1 + H^-(-\chi)\,, \qquad 0 = \omega_2 - \omega_i\,, \qquad 0 = \omega_2 - \omega_n + H^+(\chi)\,,$$

and $\omega_0 = \omega_1 + \omega_n - 2\omega_2$. In particular, if $\omega_1 \leq \omega_2 = \cdots = \omega_{n-1} \leq \omega_n$, which corresponds to the first oscillator being tuned up and the last oscillator being tuned down, then $\chi < 0$ and the traveling wave moves upward, as in Fig.10.32, that is, from the fastest to the slowest oscillator. Interestingly, such an ascending wave exists even when $H^- = 0$, that is, even when the coupling is only in the opposite, descending direction.

When there is a linear gradient of frequencies ($\omega_1 > \omega_2 > \cdots > \omega_n$ or vice versa), as in the cases of the smooth muscle of intestines or leech CPG for swimming, one may still observe a traveling wave, but with a non-constant phase difference along the chain. When the gradient is large enough, the synchronized solution corresponding to a single traveling wave disappears, and frequency plateaus may appear (Ermentrout and Kopell 1984). That is, solutions occur in which the first $k < n$ oscillators are phase-locked and the last $n - k$ oscillators are phase-locked as well, but the two pools, forming two clusters, oscillate with different frequencies. There may be many frequency plateaus.

Coupling Functions

A traveling wave solution may exist even when all the frequencies are equal, if either $H^+(0) \neq 0$ or $H^-(0) \neq 0$. As an example, consider the case of descending coupling $(H^- = 0)$

$$\varphi_i' = \omega + H^+(\varphi_{i+1} - \varphi_i) , \qquad i = 1, \ldots, n-1 .$$

From $\varphi_n' = \omega$ we find that $\omega_0 = \omega$, that is, the common frequency is the frequency of the free oscillation of the last, uncoupled oscillator. The phase lag along the chain, $\chi = \varphi_{i+1} - \varphi_i$, satisfies $n-1$ identical conditions $0 = H^+(\chi)$. Thus, the traveling wave with a constant phase shift exists when H^+ has a zero crossing with positive slope, in contrast to Fig.10.26. The sign of χ, and not the direction of coupling, determines the direction of wave propagation.

10.3.3 Networks

Now let us consider weakly connected networks (10.11) with arbitrary, possibly all-to-all coupling. To study synchronized states of the network, we need to determine whether the corresponding phase model (10.15) has equilibria and to examine their stability properties. A vector $\phi = (\phi_1, \ldots, \phi_n)$ is an equilibrium of (10.15) when

$$0 = \omega_i + \sum_{j \neq 1}^{n} H_{ij}(\phi_j - \phi_i) \qquad \text{for all } i . \tag{10.19}$$

It is stable when all eigenvalues of the linearization matrix (Jacobian) at ϕ have negative real parts, except one zero eigenvalue corresponding to the eigenvector along the circular family of equilibria (ϕ plus a phase shift is a solution of (10.19), too, since the phase differences $\phi_j - \phi_i$ are not affected).

In general, determining the stability of equilibria is a difficult problem. Ermentrout (1992) found a simple sufficient condition. Namely, if

- $a_{ij} = H_{ij}'(\phi_j - \phi_i) \geq 0$, and

- the directed graph defined by the matrix $a = (a_{ij})$ is connected (i.e., each oscillator is influenced, possibly indirectly, by every other oscillator),

then the equilibrium ϕ is neutrally stable, and the corresponding limit cycle $x(t + \phi)$ of (10.11) is asymptotically stable.

Another sufficient condition was found by Hoppensteadt and Izhikevich (1997). It states that if system (10.15) satisfies

- $\omega_1 = \cdots = \omega_n = \omega$ (identical frequencies) and

- $H_{ij}(-\chi) = -H_{ji}(\chi)$ (pairwise odd coupling)

for all i and j, then the network dynamics converge to a limit cycle. On the cycle, all oscillators have equal frequencies $1 + \varepsilon\omega$ and constant phase deviations.

The proof follows from the observation that (10.15) is a gradient system in the rotating coordinates $\varphi = \omega\tau + \phi$, with the energy function

$$E(\phi) = \frac{1}{2} \sum_{i=1}^{n} \sum_{j=1}^{n} R_{ij}(\phi_j - \phi_i) , \qquad \text{where} \qquad R_{ij}(\chi) = \int_0^{\chi} H_{ij}(s) \, ds .$$

One can check that $dE(\phi)/d\tau = -\sum(\phi_i')^2 \leq 0$ along the trajectories of (10.15), with equality only at equilibria.

10.3.4   Mean-Field Approximations

Synchronization of the phase model (10.15) with randomly distributed frequency deviations ω_i can be analyzed in the limit $n \to \infty$, often called the thermodynamic limit by physicists. We illustrate the theory using the special case $H(\chi) = \sin\chi$ (Kuramoto 1975)

$$\varphi_i' = \omega_i + \frac{K}{n} \sum_{j=1}^{n} \sin(\varphi_j - \varphi_i) , \qquad \varphi_i \in [0, 2\pi] , \tag{10.20}$$

where $K > 0$ is the coupling strength and the factor $1/n$ ensures that the model behaves well as $n \to \infty$. The complex-valued sum of all phases,

$$re^{\mathrm{i}\psi} = \frac{1}{n} \sum_{j=1}^{n} e^{\mathrm{i}\varphi_j} \qquad \text{(Kuramoto synchronization index)}, \tag{10.21}$$

describes the degree of synchronization in the network. The parameter r is often called the *order parameter* by physicists. Apparently, the in-phase synchronized state $\varphi_1 = \cdots = \varphi_n$ corresponds to $r = 1$, with ψ being the population phase. In contrast, the *incoherent* state, with all φ_i having different values randomly distributed on the unit circle, corresponds to $r \approx 0$. (The case $r \approx 0$ can also correspond to two or more clusters of synchronized neurons, oscillating anti-phase or out-of-phase and canceling each other.) Intermediate values of r correspond to a *partially synchronized* or *coherent* state, depicted in Fig.10.33. Some phases are synchronized in a cluster, while others roam around the circle.

Multiplying both sides of (10.21) by $e^{-\mathrm{i}\varphi_i}$ and considering only the imaginary parts, we can rewrite (10.20) in the equivalent form

$$\varphi_i' = \omega_i + Kr \sin(\psi - \varphi_i) ,$$

which emphasizes the mean-filed character of interactions between the oscillators: they are all pulled into the synchronized cluster ($\varphi_i \to \psi$) with the effective strength proportional to the cluster size r. This pull is offset by the random frequency deviations ω_i, which pull away from the cluster.
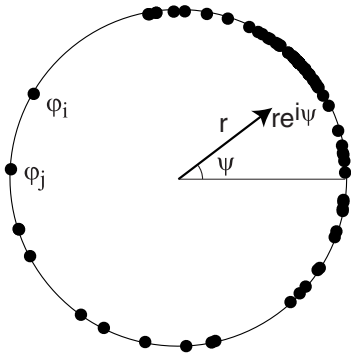
Figure 10.33: The Kuramoto synchronization index (10.21) describes the degree of coherence in the network (10.20).

Let us assume that the frequencies ω_i are distributed randomly around 0 with a symmetric probability density function $g(\omega)$ (e.g., Gaussian). Kuramoto (1975) has shown that in the limit $n \to \infty$, the cluster size r obeys the self-consistency equation

$$r = rK \int_{-\pi/2}^{+\pi/2} g(rK \sin \varphi) \cos^2 \varphi \, d\varphi \qquad (10.22)$$

derived in exercise 21. Note that $r = 0$, corresponding to the incoherent state, is always a solution of this equation. When the coupling strength K is greater than a certain critical value,

$$K_{\mathrm{c}} = \frac{2}{\pi g(0)} \; ,$$

an additional, nontrivial solution $r > 0$ appears, which corresponds to a partially synchronized state. It scales as $r = \sqrt{16(K - K_{\mathrm{c}})/(-g''(0)\pi K_{\mathrm{c}}^4)}$, as the reader can prove by expanding g in a Taylor series. Thus, the stronger the coupling K relative to the random distribution of frequencies, the more oscillators synchronize into a coherent cluster. The issue of stability of incoherent and partially synchronized states is discussed by Strogatz (2000).

10.4   Examples

Below we consider simple examples of oscillators to illustrate the theory developed in this chapter. Our goal is to understand which details of oscillators are important in shaping the PRC, the form of the function H in the phase deviation model, and, hence, the existence and stability of synchronized states.

10.4.1   Phase Oscillators

Let us consider the simplest possible kind of a nonlinear oscillator, known as the *phase oscillator*:

$$\dot{x} = f(x) + \varepsilon p(t) \; , \qquad x \in \mathbb{S}^1 \; , \qquad (10.23)$$

where $f(x) > 0$ is a periodic function, for example, $f(x) = a + \sin x$ with $a > 1$. Note that this kind of oscillator is quite different from the two- or high-dimensional

conductance-based models with limit cycle attractors that we considered in the earlier chapters. Here, the state variable x is one-dimensional, defined on a circle $\mathbb{S}^1$. It may be interpreted as a measure of distance along a limit cycle attractor of a multi-dimensional system.

Consider the unperturbed ($\varepsilon = 0$) phase oscillator $\dot{x} = f(x)$, and let $x(t)$ be its solution with some period $T > 0$. Following Kuramoto's idea, we substitute $x(\vartheta)$ into (10.23) and use the chain rule,

$$f(x(\vartheta)) + \varepsilon p(t) = \{x(\vartheta)\}' = x'(\vartheta)\, \vartheta' = f(x(\vartheta))\vartheta' \ ,$$

to get the new phase equation

$$\dot{\vartheta} = 1 + \varepsilon p(t)/f(x(\vartheta)) \ , \tag{10.24}$$

which is equivalent to (10.23) for any, not necessarily small, ε.

We can also obtain (10.24) by using any of the three methods of reduction of oscillators to phase models:

- *Malkin's* method is the easiest one. We do not even have to solve the one-dimensional adjoint equation (10.10) having the form $\dot{Q} = -f'(x(t))\,Q$, because we can obtain the solution $Q(t) = 1/f(x(t))$ directly from the normalization condition $Q(t)f(x(t)) = 1$.

- *Kuramoto's* method relies on the function $\vartheta(x)$, which we can find implicitly. Since the phase at a point $x(t)$ on the limit cycle is t, $x(\vartheta)$ is the inverse of $\vartheta(x)$. Using the rule for differentiating of inverse functions, $\vartheta'(x) = 1/x'(\vartheta)$, we find $\operatorname{grad}\vartheta = 1/f(x(\vartheta))$.

- *Winfree's* method relies on PRC (ϑ), which we find using the following procedure: A pulsed perturbation at phase ϑ moves the solution from $x(\vartheta)$ to $x(\vartheta) + A$, which is $x(\vartheta + \text{PRC}\,(\vartheta, A)) \approx x(\vartheta) + x'(\vartheta)\text{PRC}\,(\vartheta, A)$ when A is small. Hence, PRC $(\vartheta, A) \approx A/x'(\vartheta) = A/f(x(\vartheta))$, and the linear response is $Z(\vartheta) = 1/f(x(\vartheta))$ when $A \to 0$.

Two coupled identical oscillators

$$\begin{aligned} \dot{x}_1 &= f(x_1) + \varepsilon g(x_2) \\ \dot{x}_2 &= f(x_2) + \varepsilon g(x_1) \end{aligned}$$

can be reduced to the phase model (10.17) with $G(\chi) = H(-\chi) - H(\chi)$, where

$$H(\chi) = \frac{1}{T}\int_0^T Q(t)\, g(x(t+\chi))\, dt = \frac{1}{T}\int_0^T \frac{g(x(t+\chi))}{f(x(t))}\, dt \ .$$

The condition for exponential stability of the in-phase synchronized state, $\chi = 0$, can be expressed in the following three equivalent forms

$$\int_0^T g'(x(t))\, dt > 0 \quad \text{or} \quad \int_{\mathbb{S}^1} \frac{g'(x)}{f(x)}\, dx > 0 \quad \text{or} \quad \int_{\mathbb{S}^1} \frac{f'(x)}{f^2(x)}\, g(x)\, dx > 0 \ , \tag{10.25}$$

as we prove in exercise 24.
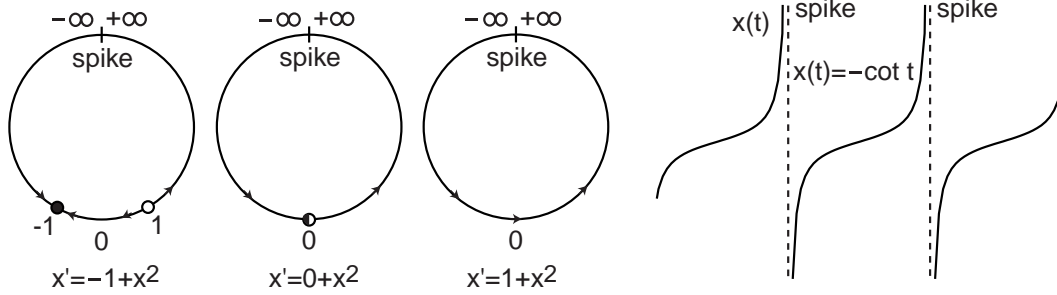
Figure 10.34: Phase portraits and typical oscillations of the quadratic integrate-and-fire neuron $\dot{x} = I + x^2$ with $x \in \mathbb{R} \cup \{\pm\infty\}$. Parameter: $I = -1, 0, +1$.
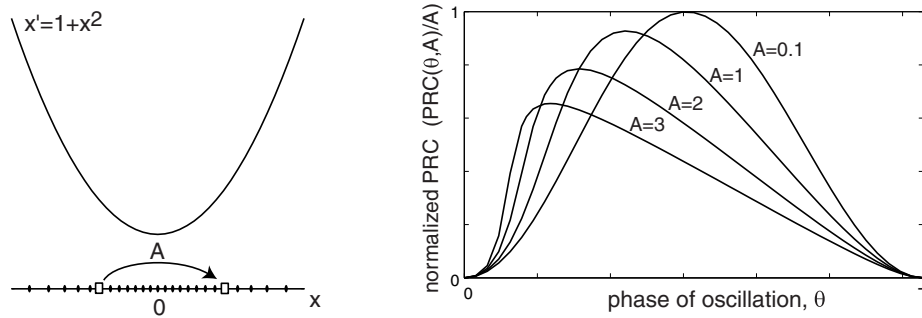
Figure 10.35: The dependence of the PRC of the quadratic integrate-and-fire model on the strength of the pulse A.

10.4.2 SNIC Oscillators

Let us go through all the steps of derivation of the phase equation using a neuron model exhibiting low-frequency periodic spiking. Such a model is near the saddle-node on invariant circle (SNIC) bifurcation studied in section 6.1.2. Appropriate rescaling of the membrane potential and time converts the model into the normal form

$$x' = 1 + x^2 , \qquad x \in \mathbb{R} .$$

Because of the quadratic term, x escapes to infinity in a finite time, producing a spike depicted in Fig.10.34. If we identify $-\infty$ and $+\infty$, then x exhibits periodic spiking of infinite amplitude. Such a spiking model is called a quadratic integrate-and-fire (QIF) neuron (see also section 8.1.3 for some generalizations of the model).

Strong Pulse

The solution of this system, starting at the spike, that is, at $x(0) = \pm\infty$, is

$$x(t) = -\cot t ,$$

as the reader can check by differentiating. It is a periodic function with $T = \pi$; hence, we can introduce the phase of oscillation via the relation $x = -\cot \vartheta$. The

corresponding PRC can be found explicitly (see exercise 9) and it has the form

$$\mathrm{PRC}\,(\vartheta, A) = \pi/2 + \mathrm{atan}\,(A - \cot \vartheta) - \vartheta \;,$$

depicted in Fig.10.35, where A is the magnitude of the pulse. Note that the PRC tilts to the left as A increases. Indeed, the density of isochrons, denoted by black points on the x-axis in the figure, is maximal at the ghost of the saddle-node point $x = 0$, where the parabola $1 + x^2$ has the knee. This corresponds to the inflection point of the graph of $x(t)$ in Fig.10.34, where the dynamics of $x(t)$ is the slowest. The effect of a pulse is maximal just before the ghost because x can jump over the ghost and skip the slow region. The stronger the pulse, the earlier it should arrive; hence the tilt.

Weak Coupling

The PRC behaves as $A \sin^2 \vartheta$, with $\vartheta \in [0, \pi]$, when A is small, as the reader can see in Fig.10.35 or prove by differentiating the function $\mathrm{PRC}\,(\vartheta, A)$ with respect to A. Therefore, $Z(\vartheta) = \sin^2 \vartheta$, and we can use Winfree's approach to transform the weakly perturbed quadratic integrate-and-fire (QIF) oscillator

$$x' = 1 + x^2 + \varepsilon p(t)$$

into its phase model

$$x' = 1 + \varepsilon(\sin^2 \vartheta)p(t) \;, \qquad \vartheta \in [0, \pi] \;.$$

The results of the previous section, $Q(\vartheta) = 1/f(x(\vartheta)) = 1/(1 + \cot^2 \vartheta) = \sin^2 \vartheta$, confirm the phase model. In fact, any neuronal model $C\dot{V} = I - I_\infty(V)$ near saddle-node on invariant circle bifurcation point $(I_{\mathrm{sn}}, V_{\mathrm{sn}})$ has infinitesimal PRC:

$$\mathrm{PRC}\,(\vartheta) = \frac{C}{I - I_{\mathrm{sn}}} \sin^2 \vartheta \;, \qquad \vartheta \in [0, \pi] \;,$$

as the reader can prove as an exercise. The function $\sin^2 \vartheta$ has the same form as $(1 - \cos \theta)$ if we change variables $\theta = 2\vartheta$ (notice the font difference). The change of variables scales the period from π to 2π.

In Fig.10.36a we compare the function with numerically obtained PRCs for the $I_{\mathrm{Na}} + I_{\mathrm{K}}$-model in the Class 1 regime. Since the ghost of the saddle-node point, revealing itself as an inflection of the voltage trace in Fig.10.36b, moves to the right as I increases away from the bifurcation value $I = 4.51$, so does the peak of the PRC.

Figure 10.36a emphasizes the common features of all systems undergoing saddle-node on invariant circle bifurcation: they are insensitive to the inputs arriving during the spike, since $\mathrm{PRC} \approx 0$ when $\vartheta \approx 0, T$. The oscillators are most sensitive to the input when they are just entering the ghost of the resting state, where PRC is maximal. The location of the maximum tilts to the left as the strength of the input increases, and may tilt to the right as the distance to the bifurcation increases. Finally, PRCs are non-negative, so positive (negative) inputs can only advance (delay) the phase of oscillation.
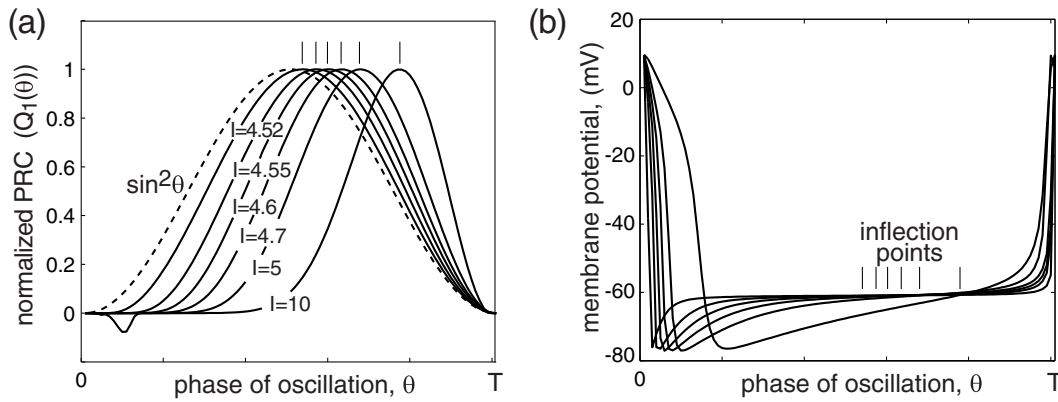
Figure 10.36: (a) Numerically found PRCs of the $I_{\text{Na}} + I_{\text{K}}$-oscillator in Class 1 regime (parameters as in Fig.4.1a) and various I using the MATLAB program in exercise 12. (b) Corresponding voltage traces show that the inflection point (slowest increase) of V moves right as I increases.

Gap Junctions

Now consider two oscillators coupled via gap junctions (discussed in section 2.3.4):

$$
\begin{aligned}
x_1' &= 1 + x_1^2 + \varepsilon(x_2 - x_1) \,, \\
x_2' &= 1 + x_2^2 + \varepsilon(x_1 - x_2) \,.
\end{aligned}
$$

Let us determine the stability of the in-phase synchronized state $x_1 = x_2$. The corresponding phase model (10.12) has the form

$$
\begin{aligned}
\vartheta_1' &= 1 + \varepsilon(\sin^2 \vartheta_1)(\cot \vartheta_1 - \cot \vartheta_2) \,, \\
\vartheta_2' &= 1 + \varepsilon(\sin^2 \vartheta_2)(\cot \vartheta_2 - \cot \vartheta_1) \,.
\end{aligned}
$$

The function (10.16) can be found analytically:

$$
H(\chi) = \frac{1}{\pi} \int_0^\pi \sin^2 t \left(\cot t - \cot(t + \chi) \right) \, dt = \frac{1}{2} \sin 2\chi \,,
$$

so that the model in the phase deviation coordinates, $\vartheta(t) = t + \varphi$, has the form

$$
\begin{aligned}
\varphi_1' &= (\varepsilon/2) \sin\{2(\varphi_2 - \varphi_1)\} \,, \\
\varphi_2' &= (\varepsilon/2) \sin\{2(\varphi_1 - \varphi_2)\} \,.
\end{aligned}
$$

The phase difference, $\chi = \varphi_2 - \varphi_1$, satisfies the equation (compare with Fig.10.26)

$$
\chi' = -\varepsilon \sin 2\chi \,,
$$

and, apparently, the in-phase synchronized state, $\chi = 0$, is always stable while the anti-phase state $\chi = \pi/2$ is not.

Weak Pulses

Now consider two weakly pulse-coupled oscillators

$$
\begin{aligned}
x_1' &= 1 + x_1^2 + \varepsilon_1 \delta(t - t_2) \,, \\
x_2' &= 1 + x_2^2 + \varepsilon_2 \delta(t - t_1) \,,
\end{aligned}
$$

where t_1 and t_2 are the moments of firing $(x(t) = \infty)$ of the first and the second oscillator, respectively, and ε_1 and ε_2 are the strengths of synaptic connections. The corresponding phase model (10.12) has the form

$$
\begin{aligned}
\vartheta_1' &= 1 + \varepsilon_1 (\sin^2 \vartheta_1) \delta(t - t_2) \\
\vartheta_2' &= 1 + \varepsilon_2 (\sin^2 \vartheta_2) \delta(t - t_1) \,.
\end{aligned}
$$

Since

$$
H(\chi) = \frac{1}{\pi} \int_0^\pi \sin^2 t \, \delta(t + \chi) \, dt = \frac{1}{\pi} \sin^2 \chi \,,
$$

the corresponding phase deviation model (10.15) is

$$
\begin{aligned}
\varphi_1' &= \frac{\varepsilon_1}{\pi} \sin^2(\varphi_2 - \varphi_1) \,, \\
\varphi_2' &= \frac{\varepsilon_2}{\pi} \sin^2(\varphi_1 - \varphi_2) \,.
\end{aligned}
$$

The phase difference $\chi = \varphi_2 - \varphi_1$ satisfies the equation

$$
\chi' = \frac{\varepsilon_2 - \varepsilon_1}{\pi} \sin^2 \chi,
$$

which becomes $\chi' = 0$ when the coupling is symmetric. In this case, the oscillators preserve (on average) the initial phase difference. When $\varepsilon_1 \neq \varepsilon_2$, the in-phase synchronized state $\chi = 0$ is only neutrally stable. Interestingly, it becomes exponentially unstable in a network of three or more pulse-coupled Class 1 oscillators (see exercise 23).

Weak Pulses with Delays

The synchronization properties of weakly pulse-coupled oscillators can change significantly when explicit axonal conduction delays are introduced. As an example, consider the system

$$
\begin{aligned}
x_1' &= 1 + x_1^2 + \varepsilon \delta(t - t_2 - d) \,, \\
x_2' &= 1 + x_2^2 + \varepsilon \delta(t - t_1 - d) \,,
\end{aligned}
$$

where $d \geq 0$ is the delay. exercise 18 shows that delays introduce simple phase shifts, so that the phase model has the form

$$
\begin{aligned}
\varphi_1' &= \frac{\varepsilon}{\pi} \sin^2(\varphi_2 - \varphi_1 - d) \,, \\
\varphi_2' &= \frac{\varepsilon}{\pi} \sin^2(\varphi_1 - \varphi_2 - d) \,,
\end{aligned}
$$
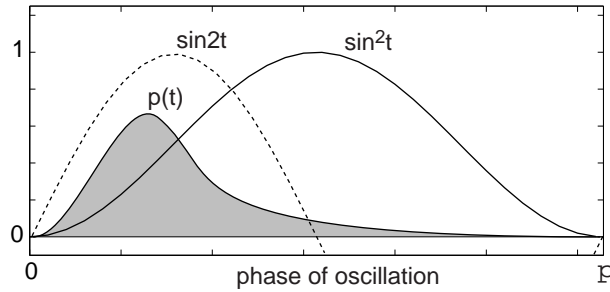
Figure 10.37: Synaptic transmission function $p(t)$ typically has an asymmetric shape with fast rise and slow decay.

The phase difference $\chi = \varphi_2 - \varphi_1$ satisfies

$$\chi' = \frac{\varepsilon}{\pi} \left(\sin^2(\chi + d) - \sin^2(\chi - d) \right) = \frac{\varepsilon \sin 2d}{\pi} \sin 2\chi \ .$$

The stability of synchronized states is determined by the sign of the function $\sin 2d$. The in-phase state $\chi = 0$ is unstable when $\sin 2d > 0$, that is, when the delay is shorter than the half-period $\pi/2$, stable when the delay is longer than the half-period but shorter than one period π, unstable for even longer delays, and so on. The stability of the anti-phase state $\chi = \pi/2$ is reversed, that is, it is stable for short delays, unstable for longer delays, then stable again for even longer delays, and so on. Finally, when the pulses are inhibitory ($\varepsilon < 0$), the (in)stability character is flipped so that the in-phase state becomes stable for short delays.

Weak Synapses

Now suppose that each pulse is not a delta function, but is smeared in time (i.e., it has a time course $p(t - t_i)$ with $p(0) = p(\pi) = 0$). That is, the synaptic transmission starts right after the spike of the presynaptic neuron and ends before the onset of the next spike. The function p has a typical unimodal shape with fast rise and slow decay, depicted in Fig.10.37. The discussion below is equally applicable to the case of $p(t, x) = g(t)(E - x)$ with $g > 0$ being the synaptic conductance with the shape in the figure and E being the synaptic reverse potential, positive (negative) for excitatory (inhibitory) synapses.

Two weakly synaptically coupled SNIC (Class 1) oscillators

$$\begin{aligned} x_1' &= 1 + x_1^2 + \varepsilon p(t - t_2) \ , \\ x_2' &= 1 + x_2^2 + \varepsilon p(t - t_1) \end{aligned}$$

can be converted into a general phase model with the connection function (10.16) in the form

$$H(\chi) = \frac{1}{\pi} \int_0^\pi \sin^2 t \, p(t + \chi) \, dt \ ,$$
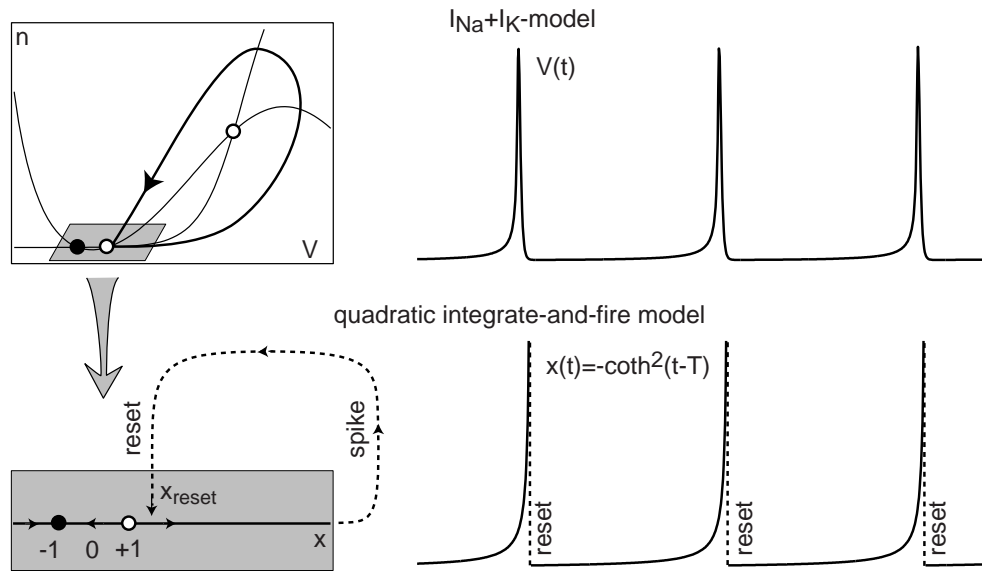
Figure 10.38: Top. Periodic spiking of the $I_{\text{Na}} + I_{\text{K}}$-neuron near saddle-node homoclinic orbit bifurcation (parameters as in Fig.4.1a with $\tau(V) = 0.167$ and $I = 4.49$). Bottom. Spiking in the corresponding quadratic integrate-and-fire model.

and it can be computed explicitly for some simple $p(t)$.

The in-phase synchronized solution, $\chi = 0$, is stable when

$$ H'(0) = \frac{1}{\pi} \int_0^\pi \sin^2 t\, p'(t)\, dt > 0 \ . $$

Since the function $\sin^2 t$ depicted in Fig.10.37 is small at the ends of the interval and large in the middle, the integral is dominated by the sign of p' in the middle. Fast-rising and slowly decaying excitatory $(p > 0)$ synaptic transmission has $p' < 0$ in the middle (as in the figure), so the integral is negative and the in-phase solution is unstable. In contrast, fast-rising slowly decaying inhibitory $(p < 0)$ synaptic transmission has $p' > 0$ in the middle, so the integral is positive and the in-phase solution is stable. Another way to see this is to integrate the equation by parts, reduce it to $-\int p(t) \sin 2t\, dt$, and note that $p(t)$ is concentrated in the first (left) half of the period, where $\sin 2t$ is positive. Hence, positive (excitatory) p results in $H'(0) < 0$, and vice versa. Both approaches confirm the theoretical results independently obtained by van Vreeswijk et al. (1994) and Hansel et al. (1995) that *inhibition, not excitation, synchronizes Class 1 (SNIC) oscillators.* The relationship is inverted for the anti-phase solution $\chi = \pi/2$ (the reader should prove this), and no relationships are known for other types of oscillators.

10.4.3   Homoclinic Oscillators

Besides the SNIC bifurcation considered above, low-frequency oscillations may also indicate the proximity of the system to a saddle homoclinic orbit bifurcation, as in
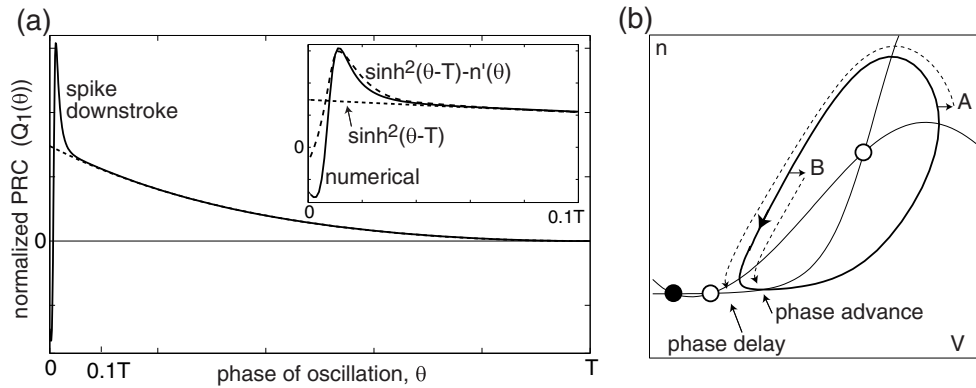
Figure 10.39: (a) Numerically found PRCs of the $I_{\mathrm{Na}} + I_{\mathrm{K}}$-oscillator near saddle-node homoclinic orbit bifurcation (as in Fig.10.38), using the MATLAB program in exercise 12. Magnification shows the divergence from the theoretical curve $\sinh^2(\vartheta - T)$ during the spike. (b) A pulsed input during the downstroke of the spike can produce a significant phase delay (pulse A) or advance (pulse B) not captured by the quadratic integrate-and-fire model.

Fig.10.38 (top). The spiking trajectory in the figure quickly approaches a small shaded neighborhood of the saddle along the stable direction, and then slowly diverges from the saddle along the unstable direction, thereby resulting in a large-period oscillation. As often the case in neuronal models, the saddle equilibrium is near a stable node equilibrium corresponding to the resting state, and the system is near the codimension-2 saddle-node homoclinic orbit bifurcation studied in section 6.3.6. As a result, there is a drastic difference between the attraction and divergence rates to the saddle, so that the dynamics in the shaded neighborhood of the saddle-node in the figure can be reduced to the one-dimensional V-equation, which in turn can be transformed into the "quadratic integrate-and-fire" form

$$x' = -1 + x^2 , \qquad \text{if } x = +\infty, \text{ then } x \leftarrow x_{\mathrm{reset}} ,$$

with solutions depicted in Fig.10.38 (bottom). The saddle and the node correspond to $x = +1$ and $x = -1$, respectively. One can check by differentiating that the solution of the model with $x(0) = x_{\mathrm{reset}} > 1$ is $x(t) = -\coth(t - T)$, where $\coth(s) = (e^s + e^{-s})/(e^s - e^{-s})$ is the hyperbolic cotangent and $T = \mathrm{acoth}(x_{\mathrm{reset}})$ is the period of oscillation, which becomes infinite as $x_{\mathrm{reset}} \to 1$.

Using the results of section 10.4.1, we find the function

$$Q(\vartheta) = 1/(-1 + \coth^2(\vartheta - T)) = \sinh^2(\vartheta - T)$$

whose graph is shown in Fig.10.39a. For comparison, we plotted the numerically found PRC for the $I_{\mathrm{Na}} + I_{\mathrm{K}}$-oscillator to illustrate the disagreement between the theoretical and numerical curves in the region $\vartheta < 0.1T$ corresponding to the downstroke of the spike. Such a disagreement is somewhat expected, since the quadratic integrate-and-fire model ignores spike downstroke. If a pulse arriving during the downstroke

displaces the trajectory to the exterior of the limit cycle (as in Fig.10.39b, pulse A), then the trajectory becomes closer to the saddle equilibrium when it reenters a small neighborhood of the saddle, thereby leading to a significant phase delay. Displacements to the interior of the cycle (as in Fig.10.39b, pulse B) push away from the saddle and lead to phase advances. The direction and the magnitude of displacements are determined by the derivative of the slow variable n' along the limit cycle.

The region of disagreement between theoretical and numerical PRCs becomes infinitesimal relative to $T \to \infty$ near the bifurcation. Theoretical PRC can be used to study anti-phase and out-of-phase synchronization of pulse-coupled oscillators, but not of in-phase synchronization, because the region of breakdown is the only important region in this case. Finally, note that as $T \to \infty$, the spiking limit cycle fails to be exponentially stable, and the theory of weakly coupled oscillators is no longer applicable to it.

Though the PRC in Fig.10.39 is quite different from the one corresponding to SNIC oscillators in Fig.10.36, there is an interesting similarity between these two cases: both can be reduced to quadratic integrate-and-fire neurons, and both have cotangent-shaped periodic spiking solutions and sine-squared-shape PRCs, except that they are "regular" in the SNIC case and hyperbolic in the homoclinic case (see also exercise 26).

10.4.4   Relaxation Oscillators and FTM

Consider two relaxation oscillators having weak fast $\to$ fast connections

$$
\begin{aligned}
\mu \dot{x}_i &= f(x_i, y_i) + \varepsilon p_i(x_i, x_k) , \\
\dot{y}_i &= g(x_i, y_i) ,
\end{aligned}
\tag{10.26}
$$

where $i = 1, 2$ and $k = 2, 1$. This system can be converted to a phase model in the relaxation limit $\varepsilon \ll \mu \to 0$ (Izhikevich 2000b). The connection functions $H_i(\chi)$ have a positive discontinuity at $\chi = 0$, which occurs because the x-coordinate of the relaxation limit cycle is discontinuous at the jump points. Hence, the phase difference function $G(\chi) = H_2(-\chi) - H_1(\chi)$ has a negative discontinuity at $\chi = 0$ (depicted in Fig.10.31). This reflects the profound difference between behaviors of weakly coupled oscillators of the relaxation and non-relaxation types, discussed in section 10.3.1: The in-phase synchronized solution, $\chi = 0$, in the relaxation limit $\mu \to 0$ is stable and persistent in the presence of the frequency mismatch ω, and it has a rapid rate of convergence. The reduction to a phase model breaks down when $\varepsilon \gg \mu \to 0$, that is, when the connections are relatively strong. One can still analyze such oscillators in the special case considered below.

Fast Threshold Modulation

Consider (10.26) and suppose that $p_1 = p_2 = p$ is a piecewise constant function: $p = 1$ when the presynaptic oscillator, x_k, is on the right branch of the cubic x-nullcline corresponding to an active state, and $p = 0$ otherwise (see Fig.10.40a). Somers and
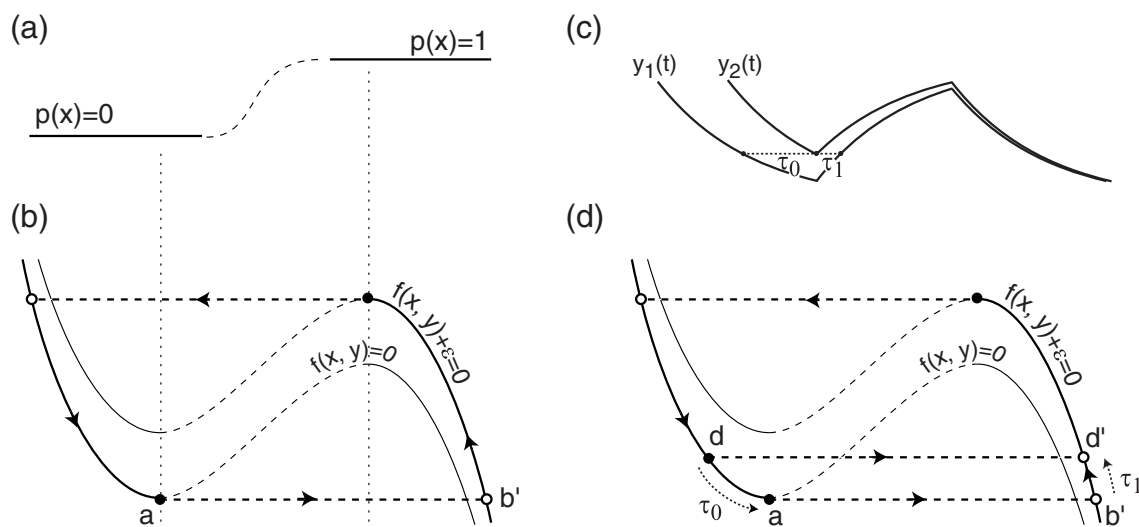
Figure 10.40: Fast threshold modulation of relaxation oscillation. (a) The Heaviside or sigmoidal coupling function $p(x)$ is constant while x is on the left or right branch of the x-nullcline. (b) In the relaxation limit $\mu = 0$, the synchronized limit cycle consists of the left branch of the nullcline $f(x, y) = 0$ and the right branch of the nullcline $f(x, y) + \varepsilon = 0$. When oscillator 1 is ahead of oscillator 2 (c), the phase difference between them decreases after the jump (d).

Kopell (1993, 1995) referred to such a coupling in the relaxation limit $\mu \to 0$ as fast threshold modulation (FTM), and found a simple criterion of stability of synchronized state that works even for strong coupling.

Since the oscillators are identical, the in-phase synchronized state exists, during which the variables x_1 and x_2 follow the left branch of the x-nullcline defined by $f(x, y) = 0$ (see Fig.10.40b) until they reach the jumping point a. During the instantaneous jump, they turn on the mutual coupling ε, and land at some point b' on the perturbed x-nullcline defined by $f(x, y) + \varepsilon = 0$. They follow the new nullcline to the right (upper) knee, and then jump back to the left branch.

To determine the stability of the in-phase synchronization, we consider the case when oscillator 1 is slightly ahead of oscillator 2, as in Fig.10.40c. We assume that the phase difference between the oscillators is so small – or alternatively, the strength of coupling is so large – that when oscillator 1 jumps and turns on its input to oscillator 2, the latter, being at point d in Fig.10.40d, is below the left knee of the perturbed x-nullcline $f(x, y) + \varepsilon = 0$ and therefore jumps, too. As a result, both oscillators jump to the perturbed x-nullcline and reverse their order. Although the apparent distance between the oscillators, measured by the difference of their y-coordinates, is preserved during such a jump, the phase difference between them usually is not.

The phase difference between two points on a limit cycle is the time needed to travel from one point to the other. Let $\tau_0(d)$ be the time needed to slide from point d to point a along the x-nullcline in Fig.10.40d (i.e., the phase difference just before

the jump). Let $\tau_1(d)$ be the time needed to slide from point b' to point d' (i.e., the phase difference after the jump). The phase difference between the oscillators during the jump changes by the factor $C(d) = \tau_1(d)/\tau_0(d)$, called the *compression function.* The difference decreases when the compression function $C(d) < 1$ uniformly for all d near the left knee a. This condition has a simple geometrical meaning: the rate of change of $y(t)$ is slower before the jump than after it, so that $y(t)$ has a "scalloped" shape, as in Fig.10.40c. As an exercise, prove that $C(d) \to |g(a)|/|g(b')|$ as $d \to a$.

If the compression function at the right (upper) knee is also less than 1, then the in-phase synchronization is stable. Indeed, the phase difference does not change while the oscillators slide along the nullclines, and it decreases geometrically with each jump. In fact, it suffices to require that the product of compression factors at the two knees be less than 1, so that any expansion at one knee is compensated for by even stronger compression at the other knee.

10.4.5   Bursting Oscillators

Let us consider bursting neurons coupled weakly through their fast variables:

$$\dot{x}_i = f(x_i, y_i) + \varepsilon p(x_i, x_j) , \qquad (10.27)$$
$$\dot{y}_i = \mu g(x_i, y_i) , \qquad (10.28)$$

$i = 1, 2$ and $j = 2, 1$. Since bursting involves two time scales, fast spiking and slow transition between spiking and resting, there are two synchronization regimes: spike synchronization and burst synchronization, illustrated in Fig.9.51 and discussed in section 9.4. Below, we outline some useful ideas and methods of studying both regimes. Our exposition is not complete, but it lays the foundation for a more detailed research program.

Spike Synchronization

To study synchronization of individual spikes within the burst, we let $\mu = 0$ in order to freeze the slow subsystem (10.28), and consider the fast subsystem (10.27) describing weakly coupled oscillators. When $y_i \approx y_j$, the fast variables oscillate with approximately equal periods, so (10.27) can be reduced to the phase model

$$\dot{\varphi}_i = \varepsilon H(\varphi_j - \varphi_i, \ y_i) ,$$

where $y_i = $ const parameterize the form of the connection function. For example, during the "circle/Hopf" burst, the function is transformed from $H(\chi) = \sin^2 \chi$ or $1 - \cos \chi$ at the beginning of the burst (saddle-node on invariant circle bifurcation) to $H(\chi) = \sin \chi$ at the end of the burst (supercritical Andronov-Hopf bifurcation). Changing y_i slowly, one can study when spike synchronization appears and when it disappears during the burst. When the slow variables y_i have different values, fast variables typically oscillate with different frequencies, so one needs to look at low-order resonances to study the possibility of spike synchronization.
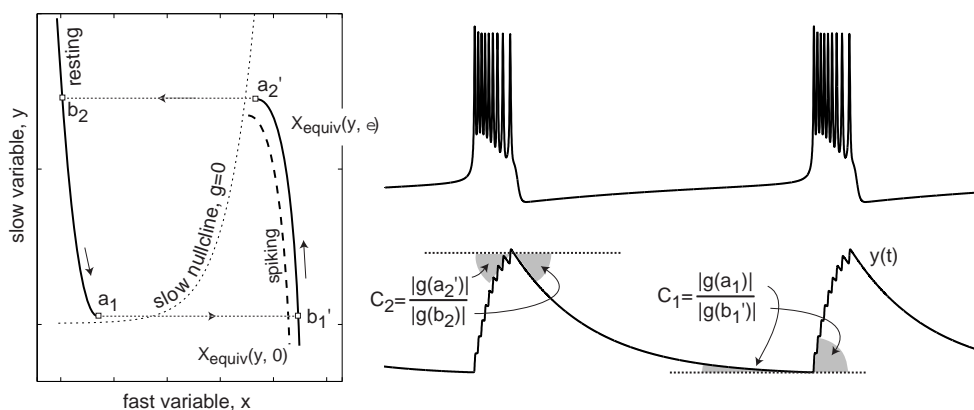
Figure 10.41: Reduction of the $I_{\mathrm{Na,p}}+I_{\mathrm{K}}+I_{\mathrm{K(M)}}$-burster to a relaxation oscillator. The slow variable exhibits "scalloped" oscillations needed for stability of in-phase burst synchronization. C_1 and C_2 are compression functions at the two jumps.

Burst synchronization

In chapter 9 we presented two methods, averaging and equivalent voltage, that remove fast oscillations and reduce bursters to slow relaxation oscillators. Burst synchronization is then reduced to synchronization of such oscillators, and it can be studied using phase reduction or fast threshold modulation (FTM) approaches.

To apply FTM, we assume that the coupling in (10.27) is piecewise constant, that is, $p(x_i, x_j) = 0$ when the presynaptic burster x_j is resting, and $p(x_i, x_j) = 1$ (or any function of x_i) when the presynaptic burster is spiking. We also assume that the slow subsystem (10.28) is one-dimensional, so that we can use the equivalent voltage method (section 9.2.4) and reduce the coupled system to

$$
\begin{aligned}
0 &= X_{\mathrm{equiv}}(y_i, \varepsilon p) - x_i \,, \\
y_i' &= g(x_i, y_i) \,.
\end{aligned}
$$

When the burster is of the hysteresis loop type (i.e., the resting and spiking states coexist), the function $x = X_{\mathrm{equiv}}(y, \varepsilon p)$ often, but not always, has a Z-shape on the slow/fast plane, as in Fig.9.16, so that the system corresponds to a relaxation oscillator with nullclines as in Fig.10.41. Fast threshold modulation occurs via the constant εp, which shifts the fast nullcline up or down. The compression criterion for stability of the in-phase burst synchronization, presented in the previous section, has a simple geometrical illustration in the figure. The slow nullcline has to be sufficiently close to the jumping points that $y(t)$ slows before each jump and produces the "scalloped" curve. Many hysteresis loop fast/slow bursters do generate such a shape. In particular, "fold/*" bursters exhibit robust in-phase burst synchronization when they are near the bifurcation from quiescence to bursting, since the slow nullcline is so close to the left knee that the compression during the resting $\rightarrow$ spiking jump (C_1 in Fig.10.41) dominates the expansion, if any, during the spiking $\rightarrow$ resting jump.

Review of Important Concepts

- Oscillations are described by their phase variables ϑ rotating on a circle $\mathbb{S}^1$. We define ϑ as the time since the last spike.

- The phase response curve, $\text{PRC}\,(\vartheta)$, describes the magnitude of the phase shift of an oscillator caused by a strong pulsed input arriving at phase ϑ.

- PRC depends on the bifurcations of the spiking limit cycle, and it defines synchronization properties of an oscillator.

- Two oscillators are synchronized in-phase, anti-phase, or out-of-phase when their phase difference, $\vartheta_2 - \vartheta_1$, equals 0, half-period, or some other value, respectively; see Fig.10.42.

- Synchronized states of pulse-coupled oscillators are fixed points of the corresponding Poincare phase map.

- Weakly coupled oscillators

$$\dot{x}_i = f(x_i) + \varepsilon \sum g_{ij}(x_j)$$

can be reduced to phase models

$$\dot{\vartheta}_i = 1 + \varepsilon \, Q(\vartheta_i) \sum g_{ij}(x_j(\vartheta_j)) \;,$$

where $Q(\vartheta)$ is the infinitesimal PRC defined by (10.10).

- Weak coupling induces a slow phase deviation of the natural oscillation, $\vartheta_i(t) = t + \varphi_i$, described by the averaged model

$$\dot{\varphi}_i = \varepsilon \left(\omega_i + \sum H_{ij}(\varphi_j - \varphi_i) \right) \;,$$

where ω_i denote the frequency deviations, and

$$H_{ij}(\varphi_j - \varphi_i) = \frac{1}{T} \int_0^T Q(t) \, g_{ij}(x_j(t + \varphi_j - \varphi_i)) \, dt$$

describes the interactions between the phases.

- Synchronization of two coupled oscillators corresponds to equilibria of the one-dimensional system

$$\dot{\chi} = \varepsilon(\omega + G(\chi)) \;, \qquad \chi = \varphi_2 - \varphi_1 \;,$$

where $G(\chi) = H_{21}(-\chi) - H_{12}(\chi)$ describes how the phase difference χ compensates for the frequency mismatch $\omega = \omega_2 - \omega_1$.
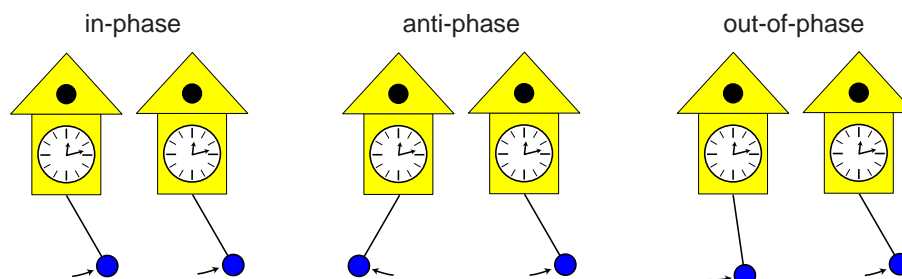
Figure 10.42: Different types of synchronization.

Bibliographical Notes

Surprisingly, this chapter turned out to be quite different from chapter 9 ("Weakly Connected Oscillators") of the book *Weakly Connected Neural Networks* by Hoppensteadt and Izhikevich (1997) and from the book *Synchronization: A Universal Concept in Nonlinear Sciences* by Pikovsky, Rosenblum, and Kurths (2001). All three texts, though devoted to the same subject, do not repeat, but rather complement, each other. The last provides an excellent historical overview of synchronization, starting with the work of the famous Dutch mathematician, astronomer, and physicist Christiaan Huygens (1629–1695), who was the first to describe synchronization of two pendulum clocks hanging from a common support (which was, incidentally, anti-phase). While providing many examples of synchronization of biological, chemical, and physical systems, the book by Pikovsky et al. also discusses the definition of a phase and synchronization of nonperiodic, e.g., chaotic, oscillators, a topic not covered here. A major part of *Spiking Neuron Models* by Gerstner and Kistler (2002) is devoted to synchronization of spiking neurons, with the emphasis on the integrate-and-fire model and the spike-response method.

The formalism of the phase response curve (PRC) was introduced by Hastings and Sweeney (1958), and it has been used extensively in the context of resetting the circadian rhythms. "Forty Years of PRC – What Have We Learned?" by Johnson (1999) gives a historical overview of this idea and some recent developments. John Guckenheimer (1975) used the theory of normally hyperbolic invariant manifolds to provide a mathematical foundation for the existence of isochrons, and their geometrical properties. An encyclopedic exposition on isochrons and phase-resettings in nature, as well as numerous anecdotes, can be found in Arthur Winfree's remarkable book *The Geometry of Biological Time* (1980, 2nd ed., 2001). In particular, Winfree describes the work of George R. Mines (1914), who was doing phase-resetting experiments by shocking rabbits at various phases of their heartbeat. He found the phase and shock that could stop a rabbit's heart (black hole in Fig.10.8), and then applied it to himself. He died.

Glass and Mackey (1988) provide a detailed exposition of circle phase maps. Although the structure of phase-locking regions in Fig.10.15 was discovered by Cartwright and Littlewood (1945), it is better known today as Arnold tongues (Arnold 1965). Gue-

Figure 10.43: Frank Hoppensteadt, the author's adviser and mentor, circa 1989.

vara and Glass (1982) found this structure analytically for the Andronov-Hopf oscillator in Fig.10.3 (radial isochron clock). Hoppensteadt (1997, 2000) provides many examples of oscillatory systems arising in biology and neuroscience (see also Hoppensteadt and Peskin 2002).

Malkin's method of reduction of coupled oscillators to phase equations has been known, at least to Russian scientists, since the early 1950s (Malkin 1949, 1956; Blechman 1971). For example, Melnikov (1963) applied Malkin's theorem to a homoclinic orbit of infinite period to obtain the transversality condition for the saddle homoclinic orbit bifurcation (Kuznetsov 1995).

Malkin's method was rediscovered in the West by Neu (1979), and hoorayed by Winfree (1980), who finally saw a mathematical justification for his usage of phase variables. Since then, the field of phase equations has been largely dominated by Bard Ermentrout and Nancy Kopell (Ermentrout 1981, 1986, 1992; Ermentrout and Kopell 1986a,b, 1990, 1991, 1994; Kopell and Ermentrout 1990; Kopell 1986; Kopell et al. 1991). In particular, they developed the theory of traveling wave solutions in chains of oscillators, building on the seminal paper by Cohen et al. (1982). Incidentally, the one-page proof of Malkin's theorem provided by Hoppensteadt and Izhikevich (1997, Sect. 9.6) is based on Ermentrout and Kopell's idea of using the Fredholm alternative; Malkin's and Neu's proofs are quite long, mostly because they reprove the alternative.

There are only a handful of examples in which the Malkin adjoint problem can be solved analytically (i.e., without resort to simulations). The SNIC, homoclinic and Andronov-Hopf cases are the most important, and have been considered in detail in this chapter. Brown et al. (2004) also derive PRCs for oscillators with homoclinic orbits to pure saddles (see exercise 25) and for Bautin oscillators.

Throughout this chapter we define the phase ϑ or φ on the interval $[0, T]$, where T is the period of free oscillation, and do not normalize it to be on the interval $[0, 2\pi]$.

Figure 10.44: Nancy Kopell in her Boston University office in 1990 (photograph provided by Dr. Kopell).

As a result, we have avoided the annoying terms $2\pi/T$ and $2\pi/\Omega$ in the formulas. The only drawback is that some of the results may have an "unfamiliar look", such as $\sin^2\vartheta$ with $\vartheta \in [0,\pi]$ for the PRC of Class 1 neurons, as opposed to $1-\cos\vartheta$ with $\vartheta \in [0,2\pi]$ used previously by many authors before.

Hansel, Mato, and Meunier (1995) were the first to note that the shape of the PRC determines the synchronization properties of synaptically coupled oscillators. Ermentrout (1996) related this result to the classification of oscillators and proved that PRCs of all Class 1 oscillators have the form of $1-\cos\vartheta$, though the proof can be found in his earlier papers with Kopell (Ermentrout and Kopell 1986a, 1986b). Reyes and Fetz (1993) measured the PRC of a cat neocortical neuron and largely confirmed the theoretical predictions. The experimental method in section 10.2.4 is related to that of Rosenblum and Pikovsky (2001). It needs to be developed further, for instance, by incorporating the measurement uncertainty (error bars). In fact, most experimentally obtained PRCs, including the one in Fig.10.24, are so noisy that nothing useful can be derived from them. This issue is the subject of active research.

Our treatment of the FTM theory in this volume closely follows that of Somers and Kopell (1993, 1995). Anti-phase synchronization of relaxation oscillators is analyzed using phase models by Izhikevich (2000b), and FTM theory, by Kopell and Somers (1995). Ermentrout (1994) and Izhikevich (1998) considered weakly coupled oscillators with axonal conduction delays and showed that delays result in mere phase shifts (see exercise 18). Frankel and Kiemel (1993) observed that slow coupling can be reduced to weak coupling. Izhikevich and Hoppensteadt (2003) used Malkin's theorem to extend the results to slowly coupled networks, and to derive useful formulas for the coupling functions and coefficients. Ermentrout (2003) showed that the result could be generalized to synapses having fast-rising and slow-decaying conductances. Goel

and Ermentrout (2002) and Katriel (2005) obtained interesting results on in-phase synchronization of identical phase oscillators.

Interactions between resonant oscillators were considered by Ermentrout (1981), Hoppensteadt and Izhikevich (1997), and Izhikevich (1999) in the context of quasi-periodic (multi-frequency) oscillations. Baesens et al. (1991) undertook the heroic task of studying resonances and toroidal chaos in a system of three coupled phase oscillators. Mean-field approaches to the Kuramoto model are reviewed by Strogatz (2000) and Acebron et al. (2005). Daido (1996) extended the theory to the general coupling function $H(\chi)$. van Hemmen and Wreszinski (1993) were the first to find the Lyapunov function for the Kuramoto model, which was generalized (independently) by Hoppensteadt and Izhikevich (1997) to the arbitrary coupling function $H(\chi)$.

Ermentrout (1986), Aronson et al. (1990), and Hoppensteadt and Izhikevich (1996, 1997) studied weakly coupled Andronov-Hopf oscillators, and discussed the phenomena of self-ignition (coupling-induced oscillations) and oscillator death (coupling-induced cessation of oscillation). Collins and Stewart (1993, 1994) and Golubitsky and Stewart (2002) applied group theory to the study of synchronization of coupled oscillators in networks with symmetries.

In this chapter we have considered either strong *pulsed* coupling or *weak* continuous coupling. These limitations are severe, but they allow us to derive model-independent results. Studying synchronization in networks of strongly coupled neurons is an active area of research, though, most such studies fall into two categories: (1) simulations and (2) integrate-and-fire networks. In both cases, the results are model-dependent. If the reader wants to pursue this line of research, he or she will definitely need to read Mirollo and Strogatz (1990), van Vreeswijk et al. (1994), Chow and Kopell (2000), Rubin and Terman (2000, 2002), Bressloff and Coombes (2000), van Vreeswijk (2000), van Vreeswijk and Hansel (2001), Pfeuty et al. (2003), and Hansel and Mato (2003).

Exercises

1. Find the isochrons of the Andronov-Hopf oscillator

$$\dot{z} = (1 + \mathrm{i})z - z|z|^2, \qquad z \in \mathbb{C},$$

   in Fig.10.3.

2. Prove that the isochrons of the Andronov-Hopf oscillator in the form

$$\dot{z} = (1 + \mathrm{i})z + (-1 + d\mathrm{i})z|z|^2, \qquad z \in \mathbb{C},$$

   are the curves

$$z(s) = s^{(-1+d\mathrm{i})}\, e^{\chi \mathrm{i}}, \qquad s > 0,$$

   where χ is the phase of the isochron (see Fig.10.45).
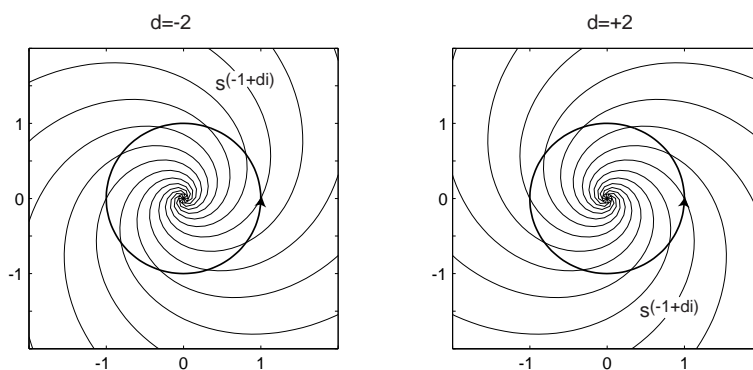
Figure 10.45: Isochrons of the Andronov-Hopf oscillator; see exercise 2.
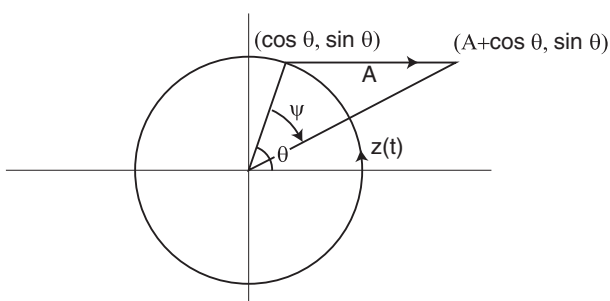
Figure 10.46: Pulsed stimulation of the Andronov-Hopf oscillator in Fig.10.3; see exercise 4.

3. [MATLAB] To determine isochrons of an oscillator $\dot{x} = F(x)$, one can start with many initial points near the limit cycle and integrate the system backwards, that is, $\dot{x} = -F(x)$. The images of the points at any time t lie on the same isochron. Write a MATLAB program that implements this algorithm.

4. Prove that the phase response curve of the Andronov-Hopf oscillator in Fig.10.3 is

$$\text{PRC}\,(\vartheta, A) = \begin{cases} -\psi & \text{when } 0 \leq \vartheta \leq \pi, \\ +\psi & \text{when } \pi \leq \vartheta \leq 2\pi, \end{cases} \tag{10.29}$$

where

$$\psi = \arccos \frac{1 + A\cos\vartheta}{\sqrt{1 + 2A\cos\vartheta + A^2}}$$

and A is the magnitude of the horizontal displacement of $z(t)$; see Fig.10.46.

5. [MATLAB] Write a program that stimulates an oscillator at different phases and determines its phase response curve (PRC).

6. Show that $Z(\vartheta) = \text{grad}\,\vartheta$, so that Winfree's phase model (10.6) is equivalent to Kuramoto's phase model (10.8).

7. Show that $Z(\vartheta) = Q(\vartheta)$, so that Winfree's phase model (10.6) is equivalent to Malkin's phase model (10.9).

8. Show that the PRC of the leaky integrate-and-fire neuron (section 8.1.1)

$$\dot{v} = b - v \,, \qquad \text{if } v \geq 1 \text{ (threshold), then } v \leftarrow 0 \text{ (reset)}$$

with $b > 1$ has the form

$$\text{PRC}\,(\vartheta) = \min\left\{\ln(b/(b\exp(-\vartheta) - A)), T\right\} - \vartheta \,,$$

where $T = \ln(b/(b-1))$ is the period of free oscillations and A is the amplitude of the pulse.

9. Prove that the quadratic integrate-and-fire neuron

$$\dot{v} = 1 + v^2 \,, \qquad \text{if } v = +\infty \text{ (peak of spike), then } v \leftarrow -\infty \text{ (reset)}$$

has $\text{PTC}\,(\vartheta) = \pi/2 + \text{atan}\,(A - \cot \vartheta)$.

10. Find the PRC of the quadratic integrate-and-fire neuron (section 8.1.3)

$$\dot{v} = b + v^2 \,, \qquad \text{if } v \geq 1 \text{ (peak of spike), then } v \leftarrow v_{\text{reset}} \text{ (reset)}$$

with $b > 0$.

11. Consider two mutually pulsed coupled oscillators with periods $T_1 \approx T_2$ and type 1 phase transition curves PTC_1 and PTC_2, respectively. Show that the locking behavior of the system can be described by the Poincare phase map

$$\chi_{n+1} = T_1 - \text{PTC}_1(T_2 - \text{PTC}_2(\chi_n)) \,,$$

where χ_n is the phase difference between the oscillators, that is, the phase of oscillator 2 when oscillator 1 fires a spike.

12. [MATLAB] Write a program that solves the adjoint equation (10.10) numerically. (Hint: Integrate the equation backward to achieve stability.)

13. [MATLAB] Write a program that finds the infinitesimal PRC using the relationship

$$\dot{\vartheta} = 1 + \text{PRC}\,(\vartheta)\ \varepsilon p(t) \,,$$

the moments of firings of a neuron (zero crossings of $\vartheta(t)$), and the injected current $\varepsilon p(t)$; see section 10.2.4 and Fig.10.24.

14. Use the approaches of Winfree, Kuramoto, and Malkin to transform the integrate-and-fire neuron $\dot{v} = b - v + \varepsilon p(t)$ in exercise 8 into its phase model

$$\dot{\vartheta} = 1 + \varepsilon\left(e^{\vartheta}/b\right)p(t) \,,$$

with $T = \ln(b/(b-1))$.

15. Use the approaches of Winfree, Kuramoto, and Malkin to transform the quadratic integrate-and-fire neuron $\dot{v} = 1 + v^2 + \varepsilon p(t)$ in exercise 9 into its phase model

$$\dot{\vartheta} = 1 + \varepsilon \left(\sin^2 \vartheta\right) p(t) ,$$

with $T = \pi$.

16. Use the approaches of Winfree, Kuramoto, and Malkin to transform the Andronov-Hopf oscillator $\dot{z} = (1 + \mathrm{i})z - z|z|^2 + \varepsilon p(t)$ with real $p(t)$ into its phase model

$$\dot{\vartheta} = 1 + \varepsilon \left(- \sin \vartheta\right) p(t) ,$$

with $T = 2\pi$.

17. (PRC for Andronov-Hopf) Consider a weakly perturbed system near supercritical Andronov-Hopf bifurcation (see section 6.1.3)

$$\dot{z} = (b + \mathrm{i})z + (-1 + d\mathrm{i})z|z|^2 + \epsilon p(t) , \qquad z \in \mathbb{C} .$$

with $b > 0$. Let $\varepsilon = b\sqrt{b}/\epsilon$ be small. Prove that the corresponding phase model is

$$\dot{\theta} = 1 + d + \varepsilon \, \mathrm{Im} \left\{ (1 + d\mathrm{i})p(t)e^{-\mathrm{i}\theta} \right\} .$$

When the forcing $p(t)$ is one-dimensional (i.e., $p(t) = cq(t)$ with $c \in \mathbb{C}$ and scalar function $q(t)$), the phase model has the sinusoidal form

$$\dot{\theta} = 1 + d + \varepsilon s \sin(\theta - \psi)q(t) ,$$

with the strength s and the phase shift ψ depending only on d and c.

18. (Delayed coupling) Show that weakly coupled oscillators

$$\dot{x}_i = f(x_i) + \varepsilon \sum_{j=1}^{n} g_{ij}(x_i(t), x_j(t - d_{ij}))$$

with explicit axonal conduction delays $d_{ij} \geq 0$ have the phase model

$$\varphi_i' = \omega_i + \sum_{j \neq i}^{n} H_{ij}(\varphi_j - d_{ij} - \varphi_i)$$

where $' = d/d\tau$, $\tau = \varepsilon t$ is the slow time, and $H(\chi)$ is defined by (10.16). Thus, explicit delays result in explicit phase shifts.

19. Determine the existence and stability of synchronized states in the system

$$\begin{aligned}
\dot{\varphi}_1 &= \omega_1 + c_1 \sin(\varphi_2 - \varphi_1) \\
\dot{\varphi}_2 &= \omega_2 + c_2 \sin(\varphi_1 - \varphi_2)
\end{aligned}$$

as a function of the parameters $\omega = \omega_2 - \omega_1$ and $c = c_2 - c_1$.

20. Consider the Kuramoto model

$$\dot{\varphi}_i = \omega + \sum_{j=1}^{n} c_{ij} \sin(\varphi_j + \psi_{ij} - \varphi_i) \, ,$$

where c_{ij} and ψ_{ij} are parameters. What can you say about its synchronization properties?

21. Derive the self-consistency equation (10.22) for the Kuramoto model (10.20).

22. Consider the phase deviation model

$$\begin{aligned} \varphi_1' &= \omega + c_1 H(\varphi_2 - \varphi_1) \\ \varphi_2' &= \omega + c_2 H(\varphi_1 - \varphi_2) \end{aligned}$$

with an even function $H(-\chi) = H(\chi)$. Prove that the in-phase synchronized state, $\varphi_1 = \varphi_2$, if it exists, cannot be exponentially stable. What can you say about the anti-phase state $\varphi_1 = \varphi_2 + T/2$?

23. Prove that the in-phase synchronized state in a network of three or more pulse coupled quadratic integrate-and-fire neurons is unstable.

24. Prove (10.25).

25. (Brown et al. 2004) Show that the PRC for an oscillator near saddle homoclinic orbit bifurcation scales as $\mathrm{PRC}\,(\vartheta) \sim e^{\lambda(T-\vartheta)}$, where λ is the positive eigenvalue of the saddle and T is the period of oscillation.

26. Consider the quadratic integrate-and-fire neuron $\dot{x} = \pm 1 + x^2$ with the resetting " if $x = +\infty$, then $x \leftarrow x_{\mathrm{reset}}$". Prove that

regime	SNIC	homoclinic
model	$x' = +1 + x^2$	$x' = -1 + x^2, (x_{\mathrm{reset}} > 1)$

period T	$\pi/2 - \mathrm{atan}\, x_{\mathrm{reset}}$	$\mathrm{acoth}\, x_{\mathrm{reset}}$
solution $x(t)$	$-\cot(t - T)$	$-\coth(t - T)$
PRC $Q(\vartheta)$	$\sin^2(\vartheta - T)$	$\sinh^2(\vartheta - T)$
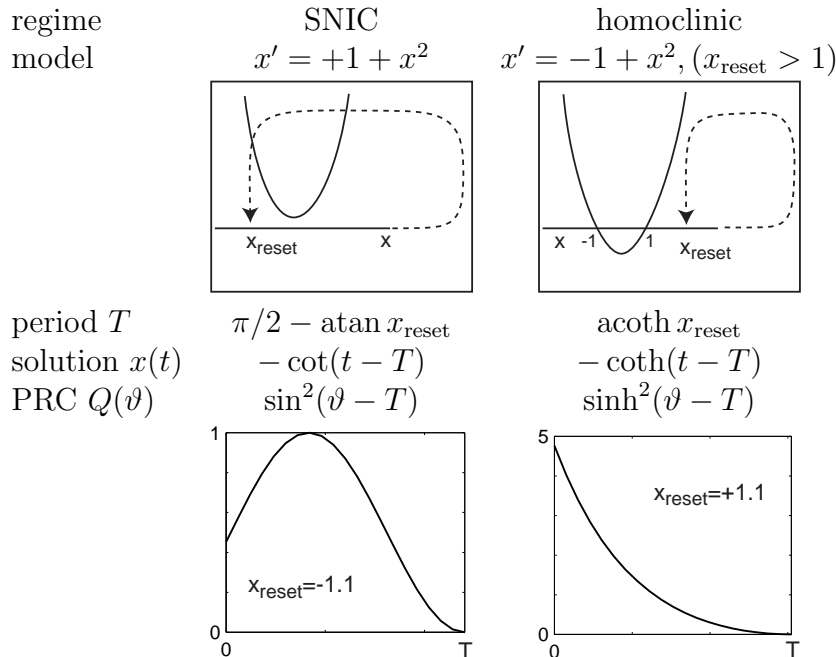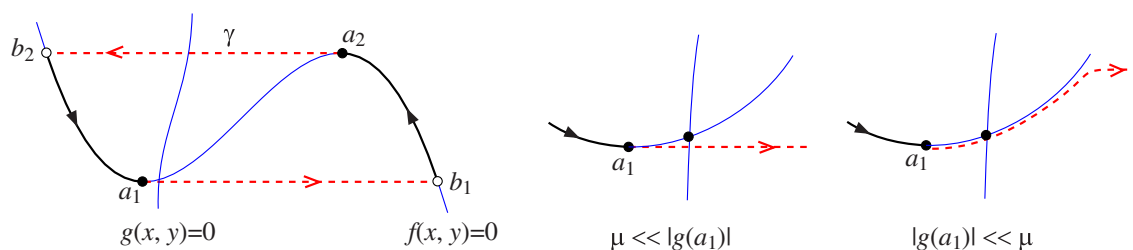
Figure 10.47: *Left:* Relaxation oscillator in the limit $\mu = 0$ near the onset of oscillation. *Middle and right*: A magnification of a neighborhood of the jump point a_1 for various $g(a_1)$ and μ. Canard solutions can appear when $g(a_1) \ll \mu$.

where coth, acoth, and sinh are hyperbolic cotangent, hyperbolic inverse cotangent and hyperbolic sine, respectively.

27. [**M.S.**] Derive the PRC for an oscillator near saddle homoclinic orbit bifurcation that is valid during the spike downstroke. Take advantage of the observation in Fig.10.39 that the homoclinic orbit consists of two qualitatively different parts.

28. [**M.S.**] Derive the PRC for a generic oscillator near fold limit cycle bifurcation (beware of the problems of defining the phase near such a bifurcation).

29. [**M.S.**] Simplify the connection function H for coupled relaxation oscillators (Izhikevich 2000b) when the slow nullcline approaches the left knee, as in Fig.10.47. Explore the range of parameters ε, μ, and $|g(a_1)|$ where the analysis is valid.

30. [**Ph.D.**] Use ideas outlined in section 10.4.5 to develop the theory of reduction of weakly coupled bursters to phase models. Do not assume that bursting trajectory is periodic.

Solutions to Chapter 10

1. In polar coordinates, $z = re^{i\vartheta}$, the system has the form

$$\dot{\vartheta} = 1 , \quad \dot{r} = r - r^3.$$

Since the phase of oscillation does not depend on the amplitude, the isochrons have the radial structure depicted in Fig.10.3.

2. In polar coordinates, the oscillator has the form

$$\dot{\vartheta} = 1 + dr^2 , \quad \dot{r} = r - r^3.$$

The second equation has an explicit solution $r(t)$, such that

$$r(t)^2 = \frac{1}{1 - (1 - 1/r(0)^2)e^{-2t}} .$$

The phase difference between $\dot{\vartheta}_{\mathrm{lc}} = 1 + d(1)^2$ and $\dot{\vartheta} = 1 + dr(t)^2$ grows as $\dot{\chi} = d(r(t)^2 - 1)$, and its asymptotic value is

$$\chi(\infty) = \int_0^\infty d(r(t)^2 - 1) = d \log r(0) \ .$$

Thus, on the χ-isochron, we have $\vartheta + d \log r = \chi$.

3. An example is the file `isochrons.m`

```
function isochrons(F,phases,x0)
% plot isochrons of a planar dynamical system x'=F(t,x)
% at points given by the vector 'phases'.
% 'x0' is a point on the limit cycle (2x1-vector)
T= phases(end); % is the period of the cycle
tau = T/600;    % time step of integration
m=200;          % spatial grid
k=5;            % the number of skipped cycles

[t,lc] = ode23s(F,0:tau:T,x0);        % forward integration
dx=(max(lc)-min(lc))'/m;              % spatial resolution
center = (max(lc)+min(lc))'/2;        % center of the limit cycle
iso=[x0-m^0.5*dx, x0+m^0.5*dx];       % isochron's initial segment

for t=0:-tau:-(k+1)*T                 % backward integration
    for i=1:size(iso,2)
        iso(:,i)=iso(:,i)-tau*feval(F,t,iso(:,i)); % move one step
    end;
    i=1;
    while i<=size(iso,2)              % remove infinite solutions
        if any(abs(iso(:,i)-center)>1.5*m*dx)    % check boundaries
            iso = [iso(:,1:i-1), iso(:,i+1:end)]; % remove
        else
            i=i+1;
        end;
    end;
    i=1;
    while i<=size(iso,2)-1
        d=sqrt(sum(((iso(:,i)-iso(:,i+1))./dx).^2)); % normalized distance
        if d > 2                         % add a point in the middle
            iso = [iso(:,1:i), (iso(:,i)+iso(:,i+1))/2 ,iso(:,i+1:end)];
        end;
        if d < 0.5                       % remove the point
            iso = [iso(:,1:i), iso(:,i+2:end)];
        else
            i=i+1;
        end;
    end;
    if (mod(-t,T)<=tau/2) & (-t<k*T+tau)         % refresh the screen
        cla;plot(lc(:,1),lc(:,2),'r'); hold on; % plot the limit cycle
    end;
    if min(abs(mod(-t,T)-phases))<tau/2   % plot the isochrons
        plot(iso(1,:),iso(2,:),'k-'); drawnow;
    end;
end;
```

```
hold off;
```

The call of the function is `isochrons('F',0:0.1:2*pi,[1;0]);` with

```
function dx = F(t,x);
z=x(1)+1i*x(2);
dz=(1+1i)*z-z*z*conj(z);
dx=[real(dz); imag(dz)];
```

4. (Hoppensteadt and Keener 1982) From calculus, $B \cdot C = |B| |C| \cos(\psi)$. Since $|B| = 1$ and $C = (A + \cos \vartheta, \sin \vartheta)$ – see Fig.10.46 – we have $B \cdot C = A \cos \vartheta + \cos^2 \vartheta + \sin^2 \vartheta$. Hence, $\cos \psi = (1 + A \cos \vartheta)/\sqrt{1 + 2A \cos \vartheta + A^2}$. When ϑ is in the upper (lower) half-plane, the phase is delayed (advanced).

5. An example is the file `prc.m`

```
function PRC=prc(F,phases,x0,A)
% plot phase-resetting curve (PRC) of system x'=F(t,x) + A delta(t)
% at points given by the vector 'phases'.
% 'x0' is a point on the limit cycle with zero phase
% A is the strength of stimulation (row-vector)
% use peaks of spikes to find the phase differences
T= phases(end); % is the period of the cycle
tau = T/6000;    % time step of integration
k=3;             % the number of cycles needed to determine the new phase
PRC=[];
[tc,lc] = ode23s(F,0:tau:k*T,x0); % find limit cycle
peak=1+find(lc(2:end-1,1)>lc(1:end-2,1)&lc(2:end-1,1)>=lc(3:end,1));
peak0 = tc(peak(end)); % the last peak is used for reference
for i=1:length(phases)
    [m,j]=min(abs(phases(i)-tc));
    [t,x] = ode23s(F,phases(i):tau:k*T,lc(j,:)+A); % stimulate
    peaks=1+find(x(2:end-1,1)>x(1:end-2,1)&x(2:end-1,1)>=x(3:end,1));
    PRC=[PRC, mod(T/2+peak0-t(peaks(end)),T)-T/2];
    subplot(2,1,2);drawnow;
    plot(phases(1:length(PRC)),PRC);
    xlabel('phase of stimulation');ylabel('induced phase difference');
    subplot(2,1,1);
    plot(tc,lc(:,1),'r',t,x(:,1),t(peaks(end)),x(peaks(end),1),'ro');
    xlabel('time');ylabel('membrane potential');
end;
```

An example of a call of the function is `PRC=prc('F',0:0.1:2*pi,[-1 0],[0.1 0]);` with

```
function dx = F(t,x);
z=x(1)+1i*x(2);
dz=(1+1i)*z-z*z*conj(z);
dx=[real(dz); imag(dz)];
```

6.

$$
\begin{aligned}
\operatorname{grad} \vartheta(x) &= \left(\frac{\vartheta(x + h_1) - \vartheta(x)}{h_1}, \ldots, \frac{\vartheta(x + h_m) - \vartheta(x)}{h_m} \right) \\
&= \left(\frac{\mathrm{PRC}_1(\vartheta(x), h_1)}{h_1}, \ldots, \frac{\mathrm{PRC}_m(\vartheta(x), h_m)}{h_m} \right)
\end{aligned}
$$

$$\text{(in the limit } h \to 0)$$

$$= \left(\frac{Z_1(\vartheta(x))h_1}{h_1}, \dots, \frac{Z_m(\vartheta(x))h_m}{h_m} \right)$$

$$= (Z_1(\vartheta(x)), \dots, Z_m(\vartheta(x))) = Z(\vartheta(x)) .$$

7. (Brown et al. 2004, appendix A) Let x be a point on the limit cycle and z be an arbitrary nearby point. Let $x(t)$ and $z(t)$ be the trajectories starting from the two points, and $y(t) = z(t) - x(t)$ be the difference. All equations below are valid up to $\mathcal{O}(y^2)$. The phase shift $\Delta\vartheta = \vartheta(z(t)) - \vartheta(x(t)) = \operatorname{grad}\vartheta(x(t)) \cdot y(t)$ does not depend on time. Differentiating with respect to time and taking $\operatorname{grad}\vartheta(x(t)) = Z(\vartheta(t))$ (see previous exercise), results in

$$
\begin{aligned}
0 &= (d/dt)\,(Z(\vartheta(t)) \cdot y(t)) = Z'(\vartheta(t)) \cdot y(t) + Z(\vartheta(t)) \cdot Df(x(t))y(t) \\
&= Z'(\vartheta(t)) \cdot y(t) + Df(x(t))^\top Z(\vartheta(t)) \cdot y(t) \\
&= \left(Z'(\vartheta(t)) + Df(x(t))^\top Z(\vartheta(t)) \right) \cdot y(t) .
\end{aligned}
$$

Since y is arbitrary, Z satisfies $Z'(\vartheta) + Df(x(\vartheta))^\top Z(\vartheta) = 0$, that is, the adjoint equation (10.10). The normalization follows from (10.7).

8. The solution to $\dot{v} = b - v$ with $v(0) = 0$ is $v(t) = b(1 - e^{-t})$ with the period $T = \ln(b/(b-1))$ determined from the threshold crossing $v(T) = 1$. From $v = b(1 - e^{-\vartheta})$ we find $\vartheta = \ln(b/(b-v))$, hence

$$\text{PRC}\,(\vartheta) = \vartheta_{\text{new}} - \vartheta = \min\,\{\ln(b/(b\exp(-\vartheta) - A), T\} - \vartheta .$$

9. The system $\dot{v} = 1 + v^2$ with $v(0) = -\infty$ has the solution (the reader should check this by differentiating) $v(t) = \tan(t - \pi/2)$ with the period $T = \pi$. Since $t = \pi/2 + \operatorname{atan} v$, we find

$$\text{PTC}\,(\vartheta) = \pi/2 + \operatorname{atan}\,[A + \tan(\vartheta - \pi/2)]$$

and

$$\text{PRC}\,(\vartheta) = \text{PTC}\,(\vartheta) - \vartheta = \operatorname{atan}\,[A + \tan(\vartheta - \pi/2)] - (\vartheta - \pi/2) .$$

10. The system $\dot{v} = b + v^2$ with $b > 0$ and the initial condition $v(0) = v_{\text{reset}}$ has the solution (the reader should check this by differentiating)

$$v(t) = \sqrt{b}\,\tan(\sqrt{b}(t + t_0))$$

where

$$t_0 = \frac{1}{\sqrt{b}}\,\operatorname{atan}\,\frac{v_{\text{reset}}}{\sqrt{b}} .$$

Equivalently,

$$t = \frac{1}{\sqrt{b}}\,\operatorname{atan}\,\frac{v}{\sqrt{b}} - t_0 .$$

From the condition $v = 1$ (peak of the spike), we find

$$T = \frac{1}{\sqrt{b}}\,\operatorname{atan}\,\frac{1}{\sqrt{b}} - t_0 = \frac{1}{\sqrt{b}}\left(\operatorname{atan}\,\frac{1}{\sqrt{b}} - \operatorname{atan}\,\frac{v_{\text{reset}}}{\sqrt{b}} \right) ,$$

Hence

$$\text{PRC}\,(\vartheta) = \vartheta_{\text{new}} - \vartheta = \min\,\{\frac{1}{\sqrt{b}}\,\operatorname{atan}\,[\frac{A}{\sqrt{b}} + \tan(\sqrt{b}(\vartheta + t_0))] - t_0, T\} - \vartheta .$$

11. Let ϑ denote the phase of oscillator 1. Let χ_n denote the phase of oscillator 2 just before oscillator 1 fires a spike (i.e., when $\vartheta = 0$). This spike resets χ_n to $\mathrm{PTC}_2(\chi_n)$. Oscillator 2 fires a spike when $\vartheta = T_2 - \mathrm{PTC}_2(\chi_n)$, and it resets ϑ to $\mathrm{PTC}_1(T_2 - \mathrm{PTC}_2(\chi_n))$. Finally, oscillator 1 fires its spike when oscillator 2 has the phase $\chi_{n+1} = T_1 - \mathrm{PTC}_1(T_2 - \mathrm{PTC}_2(\chi_n))$.

12. [MATLAB] An example is the file `adjoint.m`

```
function Q=adjoint(F,t,x0)
% finds solution to the Malkin's adjoint equation Q' = -DF^t Q
% at time-points t with t(end) being the period
% 'x0' is a point on the limit cycle with zero phase
tran=3;          % the number of skipped cycles
dx = 0.000001; dy = 0.000001;   % for evaluation of Jacobian

Q(1,:)=feval(F,0,x0)';            % initial point;
[t,x] = ode23s(F,t,x0);           % find limit cycle

for k=1:tran
  Q(length(t),:)=Q(1,:);          % initial point;
  for i=length(t):-1:2            % backward integration
    L = [(feval(F,t(i),x(i,:)+[dx 0])-feval(F,t(i),x(i,:)))/dx,...
         (feval(F,t(i),x(i,:)+[0 dy])-feval(F,t(i),x(i,:)))/dy];
    Q(i-1,:) = Q(i,:) + (t(i)-t(i-1))*(Q(i,:)*L);
  end;
end;
Q = Q/(Q(1,:)*feval(F,0,x0));     % normalization
```

An example of a call of the function is `Q=adjoint('F',0:0.01:2*pi,[1 0]);` with

```
function dx = F(t,x);
z=x(1)+1i*x(2);
dz=(1+1i)*z-z*z*conj(z);
dx=[real(dz); imag(dz)];
```

13. [MATLAB] We assume that $\mathrm{PRC}(\vartheta)$ is given by its truncated Fourier series with unknown Fourier coefficients. Then, we find the coefficients that minimize the difference between predicted and actual interspike intervals. The MATLAB file `findprc.m` takes the row vector of spike moments, not counting the spike at time zero, and the input function $p(t)$, determines the sampling frequency and the averaged period of oscillation; and then calls the file `prcerror.m` to find PRC.

```
function PRC=findprc(sp,pp)
global spikes p tau n
% finds PRC of an oscillator theta'= 1 + PRC(theta)pp(t)
% using the row-vector of spikes 'sp' (when theta(t)=0)
spikes = [0 sp];
p=pp;
tau = spikes(end)/length(p) % time step (sampling period)
n=8;     % The number of Fourier terms approximating PRC
coeff=zeros(1,2*n+1); % initial approximation
coeff(2*n+2) = spikes(end)/length(spikes); % initial period

coeff=fminsearch('prcerror',coeff);
a = coeff(1:n)      % Fourier coefficients for sin
```

```
b = coeff(n+1:2*n) % Fourier coefficients for cos
b0= coeff(2*n+1)   % dc term
T = coeff(2*n+2)   % period of oscillation
PRC=b0+sum((ones(floor(T/tau),1)*a).*sin((tau:tau:T)'*(1:n)*2*pi/T),2)+...
        sum((ones(floor(T/tau),1)*b).*cos((tau:tau:T)'*(1:n)*2*pi/T),2);
```

The following program must be in the file `prcerror.m`.

```
function err=prcerror(coeff)
global spikes p tau n
a = coeff(1:n);      % Fourier coefficients for sin
b = coeff(n+1:2*n); % Fourier coefficients for cos
b0= coeff(2*n+1);    % dc term
T = coeff(2*n+2);    % period of oscillation
err=0;
i=1;
clf;
for s=2:length(spikes)
    theta=0;
    while i*tau<=spikes(s)
        PRC=b0+sum(a.*sin((1:n)*2*pi*theta/T))+...
                sum(b.*cos((1:n)*2*pi*theta/T));
        theta = theta + tau*(1+PRC*p(i));
        i=i+1;
    end;
    err = err + (theta-T)^2;
    subplot(2,1,1);
    plot(spikes(s),T,'r.',spikes(s),theta,'b.');hold on;
end;
axis([0 spikes(end) 0.75*T 1.25*T])
subplot(2,1,2);
PRC=b0+sum((ones(floor(T/tau),1)*a).*sin((tau:tau:T)'*(1:n)*2*pi/T),2)+...
        sum((ones(floor(T/tau),1)*b).*cos((tau:tau:T)'*(1:n)*2*pi/T),2);
plot(PRC);
err = (err/(length(spikes)-1))^0.5;  % normalization
text(0,mean(PRC),['err=' num2str(err)]);
drawnow;
```

14. *Winfree approach:* Using results of exercise 8,

$$\frac{\partial}{\partial A} \ln \frac{b}{be^{-\vartheta} - A} = \frac{1}{be^{-\vartheta} - A}$$

and setting $A = 0$, we obtain $Z(\vartheta) = e^{\vartheta}/b$.

Kuramoto approach: The solution is $v(\vartheta) = b(1 - e^{-\vartheta})$ with $T = \ln(b/(b-1))$ and $f(v(\vartheta)) = be^{-\vartheta}$. From the condition (10.7), $\operatorname{grad}(\vartheta) = 1/f(v(\vartheta)) = e^{\vartheta}/b$.

Malkin approach: $Df = -1$; hence $\dot{Q} = 1 \cdot Q$ has the solution $Q(t) = Ce^{t}$. The free constant $C = 1/b$ is found from the normalization condition $Q(0) \cdot (b - 0) = 1$.

15. *Winfree approach:* Using results of exercise 10 and the relation PRC=PTC$-\vartheta$, we obtain,

$$\frac{\partial}{\partial A} (\pi/2 + \operatorname{atan}(A - \cot \vartheta) - \vartheta) = \frac{1}{1 + (A - \cot \vartheta)^2}$$

and, setting $A = 0$, $Z(\vartheta) = \sin^2 \vartheta$.

Kuramoto approach: The solution is $v(\vartheta) = -\cot \vartheta$ with $T = \pi$ and $f(v(\vartheta)) = 1/\sin^2 \vartheta$. From the normalization condition (10.7), $\operatorname{grad}(\vartheta) = 1/f(v(\vartheta)) = \sin^2 \vartheta$.

Malkin approach: $Df = 2v$, hence $\dot{Q} = 2\cot(t) \cdot Q$ has the solution $Q(t) = C \sin^2 t$. The free constant $C = 1$ is found from the normalization condition $Q(\pi/2) \cdot (1 + 0^2) = 1$.

16. *Winfree approach:* Using results of exercise 4,

$$Z(\vartheta) = \frac{\partial}{\partial A} \operatorname{acos} \frac{1 + A\cos\vartheta}{\sqrt{1 + 2A\cos\vartheta + A^2}} = -\sin\vartheta$$

at $A = 0$.

Kuramoto approach: Since $\operatorname{grad}\vartheta(x)$ is orthogonal to the contour line of the function $\vartheta(x)$ at x (i.e., the isochron of x) and the results of exercise 1 that isochrons are radial, we obtain $\operatorname{grad}(\vartheta) = (-\sin\vartheta, \cos\vartheta)$, using purely geometrical considerations. Since $p(t)$ is real, we need to keep only the first component.

Malkin approach: Let us work in the complex domain. On the circle $z(t) = e^{\dot{\mathrm{i}}t}$ we obtain $Df = \mathrm{i}$. Since $Df^\top$ is equivalent to complex-conjugation in the complex domain, we obtain $\dot{Q} = \mathrm{i} \cdot Q$, which has the solution $Q(t) = Ce^{\dot{\mathrm{i}}t}$. The free constant $C = \mathrm{i}$ is found from the normalization condition $Q(0)^*\mathrm{i} = 1$, where * means complex-conjugate.

Alternatively, on the circle $z(t) = e^{\dot{\mathrm{i}}t}$, we have $f(z(t)) = f(e^{\dot{\mathrm{i}}t}) = \mathrm{i}e^{\dot{\mathrm{i}}t}$. From the normalization condition $Q(t)^* f(z(t)) = 1$ we find $Q(t) = \mathrm{i}e^{\dot{\mathrm{i}}t} = -\sin\vartheta + \mathrm{i}\cos\vartheta$.

17. Rescaling the state variable $z = \sqrt{b}u$ and the time, $\tau = \epsilon t$, we obtain the reduced system

$$u' = (1 + \mathrm{i})u + (-1 + d\mathrm{i})u|u|^2 + \varepsilon p(t) .$$

We can apply the theory only when ε is small. That is, the theory is guaranteed to work in a very weak limit $\epsilon \ll b\sqrt{b} \ll 1$. As is often the case, numerical simulations suggest that the theory works well outside the guaranteed interval. Substituting $u = re^{\dot{\mathrm{i}}\theta}$ into this equation,

$$r'e^{\dot{\mathrm{i}}\theta} + re^{\dot{\mathrm{i}}\theta}\mathrm{i}\theta' = (1 + \mathrm{i})re^{\dot{\mathrm{i}}\theta} + (-1 + d\mathrm{i})r^3 e^{\dot{\mathrm{i}}\theta} + \varepsilon p(t) ,$$

dividing by $e^{\dot{\mathrm{i}}\theta}$, and separating real and imaginary terms, we represent the oscillator in polar coordinates

$$
\begin{aligned}
r' &= r - r^3 + \varepsilon \operatorname{Re} p(t)e^{-\dot{\mathrm{i}}\theta} \\
\theta' &= 1 + dr^2 + \varepsilon \operatorname{Im} r^{-1}p(t)e^{-\dot{\mathrm{i}}\theta} .
\end{aligned}
$$

When $\varepsilon = 0$, this system has a limit cycle attractor $r(t) = 1$ and $\theta(t) = (1 + d)t$, provided that $d \neq -1$. On the attractor, the solution to Malkin's adjoint equation (10.10),

$$Q' = - \begin{pmatrix} -2 & 0 \\ 2d & 0 \end{pmatrix}^\top Q \quad \text{with} \quad Q(t) \cdot \begin{pmatrix} 0 \\ 1 + d \end{pmatrix} = 1 ,$$

is $Q(t) = (d,\ 1)/(1+d)$. Indeed, the normalization condition results in $Q_2(t) = 1/(1+d)$. Hence, unique periodic solution of the first equation, $Q_1' = 2Q_1 - 2d/(1 + d)$, is $Q_1(t) = d/(1 + d)$. One can also use Kuramoto's approach and the results of exercise 2. The corresponding phase model,

$$\vartheta' = 1 + \varepsilon\{d\operatorname{Re} p(t)e^{-\dot{\mathrm{i}}(1+d)\vartheta} + \operatorname{Im} p(t)e^{-\dot{\mathrm{i}}(1+d)\vartheta}\}/(d + 1) ,$$

can be simplified via $\theta = (1 + d)\vartheta$ (notice the font difference) to get the result.

18. (Delayed coupling) Let $\vartheta(t) = t + \varphi(\tau)$, where $\tau = \varepsilon t$ is the slow time. Since $\vartheta(t - d) = t - d + \varphi(\tau - \varepsilon d) = t - d + \varphi(\tau) + \mathcal{O}(\varepsilon)$, we have $x_j(\vartheta_i(t - d_{ij})) = x_j(t - d_{ij} + \varphi(\tau))$, so that we can proceed as in section 10.2.5, except that there is an extra term, $-d_{ij}$, in (10.16). See also Izhikevich (1998).

19. Let $\chi = \varphi_2 - \varphi_1$; then we have

$$\dot{\chi} = \omega - c \sin \chi .$$

If $|\omega/c| \leq 1$, then there are two synchronized states, $\chi = \arcsin(\omega/c)$ and $\chi = \pi - \arcsin(\omega/c)$, one stable and the other unstable.

20. From the theorem of Hoppensteadt and Izhikevich (1997), presented in section 10.3.3, it follows that Kuramoto's model is a gradient system when $c_{ij} = c_{ji}$ and $\psi_{ij} = -\psi_{ji}$. From Ermentrout's theorem presented in the same section, it follows that the synchronized state $\varphi_i = \varphi_j$ is stable if, for example, all $\psi_{ij} = 0$ and $c_{ij} > 0$.

21. Since the probability density function $g(\omega)$ is symmetric, the averaged frequency deviation of the network is zero, and, rotating the coordinate system, we can make the cluster phase $\psi = 0$. The network is split into two populations: One oscillating with the cluster ($|\omega| < Kr$), thereby forming the cluster, and one drifting in and out of the cluster. The latter does not contribute to the Kuramoto synchronization index, because contributions from different oscillators cancel each other on average. In the limit $n \to \infty$, the sum (10.21) becomes the integral

$$r = \int e^{\mathbf{i}\varphi(\omega)} g(\omega) d\omega \approx \int_{|\omega|<Kr} e^{\mathbf{i}\varphi(\omega)} g(\omega) d\omega .$$

Next, since there are as many oscillators with positive φ as with negative, the imaginary parts of $e^{\mathbf{i}\varphi(\omega)}$ cancel each other, so that

$$r = \int_{|\omega|<Kr} \cos \varphi(\omega) g(\omega) d\omega .$$

Using the condition for locking with the cluster, $\omega = Kr \sin \varphi$, we change the variables in the integral and obtain (10.22).

22. Let $\chi = \varphi_2 - \varphi_1$; then $\chi' = (c_2 - c_1) H(\chi)$. The in-phase state $\chi = 0$ exists when either $c_1 = c_2$ or $H(0) = 0$. Since $H(\chi)$ is even, $H'(0) = 0$, and hence it is neutrally stable in either case. The anti-phase state $\chi = T/2$ exists when $H(T/2) = 0$, and it can be exponentially stable or unstable, depending on the sign of $H'(T/2)$.

23. See Izhikevich (1999), Sect IVB.

24. The exponential stability requirement is $G'(0) = -2H'(0) < 0$. Since $x'(t) = f(x(t))$, we have

$$TH'(0) = \int_0^T \frac{g'(x(t)) f(x(t))}{f(x(t))} \, dt = \int_0^T g'(x(t)) \, dt = \int_{\mathbb{S}^1} \frac{g'(x)}{f(x)} \, dx > 0$$

Integrating the latter equation by parts, or differentiating

$$H(\chi) = \frac{1}{T} \int_0^T \frac{g(x(t))}{f(x(t - \chi))} \, dt \qquad \text{at } \chi = 0, \text{ we obtain} \qquad \int_{\mathbb{S}^1} \frac{f'(x)}{f^2(x)} g(x) \, dx > 0 .$$

25. (Brown et al. 2004) The solution of $x' = \lambda x$ with $x(0) = x_0$ is $x(t) = x_0 e^{\lambda t}$. The period $T = \log(\Delta/x_0)/\lambda$ is found from the condition $x(T) = \Delta$. Hence, $Q(\vartheta) = 1/(\lambda x(\vartheta)) = 1/(\lambda x_0 e^{\lambda\vartheta}) = e^{\lambda(T-\vartheta)}/(\Delta\lambda)$.

26. Let us first consider the SNIC case $\dot{x} = 1 + x^2$. The solution starting with $x(0) = x_{\text{reset}}$ has the form (the reader should check by differentiating) $x(t) = \tan(t + t_0)$, where $t_0 = \operatorname{atan} x_{\text{reset}}$. The period should be found from the condition $\tan(T + t_0) = +\infty$, and it is $T = \pi/2 - t_0$. Hence, $x(t) = \tan(t + \pi/2 - T) = -\cot(t - T)$. Now, $Q(\vartheta) = 1/(1 + x(\vartheta)^2) = 1/(1 + \cot^2(\vartheta - T)) = \sin^2(\vartheta - T)$.

The homoclinic case $\dot{x} = -1 + x^2$ is quite similar. The solution starting with $x(0) = x_{\text{reset}} > 1$ has the form (the reader should check by differentiating) $x(t) = -\coth(t + t_0)$, where $t_0 = \operatorname{acoth}(-x_{\text{reset}}) = -\operatorname{acoth}(x_{\text{reset}})$. The period is found from the condition $-\coth(T + t_0) = +\infty$ resulting in $T = -t_0$. Hence, $x(t) = -\coth(t - T)$. Finally, $Q(\vartheta) = 1/(-1 + x(\vartheta)^2) = 1/(1 + \coth^2(\vartheta - T)) = \sinh^2(\vartheta - T)$.